



*Viktor Epp, Dipl.-Phys.*

LITHIUM DIFFUSIVITY  
— *in* —  
FAST SOLID-STATE IONIC CONDUCTORS  
≈  
*NMR and impedance spectroscopic studies*

DISSERTATION

zur Erlangung des akademischen Grades

*Doktor der Naturwissenschaften (Dr. rer. nat.)*

eingereicht an der

Technischen Universität Graz

Betreuer

*Univ.-Prof. Dr. Martin Wilkening*

Institut für Chemische Technologie von Materialien  
(ICTM)

Graz, September 2014



## **Affidavit**

I declare that I have authored this thesis independently, that I have not used other than the declared sources/resources, and that I have explicitly indicated all material which has been quoted either literally or by content from the sources used. The text document uploaded to TUGRAZonline is identical to the present doctoral dissertation.

## **Eidesstattliche Erklärung**

Ich erkläre an Eides statt, dass ich die vorliegende Arbeit selbstständig verfasst, andere als die angegebenen Quellen/Hilfsmittel nicht benutzt, und die den benutzten Quellen wörtlich und inhaltlich entnommenen Stellen als solche kenntlich gemacht habe. Das in TUGRAZonline hochgeladene Textdokument ist mit der vorliegenden Dissertation identisch.

---

Date / Datum

---

Signature / Unterschrift

*Mame & Pane*  
(to my parents)

Science's models are not *true*, and that's exactly what makes them useful. They tell simple stories that our minds can grasp. They are lies-to-children, simplified teaching stories, and none the worse for that. The progress of science consists of telling ever more convincing lies to ever more sophisticated children.

Terry Pratchett, Ian Stewart, and Jack Cohen  
*The Science of Discworld II – The Globe*



## Abstract

Problems associated with human-induced climate change seem to grow in frequency and severity. The fact that the impact of climate change is largely irreversible is by now established in the scientific community and slowly taking hold in the general population. Mitigation of its effects can only be achieved by a significant reduction in the output of greenhouse gases, which certainly will involve a shift from fossil fuels to green, renewable energy sources. As these new energy sources are mostly intermittent, efficient and safe energy storage systems are required — a rôle expected to be filled by Li-ion batteries, in the medium run. Here, the field of materials sciences plays a major part in the research for new and better solid ion conductors as components in future battery systems. Not only does it supply the much-needed materials, it also provides a wide range of methods for their thorough characterization.

The present work tries to approach this problem from the perspective of two such methods. Nuclear magnetic resonance (NMR) and impedance spectroscopy are used to characterize Li-ion conductors, providing a means to identify potential candidates to be used as solid electrolytes in safe all-solid-state batteries. The advantage of the methods applied lies in their wide dynamic window and temperature range. The results are presented cumulatively in the form published and peer-reviewed papers.

The materials investigated can be subdivided into three main categories of Li-ion conductors, *viz.* (i) fast, structurally complex compounds (Li argyrodites, garnet-type oxides), (ii) layer-structured compounds (hexagonal  $\text{LiBH}_4$ , Li-intercalated  $3\text{R-NbS}_2$ ,  $\text{LiC}_6$ ), and (iii) structurally disordered compounds (nanoengineered  $\text{LiBH}_4$  and  $\text{LiBH}_4\text{:Al}_2\text{O}_3$ , amorphous Li-Al-Si oxides). Here, two members of the first group can be regarded as promising candidates for solid electrolytes. The lithium argyrodite  $\text{Li}_6\text{PS}_5\text{Br}$  exhibits an extremely high Li-ion mobility, showing in jump rates in the order of  $10^9 \text{ s}^{-1}$  at ambient temperature and an activation energy of 0.2 eV. This corresponds to DC-conductivity values of  $10^{-3} \text{ S/cm}$  to  $10^{-2} \text{ S/cm}$ . The garnet “ $\text{Li}_{6.5}\text{La}_{2.5}\text{Ba}_{0.5}\text{ZrTaO}_{12}$ ” also shows high DC-conductivity values of  $10^{-4} \text{ S/cm}$  at room temperature, which NMR measurements indicate to be due to purely ionic motion. As a further prerequisite for the use as a solid electrolyte, the garnet additionally exhibits a very good chemical compatibility with the cathode material  $\text{Li}_2\text{FeMn}_3\text{O}_8$ . Of the layered compounds,  $\text{LiBH}_4$  and  $\text{Li}_{0.7}\text{NbS}_2$  turned out to be particularly interesting. Using frequency-dependent and temperature-variable NMR it was possible to measure spin-lattice relaxation (SLR) rate maxima showing a logarithmic frequency dependence on their high-temperature side. This characteristic unequivocally points to a two-dimensional diffusion process, thought to be responsible for the high Li diffusivity observed. Finally, in the nanoengineered two-phase composite  $\text{LiBH}_4\text{:Al}_2\text{O}_3$  a further model system was found, showing how high-energy ball milling can be used to modify the Li-ion mobility in otherwise poor conductors. Here, the introduction of a large volume fraction of hetero-interfaces has significantly enhanced the Li diffusivity, observed in increased SLR rates and a second, motionally narrowed contribution to the NMR line.

*Keywords: NMR, relaxation, impedance spectroscopy, Li diffusion, fast ion conducting materials, solid electrolytes, 2D diffusion, nanostructured materials*



# Contents

<b>1</b>	<b>Introduction</b>	<b>1</b>
<b>2</b>	<b>Diffusion in solids</b>	<b>3</b>
2.1	The concept of diffusion . . . . .	3
2.1.1	Introduction . . . . .	3
2.1.2	The continuum approach to diffusion . . . . .	4
2.1.3	The atomistic approach to diffusion . . . . .	5
2.1.4	The various types of diffusion coefficients . . . . .	9
2.1.5	The temperature dependence of the diffusion coefficient . . . . .	10
2.1.6	Diffusion and defects . . . . .	11
2.1.7	Mechanisms of diffusion . . . . .	12
2.2	The measurement of diffusion coefficients . . . . .	14
2.2.1	Direct methods . . . . .	14
2.2.2	Indirect methods . . . . .	15
2.3	Solid-state nuclear magnetic resonance . . . . .	18
2.3.1	Introduction . . . . .	18
2.3.2	Basics of NMR . . . . .	18
2.3.3	NMR relaxation . . . . .	26
2.3.4	Spin-alignment echo NMR . . . . .	34
2.4	Basics of impedance spectroscopy . . . . .	36
2.4.1	Introduction . . . . .	36
2.4.2	Conductivity spectra and diffusion . . . . .	39
<b>3</b>	<b>Results</b>	<b>43</b>
3.1	Introduction . . . . .	43
3.2	Argyrodite-type Li-ion conductors . . . . .	46
3.2.1	Long-range Li <sup>+</sup> dynamics in the lithium argyrodite Li <sub>7</sub> PSe <sub>6</sub> as probed by rotating-frame spin-lattice relaxation NMR . . . . .	46
3.2.2	Highly mobile ions: Low-temperature NMR directly probes extremely fast Li <sup>+</sup> hopping in argyrodite-type Li <sub>6</sub> PS <sub>5</sub> Br . . . . .	57
3.3	Garnet-type Li-ion conductors . . . . .	64
3.3.1	Spin-alignment echo NMR: Probing Li <sup>+</sup> hopping motion in the solid electrolyte Li <sub>7</sub> La <sub>3</sub> Zr <sub>2</sub> O <sub>12</sub> with garnet-type tetragonal structure . . . . .	64

---

3.3.2	Macroscopic and microscopic Li <sup>+</sup> transport parameters in cubic garnet-type “Li <sub>6.5</sub> La <sub>2.5</sub> Ba <sub>0.5</sub> ZrTaO <sub>12</sub> ” as probed by impedance spectroscopy and NMR . . . . .	73
3.4	Layer-structured Li-ion conductors . . . . .	83
3.4.1	Fast Li diffusion in crystalline LiBH <sub>4</sub> due to reduced dimensionality: Frequency-dependent NMR spectroscopy . . . . .	83
3.4.2	Two-dimensional diffusion in Li <sub>0.7</sub> NbS <sub>2</sub> as directly probed by frequency-dependent <sup>7</sup> Li NMR . . . . .	88
3.4.3	Lithium motion in the anode material LiC <sub>6</sub> as seen via time-domain <sup>7</sup> Li NMR . . . . .	96
3.5	Structurally disordered Li-ion conductors . . . . .	106
3.5.1	Motion of Li <sup>+</sup> in nanoengineered LiBH <sub>4</sub> and LiBH <sub>4</sub> :Al <sub>2</sub> O <sub>3</sub> — Comparison with the microcrystalline form . . . . .	106
3.5.2	Studying Li dynamics in a gas-phase synthesized amorphous oxide by NMR and impedance spectroscopy . . . . .	115
<b>4</b>	<b>Conclusion and outlook</b>	<b>129</b>
<b>A</b>	<b>Supplemental material</b>	<b>131</b>
<b>B</b>	<b>Experimental</b>	<b>135</b>
B.1	Apparatus . . . . .	135
B.1.1	Solid-state NMR setup . . . . .	135
B.1.2	Impedance spectroscopy setup . . . . .	136
B.2	Software . . . . .	137
B.3	NMR pulse sequences . . . . .	138
B.3.1	Saturation recovery pulse sequence . . . . .	138
B.3.2	Solid-state echo pulse sequence . . . . .	139
B.3.3	<sup>7</sup> Li NMR SAE pulse sequence . . . . .	139
<b>C</b>	<b>List of publications</b>	<b>143</b>
C.1	Journal articles . . . . .	143
C.2	Poster presentations . . . . .	144
	<b>Bibliography</b>	<b>147</b>
	<b>Acknowledgments</b>	<b>157</b>

# 1 Introduction

The overwhelming consensus of the scientific community today is that the phenomenon of human-induced climate change is not only undeniable but that its impact is largely irreversible. It seems that our best hope is its mitigation by reducing the output of greenhouse gases and an adaptation to the changes already in effect.<sup>[1,2]</sup> Challenged with this problem, we as a society cannot help but change our habits vis-à-vis over-reliance on and overuse of fossil fuels. This is hoped to be achieved by a shift towards green, renewable energy sources. However, considering *e. g.* solar energy, wind power, or hydropower, these sources are largely intermittent, *i. e.* they are not equally readily available at all times. This calls for a means to store the energy generated in such a way as to allow a steady supply.<sup>[3]</sup> Moreover, a massive-scale introduction of hybrid vehicles and plug-in electric cars is expected to significantly curb world-wide emission of greenhouse gases (as well as reduce local air pollution levels).<sup>[3,4]</sup> This requires efficient and above all safe energy storage systems. Additionally, improved battery technology is certainly in high demand due to the enormous growth portable consumer electronics and electric tools have seen in the last two decades.

Currently, the rôle of such energy storage systems is filled by secondary Li-ion batteries, and this is expected to continue in the medium run. The two key aspects to consider in this regard are performance and safety.<sup>[5-7]</sup> One strategy of enhancing the latter is the development of all-solid-state batteries, replacing the volatile and flammable liquid electrolyte by a fast ion conducting solid. As for the performance, this relies on the research on new energy materials, or on the improvement of already known ones. Here, the last point is not to be underrated, as it can be as effective as the synthesis of wholly new materials. Particularly, the introduction of structural disorder as well as different kinds of interfaces via high-energy ball milling can lead to a dramatic enhancement of the transport properties of a given compound.<sup>[8-11]</sup> In this regard, layer-structured materials into which Li can be reversibly inserted are not only interesting as electrode materials in rechargeable batteries. Considering the relative scarcity of experimental studies from an atomic-scale point of view, many examples can be found also showing enhanced transport properties in such compounds.<sup>[12-18]</sup>

The field of materials science is of significant importance in the research on highly conductive solids suitable for the employment in Li-ion batteries, either as electrolytes or as electrodes. For whatever the route of preparation, in order to understand the origins of fast ion mobility, a thorough characterization of the materials is indispensable. Illuminating structure–property relationships is hoped to allow for a knowledge-based manipulation of ion dynamics in future battery materials. This can only be realized by thorough, reliable and detailed investigations of diffusion parameters, ideally probed on complementary time and length scales, as well as over a wide temperature range.

An appropriate tool for such fundamental studies is certainly found in solid-state nuclear magnetic resonance (NMR), which offers a great variety of techniques covering a wide dynamic window from an atomic-scale point of view. This enables access to diffusion parameters recorded on quite different time and length scales. In favorable cases, *i. e.* when so-called NMR spin-lattice relaxation (SLR) rate peak maxima can be recorded, diffusion coefficients can be calculated in a relatively model-independent way. What is more, recording the rates as a function of temperature and resonance frequency allows one to study the influence of correlation effects and dimensionality of the diffusion process, respectively. In some cases, the jump rate of a single particle can be directly measured by spin-alignment echo (SAE) NMR. As a complementary technique impedance spectroscopy (IS) was employed to gain access to long range Li ion dynamics from a macroscopic point of view in a fairly straightforward way.\*

This dissertation will begin with an introductory theoretical chapter, where the reader is familiarized with the concept of diffusion (Sect. 2.1). It is followed by a brief overview of some methods available to the field of solid state ionics for the measurement of diffusion coefficients (Sect. 2.2). The techniques used to acquire the data presented here will be covered in some more detail in sections 2.3 (NMR) and 2.4 (IS). In chapter 3 the results obtained in the course of this dissertation will be presented cumulatively in the form of published (and peer-reviewed) papers. This thesis will conclude with a short summary and an outlook on possible future work. Additionally, in the appendices the supplemental material to two of the papers and experimental information will be found.

---

\* Provided that  $\text{Li}^+$  is the only mobile charge carrier. Otherwise, the very simple experimental setup is complicated by the necessity to exclude contributions from other charge carriers.

## 2 Diffusion in solids

### 2.1 The concept of diffusion

#### 2.1.1 Introduction

The ubiquity and importance of solid state diffusion in the natural sciences are highlighted in many of the texts on this topic, *cf. e. g.* Refs. [19–22]. To use the words of Mehrer<sup>[22]</sup> as an important representative in this field:

☞ Diffusion is the transport of matter from one point to another by thermal motion of atoms or molecules. It is relatively fast in gases, slow in liquids, and very slow in solids. Diffusion plays a key rôle in many processes as diverse as intermixing of gases and liquids, permeation of atoms or molecules through membranes, evaporation of liquids, drying of timber, doping silicon wafers to make semiconductor devices, and transport of thermal neutrons in nuclear power reactors. Rates of important chemical reactions are limited by how fast diffusion can bring reactants together or deliver them to reaction sites on enzymes or other catalysts. ☞

Diffusion, *viz.* the transport of particles against a concentration gradient driven by their thermal motion, was first given a mathematical framework by the then very young physiologist Adolf Fick<sup>[23]</sup> in 1855 in the form of what are now known as *Fick's laws of diffusion*.<sup>[24,25]</sup> These laws were derived phenomenologically in analogy to the conduction of heat and electricity, regarding diffusion in a continuous medium (initially for liquid diffusion). In the publication introducing his “fundamental law”<sup>[25]</sup>, Fick also developed the concept of the diffusion coefficient, now a very important characteristic parameter in materials science, particularly in the field of solid state ionics.

While Fick's phenomenological approach provides an appropriate description of diffusion in a continuous medium under a chemical potential gradient, it is somewhat unsatisfactory in light of the microscopic structure of real matter. With the ever increasing acceptance of the physical reality of the atomistic picture of solid state matter towards the end of the 19th and the beginning of the 20th century—*i. e.*, in the context of an ordered, crystalline structure—the dependence of the ionic movement on the existence of atomic defects became obvious and an atomistic description of diffusion necessary. This was provided 50 years after Fick's work with several publications on *Brownian motion* by Albert Einstein starting in 1905 and—working independently of him—by Marian von Smoluchowski in 1906.<sup>[26–29]</sup>

The history of scientific discoveries is certainly very interesting in and of itself, and this is no less true for the historical development of diffusion and the field of solid state ionics, so closely associated with it. However, a complete (or, for that matter, even a cursory) account is clearly beyond the scope of this thesis and the interested reader is referred to suitable sources covering more of the historical background and illuminating the rôle of many of the key figures active in the development of our understanding of diffusion processes. Just to name a few: Jean Philiberts article “One and a Half Century of Diffusion: Fick, Einstein, before and beyond”<sup>[23]</sup> covers the very beginnings of the conceptualization of diffusion with its most prominent protagonists at the center. The article was published in the otherwise also very interesting second volume of the online journal **diffusion-fundamentals.org**, containing the electronic contributions to the first Diffusion-Fundamentals Conference in Leipzig, Germany in 2005. Later, these contributions were edited by Jörg Kärger in the form of the very nice book “Leipzig, Einstein, Diffusion”.<sup>[30]</sup> Also of great interest is Helmut Mehrers “Diffusion in Solids”,<sup>[22]</sup> not only does it contain a fair amount of the history of diffusion in its first chapter, it is also a very detailed introduction to the principles of diffusion and is recommended to anyone interested in familiarizing themselves with solid state diffusion. The emergence and development of the field of *solid state ionics* itself is discussed in a very recent review by Klaus Funke, placing a focus on its history from a European perspective.<sup>[31]</sup>

### 2.1.2 The continuum approach to diffusion

First, let us consider the diffusion of particles in an isotropic medium in an arbitrary direction  $x$ . Drawing parallels to the theory of heat transport and the conduction of electricity, Fick postulated what is now known as *Fick's first law*. Here, the particle flux in  $x$ -direction  $j_x$  is related to the concentration of the particles  $c$ —or, to be more precise, to the gradient of the concentration in  $x$ -direction  $\partial c/\partial x$ —in such a way that

$$j_x = -D \frac{\partial c}{\partial x} . \quad (2.1)$$

The minus sign signifies the fact that a concentration gradient will always result in a particle flux leading to the equalization of the concentration. The constant of proportionality  $D$  is the *diffusion coefficient* (also known as the *diffusivity*). The generalization to three dimensions is straightforward and achieved by a shift to vector quantities:

$$\mathbf{j} = -D \nabla c . \quad (2.2)$$

Here, the symbol *nabla*  $\nabla \equiv (\partial/\partial x, \partial/\partial y, \partial/\partial z)$  represents the vector differential operator and  $\mathbf{j} \equiv (j_x, j_y, j_z)$  the three-dimensional particle flux. In an isotropic medium the diffusion coefficient in Eqs. (2.1) and (2.2) is indeed the same. This is a special case; generally,  $D$  is dependent on the direction of the concentration gradient and denoted by a tensor  $\hat{D}$ . However, in the context of the present work the equations for isotropic diffusion still hold. Here, the

experiments were performed on polycrystalline powders, which *per se* have no macroscopic crystalline orientation, and thus an average diffusion coefficient  $D \equiv \langle D \rangle$  is measured.

Since it is extremely difficult to measure the particle flux in solid state matter directly,<sup>[20]</sup> Eq. (2.2) is combined with the *equation of continuity*

$$\frac{\partial c}{\partial t} = -\nabla \cdot \mathbf{j} . \quad (2.3)$$

The premise of the validity of this equation is the assumption that the number of the diffusing particles is conserved. The combination of both equations results in *Fick's second law*<sup>\*</sup>

$$\frac{\partial c}{\partial t} = \nabla \cdot (D \nabla c) , \quad (2.4)$$

a second-order partial differential equation. It is non-linear if  $D$  is a function of concentration, as in the case of the *interdiffusion coefficient* (*i. e.*, for diffusion in a chemical composition gradient; see below), and can usually be only solved numerically. If, however, the diffusivity is independent of concentration (*i. e.*, diffusion in a chemically homogeneous material) Eq. (2.4) can be simplified to

$$\frac{\partial c}{\partial t} = D \nabla^2 c \equiv D \Delta c , \quad (2.5)$$

where  $\Delta \equiv \nabla^2 \equiv \partial^2/\partial x^2 + \partial^2/\partial y^2 + \partial^2/\partial z^2$  signifies the Laplace operator. This expression can be solved analytically for a number of initial and boundary conditions. The conditions are chosen according to the problem under investigation. The resulting solution  $c(x, t)$  can be used as a fitting function with the diffusivity  $D$  as a parameter.  $D$  is then obtained by simply fitting the analytical solution to the experimental concentration profile  $c_{\text{exp}}(x, t)$ . Various solutions of the diffusion equation can be found in the works of, *e. g.*, Murch<sup>[20]</sup> and Mehrer<sup>[22]</sup> and the references given therein.

### 2.1.3 The atomistic approach to diffusion

Einstein and Smoluchowski derived an atomistic description for diffusion by trying to find an explanation for one of the unsolved questions of their time, *viz.* the Brownian motion of microscopic particles (*i. e.* particles with diameters in the  $\mu\text{m}$  range) suspended in a liquid. This erratic, random motion was described by the botanist Robert Brown in 1828<sup>[32]</sup> and lacked a satisfying explanation up to the publications of Einstein and Smoluchowski.<sup>[26,28]</sup> Both realized the significance of the *mean square displacement* of the particles as the basic quantity of diffusion. They related the motion of the comparatively large particles to the motion of the molecules of the liquid and thus made a compelling case for the real existence of atoms—which was still a hotly debated subject at that time.<sup>[23]</sup> Below, an expression for the

\* Which is sometimes also known as the *diffusion equation*.

diffusion coefficient will be deduced, following the derivation shown by Mehrer,<sup>[22]</sup> who in turn follows that of Einstein.<sup>[26]</sup> This derivation is based on the premise that the observed macroscopic displacement of particles is the sum of their successive microscopic jumps.

Let us consider the most simple case of particles diffusing on a cubic lattice.\* The total displacement  $\mathbf{R} = (X, Y, Z)$  of a particle is the sum of its individual jumps  $\mathbf{r}_i = (x_i, y_i, z_i)$  and is given as

$$\mathbf{R} = \sum_i \mathbf{r}_i . \quad (2.6)$$

For the sake of simplicity, we regard the projection of  $\mathbf{R}$  onto the  $x$ -axis and keep in mind that the following steps are equally valid for the other components. Then, the probability that a particle will be found at position  $X$  after a period of time  $\Delta t$  can be encoded with the *distribution function*  $W(X, \Delta t)$ . Its exact form does not need to be known; we assume that  $W(X, \Delta t)$  is independent of the particle's origin and that it is normalized:

$$\sum_X W(X, \Delta t) = 1 . \quad (2.7)$$

Additionally, it can be used to define moments of  $n$ -th order:

$$\langle X^n \rangle = \sum_X X^n W(X, \Delta t) . \quad (2.8)$$

Here, as well as below, the sum is performed over all lattice planes  $X$ . Further assuming that the total number of diffusing particles is conserved, the concentration  $c(x, t + \Delta t)$  in the plane  $x$  at the time  $t + \Delta t$  can be related to their concentration at  $x - X$  and  $t$  by

$$c(x, t + \Delta t) = \sum_X c(x - X, t) W(X, \Delta t) . \quad (2.9)$$

A Taylor series expansion around  $\Delta t = 0$  and  $X = 0$  results in

$$c(x, t) + \frac{\partial c}{\partial t} \Delta t + \dots = \sum_X \left( c(x, t) - \frac{\partial c}{\partial x} X + \frac{1}{2} \frac{\partial^2 c}{\partial x^2} X^2 + \dots \right) W(X, \Delta t) . \quad (2.10)$$

For small values of  $\Delta t$  the higher order terms on the left-hand side can be discarded; also, in this case the distribution function will be localized around  $X = 0$ . Thus the terms of the third order and higher can be also neglected on the right-hand side. Given that the concentration

---

\* As we shall see in Sect. 2.1.7, this is the case for the migration of interstitials on the interstice sub-lattice of a simple cubic crystal.

terms no longer depend on  $X$  they can be written outside the summation operator and Eq. (2.10) simplifies to

$$c(x, t) + \frac{\partial c}{\partial t} \Delta t = c(x, t) \sum_X W(X, \Delta t) - \frac{\partial c}{\partial x} \sum_X XW(X, \Delta t) + \frac{1}{2} \frac{\partial^2 c}{\partial x^2} \sum_X X^2 W(X, \Delta t). \quad (2.11)$$

Taking Eqs. (2.7) and (2.8) into account, Eq. (2.11) can be rewritten as

$$\frac{\partial c}{\partial t} = -\frac{\langle X \rangle}{\Delta t} \frac{\partial c}{\partial x} + \frac{\langle X^2 \rangle}{2\Delta t} \frac{\partial^2 c}{\partial x^2}. \quad (2.12)$$

Here, the first moment term corresponds to a drift term and vanishes if no external driving force (e. g. an electric field) is present. We are left with the second moment term corresponding to the diffusion term. Now, Eq. (2.12) formally resembles the diffusion equation (2.5) in  $x$ -direction and an expression for the corresponding diffusion coefficient can be derived:

$$D_x = \frac{\langle X^2 \rangle}{2\Delta t}. \quad (2.13)$$

The same derivation holds for the components  $Y$  and  $Z$ , so that

$$D_y = \langle Y^2 \rangle / 2\Delta t \quad (2.14a)$$

$$D_z = \langle Z^2 \rangle / 2\Delta t. \quad (2.14b)$$

For an isotropic medium the diffusion coefficients along directions  $x$ ,  $y$ , and  $z$  will be equal:

$$D_x = D_y = D_z \equiv D. \quad (2.15)$$

Thus, the same will be true for the second moments, and using  $\langle R^2 \rangle = \langle X^2 \rangle + \langle Y^2 \rangle + \langle Z^2 \rangle$  (cf. equation (2.8)),

$$\langle X^2 \rangle = \langle Y^2 \rangle = \langle Z^2 \rangle = \frac{1}{3} \langle R^2 \rangle \quad (2.16)$$

can be arrived at. Here,  $\langle R^2 \rangle$  is the *mean square displacement* of a given particle. Combining Eqs. (2.13), (2.15), and (2.16) and introducing the dimensionality of the diffusion process  $d$ , the isotropic diffusion coefficient is expressed by

$$D = \frac{\langle R^2 \rangle}{2d\Delta t}. \quad (2.17)$$

This equation is now known as the *Einstein-Smoluchowski relation*.

Now, let us consider the mean square displacement  $\langle R^2 \rangle$  in Eq. (2.17). Taking the total displacement  $\mathbf{R}$  as a sum of  $n$  elementary jumps  $\mathbf{r}_i$  (cp. equation (2.6)), the square displacement  $R^2$  can be then written

$$\mathbf{R}^2 = \left( \sum_{i=1}^n \mathbf{r}_i \right)^2 = \sum_{i=1}^n \mathbf{r}_i^2 + 2 \sum_{i=1}^{n-1} \sum_{j=i+1}^n \mathbf{r}_i \mathbf{r}_j. \quad (2.18)$$

Using  $\langle \dots \rangle$  to denote the average over the particle ensemble, the mean square displacement is then given as

$$\langle \mathbf{R}^2 \rangle = \sum_{i=1}^n \langle \mathbf{r}_i^2 \rangle + 2 \sum_{i=1}^{n-1} \sum_{j=i+1}^n \langle \mathbf{r}_i \mathbf{r}_j \rangle. \quad (2.19)$$

The grouping into the two terms becomes apparent, if we first consider uncorrelated movement of the particles, *i. e.*, if their individual jumps are not influenced by their previous positions. Then, the double sum vanishes because in an ensemble average for every product  $\mathbf{r}_i \mathbf{r}_j$  there will be another one with an equal absolute value  $|\mathbf{r}_i \mathbf{r}_j|$  but the opposite sign. Thus, for a truly random, uncorrelated diffusion process we can define

$$\langle \mathbf{R}^2 \rangle_{\text{uc}} = \sum_{i=1}^n \langle \mathbf{r}_i^2 \rangle. \quad (2.20)$$

Assuming the simple case of a cubic lattice, the individual jumps will be all of the same length  $|\mathbf{r}_i| = \ell$  and the sum in Eq. (2.20) can be expressed as

$$\sum_{i=1}^n \langle \mathbf{r}_i^2 \rangle = n\ell^2. \quad (2.21)$$

This can now be combined with Eq. (2.17) to arrive at an expression for the *uncorrelated diffusion coefficient*

$$D^{\text{uc}} = \frac{n\ell^2}{2d\Delta t} = \frac{\ell^2}{2d\bar{\tau}}, \quad (2.22)$$

where  $\bar{\tau} = \Delta t/n$  is the mean residence time of a particle on a lattice site, and  $\bar{\tau}^{-1}$  its mean jump rate.

However, generally correlation effects will be present; in a crystal, this is always the case if diffusion is not caused solely by the interstitial mechanism (*cf. e. g.* Refs. [20, 22]). They can then be formally accounted for by a *correlation factor*  $f$  defined as the ratio between Eqs. (2.19) and (2.20)

$$f = \lim_{n \rightarrow \infty} \frac{\langle \mathbf{R}^2 \rangle}{\langle \mathbf{R}^2 \rangle_{\text{uc}}} = 1 + 2 \lim_{n \rightarrow \infty} \frac{\sum_{i=1}^{n-1} \sum_{j=i+1}^n \langle \mathbf{r}_i \mathbf{r}_j \rangle}{\sum_{i=1}^n \langle \mathbf{r}_i^2 \rangle}. \quad (2.23)$$

The limit  $n \rightarrow \infty$  is applied in order to consider all possible correlations.<sup>[20]</sup> A comparison of Eqs. (2.17), (2.22), and (2.23) shows that a diffusion coefficient  $D^{\text{tr}}$  accounting for correlation effects is expressed by

$$D^{\text{tr}} = fD^{\text{uc}} = f \frac{\ell^2}{2d\bar{\tau}}. \quad (2.24)$$

$D^{\text{tr}}$  is known as the *tracer diffusion coefficient* and refers to microscopic (tracer) diffusion in a chemically homogeneous lattice.

### 2.1.4 The various types of diffusion coefficients

Depending on the conditions in which diffusion takes place, various diffusion coefficients can be differentiated. Here, the discussion will be limited to the common cases of bulk diffusion in binary systems, since complications such as ternary systems or diffusion along grain boundaries introduce additional complexities, which are beyond the scope of the present work and are dealt with in the appropriate literature; see *e. g.* Ref. [22].

#### Tracer diffusion coefficients

The diffusion coefficient most pertinent to this work is the *tracer diffusion coefficient*. Here, two cases are distinguished, depending on whether the diffusing tracer is chemically the same as the host material or a different species. In the first case the diffusion coefficient is called the *self-diffusion coefficient*, in the second case it is known as the *impurity diffusion coefficient*.

The most basic example for self-diffusion is the migration of atoms in a pure metal. In order to measure the self-diffusion coefficient a concentration gradient of tracer atoms is introduced by depositing a thin layer of the tracer on one side of the sample. Suitable tracer atoms are distinguished from the host metal by either their radioactivity or their isotopic mass; methods for the determination of concentration profiles exist for both cases (*cf.* Sect. 2.2). All these methods have in common that the sample is held at a constant temperature  $T$  for a certain duration  $t$ . Subsequently, the distribution of the tracer atoms is probed along their concentration gradient. The resulting concentration profile is compared to the solution of the diffusion equation (2.5) applicable to the initial and boundary conditions at hand and the diffusion coefficient  $D^{\text{tr}}$  is derived as a fitting parameter.

The above also applies to systems of a more complex composition such as ionic crystals, if only one species shows significant mobility and the rest can be considered as an immobile matrix. The overall tracer concentration is kept low so as to exclude interactions between the tracer atoms, but also in order to preclude a chemical composition gradient in the sample. As such, tracer diffusion takes place in chemical equilibrium.

In the case of impurity diffusion similar considerations apply as for self-diffusion, with the difference that here the tracer atoms are chemically different from the host material.\* From this follows that the impurity diffusion coefficient is dependent on the tracer as well as the host material.

### Chemical diffusion coefficient

Generally, a concentration gradient is not the sole driving force for the migration of particles. In a situation where a chemical composition gradient is present—thus, in distinction from tracer diffusion—a *chemical diffusion coefficient* (also known as *interdiffusion coefficient*)  $\tilde{D}$  is measured. Here, the particle flux is proportional to a gradient of the chemical potential resulting from a non-ideal mixture of the components involved. This means that the diffusion coefficient is no longer independent of the concentration  $c$  and that the non-simplified form of the diffusion equation (2.4) has to be used to determine  $\tilde{D}(c)$ . For a constant volume, this is usually achieved by the Boltzmann-Motano method; related methods accounting for volume changes were derived by Sauer and Freise and den Broeder (see Ref. [22] and the references therein for a description of the methods).

### Intrinsic diffusion coefficients

Closely related to the chemical diffusion coefficient are the *intrinsic diffusion coefficients* (also known as *compound diffusion coefficients*). Given a binary alloy of the form A-B the diffusion coefficients  $D_A^I$  and  $D_B^I$  characterize the diffusion of the individual components A and B relative to the lattice planes of the sample.  $D_A^I$  and  $D_B^I$  are usually not equal, thus a net flux of atoms across the lattice planes exists. Consequently, this leads to a phenomenon known as *Kirkendall effect*, whereby the lattice planes themselves shift relative to a fixed coordinate system outside the sample (or rather, outside the diffusion zone). The velocity of this shift, the Kirkendall velocity  $v_K$ , can be measured by the incorporation of inert markers and the observation of their movement over time. The intrinsic diffusion coefficients can then be deduced from the chemical diffusion coefficient  $\tilde{D}$  and the Kirkendall velocity using the *Darken relations* or the more complete *Darken-Manning relations*.<sup>[20–22]</sup>

#### 2.1.5 The temperature dependence of the diffusion coefficient

The temperature dependence of the diffusion coefficient is often found to follow Arrhenius behavior

$$D = D_0 \exp\left(-\frac{\Delta H}{k_B T}\right), \quad (2.25)$$

\* Again, the concentration of the tracer has to be kept so low that the composition of the sample can be assumed as nearly constant.

where  $D_0$  is the pre-exponential factor,  $\Delta H$  the activation enthalpy,  $k_B$  Boltzmann's constant, and  $T$  the temperature. At a constant pressure  $p$ ,  $\Delta H$  can be expressed as  $\Delta H = \Delta E + p\Delta V$ . Here,  $\Delta E$  denotes the activation energy (often given as  $E_A$ ) and  $\Delta V$  the activation volume. For solid state matter, the activation volume term can be neglected at ambient pressure and Eq. (2.25) simplifies to

$$D = D_0 \exp\left(-\frac{E_A}{k_B T}\right). \quad (2.26)$$

However, it should be noted that this Arrhenius behavior is derived empirically and can by no means be regarded as a universal feature of the diffusion coefficient over the whole temperature range.<sup>[21,22]</sup>

### 2.1.6 Diffusion and defects

It should be again brought to mind that defects in a crystalline lattice are a prerequisite for the migration of atoms; in an ideal crystal, *i. e.* in a crystal without atomic imperfections, no diffusion would be possible. The various diffusion mechanisms by which atomic motion is facilitated require a vacant spot as a neighbor of the diffusing atoms, either on a regular lattice site or on an interstitial site. These vacancies are generated by crystallographic defects and their interactions with each other. Classically, these defects are categorized according to their dimensionality:

**Zero-dimensional defects.** — *Point defects* are present in a crystal at thermal equilibrium and include *Frenkel disorder* and *Schottky disorder*, both of which are thermally activated.<sup>[22,33,34]</sup> Since point defects are able to move through the crystal they often play a key rôle in the mediation of atomic diffusion. This means that above 0 K they—and thus diffusion—are present even in “perfect” single crystals. Frenkel disorder describes a defect pair where an atom occupying a regular site on the crystal lattice is moved to an interstitial site forming an interstitial and leaving behind a vacancy on the regular site. In ionic crystals, Schottky disorder applies to a situation in which vacancies are formed on both the anion and the cation sub-lattice in stoichiometric amounts so as to preserve charge neutrality. If cation sites are occupied by anions (and *vice versa*) this is known as *anti-site defects*. Obviously, if the number of such sites on both sub-lattices is not equal then the stoichiometry of the compound will shift.<sup>[34]</sup> Further point defects involve *impurity atoms*, which may be homovalent or heterovalent and occupy interstitial or regular lattice sites. In the case of heterovalent doping, charge neutrality dictates the formation of additional vacancies on the sub-lattice of opposite valency. Homovalent doping will usually result in a distortion in the crystal lattice, thus exerting an influence on the diffusion of atoms in the vicinity of the dopant.\* For more information on point defects, *cf. e. g.* Refs. [33] and [35].

\* Of course, the same also holds true for heterovalent doping.

**One-dimensional defects.** — *Dislocations* are *line defects* and belong to the class of non-equilibrium defects. Here, two limiting cases are distinguished, the first being *edge dislocations* and the second *screw dislocations*; often both occur in combination as *mixed* (or *general*) *dislocations*.<sup>[33,36]</sup> They move easily and are responsible for plastic deformation of the crystal lattice. Pertaining to diffusion, moving dislocations can create (or annihilate) vacancies and interstitials. For an extensive discussion on dislocations see *e. g.* Refs. [33] and [37].

**Two-dimensional defects.** — These are *planar defects* and include *stacking faults*, extensively discussed in Ref. [36], and *grain boundaries*, which are interfaces between either crystallites of the same phase but different orientations or between crystallites of different phases, see *e. g.* Refs. [33] and [36]. In polycrystalline solids, grain boundaries often exhibit enhanced diffusion parameters as compared to the bulk material, providing the mobile ions with fast diffusion pathways.<sup>[21,22,38]</sup>

**Three-dimensional defects.** — *Voids* (also known as *pores*) and *precipitates* belong to the class of *bulk* (or *volume*) *defects*. The former can be thought of as clusters of a large number vacancies, while the latter corresponds to clusters of impurities forming inclusions of a different phase inside a crystal structure. Both can greatly impact the diffusional properties of a given material. For more on bulk defects see *e. g.* Ref. [39].

### 2.1.7 Mechanisms of diffusion

Depending on the nature of the defects present in a solid, the motion of the atomic particles can be facilitated by various mechanisms, the most common of which shall be briefly presented below. For a more detailed consideration see, *e. g.*, Refs. [20] and [22].

**Interstitial mechanism.** — Conceptually the simplest mechanism of diffusion, the *interstitial mechanism* is also known as the *direct interstitial mechanism*. It is a diffusion mechanism that works without the help of defects and, as a consequence of this, results in high diffusion coefficients when compared to other mechanisms. It involves solute atoms considerably smaller than the solvent atoms forming a solid solution with the host lattice by occupying interstitial sites. An interstitial solute atom then migrates through the lattice by jumping to one of its neighboring (unoccupied) interstices. See Fig. 2.1a.

**Interstitialcy mechanism.** — If the interstitial atom is of about the same size as the lattice atoms (of if self-interstitials are considered) a direct jump to an interstice is energetically unfavorable and diffusion is more likely to be mediated by the *interstitialcy mechanism* (also denoted as the *indirect interstitial mechanism*). Here, the interstitial atom jumps to a neighboring regular site while the atom presently occupying this site jumps to another available interstitial site. *Cp.* Fig. 2.1b.

**Vacancy mechanism.** — Considered the most important diffusion mechanism, the *vacancy mechanism* is the dominant one in metals and alloys for the diffusion of both the matrix atoms and the solute atoms. Here, the atoms move by simply exchanging places with a vacancy; *cf.* Fig. 2.1c. The diffusivity thus strongly depends on the availability and the mobility of vacancies.

Furthermore, in the case of substitutional solutes attractive or repulsive interactions with the vacancy can be the source of correlations effects.<sup>[20]</sup>

**Divacancy mechanism.** — Closely related to the vacancy mechanism, and very similar to it, is the *divacancy mechanism*; see Fig. 2.1d. Provided an existing binding energy, vacancy pairs (or divacancies) can form from simple vacancies (monovacancies). The generation of both monovacancies and divacancies is thermally induced. However, at higher temperatures divacancies may gain in significance since their concentration increases at a higher rate than that of monovacancies. Indeed, the divacancy mechanism becomes important in fcc metals because of the higher mobility of divacancies; this is exemplified by the curvature in the Arrhenius plot of the diffusion coefficient vs. inverse temperature.<sup>[20,22]</sup> Furthermore, in alkali halides bound vacancies were found to contribute significantly to the diffusivity.<sup>[20]</sup>

**Interstitial-substitutional mechanisms.** — This is a collective term for two related mechanisms. Provided that solute atoms can occupy both interstitial and substitutional sites in the host matrix, they then may diffuse by means of the *dissociative mechanism* or the *kick-out mechanism*. In both cases an interstitial solute first migrates via the interstitial mechanism. If it combines with a vacancy the mechanism is known as *dissociative mechanism*. If on the other hand it interacts with a matrix atom via the interstitialcy mechanism the mechanism is denoted as *kick-out mechanism*. See Fig. 2.1e.

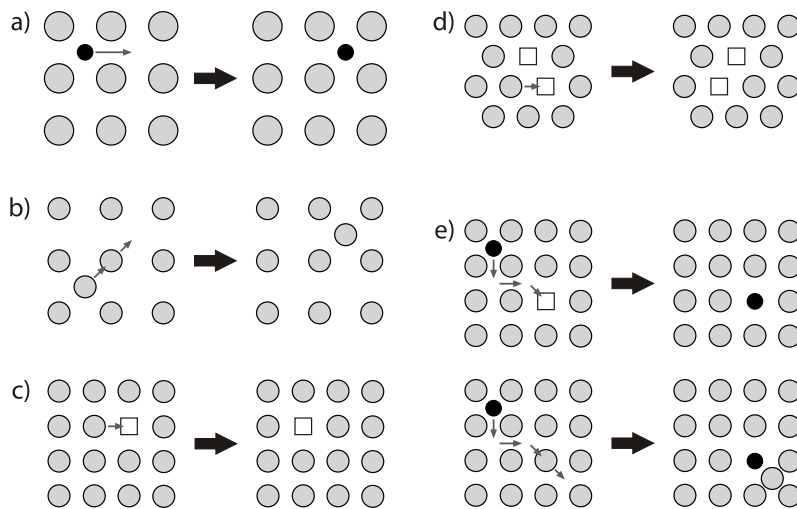


**Figure 2.1:** Schematic representations of the various mechanisms of diffusion: a) The interstitial mechanism. b) The interstitialcy mechanism. c) The vacancy mechanism. d) The divacancy mechanism. e) The interstitial-substitutional mechanisms. *Top*: dissociative mechanism; *bottom*: kick-out mechanism. Adapted from Refs. [20] and [22].

## 2.2 The measurement of diffusion coefficients

### 2.2.1 Direct methods

Direct methods are based *directly* on Fick's laws of diffusion and are as such almost exclusively macroscopic methods. With the exception of field gradient NMR measurements (see below), direct methods entail the recording of concentration profiles and are chosen according to their suitability with regard to the diffusing nucleus and its diffusion length.

#### Tracer method

Since the tracer diffusion coefficient is the most pertinent one to the present work, a short description of the *tracer method* will be given (see also Sect. 2.1.4). Performed with care, this method is able to yield very accurate values for diffusion coefficients in solids.

The tracer is deposited on the surface of the sample as a thin film and since only relatively small amounts of tracer atoms are necessary, the influence on the chemical composition of the sample is negligible—even in the case of impurity tracers. Several techniques are available for deposition, *e. g.* evaporation, dripping (in case of a liquid solution), or electrodeposition. Subsequently, the prepared sample is annealed at a constant temperature  $T$  in vacuum or an inert atmosphere for a diffusion time  $t$ . The resulting concentration profile of the tracer in the sample can then be recorded by a variety of techniques. These include *mechanical sectioning*, *ion-beam sputter sectioning* (IBS), *secondary ion mass spectrometry* (SIMS), *electron microprobe analysis* (EMPA), *Auger electron spectroscopy* (AES), *Rutherford backscattering spectrometry* (RBS), and *nuclear reaction analysis* (NRA). Informative reviews of the techniques are given in Refs. [22, 40], for brief descriptions [20, 21] can be referred to.

If the thickness of the tracer layer is small compared to the diffusion length  $\sqrt{Dt}$ , then the diffusion equation (2.5) is solved by a Gaussian distribution

$$c(x,t) = \frac{M}{\sqrt{\pi Dt}} \exp\left(-\frac{x^2}{4Dt}\right), \quad (2.27)$$

where  $M$  is the number of tracer atoms per unit area and  $x$  the coordinate normal to the layer (see *e. g.* Ref. [22]). Thus, plotting  $\ln c(x,t)$  as a function of  $x^2$  results in a linear relation with the slope  $-1/4Dt$ , from which the diffusion coefficient  $D$  can be determined at a given temperature  $T$ .

With the appropriate sample preparation the measurement of the chemical diffusion coefficient and the intrinsic diffusion coefficients is performed analogously; examples of corresponding experiments are presented in Ref. [22].

#### Field gradient NMR method

As the name suggests, field gradient NMR experiments are nuclear magnetic resonance measurements performed in a magnetic field gradient  $G$ . The gradient is usually linear along

the direction of the external magnetic field  $B_0$  and causes the nuclei at different locations in the sample to experience different magnetic fields. This effectively labels the spins by their different Larmor (precession) frequencies. Their diffusivity is then probed by spin-echo experiments<sup>[41]</sup> with an appropriate pulse sequence, *e. g.*,  $\pi/2_X - t_p - \pi_X - t_p$ -echo (*cp.* also Sect. B.3.2 in the appendices). The diffusion of spins in a field gradient results in a random (*i. e.* irreversible) phase shift of the individual spin vectors, leading to a decrease in the transverse component of the magnetization. The decrease stemming from diffusional motion, however, is in competition to a decrease induced by transverse relaxation processes. The echo amplitude  $A$  is expressed by

$$A(2t_p) = A(0) \exp\left(-\frac{2t_p}{T_2}\right) \exp\left(-\frac{2}{3}\gamma^2 DG^2 t_p^3\right), \quad (2.28)$$

where  $T_2$  is the transverse (or spin-spin) relaxation time (see Sect. 2.3.3),  $D$  the self-diffusion coefficient, and  $\gamma$  the gyromagnetic ratio. If  $T_2$  is known and its value is sufficiently high, the first term in the exponential can be subtracted out (or ignored), thus giving direct access to the diffusion coefficient  $D$ . The measurements can be performed in a static field gradient (SFG) or a pulsed field gradient (PFG); here, the reader may be referred to a review by Stilbs.<sup>[42]</sup> Of further interest may also be Refs. [21, 22, 43].

### 2.2.2 Indirect methods

In contrast to direct methods, indirect methods do not depend on solutions of the diffusion equation. These methods involve the study of phenomena that are influenced by diffusional processes, hence the term ‘indirect’. Also, the methods rely on microscopic models to obtain a diffusion coefficient, and as such these diffusion coefficients are necessarily approximations to those measured by direct means. Usually relaxation times or linewidths are measured, from which mean residence times can be calculated. These are then used to determine diffusion coefficients via the Einstein-Smoluchowski relation in the form of Eq. (2.24). Indirect methods can be classified into two main categories, *viz.* *relaxation methods* and *nuclear methods*.<sup>[20,21]</sup> In this context, impedance spectroscopy takes a special status and will be discussed in Sect. 2.4.

#### Relaxation methods

Relaxation methods have in common that they are based on effects which cause an anelastic relaxation in a system after it has been subject to mechanical stress. As such, anelastic measurements are summarily also known as *mechanical spectroscopy*. A short overview of the effects involved is presented below. More details can be found in Refs. [22, 44].

*Gorsky relaxation.* — The Gorsky effect was first theoretically predicted by its namesake in 1935.<sup>[45]</sup> In a bending experiment a mechanical stress gradient is produced from the compressed to the dilated side of the sample. This results in a gradient of chemical potential of

present interstitials, inducing long-range diffusion of these interstitial atoms, which leads to an additional curvature of the sample. Once the initial gradient in chemical potential is compensated, the structure relaxes again with a characteristic time constant. This relaxation time  $\tau_G$  can be used to calculate a diffusion coefficient according to

$$D = \frac{d^2}{\pi^2 \Phi \tau_G} . \quad (2.29)$$

Here,  $d$  is the thickness of sample and  $\Phi$  signifies the thermodynamic factor (*cf.* Ref. [22]). Gorsky relaxation has been mainly used to determine the diffusion coefficient of hydrogen in metals. Discussions of the effect and examples can be found in Refs. [19, 46–49].

*Snoek relaxation.* — The Snoek effect originally describes anelastic relaxation due to heavy interstitial impurity atoms (*e. g.* O, N, C) in bcc metals.<sup>[50,51]</sup> Here, the interstitials occupying octahedral interstitial sites will cause directed lattice distortions with a lower symmetry than the matrix. This corresponds to elastic dipoles associated with the three lattice directions. Without external stress, the occupation probabilities for the three different sites is equal. Introducing (tensile) mechanical stress along one direction will cause the occupation of the corresponding site to be energetically more favorable than the other two; reversing the stress then leads to the reverse process. The result is a periodic oscillation of occupation numbers. The relaxation time  $\tau_S$  associated with the Snoek effect can be used to calculate the diffusion coefficient of the impurity atoms according to

$$D = \frac{a^2}{36\tau_S} , \quad (2.30)$$

where  $a$  is the lattice parameter of the pure metal. For more information the reader is referred to Refs. [19, 52]; the effect is also covered extensively by Blanter *et al.* in [44].

*Zener relaxation.* — The Zener effect is similar to the Snoek effect in that it involves a reorientation of elastic dipoles caused by mechanical stress. In this case, the dipoles can be formed by pairs of solute atoms on substitutional or interstitial sites or by pairs of vacancies. The initially isotropic distribution of dipoles can be disturbed by external stress and relaxes when stress is removed. However, since the nature of the atomic jumps involved in the reorientation is not well known, there is no straightforward relation to the diffusion parameters of the solute atoms. More can be found in Refs. [53–55]. Also, the interested reader is again referred to Blanter *et al.*<sup>[44]</sup> and the references therein.

### Nuclear methods

Nuclear methods allow the study of diffusional processes on a microscopic level. Below, Mössbauer spectroscopy (MS) and quasielastic neutron scattering (QENS) are briefly touched upon. More information can be found in the indicated literature. Methods based on nuclear

magnetic resonance (NMR)—being most relevant for the present work—will be covered separately and in more detail in Sect. 2.3.

*Mössbauer spectroscopy.* — MS is based on an effect discovered by Rudolf L. Mößbauer in 1957<sup>[56]</sup> for which he received the Nobel Prize in Physics four years later.<sup>[57,58]</sup> The Mössbauer effect describes recoil-free emission and absorption of  $\gamma$ -radiation by atoms incorporated in a crystalline lattice. Information about the motion of a few select nuclei can be extracted from the broadening of the absorption line, provided a suitable Mössbauer isotope exists. These are  $^{57}\text{Fe}$ ,  $^{119}\text{Sn}$ ,  $^{151}\text{Eu}$ , and  $^{161}\text{Dy}$ . Normally, the natural linewidth  $\Gamma_0$  is very small; however, if the motion of the investigated nuclei at higher temperatures is fast enough, an additional broadening contribution  $\Delta\Gamma$  to the experimental linewidth  $\Gamma = \Gamma_0 + \Delta\Gamma$  is introduced. The broadening can then be used to calculate an approximated value for the diffusion coefficient. For example, assuming jump diffusion on a lattice with a jump length  $\ell$  and also ignoring correlation effects, the diffusion coefficient is expressed by<sup>[22]</sup>

$$D \approx \frac{\ell^2 \Delta\Gamma}{12\hbar} . \quad (2.31)$$

Additional information and more details can be found in Refs. [22, 59, 60] and the references therein.

*Quasielastic neutron scattering.* — As in the case of Mössbauer spectroscopy, here the motion of the investigated nuclei results in a line broadening  $\Delta\Gamma$ , which allows an inference on the diffusion coefficient. In QENS experiments, slow neutrons are used as probes. The prerequisites are a high-intensity neutron source and a high-resolution neutron spectrometer. Since neutrons exhibit only weak interaction with matter, bulk properties are accessible by QENS. Besides structural properties, this method also allows to gain information about dynamics on a microscopic level. However, the nuclei available for study are determined by their scattering cross section for neutrons. Also, dynamical studies via QENS are again only applicable to relatively fast diffusing particles. For small scattering angles the diffusion coefficient is given by

$$D \approx \frac{\Delta\Gamma}{2Q^2} , \quad (2.32)$$

where  $Q$  the modulus of the scattering vector.<sup>[22]</sup> Further information can be found in Refs. [22, 59–64].

## 2.3 Solid-state nuclear magnetic resonance

### 2.3.1 Introduction

Since its experimental observation in 1945 by Purcell, Torrey and Pound and, independently of them, by Bloch, Hansen and Packard, the field of nuclear magnetic resonance (NMR) has developed various techniques for the study of bulk properties of matter. Bloch and Purcell received the Nobel Prize in Physics in 1952 for their discovery and it is, indeed, very interesting to read as they describe their findings and report on the very beginnings of the study of material properties in their Nobel Lectures<sup>[65]</sup>—already anticipating the impact NMR would have on the natural sciences in the years to come. Its usefulness and vast range of application is aptly emphasized by Levitt in the introduction to his exhaustive textbook on the subject.<sup>[66]</sup>

☞ [...] NMR has become an incredible physical tool for investigating matter. Its range is staggering, encompassing such diverse areas as brains, bones, cells, ceramics, inorganic chemistry, chocolate, liquid crystals, laser-polarized gases, protein folding, surfaces, superconductors, zeolites, blood flow, quantum geometric phases, drug development, polymers, natural products, electrophoresis, geology, colloids, catalysis, food processing, metals, gyroscopic navigation, cement, paint, wood, quantum exchange, phase transitions, ionic conductors, membranes, plants, micelles, grains, antiferromagnets, soil, quantum dots, explosives detection, coal, quantum computing, rubber, glasses, oil wells and Antarctic ice. ☞

In the following, a short introduction to the theoretical basis of nuclear magnetic resonance is given. Here, basic quantum mechanical concepts will be followed by a brief treatment of the most important interactions (as they pertain to the present work) the studied nuclei are subject to. Finally, the most relevant NMR techniques, such as *relaxometry* and *spin-echo alignment*, are presented and the extraction of diffusion-related parameters from these is outlined. The specific experiments used to acquire NMR data are given in the appendices (Sect. B.3).

### 2.3.2 Basics of NMR

Nuclear magnetic resonance is a phenomenon observed for nuclei with a non-vanishing spin angular momentum  $I$  (also known as nuclear spin).<sup>\*</sup> They then also possess a dipolar magnetic moment  $\mu$ , which is collinear to the nuclear spin and connected to it by the gyromagnetic ratio  $\gamma$ , following the relation

$$\mu = \gamma I . \quad (2.33)$$

\* In the literature dealing with NMR such nuclei are usually referred to as spins.

The *gyromagnetic ratio* (also known as the *magnetogyric ratio*) is an experimentally determined, nucleus-dependent constant and can be both, positive and negative.\*

As we are dealing with a quantum mechanical concept such as the spin, a certain familiarity with this subject is required in the following discussion. Since a thorough introduction is clearly beyond the scope of this work, the reader is referred to one of many text books available.<sup>[67-70]</sup> There are also very informative works specifically dealing with quantum mechanics in the context of NMR.<sup>[66,71,72]</sup>

In this framework, the vectors  $\boldsymbol{\mu}$  and  $\mathbf{I}$  are treated as vector operators and will be marked with a “hat” in order to distinguish them from other vectorial quantities. From  $\hat{\mathbf{I}} = (\hat{I}_x, \hat{I}_y, \hat{I}_z)$  a set of convenient spin operators can be defined, *viz.* the spin angular momentum operator squared  $\hat{I}^2$ , its  $z$  component  $\hat{I}_z$ , and the raising and lowering operators<sup>†</sup>  $\hat{I}_{\pm} = \hat{I}_x \pm i\hat{I}_y$ , where  $\hat{I}_x$  and  $\hat{I}_y$  are the  $x$  and  $y$  component of  $\hat{\mathbf{I}}$ , respectively.  $\hat{I}^2$  is characterized by the spin quantum number  $I$ ,  $\hat{I}_z$  by the magnetic quantum number  $m$ , and the lowering and raising operators are characterized by both quantum numbers. The spin quantum number takes values of integers or half integers (or zero)  $I = 0, 1/2, 1, 3/2, \dots$ , while the magnetic quantum number takes the  $2I + 1$  values  $m = I, I - 1, \dots, -I$ . Further, the state of the nuclear spin can be described using a set of orthonormal eigenstates  $\psi_{I,m}$ . The eigenvalues of the spin operators  $\hat{I}^2$  and  $\hat{I}_z$  corresponding to  $\psi_{I,m}$  are defined by

$$\hat{I}^2 |I,m\rangle = \hbar^2 I(I+1) |I,m\rangle \quad (2.34a)$$

$$\hat{I}_z |I,m\rangle = \hbar m |I,m\rangle, \quad (2.34b)$$

where  $\hbar$  is the reduced Planck constant and  $|I,m\rangle$  represents  $\psi_{I,m}$  in the bra-ket notation. The name of the raising and lowering operators  $\hat{I}_{\pm}$  becomes apparent when their effect on a wavefunction  $\psi_{I,m} = |I,m\rangle$  is considered. It can be shown that

$$\hat{I}_+ |I,m\rangle = \hbar \sqrt{I(I+1) - m(m+1)} |I,m+1\rangle \quad (2.35a)$$

$$\hat{I}_- |I,m\rangle = \hbar \sqrt{I(I+1) - m(m-1)} |I,m-1\rangle, \quad (2.35b)$$

*i. e.* the shift operators generate new wavefunctions increasing (+) or decreasing (–) the quantum number  $m$  by 1, while leaving  $I$  unchanged. Applying  $\hat{I}_+$  on a wavefunction with a maximum value of  $m$  results in the destruction of this state:  $\hat{I}_+ |I, I\rangle = 0$ . The same applies to the application of  $\hat{I}_-$  to  $|I, -I\rangle$ .

The spins are subject to interactions with various external and internal fields, which can be expressed by a Hamiltonian  $\hat{H} = \sum_i \hat{H}_i$ , written as a sum of the individual interaction Hamiltonians. The fields most important to the present work are (1) the external static magnetic field  $\mathbf{B}_0$ , resulting in a splitting of normally degenerate energy states; (2) the oscillating external

\* Strictly speaking, the gyromagnetic ratio also depends on the state of the nucleus in question. However, in NMR usually only the ground state is observed.

† Which are also known as shift operators.

radio-frequency field  $\mathbf{B}_1(t)$ , used to induce transitions between the energy levels split by  $\mathbf{B}_0$ ; (3) local fields generated by neighboring dipolar magnetic moments, resulting in homonuclear or heteronuclear dipole–dipole interactions; and (4) electric field gradients generated by the local electronic distribution, which can interact with an electric quadrupole moment of a nucleus, if existent. These interactions will be briefly discussed below.

### Zeeman splitting

The interaction of a magnetic moment  $\boldsymbol{\mu}$  with a static magnetic field  $\mathbf{B}_0$  is described by the simple Hamiltonian

$$\hat{H}_Z = -\hat{\boldsymbol{\mu}}\mathbf{B}_0 = -\gamma\hat{\mathbf{I}}\mathbf{B}_0 . \quad (2.36)$$

Taking  $\mathbf{B}_0$  to point along an arbitrarily chosen direction  $z$ , the Zeeman Hamiltonian has the form

$$\hat{H}_Z = -\gamma\hat{\mathbf{I}}\mathbf{e}_z B_0 = -\gamma\hat{I}_z B_0 , \quad (2.37)$$

where  $\mathbf{e}_z$  is the unit vector codirectional with the  $z$  axis. Seeing that  $\hat{H}_Z$  is proportional to  $\hat{I}_z$ , the eigenstates  $|I, m\rangle$  of  $\hat{I}_z$  are also the eigenstates of  $\hat{H}_Z$ . The eigenvalues of  $\hat{H}_Z$  are then the energy levels  $E_{Z,m}$  the given spin system can take. Using the time-independent Schrödinger equation and Eqs. (2.37) and (2.34b) these are expressed as

$$\hat{H}_Z |I, m\rangle = -\gamma B_0 \hat{I}_z |I, m\rangle = -\gamma B_0 \hbar m |I, m\rangle = E_{Z,m} |I, m\rangle \quad (2.38a)$$

$$\Rightarrow E_{Z,m} = -\gamma \hbar m B_0 . \quad (2.38b)$$

The levels are equally spaced and the difference between them can be calculated as  $\Delta E_Z = -\gamma \hbar B_0$ . This is the energy necessary for transitions between adjacent levels, from which follows the resonance condition

$$\hbar \omega_0 = \Delta E_Z = -\gamma \hbar B_0 \quad (2.39a)$$

$$\Leftrightarrow \omega_0 = -\gamma B_0 , \quad (2.39b)$$

with  $\omega_0$  being the resonance frequency. As can be seen, the frequency  $\nu_0 = \omega_0/2\pi$  of the alternating field used to induce the energy transitions is proportional to the strength of the static magnetic field. For the relevant nuclei and for magnetic fields of the order of 10 T this corresponds to frequencies ranging from some tens to some hundreds of megahertz.

At equilibrium—assuming no interaction between spins—the eigenstates are occupied according to a Boltzmann distribution. For nuclei with  $I > 0$ , we find that any given spin can exist in one of  $2I + 1$  states  $\psi_{I,m}$  with a corresponding energy  $E_{Z,m}$ . The population  $p_m$  of a state with the quantum number  $m$  is then expressed by

$$p_m = \frac{1}{Z} \exp(-E_{Z,m}/k_B T) , \quad (2.40)$$

with  $Z = \sum_{m'} \exp(-E_{Z,m'}/k_B T)$  being the canonical partition function.\*

The transition of a spin system from one state to another is subject to specific selection rules, of which the one relevant to the present problem is  $\Delta m = \pm 1$ , *e. g.* the only transitions allowed are those which either raise or reduce the quantum number  $m$  by 1. Thus, the relative population of two eigenstates which allow such transitions is

$$\frac{p_{m^{(1)}}}{p_{m^{(2)}}} = \exp\left(-\frac{E_{Z,m^{(1)}} - E_{Z,m^{(2)}}}{k_B T}\right). \quad (2.41)$$

The difference in the occupation numbers is very low. This point can be well illustrated by using hydrogen—a spin- $1/2$  nucleus—as a simple example. Its gyromagnetic ratio is  $\gamma_{\text{H}} \approx 2.68 \times 10^8 \text{ rad T}^{-1} \text{ s}^{-1}$ . Placing a  $^1\text{H}$  containing sample in a magnetic field of 10 T at a temperature of 300 K, Eqs. (2.41) and (2.39) can be used to calculate

$$\frac{p_{+1/2}}{p_{-1/2}} = \exp(-\gamma \hbar B_0 / k_B T) \approx 0.999932. \quad (2.42)$$

Thus the difference in the population of the two states is about 70 ppm.

In terms of a spin ensemble, the spin system can occupy each of the eigenstates  $\psi_{I,m}$ , with the probability of finding the system in that state being  $p_m$ . Since only an ensemble average can be observed, a mathematically equivalent approach is to describe the spin system by a superposition state

$$\Psi = \sum_m \sqrt{p_m} \psi_{I,m}. \quad (2.43)$$

### External radio-frequency field

In the presence of an additional field  $\mathbf{B}_1$  oscillating with an angular frequency  $\omega_{\text{RF}}$  assumed to lie perpendicular to  $\mathbf{B}_0$ , *e. g.* along the  $x$ -axis, the total magnetic field is given by

$$\mathbf{B}_{\text{tot}} = \mathbf{B}_0 + \mathbf{B}_1 = \mathbf{e}_z B_0 + \mathbf{e}_x 2B_1 \cos(\omega_{\text{RF}} t). \quad (2.44)$$

In analogy to Eqs. (2.36) and (2.37), the Hamiltonian for the interaction with the total field is then written as

$$\hat{H} = -\hat{\boldsymbol{\mu}} \mathbf{B}_{\text{tot}} = -\gamma \hat{I}_z B_0 - 2\gamma \hat{I}_x B_1 \cos(\omega_{\text{RF}} t). \quad (2.45)$$

Here, it is convenient to express the linearly oscillating RF-term as a superposition of two circularly polarized fields, one rotating with  $\omega_{\text{RF}}$  about the  $z$ -axis, the other in the opposite

---

\* For  $I = 1/2$  the partition function is  $Z \approx 2$ .

direction with  $-\omega_{\text{RF}}$ . Further, employing the resonance condition (2.39) and accordingly using  $\omega_1 = -\gamma B_1$ , the Hamiltonian (2.45) assumes the mathematically equivalent form

$$\hat{H} = \omega_0 \hat{I}_z + \omega_1 \left[ (\hat{I}_x \cos(\omega_{\text{RF}} t) + \hat{I}_y \sin(\omega_{\text{RF}} t)) + (\hat{I}_x \cos(\omega_{\text{RF}} t) - \hat{I}_y \sin(\omega_{\text{RF}} t)) \right]. \quad (2.46)$$

As the field  $B_1$  is weak compared to  $B_0$ , the non-resonant contribution, *i. e.* that rotating with  $-\omega_{\text{RF}}$ , has no significant effect and the last term in Eq. (2.46) can be neglected.<sup>[66]</sup> Further, using the identity  $\hat{I}_x \cos(\omega_{\text{RF}} t) + \hat{I}_y \sin(\omega_{\text{RF}} t) = e^{-\frac{i}{\hbar} \omega_{\text{RF}} t \hat{I}_z} \hat{I}_x e^{\frac{i}{\hbar} \omega_{\text{RF}} t \hat{I}_z}$  derived in any of the textbooks on quantum mechanics referenced above (see *e. g.* Ref. [71]) the Hamiltonian takes the form

$$\hat{H} = \omega_0 \hat{I}_z + \omega_1 e^{-\frac{i}{\hbar} \omega_{\text{RF}} t \hat{I}_z} \hat{I}_x e^{\frac{i}{\hbar} \omega_{\text{RF}} t \hat{I}_z}. \quad (2.47)$$

Since the Hamiltonian  $\hat{H}$  is a function of time, the time-dependent Schrödinger equation  $i\hbar \frac{\partial}{\partial t} \Psi = \hat{H} \Psi$  has to be solved in order to find the corresponding wavefunctions  $\Psi$ . This problem can be simplified by switching into a rotating frame of reference using the rotation operator  $\hat{R}_z(\omega_{\text{RF}} t) = e^{-\frac{i}{\hbar} \omega_{\text{RF}} t \hat{I}_z}$ . The Hamiltonian and the wavefunctions in the new frame (marked by a subscript circle) can then be calculated as

$$\Psi_{\circ} = \hat{R}_z^{-1}(\omega_{\text{RF}} t) \Psi = e^{i\omega_{\text{RF}} t \hat{I}_z} \Psi \quad (2.48a)$$

$$\hat{H}_{\circ} = \hat{R}_z^{-1}(\omega_{\text{RF}} t) \hat{H} \hat{R}_z(\omega_{\text{RF}} t) - \omega_{\text{RF}} \hat{I}_z = (\omega_0 - \omega_{\text{RF}}) \hat{I}_z + \omega_1 \hat{I}_x. \quad (2.48b)$$

Finally, the Hamiltonian simplifies in the case of a resonant RF-field, *i. e.* if  $\omega_{\text{RF}} = \omega_0$ . Now, the Schrödinger equation

$$i\hbar \frac{\partial}{\partial t} \Psi_{\circ} = \hat{H}_{\circ} \Psi_{\circ} = \omega_1 \hat{I}_x \Psi_{\circ} \quad (2.49)$$

can be easily solved in the rotating frame of reference. The effect of the operator  $\hat{I}_x = \frac{1}{2}(\hat{I}_+ + \hat{I}_-)$  on  $\Psi_{\circ}$  can be evaluated using the definition of the shift operators (2.35). The wavefunctions in the laboratory frame are obtained by reversing the transformation seen in Eq. (2.48a); thus  $\Psi = \hat{R}_z(\omega_{\text{RF}} t) \Psi_{\circ}$ .

Using a superposition state as in Eq. (2.43), it can be shown that in the presence of  $B_1$  the populations of the Zeeman states oscillate with the frequency  $\omega_1/2\pi$ . Considering that the macroscopic net-magnetization in the sample is generated by the difference in the populations of the Zeeman states, this means that depending on the pulse length  $t_{\text{pulse}}$  the magnetization can be rotated about the  $x$  axis by an arbitrary angle  $\omega_1 t_{\text{pulse}}$ .

Assuming a spin- $1/2$  system in equilibrium as an example, the populations  $p_{\pm 1/2}$  of the two states can be manipulated in such a way that an RF-pulse which satisfies the condition  $\omega_1 t_{\text{pulse}} = \pi/2$  results in  $p_{+1/2}(t_{\text{pulse}}) = p_{-1/2}(t_{\text{pulse}})$ . Here, both states are equally populated and the net-magnetization along the  $z$ -axis is zero; this is known as a  $\pi/2$ -pulse. A pulse of the duration  $t_{\text{pulse}} = \pi/\omega_1$  results in  $p_{+1/2}(t_{\text{pulse}}) = p_{-1/2}(0)$  and  $p_{-1/2}(t_{\text{pulse}}) = p_{+1/2}(0)$ , where

$p_{\pm 1/2}(0)$  are the populations at equilibrium. This means that the initial magnetization has been inverted by a so-called  $\pi$ -pulse.

### Dipolar interactions

A nuclear spin—having a magnetic moment  $\hat{\mu} = \gamma\hat{I}$ —generates a magnetic field according to its orientation in space. A neighboring spin is thus able to interact with this field. The interaction is mutual since the second spin also generates a magnetic field at the location of the first one. This interaction is known as *direct dipole–dipole coupling* and will be the subject of the brief discussion below. It is differentiated from the *indirect dipole–dipole coupling* mediated by local electrons. A thorough discussion of the later can be found in, e. g., Ref. [66].

The Hamiltonian describing the interaction between two nuclear spins  $j$  and  $k$  takes the form

$$\hat{H}_D = \frac{\mu_0 \gamma_j \gamma_k}{4\pi r_{jk}^3} (\hat{I}_j \hat{I}_k - 3[(\hat{I}_j \mathbf{e}_{jk})(\hat{I}_k \mathbf{e}_{jk})]) , \quad (2.50)$$

where  $r_{jk} = |\mathbf{r}_{jk}|$  is the distance between both spins and  $\mathbf{e}_{jk} = \mathbf{r}_{jk}/r_{jk}$  a unit vector parallel to the line joining them. No assumptions have been made yet as to whether the coupling is between like spins or unlike spins.

Employing shift operators and spherical coordinates Eq. (2.50) can be rewritten as

$$\hat{H}_D = \frac{\mu_0 \gamma_j \gamma_k}{4\pi r_{jk}^3} (A + B + C + D + E + F) , \quad (2.51)$$

with the terms  $A$  to  $F$  being

$$\begin{aligned} A &= \hat{I}_j^z \hat{I}_k^z (1 - 3 \cos^2 \theta_{jk}) , \\ B &= -\frac{1}{4} (\hat{I}_j^+ \hat{I}_k^- + \hat{I}_j^- \hat{I}_k^+) (1 - 3 \cos^2 \theta_{jk}) , \\ C &= -\frac{3}{2} (\hat{I}_j^+ \hat{I}_k^z + \hat{I}_j^z \hat{I}_k^+) \sin \theta_{jk} \cos \theta_{jk} e^{-i\phi_{jk}} , \\ D &= -\frac{3}{2} (\hat{I}_j^- \hat{I}_k^z + \hat{I}_j^z \hat{I}_k^-) \sin \theta_{jk} \cos \theta_{jk} e^{+i\phi_{jk}} , \\ E &= -\frac{3}{4} \hat{I}_j^+ \hat{I}_k^+ \sin^2 \theta_{jk} e^{-i2\phi_{jk}} , \\ F &= -\frac{3}{4} \hat{I}_j^- \hat{I}_k^- \sin^2 \theta_{jk} e^{+i2\phi_{jk}} . \end{aligned} \quad (2.52)$$

It can be shown that the net-effect of the terms  $C$  to  $F$  is negligible so that they can be dropped from Eq. (2.51).<sup>[71,73]</sup> The resulting secular part of  $\hat{H}_D$  commutes with the Zeeman Hamiltonian and in the case of homonuclear interactions is expressed by

$$\hat{H}_{D,\text{sec}}^{\text{homo}} = -\frac{1}{2} \frac{\mu_0}{4\pi} \frac{\gamma_I^2}{r_{jk}^3} (\hat{\mathbf{I}}_j \hat{\mathbf{I}}_k - 3\hat{I}_j^z \hat{I}_k^z) (1 - 3 \cos^2 \theta_{jk}) . \quad (2.53)$$

Here the identities  $\hat{I}_j^+ \hat{I}_k^- + \hat{I}_j^- \hat{I}_k^+ = 2(\hat{\mathbf{I}}_j \hat{\mathbf{I}}_k - \hat{I}_j^z \hat{I}_k^z)$  and  $\gamma_j = \gamma_k = \gamma_I$  have been used. In the case of heteronuclear interactions only the term  $A$  retains significance and the secular part of the dipole–dipole Hamiltonian is given by<sup>[71]</sup>

$$\hat{H}_{D,\text{sec}}^{\text{hetero}} = \frac{\mu_0}{4\pi} \frac{\gamma_j \gamma_k}{r_{jk}^3} \hat{I}_j^z \hat{I}_k^z (1 - 3 \cos^2 \theta_{jk}) . \quad (2.54)$$

The direct dipole–dipole coupling is a short-range coupling ( $\hat{H}_D \propto r^{-3}$ ) and as such usually only direct neighbors will interact with each other. Also, it is usually several orders of magnitude weaker than the Zeeman interaction ( $\|\hat{H}_D\| \ll \|\hat{H}_Z\|$ ) and can be considered in terms of a perturbation to the Zeeman Hamiltonian. In solids, it is one of the major contributions to line broadening and relaxation processes.

### Quadrupolar interactions

NMR active nuclei with a spin  $I \geq 1$  possess an additional nuclear quadrupole moment due to the non-spherical distribution of the charge carrying protons. This electric quadrupole moment is able to interact with an electric field gradient (EFG) present at the nuclear site. An EFG is generated by the local electronic structure and is always present at sites of non-cubic symmetry. The quadrupole Hamiltonian describing this interaction has the basic form<sup>[66]</sup>

$$\hat{H}_Q = \frac{eQ}{2I(2I-1)\hbar} \hat{\mathbf{I}} \cdot \mathbf{V} \cdot \hat{\mathbf{I}} , \quad (2.55)$$

where  $\mathbf{V}$  is the symmetric and traceless EFG tensor at the nuclear site and  $eQ$  is generally known as the electric quadrupole moment of the nucleus, with  $e$  being the proton charge. In its principal axis frame (PAF)  $\mathbf{V}$  can be represented by a diagonal  $3 \times 3$  matrix with its principal values  $V_{XX}$ ,  $V_{YY}$ , and  $V_{ZZ}$  as the diagonal entries.\* Given that the electric field gradient tensor is traceless, *i. e.*  $V_{XX} + V_{YY} + V_{ZZ} = 0$ , two parameters are enough to specify the electric field gradient at the nucleus site. These are usually  $eq$ , the anisotropy of the EFG

\* Here, the convention is adopted to use lower case coordinates ( $x, y, z$ ) to refer to the laboratory frame of reference while upper case coordinates ( $X, Y, Z$ ) to the principal axis frame of the EFG tensor.

tensor (its largest principal value), and  $\eta_Q$ , the biaxiality of the EFG tensor, often also referred to as the asymmetry parameter, but *cf.* Ref. [66] on this terminology. Their values are given as

$$eq = V_{ZZ} \quad \text{and} \quad \eta_Q = \frac{V_{XX} - V_{YY}}{V_{ZZ}}, \quad (2.56)$$

where  $e$  again denotes the proton charge. Alternatively the quadrupole-coupling constant

$$C_Q = \frac{V_{ZZ}eQ}{\hbar} = \frac{e^2qQ}{\hbar} \quad (2.57)$$

can be used as a parameter instead of  $eq$ . Here,  $\hbar$  is as usual the reduced Planck constant and  $C_Q$  is given in angular frequency units.

Expanding the tensor product  $\hat{I} \cdot \mathbf{V} \cdot \hat{I}$  in Eq. (2.55) and expressing it in the principal axis frame of the EFG tensor, the quadrupolar Hamiltonian takes the form<sup>[71,74]</sup>

$$\hat{H}_Q = \frac{C_Q}{4I(2I-1)} [3\hat{I}_Z^2 - \hat{I}^2 + \eta_Q(\hat{I}_X^2 - \hat{I}_Y^2)], \quad (2.58)$$

where the definitions of Eqs. (2.56) and (2.57) have been used. However, since the Zeeman interaction dominates over the quadrupolar one,  $\hat{H}_Q$  has to be expressed in the laboratory frame of the Zeeman Hamiltonian in order to be useful. This can be relatively easily done by rotating the principle axis frame ( $X, Y, Z$ ) into the laboratory frame ( $x, y, z$ ). Further, since usually  $\|\hat{H}_Q\| \ll \|\hat{H}_Z\|$ , the quadrupolar Hamiltonian can again be expressed in terms of the secular approximation. Expressing the orientation of the PAF with respect to the external field  $\mathbf{B}_0$  in polar coordinates ( $\theta, \phi$ ), the secular part of  $\hat{H}_Q$  is given by

$$\hat{H}_Q^{\text{sec}} = \frac{C_Q}{8\hbar I(2I-1)} (3\hat{I}_z^2 - \hat{I}^2) (3\cos^2\theta - 1 + \eta_Q \sin^2\theta \cos 2\phi). \quad (2.59)$$

Using the time-independent Schrödinger equation  $\hat{H}_Q^{\text{sec}} |I, m\rangle = E_Q^m |I, m\rangle$  with the eigenstates of the Zeeman Hamiltonian, the energy by which the Zeeman states for a given  $I$  are shifted can be calculated as

$$E_Q^m = \frac{\hbar C_Q}{8I(2I-1)} (3m^2 - I(I+1)) f(\theta, \phi), \quad (2.60)$$

where the part representing the orientation of the electric field gradient is abbreviated by

$$f(\theta, \phi) = 3\cos^2\theta - 1 + \eta_Q \sin^2\theta \cos 2\phi. \quad (2.61)$$

Thus, for an  $I = 3/2$  nucleus, the Zeeman states are shifted by  $E_Q^{\pm 3/2} = \hbar C_Q f(\theta, \phi)/8$  and  $E_Q^{\pm 1/2} = -\hbar C_Q f(\theta, \phi)/8$ . This means that the transition frequency for the transition  $m = +1/2 \rightarrow m = -1/2$  (*central transition*) does not change, while the transition frequencies for  $+3/2 \rightarrow +1/2$  and  $-1/2 \rightarrow -3/2$  (*satellite transitions*) are raised or lowered by  $C_Q f(\theta, \phi)/4$ , depending on the

sign of  $C_Q$ . This value can be defined as the (orientation dependent) quadrupole angular frequency (*cf.* Fig. 2.2)

$$\omega_Q(\theta, \phi) = \frac{1}{4} C_Q f(\theta, \phi) . \quad (2.62)$$

It follows that the spectrum of a  $3/2$ -spin nucleus features additional intensities left and right of the central line (see Fig. 2.3). For a single crystal, two satellite lines are observed at the position  $\omega_0 \pm \omega_Q$  when the assumption of a non-zero quadrupole frequency is made (*i. e.*, if  $f(\theta, \phi) \neq 0$ , *cf.* Fig. 2.3a). In the case of a solid powder, the crystallites are randomly oriented, leading to a distribution of EFG orientations. This results in a so-called powder pattern, an example of which is shown in Fig. 2.3b for a uniaxial EFG tensor ( $\eta_Q = 0$ ). In this representation, the quadrupole coupling constant  $C_Q$  can be easily determined as the distance between the outermost shoulders of the spectrum. On the calculation of such powder patterns see *e. g.* Ref. [73].

Depending on the value of the electric quadrupole moment  $eQ$  of the nucleus, quadrupolar interactions can significantly contribute to nuclear relaxation processes. Indeed, dipolar interaction can often be ignored in favor of quadrupolar interactions on similar length scales.

### 2.3.3 NMR relaxation

As seen in the previous section (see p. 21ff.), the population of energy states can be manipulated by resonant RF pulses. Let us assume a spin system in an external magnetic field  $\mathbf{B}_0$  initially in thermal equilibrium with its surroundings (also denoted as the *lattice*).<sup>\*</sup> The populations are then given by the Boltzmann distribution and can be disturbed by an appropriate RF signal, which can simultaneously create single-quantum coherences. After switching off the disturbance, the system will gradually return to equilibrium by processes known as *nuclear spin* (or *NMR*) *relaxation* caused by interactions with temporal fluctuations of local fields. Given the right frequency contributions, these fluctuations can induce transitions between the energy states leading the system back to a Boltzmann distribution of the populations. This

\* The term 'lattice' is used irrespective of the nature of the surroundings, *i. e.* it is equally applied to solid matter, liquids and gases.

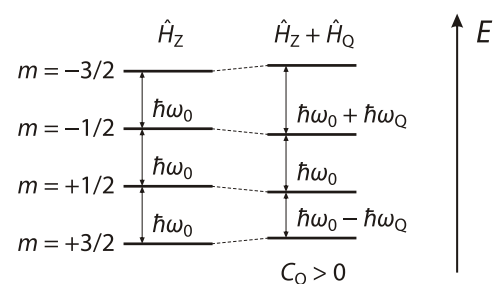


**Figure 2.2:** Schematic representation of the effect of the quadrupole Hamiltonian  $\hat{H}_Q^{\text{sec}}$  on the Zeeman states of spin- $3/2$  nuclei in the case of a positive quadrupole-coupling constant  $C_Q > 0$ .

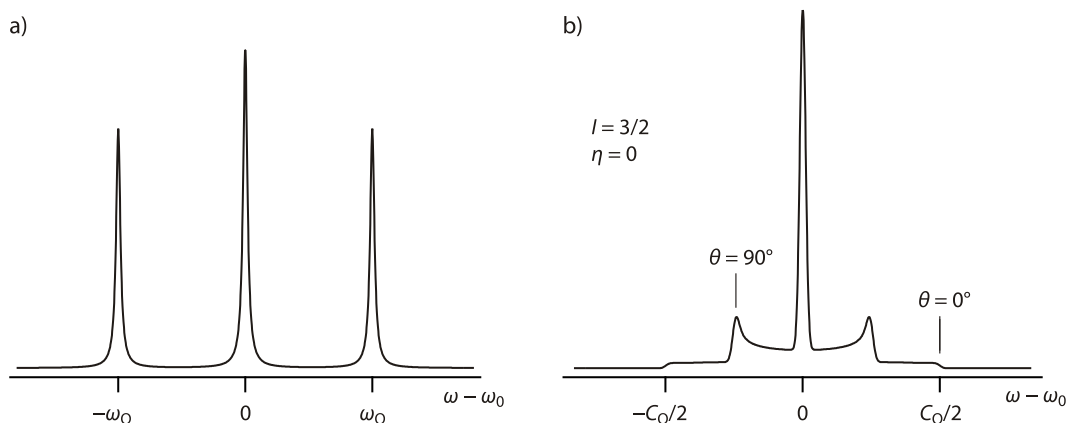


**Figure 2.3:** Typical spin- $3/2$  quadrupole spectra for a) a single crystalline sample with the EFG oriented so that  $f(\theta, \phi) \neq 0$ , and b) a powder sample assuming a uniaxial EFG tensor (*i. e.*  $\eta_Q = 0$ ), in both cases taking into account dipolar broadening. The powder pattern allows to directly read out the quadrupole coupling constant  $C_Q$  as the distance between the outer shoulders ( $\theta = 0^\circ$ ) of the spectrum.

type of relaxation is known as the *spin-lattice relaxation* (SLR) or the *longitudinal relaxation* and occurs with the characteristic time constant  $T_1$ . Another type of relaxation—the *spin-spin relaxation* (SSR) or *transverse relaxation*—is concerned with the decay of said single-quantum coherences and is associated with the time constant  $T_2$ .

In solids, the fluctuating fields are for the most part due to the motion of the spin-carrying nuclei themselves in an otherwise static lattice. As such, the study of NMR relaxation can yield valuable information on diffusion processes in a given system.

### Spectral density and relaxation rates

Most pertinent to the cases presented in this work are interactions with fluctuating magnetic fields (*direct dipole-dipole coupling*) and—for nuclei with spins  $I \geq 1$ —electric field gradients (*electric quadrupole coupling*), generally described by the interaction Hamiltonian  $\hat{H}_1$ . Using the matrix elements of  $\hat{H}_1$  for transitions between the states  $|j\rangle$  and  $|k\rangle$ , the temporal fluctuations can then be described by a correlation function<sup>[73]</sup>

$$G_{jk}(\tau) = \overline{\langle j | \hat{H}_1(t - \tau) | k \rangle \langle k | \hat{H}_1(t) | j \rangle}, \quad (2.63)$$

where the bar denotes an ensemble average. As the name suggest,  $G_{jk}(\tau)$  correlates the value of  $\hat{H}_1$  at the time  $t - \tau$  to its value at a later time  $t$ , *i. e.* the smaller  $\tau$  is as compared to the fluctuation time scale the more similar the values of  $\hat{H}_1$  will be. The fluctuation time scale characterizing the correlation function is quantified by the *correlation time*  $\tau_c$ , which is the mean time period between transition inducing fluctuations.

The spectral density function  $J_{jk}(\omega)$  of the fluctuating field is given as the Fourier transform of the correlation function  $G_{jk}(\tau)$

$$J_{jk}(\omega) = \int_{-\infty}^{\infty} G_{jk}(\tau) \exp(-i\omega\tau) d\tau. \quad (2.64)$$

NMR relaxation processes will be induced when  $J_{jk}(\omega)$  has contributions at the transition frequency  $\omega_0$ . The spectral density is approximately related to the spin–lattice relaxation rate via the proportionality  $T_1^{-1} \propto J(\omega_0)$ .

Taking into account the respective interactions in the form of their Hamiltonians (see previous section), more detailed expressions for the NMR relaxation rates can be derived.<sup>[74,75]</sup> In the case of homonuclear dipolar relaxation this results in

$$T_{1,D}^{-1} \equiv R_{1,D} = \frac{3}{2} \gamma^4 \hbar^2 I(I+1) [J_D^{(1)}(\omega_0) + J_D^{(2)}(2\omega_0)], \quad (2.65a)$$

$$T_{2,D}^{-1} \equiv R_{2,D} = \frac{3}{8} \gamma^4 \hbar^2 I(I+1) [J_D^{(0)}(0) + 10J_D^{(1)}(\omega_0) + J_D^{(2)}(2\omega_0)], \quad (2.65b)$$

where  $I$  signifies the spin of the relaxing nuclei,  $\gamma$  their gyromagnetic ratio and  $\hbar$  the reduced Planck constant.  $J_D^{(q)}(\omega)$  are the spectral densities, which facilitate transitions of spin pairs resulting in  $\Delta m = \pm q$ ; that is,  $q = 0, 1, 2$  denotes the change in the total angular momentum caused by the corresponding spectral density.<sup>[76]</sup>

Analogously, the relaxation rates in the case of quadrupolar interactions are given as<sup>[74,75]</sup>

$$T_{1,Q}^{-1} \equiv R_{1,Q} = \frac{9}{160} \left( \frac{eQ}{\hbar I} \right)^2 \frac{2I+3}{2I-1} [J_Q^{(1)}(\omega_0) + J_Q^{(2)}(2\omega_0)], \quad (2.66a)$$

$$T_{2,Q}^{-1} \equiv R_{2,Q} = \frac{9}{128} \left( \frac{eQ}{\hbar} \right)^2 [J_Q^{(0)}(0) + 10J_Q^{(1)}(\omega_0) + J_Q^{(2)}(2\omega_0)], \quad (2.66b)$$

where  $eQ$  is the electric quadrupole moment of the nuclei and  $R_{2,Q}$  is expressed for the special case  $I = 1$ .<sup>[75]</sup>

The results for  $R_2$  given above are only applicable when the NMR lines are sufficiently narrowed by molecular motion (*motional-narrowing regime*), *i. e.* when  $J^{(0)}(0)\tau_c \ll 1$  holds. At low temperatures, in the so-called “*rigid-lattice regime*” ( $J^{(0)}(0)\tau_c \gg 1$ ), the spin–spin relaxation rate is constant and given by

$$R_2 = R_{20} \equiv \sqrt{\langle \Delta\omega^2 \rangle}, \quad (2.67)$$

where  $\langle \Delta\omega^2 \rangle$  is the second moment; see *e. g.* Refs. [73, 74, 77–79].

Equations (2.65) and (2.66) give the nuclear spin relaxation rates in the laboratory frame of reference. Kelly and Sholl have developed a relatively simple method to deduce the corre-

sponding rates in the rotating frame (SLR $\rho$ ).<sup>[75]</sup> Here, the spin–lattice relaxation rates take the form

$$T_{1\rho,D}^{-1} \equiv R_{1\rho,D} = \frac{3}{8} \gamma^4 \hbar^2 I(I+1) [J_D^{(0)}(2\omega_1) + 10J_D^{(1)}(\omega_0) + J_D^{(2)}(2\omega_0)] , \quad (2.68a)$$

$$T_{1\rho,Q}^{-1} \equiv R_{1\rho,Q} = \frac{9}{640} \left( \frac{eQ}{\hbar I} \right)^2 \frac{2I+3}{2I-1} [J_Q^{(0)}(2\omega_1) + 10J_Q^{(1)}(\omega_0) + J_Q^{(2)}(2\omega_0)] . \quad (2.68b)$$

A comparison with the spin–lattice relaxation rates in the laboratory frame (Eqs. (2.65a) and (2.66a)) shows that that the expressions in the rotating frame have a similar form, though additionally containing a spectral density term  $J^{(0)}(2\omega_1)$  at two times the frequency of the RF signal. As will be seen below, this term dominates the relaxation rate in the limit  $\omega_0 \tau_c \gtrsim 1$ .

### 3D diffusion: BPP model

The well-established BPP model is based on a simplified assumption about the form of the correlation function  $G(\tau)$  proposed by Bloembergen, Purcell and Pound.<sup>[77]</sup> Although being a purely phenomenological approach, it reproduces very well the general characteristics of three-dimensional diffusion via uncorrelated atomic jumps on a regular lattice, as well as experimental data in many cases. What is more, the BPP model can be modified in such a way, that it also accommodates cases of correlated jump diffusion.\*

The correlation function is assumed to be a simple exponential

$$G^{(q)}(\tau) = G^{(q)}(0) \exp(-|\tau|/\tau_c) , \quad (2.69)$$

where  $\tau_c$  is the correlation time. Fourier transformation according to Eq. (2.64) results in the Lorentzian-shaped spectral density function

$$J^{(q)}(\omega) = G^{(q)}(0) \frac{2\tau_c}{1 + (\omega\tau_c)^2} . \quad (2.70)$$

For an isotropic distribution of the spins and short correlation times, it can be shown that  $G^{(0)}(0) : G^{(1)}(0) : G^{(2)}(0) = 6 : 1 : 4$ .<sup>[74,77]</sup> Thus, the relaxation rates (Eqs. (2.65), (2.66), (2.68)) can be expressed as

$$R_1 = C_1' [J^{(1)}(\omega_0) + 4J_Q^{(1)}(2\omega_0)] , \quad (2.71a)$$

$$R_2 = C_2' [6J^{(1)}(0) + 10J^{(1)}(\omega_0) + 4J^{(1)}(2\omega_0)] , \quad (2.71b)$$

$$R_{1\rho} = C_{1\rho}' [6J^{(1)}(2\omega_1) + 10J^{(1)}(\omega_0) + 4J^{(1)}(2\omega_0)] . \quad (2.71c)$$

\* An overview of more sophisticated models can be found in Ref. [80].

Here, due to their formal similarity, the representation of the equations for dipolar and quadrupolar interactions has been conflated and the respective constants combined into  $C'_n$  ( $n = 1, 2, 1\rho$ ). The combination of Eqs. (2.70) and (2.71) results in the expressions

$$R_1 = C_1 \left[ \frac{\tau_c}{1 + (\omega_0 \tau_c)^2} + \frac{4\tau_c}{1 + (2\omega_0 \tau_c)^2} \right], \quad (2.72a)$$

$$R_2 = C_2 \left[ 6\tau_c + \frac{10\tau_c}{1 + (\omega_0 \tau_c)^2} + \frac{4\tau_c}{1 + (2\omega_0 \tau_c)^2} \right], \quad (2.72b)$$

$$R_{1\rho} = C_{1\rho} \left[ \frac{6\tau_c}{1 + (2\omega_1 \tau_c)^2} + \frac{10\tau_c}{1 + (\omega_0 \tau_c)^2} + \frac{4\tau_c}{1 + (2\omega_0 \tau_c)^2} \right], \quad (2.72c)$$

where the constants have again been simplified to  $C_n = 2G^{(1)}(0)C'_n$ . The temperature dependence of the expressions is determined by the correlation time  $\tau_c$ , which is described by an Arrhenius law. Its inverse, the correlation rate

$$\tau_c^{-1} = \tau_{c0}^{-1} \exp\left(\frac{-E_A}{k_B T}\right), \quad (2.73)$$

is of the order of the jump rate  $\tau^{-1} \approx \tau_c^{-1}$  governing the diffusion process.  $E_A$  is the activation energy and  $k_B$  the Boltzmann constant. Taking this into account, Eqs. (2.72) (and (2.67)) can be used as fitting functions to deduce diffusion parameters (*i. e.* the attempt frequency  $\tau_0^{-1} \approx \tau_{c0}^{-1}$  and the activation energy  $E_A$ ) from experimental  $R_1$ ,  $R_{1\rho}$  and  $R_2$  data.

The temperature dependence of the relaxation rates in the case of dipolar interactions is shown schematically in Fig. 2.4a. Here, the constants  $C_n$  are related in such a way, that  $C_2 = C_{1\rho} = 1/4C_1$ , *cp.* Eqs. (2.65) and (2.68). Plotting the logarithm of  $R_1$  as a function of inverse temperature results in a relaxation peak maximum, for which the condition  $\omega_0 \tau_c \approx 1$  holds.\* The flanks on either side of the maximum exhibit the following proportionality:

$$R_1 \propto \tau_c \quad \text{for } \omega_0 \tau_c \ll 1, \quad (2.74a)$$

$$R_1 \propto \tau_c^{-1} \omega_0^{-2} \quad \text{for } \omega_0 \tau_c \gg 1, \quad (2.74b)$$

from which can be seen that the peaks are symmetrical with respect to the position of their maximum. The slope of the flanks  $\pm \frac{E_A}{k_B}$  in the Arrhenius representation gives direct access to the activation energy. The first limit  $\omega_0 \tau_c \ll 1$  is also known as the *high-temperature limit* and  $\omega_0 \tau_c \gg 1$  as the *low-temperature limit* (or *low-frequency limit* and *high-frequency limit*, respectively). Further, we see that the SLR rates in the LT limit exhibit a quadratic frequency dependence absent in the HT limit. This dependence is also demonstrated in Fig. 2.4a, where SLR rate peaks are shown for three different resonance frequencies  $\omega_0^I > \omega_0^{II} > \omega_0^{III}$ . Here, the

\* The maximum condition is exactly  $\omega_0 \tau_c = 1$  if only the first term in the brackets of Eq. (2.72a) is considered. Taking the complete expression, the condition is  $\omega_0 \tau_c \approx 0.62$ .

lowering of  $\omega_0$  results in a raising of the rates on the LT flank, and a corresponding shift of the maximum to lower temperatures.

The solid lines in Fig. 2.4a represent relaxation rates belonging to the same resonance frequency  $\omega_0^{\text{II}}$ . In the limit  $\omega_0 \tau_c \gtrsim 1$  the SLR rates  $R_{1\rho}$  behave essentially the same as in the laboratory frame, with the difference that here the resonance frequency  $\omega_1$  (known as the *locking frequency*) is several orders of magnitude lower than  $\omega_0$ ,\* and thus diffusion processes are probed on much longer time (and length) scales. As mentioned above, the linear progression of the SSR rates  $R_2$  is only valid in the regime of motional narrowing. At lower temperatures the rates are limited by the NMR line width to the value of the second moment  $R_{20}$ , cf. Eq. (2.67).

Often, experimental data does not show symmetrical SLR rate peaks, but LT flanks with lower slopes than those in the HT limit, as well as a sub-quadratic frequency dependence. This is particularly the case in structurally disordered systems (such as glasses), where the assumption of a purely isotropic diffusion processes can no longer be assumed to be valid. Instead, a complex interplay between structural disorder and Coulomb forces is expected; see *e. g.* Bunde *et al.*<sup>[81]</sup> and the references given therein. But this behavior is also found in structurally ordered materials, where the effect is generally associated with correlated motion of the mobile spins.<sup>[82]</sup>

\* From Eq. (2.72c) the maximum condition is derived as  $\omega_1 \tau_c = 0.5$ , which can be still assumed as  $\omega_1 \tau_c \approx 1$  if only order-of-magnitude approximations are considered.

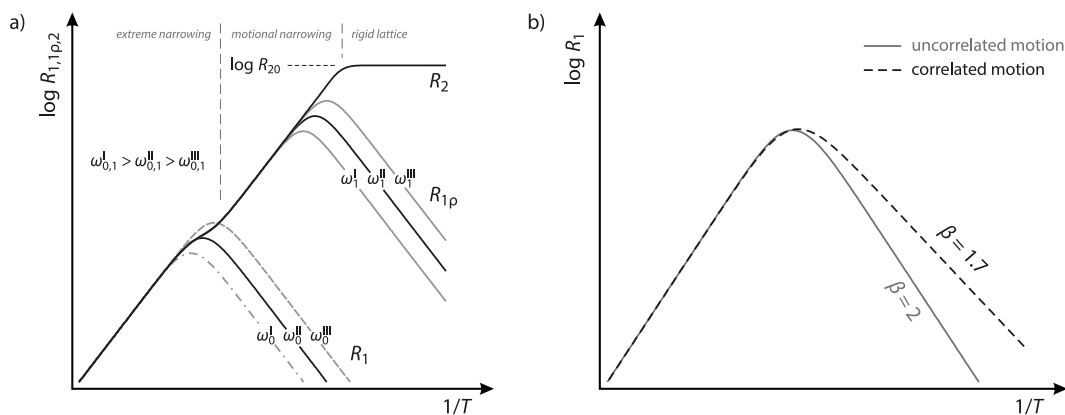


**Figure 2.4:** a) Schematic representation of the temperature dependence of the relaxation rates  $R_1$ ,  $R_{1\rho}$  and  $R_2$  resulting from dipol–dipole interactions via uncorrelated three-dimensional jump diffusion processes. See text for further details. b) Depiction of the influence of correlation effects on the NMR SLR rates  $R_1$ . The solid line represents a relaxation rate peak according to the BPP model for isotropic 3D-diffusion ( $\beta = 2$ ), while the dashed line accounts for correlated diffusion ( $\beta = 1.7$ ) due to structural disorder and Coulomb interactions.

In this case, a spectral density function modifying the BPP approach is available as<sup>[82,83]</sup>

$$J(\omega) = G(0) \frac{2\tau_c}{1 + (\omega\tau_c)^\beta}, \quad (2.75)$$

where  $1 < \beta < 2$  accommodates correlation effects. Thus, the expression for the SLR rate in the laboratory frame (Eq. (2.72a)) simply changes to

$$R_1 = C_1 \left[ \frac{\tau_c}{1 + (\omega_0\tau_c)^\beta} + \frac{4\tau_c}{1 + (2\omega_0\tau_c)^\beta} \right]. \quad (2.76)$$

The impact of this modification on the SLR rate is demonstrated in Fig. 2.4b for a value of  $\beta = 1.7$ . As can be seen, the slope of the HT flank ( $\omega_0\tau_c \ll 1$ ) does not change for correlated diffusion, while it is reduced on the LT side ( $\omega_0\tau_c \gg 1$ ). Evaluating both temperature limits, we get

$$R_1 \propto \tau_c \quad \text{for } \omega_0\tau_c \ll 1, \quad (2.77a)$$

$$R_1 \propto \tau_c^{1-\beta} \omega_0^{-\beta} \quad \text{for } \omega_0\tau_c \gg 1. \quad (2.77b)$$

From Eqs. (2.77b) and (2.73) it can be derived that the reduction of the slope corresponds to a reduction of the activation energy  $E_A^{\text{LT}} = (\beta - 1)E_A$  in the LT limit. This limit ( $\omega_0\tau_c \gg 1$ ) is generally connected to diffusional motion on short time scales and length scales, while the HT limit ( $\omega_0\tau_c \ll 1$ ) represents long-range diffusion.<sup>[84]</sup>

## 2D diffusion: Richards' model

Part of the present work is concerned with structurally confined ionic motion. It will come as no surprise that this confinement should be reflected in NMR experiments. Indeed, given the right conditions, frequency-dependent SLR NMR measurements provide a relatively simple way to unequivocally determine the dimensionality of a diffusion process.

Since the diffusivity of the mobile spins is thermally activated (see Eq. (2.26)), it follows that in the LT limit the spins will perform only few jumps. Confining the motion, for example, to a plane (2D diffusion) will thus have little effect in this limit as compared to motion in three dimensions. However, in the HT limit, where they will perform many jumps and long-range movement is probed, the confinement should be visible in experimental data.

From appropriate models, the temperature limits of the spectral density function for uncorrelated 2D-diffusion can be derived as<sup>[82,85,86]</sup>

$$J^{2D}(\omega, \tau_c) \propto \tau_c \ln(1/\omega\tau_c) \quad \text{for } \omega\tau_c \ll 1, \quad (2.78a)$$

$$J^{2D}(\omega, \tau_c) \propto \tau_c^{-1} \omega^{-2} \quad \text{for } \omega\tau_c \gg 1. \quad (2.78b)$$

As expected, the expression in the high-frequency limit ( $\omega\tau_c \gg 1$ ) is the same as that given by the BPP model for isotropic diffusion on a three dimensional lattice, *cf.* Eq. (2.74b). In

the low-frequency limit, however, a logarithmic frequency dependence is arrived at. The temperature (and frequency) limits (2.78) are neatly combined by the empirical spectral density function

$$J^{2D}(\omega, \tau_c) \propto \tau_c \ln \left( 1 + \frac{1}{(\omega \tau_c)^2} \right), \quad (2.79)$$

proposed by Richards.<sup>[87]</sup> Consequently, the two-dimensional SLR rate (see Eq. (2.71a)) can be expressed as

$$R_1^{2D} = C_1^{2D} \left[ \tau_c \ln \left( 1 + \frac{1}{(\omega_0 \tau_c)^\beta} \right) + 4\tau_c \ln \left( 1 + \frac{1}{(2\omega_0 \tau_c)^\beta} \right) \right], \quad (2.80)$$

where the exponent  $\beta \leq 2$  is again accounting for potential correlation effects.<sup>[82,88]</sup>

The SLR rates calculated using Eq. (2.80) are depicted in Fig. 2.5 (solid lines), where they are compared to those derived from the BPP model (dashed lines). While the rates coincide on their corresponding LT flanks, showing the same temperature and frequency dependence, there is a marked difference in the HT limit. Here, not only are the slopes reduced in comparison to the three-dimensional case,\* but there is also a frequency dependence characteristic of lower-dimensional diffusion processes. Thus, measuring the NMR SLR rate  $R_1$  at a constant temperature in the HT limit as a function of  $\omega_0$  provides an elegant method to distinguish a two-dimensional diffusion process from a three-dimensional one.

\* It should be noted that strictly speaking the slope in the high-temperature limit cannot any longer be described by an Arrhenius law (*cf.* Eq. (2.78a)). However, due to the, in most cases, limited temperature range in which experimental data can be acquired, the slope—and accordingly the activation energy—appear to be simply reduced by a factor of about  $3/4$ .

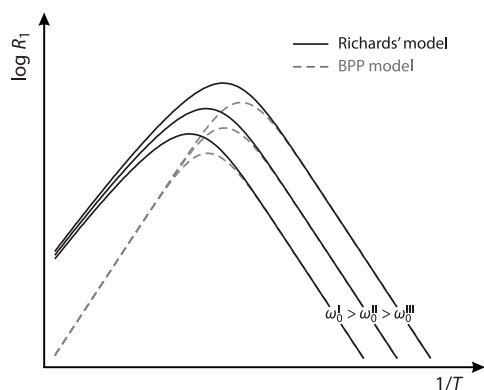


**Figure 2.5:** Comparison between the SLR rates derived using Richards' spectral density (solid lines, Eq. (2.80), 2D) with those of the BPP model (dashed lines, Eq. (2.76), 3D) at three different resonance frequencies  $\omega_0^I > \omega_0^{II} > \omega_0^{III}$ . The ionic motion was assumed to be uncorrelated ( $\beta = 2$ ) and the proportionality constants were chosen such that  $C_1 = C_1^{2D}$ . See text for further details.

### Diffusion coefficient

As mentioned above, the correlation rate (2.73) can be identified with the jump rate  $\tau^{-1}$ . Recalling the maximum condition  $\omega_0\tau \approx 1$  for measurements in the laboratory frame of reference (see above), the jump rate of a given nucleus at the temperature of the SLR maximum can be assumed (in a relatively model-independent way)<sup>[84]</sup> as  $\tau^{-1} \approx \omega_0$ . Then, the Einstein-Smoluchowski equation (2.22) can be used to calculate the corresponding diffusion coefficients. Analogously, diffusion coefficients are derived from measurements in the rotating frame using the condition  $\omega_1\tau = 0.5$ .

### 2.3.4 Spin-alignment echo NMR

A clear and easy to follow treatment of the spin-alignment echo (SAE) technique—particularly referring to  $^7\text{Li}$  nuclei—can be found in the dissertations of Qi<sup>[89]</sup> and Wilkening.<sup>[79]</sup> The main points shall be briefly summarized below.

As discussed in the previous section, the most straight-forward method to obtain diffusion parameters via NMR relaxation experiments is the recording of SLR rate maxima. Here, the jump rate of the diffusing particles probed is in the order of the resonance frequency. Thus, typical jump rates accessible are in the order of  $10^8 \text{ s}^{-1}$  and  $10^4 \text{ s}^{-1}$  when the measurements are performed in the laboratory frame and in the rotating frame, respectively. The attainable temperatures are prespecified by the experimental set-up and, using standard probe heads, typically range between about 450 K and 150 K. These limits can be pushed employing specialized equipment, such as cryoprobes (down to  $\sim 10 \text{ K}$ ) and high-temperature probes (up to  $\sim 600 \text{ K}$ ).<sup>\*</sup> In solids, diffusion-induced SLR maxima are usually found well above room temperature, even when measurements are performed in the rotating frame of reference. Also, for slower diffusion processes the maxima are shifted to higher temperatures, which means that here the investigated sample material itself becomes the limiting factor insofar as decomposition, phase transitions or even crystallite growth have to be considered.

An appropriate tool in the study of slow dynamics is found in SAE NMR.<sup>[17,79,89,91–94]</sup> Here, the interaction between the electric quadrupole moment of the probed nucleus and the EFG at its site is utilized to correlate the quadrupole frequencies at two different points of time. By increasing the interval between these points a decaying correlation function can be recorded. Ideally, this gives direct (*i. e.* model-free) access to the jump rate of the diffusing nucleus. The prerequisite is that the nucleus follows a path of electrically inequivalent sites.

SAE NMR experiments are performed using the Jeener–Broekaert pulse sequence<sup>[95]</sup>

$$\beta_{1,\phi_1} - t_p - \beta_{2,\phi_2} - t_m - \beta_{3,\phi_3} - t - \text{echo} , \quad (2.81)$$

\* Home-built HT probes can be constructed to reach temperatures up to 1200 K (see *e. g.* Ref. [90]). However, such probes require an intricate cooling system and are generally characterized by a reduced operational life span and/or extensive maintenance.

where the  $\beta_i$  denote the angle of the pulses and  $\phi_i$  their respective phases. The time intervals  $t_p$  and  $t_m$  between the pulses are the preparation time and the mixing (or evolution) time, respectively. Choosing the phases of  $\beta_1$  and  $\beta_2$  such that  $|\phi_1 - \phi_2| = \pi/2$ , the first two pulses in the sequence generate a quadrupolar alignment state from an initial equilibrium longitudinal magnetization, which can be used to store the phase information  $\omega_Q(t_m = 0)t_p$ , where  $\omega_Q$  is the quadrupole angular frequency defined in Eq. (2.62). During the mixing time, the nucleus diffuses and has the opportunity to visit sites where it is subject to different EFGs. The third pulse is then used to transfer the state into an observable magnetization, multiplying it with a second phase information  $\omega_Q(t_m)t$  at the end of  $t_m$ . The spin echo is then acquired some time  $t$  after the third pulse, having its maximum at  $t = t_p$ . With the pulse lengths set so that  $\beta_1 = \pi/2$  and  $\beta_2 = \beta_3 = \pi/4$ , the amplitude of the echo signal is the two-time correlation function<sup>[79,89,93,96,97]</sup>

$$S_2(t_p, t_m, t) = \frac{9}{20} \sin[\omega_Q(0)t_p] \sin[\omega_Q(t_m)t]. \quad (2.82)$$

Accounting for the fact that powder samples can be mathematically described by an ensemble average (here denoted by  $\langle \dots \rangle$ ) and also factoring in relaxation processes taking place between the pulses, the echo amplitude then takes the form

$$S_2(t_p, t_m, t) = \frac{9}{20} \langle \sin[\omega_Q(0)t_p] \sin[\omega_Q(t_m)t] \rangle \exp\left(-\frac{2t_p}{T_2}\right) \exp\left(-\frac{t_m}{T_1}\right). \quad (2.83)$$

Here, echo damping via NMR relaxation is described by simple exponentials, though often stretched exponentials are observed experimentally. Equation (2.83) exemplifies nicely, that the correlation time  $\tau_{\text{SAE}}$  accessible by SAE experiments is limited by  $T_2 \leq \tau_{\text{SAE}} \leq T_1$ . At sufficiently low temperatures, the echo amplitude can be additionally damped by spin-diffusion effects, see *e. g.* Refs. [98, 99] (pages 47ff. and 65ff. of this work).

Appropriate phase cycling helps to compensate for deviations of the real pulse lengths and phases from the ideal ones. Even more, in the case of SAE NMR experiments the right phase cycling is essential to the generation of pure quadrupolar spin-alignment states in that it is used to suppress unwanted signal contributions (*e. g.* multiple quantum coherences).<sup>[89,96,100]</sup> The phase cycling employed in the experiments presented here can be found in the literature<sup>[89,90,96,101]</sup> but is also given in Appendix B.3, for the sake of convenience.

The correlation times obtained are independent of the strength of the quadrupole coupling. This means they are independent of the field the experiment is performed in and are also unaffected by changes in the quadrupole coupling constant due to temperature.<sup>[102]</sup> As mentioned above, the correlation rates can be identified with the jump rates of the diffusing nuclei.<sup>[17,79,93,94,103,104]</sup> Using the Einstein-Smoluchowski relation in the form of Eq. (2.22), these correlation times can be easily converted into diffusion coefficients. Interestingly, these are often found to have similar values as those deduced either from NMR relaxometry,<sup>[17,79,92,93,103,105]</sup> using the maximum condition (see above) or from impedance-spectroscopy measurements,<sup>[93,94,103,105,106]</sup> using the Nernst-Einstein equation (*cf.* the following section).

## 2.4 Basics of impedance spectroscopy

### 2.4.1 Introduction

In a short introductory text,<sup>[107]</sup> J. Ross Macdonald, one of the pioneers of modern impedance spectroscopy, gives a very succinct description of this method, which is well worth quoting verbatim:

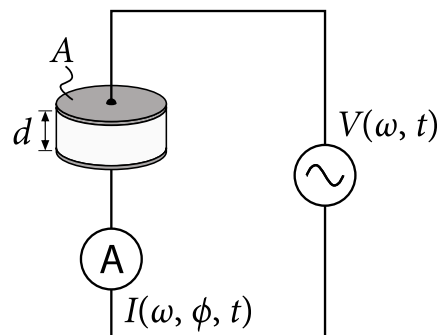
☞ Impedance spectroscopy (IS) is a general term that subsumes the small-signal measurement of the linear electrical response of a material of interest (including electrode effects) and the subsequent analysis of the response to yield useful information about the physicochemical properties of the system. Analysis is generally carried out in the frequency domain, although measurements are sometimes made in the time domain and then Fourier transformed to the frequency domain. IS is by no means limited to the measurement and analysis of data at the impedance level (*e.g.*, impedance vs. frequency) but may involve any of the four basic immittance levels: thus, most generally, IS stands for immittance spectroscopy. ☞

Compared to other methods, the experimental set-up for IS measurements is relatively simple: all that is needed is an AC-voltage source, an ammeter, and a means to establish the phase difference  $\phi$  between the input voltage  $V(\omega)$  and output current  $I(\omega)$ . Modern impedance spectrometers combine these functions into a single device giving access to a wide frequency range of  $10^{-5} \dots 10^7$  Hz\* and able to measure impedances as high as  $10^{14} \Omega$ .

The principle of impedance spectroscopy is based on the application of a (usually sinusoidal) alternating voltage  $V(\omega)$  with frequency  $\nu = \omega/2\pi$  to the system under investigation and the measurement of the resulting current  $I(\omega)$ , *cf.* Fig. 2.6 for a basic experimental setup. Provided a small enough voltage amplitude  $V_0$ , the response of the system will be linear

\* Through careful design of the impedance cell, frequencies in the gigahertz range are accessible by high-frequency RF impedance analyzers; see Sect. B.1.2 for an example.

**Figure 2.6:** Schematic representation of the most basic IS experiment for ion conducting solids. An AC-voltage generator ( $\sim$ ) is contacted to the electrodes of the sample and the induced current is measured by means of an ammeter (A). The area of the electrodes  $A$  and their distance  $d$  to each other are used to normalize the resistivity  $\tilde{\rho}$  and the conductivity  $\tilde{\sigma}$  to the sample geometry (see text for further explanations).



and the current will have the same shape and frequency, generally exhibiting an additional, frequency dependent phase offset  $\phi(\omega)$  when compared to the voltage:

$$V(\omega) = V_0 \sin(\omega t), \quad (2.84a)$$

$$I(\omega) = I_0 \sin(\omega t - \phi(\omega)). \quad (2.84b)$$

In the case of purely resistive elements the phase difference  $\phi$  is zero and the resistance  $R$  is given as the ratio of voltage and current  $R = V_0/I_0$ , a principle commonly known as *Ohm's law*. Taking a non-vanishing phase offset into account, a more general concept is found in the impedance, which can be defined as a complex resistance. Here, it is convenient to switch to complex quantities, which will be indicated by a tilde in the following discussion. Thus, equations (2.84) are expressed as

$$\tilde{V}(\omega) = V_0 \exp(i\omega t), \quad (2.85a)$$

$$\tilde{I}(\omega) = I_0 \exp(i\omega t - i\phi(\omega)), \quad (2.85b)$$

and the impedance is given by the Ohm's law-like relation  $\tilde{Z}(\omega) = \tilde{V}(\omega)/\tilde{I}(\omega) = |\tilde{Z}(\omega)| \exp(i\phi)$ , with the absolute value of  $\tilde{Z}$  being  $|\tilde{Z}(\omega)| = V_0/I_0$ .<sup>\*</sup> Using *Euler's formula* this can be written as

$$\begin{aligned} \tilde{Z} &= |\tilde{Z}|(\cos(\phi) + i \sin(\phi)) \\ &\equiv Z' + iZ'', \end{aligned} \quad (2.86)$$

where the real part  $Z' = |\tilde{Z}| \cos(\phi)$  and imaginary part  $Z'' = |\tilde{Z}| \sin(\phi)$  are marked by primes. As indicated in Fig. 2.7, the impedance can be thought of as a vector in the complex plane, with  $Z'$  and  $Z''$  being the rectangular coordinates and  $|\tilde{Z}|$  and  $\phi$  the polar coordinates. From the figure and Eq. (2.86) it is easy to see that  $|\tilde{Z}| = \sqrt{Z'^2 + Z''^2}$  and  $\phi = \arctan(Z''/Z')$ .

\* Provided that the voltage amplitude  $V_0$  is constant, it should be noted that in the case of non-resistive contributions to the impedance, the current amplitude  $I_0$  also will generally be a function of frequency. For the sake of conciseness the explicit dependence on  $\omega$  will be left implicit in the notation from hereon, unless clarity requires otherwise.

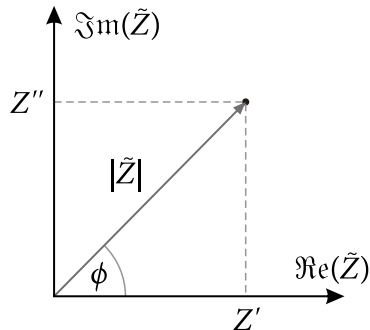


**Figure 2.7:** Complex plane plot of the impedance  $\tilde{Z}$  illustrating the use of rectangular ( $Z'$ ,  $Z''$ ) and polar ( $|\tilde{Z}|$ ,  $\phi$ ) coordinates.

Again, in analogy to the electrical conductance  $G = R^{-1}$ , the admittance  $\tilde{Y} = \tilde{Z}^{-1}$  is defined as the inverse of the impedance, thus giving

$$\begin{aligned}\tilde{Y} &= |\tilde{Y}| \exp(-i\phi) \\ &= |\tilde{Y}|(\cos(\phi) - i \sin(\phi))\end{aligned}\quad (2.87)$$

in polar coordinates (the absolute value being  $|\tilde{Y}| = |\tilde{Z}|^{-1}$ ) and

$$\begin{aligned}\tilde{Y} &= \frac{Z'}{|\tilde{Z}|^2} - i \frac{Z''}{|\tilde{Z}|^2} \\ &\equiv Y' + iY''\end{aligned}\quad (2.88)$$

in rectangular coordinates.

The impedance and the admittance are two of the four more commonly used quantities pertaining to IS, the other two being the modulus function  $\tilde{M} \equiv M' + iM'' = i\omega C_0 \tilde{Z}$  and the dielectric permittivity  $\tilde{\epsilon} \equiv \epsilon' - i\epsilon'' \equiv \tilde{M}^{-1} = \tilde{Y}/i\omega C_0$ . Here,  $C_0 \equiv \epsilon_0 A/d$  is the capacitance of the empty cell with electrode area  $A$  and electrode distance  $d^*$  (cf. Fig. 2.6). See Ref. [108] for more information on these functions, generally known as immittances.

As far as information on diffusivity is concerned, arguably, one of the most important quantities accessible by IS is the DC-conductivity  $\sigma_{DC}$ , provided the conductivity is governed solely (or nearly so) by the motion of ions. This quantity is derived from conductivity spectra, *i.e.*, from plots where the real part of the conductivity  $\tilde{\sigma}$  is given as a function of frequency  $\omega$ , or from complex impedance plots. The conductivity  $\tilde{\sigma} \equiv \sigma' + i\sigma''$  is a material specific quantity and as such independent of the geometry of the investigated sample. It is calculated by means of a normalizing geometry constant  $\kappa \equiv A/d$  and the admittance  $\tilde{Y}$ . For obvious reasons, similar considerations apply to the resistivity  $\tilde{\rho} \equiv \rho' + i\rho'' = 1/\tilde{\sigma}$ . Thus,  $\tilde{\sigma}$  and  $\tilde{\rho}$  are given by

$$\tilde{\sigma} = \tilde{Y}/\kappa \quad \text{and} \quad (2.89a)$$

$$\tilde{\rho} = \tilde{Z} \cdot \kappa, \quad (2.89b)$$

respectively. The normalizing constant  $\kappa$  is defined by the parameters of the cell geometry as they are given in the description of the dielectric permittivity (see above).

The interpretation of IS data of real systems was greatly advanced with the adaptation of complex-plane analyses to the four basic immittance functions  $\tilde{Z}$ ,  $\tilde{Y}$ ,  $\tilde{\epsilon}$ , and  $\tilde{M}$  in the forties [109–112] and the employment of complex nonlinear least square fitting in the late seventies. [113–115] The first had to that point already been successfully used in the field of electrical engineering, [112,116] the latter had become readily available with the advent of powerful and increasingly cheap computer technology. [108,117,118] Equivalent circuits have played an impor-

\* The quantity  $\epsilon_0 = 8.854187817 \times 10^{-12}$  F/m is the vacuum permittivity, defined as the inverse of the product of the vacuum permeability and speed of light squared, *i. e.*,  $\epsilon_0 \equiv 1/\mu_0 c^2$ .

tant role since the very beginnings.<sup>[110,112]</sup> They provide an approximation, an idealized model concept for the processes in the system under investigation by arranging various (ideal) electric circuit elements in such a way as to reproduce the experimental impedance of the system. A resistor in such an electrical network could represent a certain conductive pathway, *i. e.* the conductivity inside the bulk material or along grain boundaries, whereas a capacitor could account for a space charge polarization region as it may form across a grain boundary. However, further discussion is beyond the scope of the analysis presented in this work and the interested reader is referred to the appropriate literature. For example, Ref. [108] provides an extensive overview of the subject matter at hand.

### 2.4.2 Conductivity spectra and diffusion

As referred to at the beginning of this section, conductivity measurements can be carried out over a very wide range of frequencies ( $10^{-5} \dots 10^7$  Hz) and temperatures (113 ... 623 K). The data gathered can be processed in various ways, one of them being in the form of conductivity spectra. These are double logarithmic plots of the real part of the conductivity  $\sigma'$  as a function of frequency  $\nu$  measured at various temperatures. An example of a solid with negligible electronic contributions is shown in Fig. 2.8, demonstrating the most important properties of conductivity spectra at frequencies up to the MHz range:

- (i.) At low frequencies (and intermediate temperatures) the spectra feature a frequency independent plateau with the value  $\sigma' = \sigma_{\text{DC}}$ , known as the DC-conductivity. In solids with predominantly ionic conductivity  $\sigma_{\text{DC}} T$  is usually Arrhenius activated:  $\sigma_{\text{DC}} T \propto \exp(-E_{\text{A}}^{\text{DC}}/k_{\text{B}} T)$ , with the activation energy  $E_{\text{A}}^{\text{DC}}$  and Boltzmann's constant  $k_{\text{B}}$ .
- (ii.) At higher frequencies the conductivity  $\sigma'(\nu)$  increases monotonically with  $\nu$  up to the order of phonon frequencies. This dispersive regime originates from non-ideal behavior of real solids. Thus, various correlation effects introduced by interactions between the diffusing ions, lattice defects, the motion of a large number of charge carriers, and the response of the rigid lattice to ion jumps can contribute to the frequency dependence of the conductivity.<sup>[120]</sup>
- (iii.) Taking both previous points together, the initial part of the spectra can be reasonably well described by the *Jonscher power law*  $\sigma' = \sigma_{\text{DC}} + A\nu^p$ . In the log-log plot, the exponent  $p$ —usually being between 0.6 and 0.7—corresponds to the slope of the dispersive part. This behavior is observed in a wide range of solids and is known as the “universal dielectric response”.<sup>[121]</sup>
- (iv.) With decreasing temperatures the onset of the dispersive regime is shifted to lower frequencies and its slope approaches the value of 1. Also, the temperature dependence of the conductivity decreases, which amounts to  $\sigma' \propto \nu$ . This corresponds to a frequency independent dielectric loss  $\epsilon'' \neq f(\nu)$ , a phenomenon commonly known as *nearly constant loss* (NCL). Although NCL behavior is found for a wide range of ion conducting

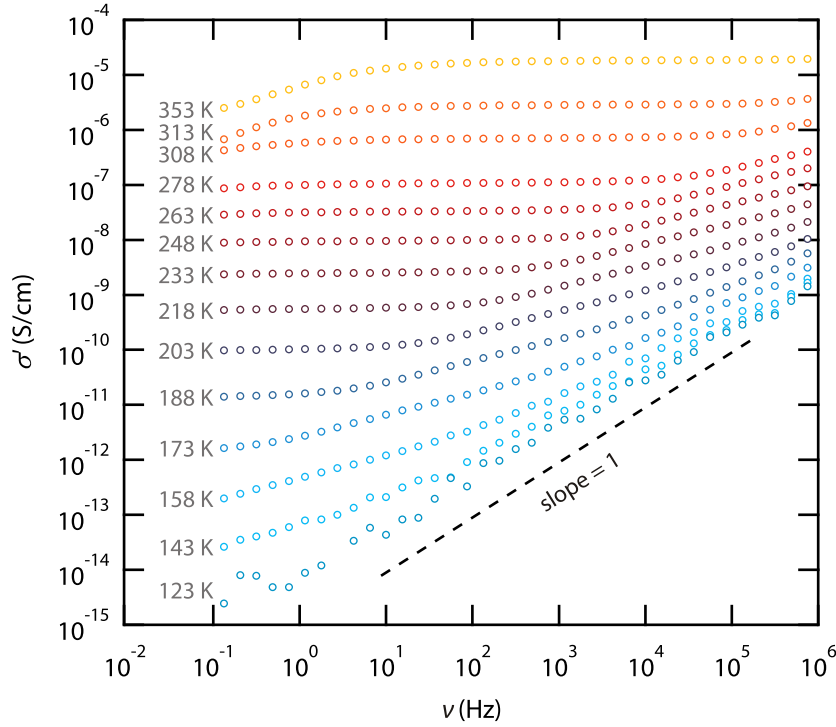


**Figure 2.8:** Selected conductivity spectra of microcrystalline  $\text{LiBH}_4$  exemplifying common features found nearly universally in IS. Data is excerpted from Ref. [119] (see also p. 110).

solids<sup>[122–128]</sup> it is yet not fully understood. However, it is often associated with strictly localized motions and should not be mixed up with “real” translational jumps of the conducting ions.<sup>[129–131]</sup>

- (v.) At elevated temperatures, the mobility of the migrating ions becomes significant enough to be observed in the form of polarization effects at the ion blocking electrodes. This is reflected by a reduction of  $\sigma'$  for decreasing frequencies.
- (vi.) While not displayed in Fig. 2.8, at very high frequencies—typically in the GHz range—the conductivity of ionic solids is governed by vibrational contributions, showing a  $\nu^2$  frequency dependence on their low-frequency flank.<sup>[129,130,132]</sup> See for example Fig. 2b on page 110.

It should be noted that  $\sigma_{\text{DC}} = \sum_i \sigma_{\text{DC}}^i$  is generally a sum of conductivities of the ionic species  $i$  involved. In the materials presented in this thesis however, Li is the only species with significant diffusivity, so that  $\sigma_{\text{DC}}$  is assumed to have only one contribution.

Thus, given the points above, the most easily accessible quantity of IS driven by diffusion processes in the investigated system—and indeed the most closely related to the diffusion of

ions—is the ionic DC-conductivity  $\sigma_{\text{DC}}$ . The relation to the charge diffusion coefficient  $D^\sigma$  is given by the *Nernst–Einstein* equation<sup>[26,133–135]</sup>

$$D^\sigma = \frac{\sigma_{\text{DC}} k_{\text{B}} T}{nq^2}, \quad (2.90)$$

where  $n$  signifies the charge-carrier density and  $q$  the charge of the ions. Since  $D^\sigma$  is strictly speaking not defined in the sense of Fick’s first law but through Eq. (2.90), it should formally not be regarded as a “real” diffusion coefficient.<sup>[20,136]</sup> However, it has the dimensions of a diffusion coefficient and can be thought of as “the diffusion coefficient of the *assembly* of ions as if the assembly itself acts like a single (hypothetical) particle.”<sup>[20]</sup> The conventional relation to the tracer diffusion coefficient  $D^{\text{tr}}$  introduced in section 2.1.3 is given by the *Haven ratio*  $H_{\text{R}} \equiv D^{\text{tr}}/D^\sigma$ , which allows for the access to useful information about the diffusion mechanism in a given system.  $H_{\text{R}}$  represents correlation effects present in ion diffusion<sup>[20,136–139]</sup> and is usually of the order of 1, having a slightly smaller value, though  $H_{\text{R}} > 1$  is also observed.<sup>[63,136,140,141]</sup> In some cases, however, values of one or several orders of magnitude larger than 1 are also known.<sup>[142,143]</sup> For uncorrelated motion of the ions, the Haven ratio—just as the tracer correlation factor  $f$  (*cf.* Eq. (2.23))—takes on the value of one,  $H_{\text{R}} = f = 1$ ,<sup>[20]</sup> and the measurement of the DC-conductivity  $\sigma_{\text{DC}}$  gives direct access to the mean jump rate  $\bar{\tau}^{-1}$  via the microscopic diffusion coefficient  $D^{\text{tr}}$  (see Eq. (2.24)):

$$\bar{\tau}^{-1} = \frac{H_{\text{R}}}{f} \cdot \frac{2dk_{\text{B}}T}{nq^2\ell^2} \cdot \sigma_{\text{DC}}. \quad (2.91)$$

Here,  $d$  and  $\ell$  are the dimension of the diffusion process and the mean jump length, respectively, as defined in section 2.1.3. Interestingly, in the special case of diffusion via a vacancy mechanism the factor  $H_{\text{R}}/f$  in Eq. (2.91) is roughly 1 even in the case of correlated motion.<sup>[136]</sup> Indeed, in the limit of an almost full or an almost empty lattice of charge carriers the Haven ratio is equal to the tracer correlation factor  $H_{\text{R}} = f$ .<sup>[20,138,139]</sup>



## 3 Results

### 3.1 Introduction

Below, the results of this dissertation are presented cumulatively in the form of papers published in peer-reviewed journals. The articles have been arranged into four sections defined by common attributes of the studied materials, *viz.* argyrodite-type Li-ion conductors (Sect. 3.2), garnet-type Li-ion conductors (Sect. 3.3), layer-structured Li-ion conductors (Sect. 3.4), and structurally disordered Li-ion conductors (Sect. 3.5).

Thus, a start is made by two articles on lithium argyrodites, representing a new class of Li<sup>+</sup> containing solids. The work was done in collaboration with the group of Prof. Dr. Deiseroth (Siegen, Germany), where the sample material was synthesized. The first paper covers the compound Li<sub>7</sub>PSe<sub>6</sub> (“Long-range Li<sup>+</sup> dynamics in the lithium argyrodite Li<sub>7</sub>PSe<sub>6</sub> as probed by rotating-frame spin–lattice relaxation NMR”,<sup>[99]</sup> pp. 47–56) while the second one discusses the chalcogenated compounds Li<sub>6</sub>PSe<sub>5</sub>Cl and Li<sub>6</sub>PS<sub>5</sub>Br (“Highly Mobile Ions: Low-Temperature NMR Directly Probes Extremely Fast Li<sup>+</sup> Hopping in Argyrodite-Type Li<sub>6</sub>PS<sub>5</sub>Br”,<sup>[144]</sup> pp. 58–63). It turned out that lithium argyrodites exhibit a Li-ion diffusivity sufficiently high to be considered as solid electrolytes in all-solid-state batteries. Particularly, with a jump rate in the order of 10<sup>9</sup> s<sup>-1</sup> at room temperature, Li<sub>6</sub>PS<sub>5</sub>Br has been found to have the highest Li<sup>+</sup> mobility of the three samples. Indeed, the results point to it being one of the fastest solid Li-ion conductors to have been investigated by <sup>7</sup>Li NMR, so far. Probing Li-ion dynamics by NMR SLR measurements in the rotating frame of reference, it was possible to record complete diffusion-induced R<sub>1ρ</sub> rate peaks for all three samples. A systematic comparison of the results certainly brought us one step closer to an understanding of how cation diffusivity may be improved by anion substitution.

The next set of articles involves representatives of another family of Li-ion conductors, interesting because of the potential application as solid electrolytes in current batteries, *viz.* garnet-type oxides. The work presented originated from a collaboration between our work-group and that of Prof. Dr. Thangadurai (Calgary, Canada). In “Spin-alignment echo NMR: probing Li<sup>+</sup> hopping motion in the solid electrolyte Li<sub>7</sub>La<sub>3</sub>Zr<sub>2</sub>O<sub>12</sub> with garnet-type tetragonal structure” (pp. 65–72) the tetragonal modification of Li<sub>7</sub>La<sub>3</sub>Zr<sub>2</sub>O<sub>12</sub> was studied by <sup>7</sup>Li SAE NMR, a method sensitive to relatively slow diffusion processes. The results obtained here from an atomic-scale point of view are in line with those deduced from impedance spectroscopy reflecting macroscopic Li migration, indicating that both methods probe basically the same correlation function. In the second paper (“Macroscopic and microscopic Li<sup>+</sup> transport parameters in cubic garnet-type ‘Li<sub>6.5</sub>La<sub>2.5</sub>Ba<sub>0.5</sub>ZrTaO<sub>12</sub>’ as probed by impedance spectroscopy and NMR”, pp. 74–82), results from complementary impedance spectroscopy and <sup>7</sup>Li NMR

measurements on cubic “ $\text{Li}_{6.5}\text{La}_{2.5}\text{Ba}_{0.5}\text{ZrTaO}_{12}$ ” are presented. It was found that the high conductivity of the compound ( $\sigma_{\text{DC}} \approx 10^{-4}$  S/cm at RT) is due to long-range Li-ion transport. Further, examinations in Thangadurai’s group showed good chemical stability with the cathode material  $\text{Li}_2\text{FeMn}_3\text{O}_8$  underlining its potential use as a solid electrolyte in all-solid-state batteries.

This section is then followed by three publications on layer-structured materials. In “Fast Li diffusion in crystalline  $\text{LiBH}_4$  due to reduced dimensionality” (pp. 84–87) lithium borohydride was studied by temperature-variable as well as frequency-dependent  $^{6,7}\text{Li}$  NMR SLR.  $\text{LiBH}_4$  exists in two structurally distinct modifications, undergoing a reversible phase transition at about 381 K, which is tellingly reflected in the NMR data obtained. The low-temperature modification exhibits an orthorhombic symmetry, while the high-temperature modification is hexagonal. Hexagonal lithium borohydride has been found to display a rather high Li-ion diffusivity, giving it the potential to be employed as a solid electrolyte if its layer structure could be stabilized down to ambient temperature. The high  $\text{Li}^+$  mobility is attributable to diffusion in reduced dimensions, which is unequivocally demonstrated by a characteristic frequency dependence on the high-temperature side of the diffusion induced SLR rate maximum. Further layer-structured materials investigated were lithiated  $3\text{R-NbS}_2$  and  $\text{LiC}_6$  presented in the articles “Two-dimensional diffusion in  $\text{Li}_{0.7}\text{NbS}_2$  as directly probed by frequency-dependent  $^7\text{Li}$  NMR” (pp. 89–95) and “Lithium motion in the anode material  $\text{LiC}_6$  as seen via time-domain  $^7\text{Li}$  NMR” (pp. 97–105), respectively. The first of these resulted from a collaboration with the group of Prof. Dr. Lerch (Berlin, Germany), where the lithiated  $\text{NbS}_2$  was prepared. The measurements on  $\text{LiC}_6$  were performed by my colleague DI Julia Langer (Graz, Austria). Both solids are of great interest in that layer-structured materials which allow the reversible insertion of Li ions are well-suited to be used as electrodes in current secondary batteries. In both cases, SLR NMR experiments in the rotating frame, particularly, were found to be the method of choice to probe Li diffusion parameters. And while a logarithmic frequency dependence of the SLR rates characteristic of two-dimensional diffusion has been indeed measured in  $\text{Li}_{0.7}\text{NbS}_2$ , the experimental realization of corresponding measurements for  $\text{LiC}_6$  proved to be difficult. Particularly, the magnitude of the locking pulses was found to be too high to be handled correctly by the spectrometer, prohibiting a frequency-dependent NMR study. However, it was possible to record a complete, diffusion-induced NMR SLR rate maximum and to compare the results with appropriate diffusion models. Considering that previous  $\beta$ -NMR results point towards low-dimensional Li-ion migration,<sup>[145,146]</sup> our results seem to indicate a non-negligible inter-layer hopping process.

The last section covers the articles on disordered Li-ion conductors, *viz.* “Motion of  $\text{Li}^+$  in Nanoengineered  $\text{LiBH}_4$  and  $\text{LiBH}_4:\text{Al}_2\text{O}_3$  – Comparison with the Microcrystalline Form” (pp. 107–114) and “Studying Li Dynamics in a Gas-Phase Synthesized Amorphous Oxide by NMR and Impedance Spectroscopy” (pp. 116–127). The first of these, constitutes the continuation of the work done on microcrystalline  $\text{LiBH}_4$  (see above).<sup>[147]</sup> An attempt has been made to preserve the high ionic conductivity of the hexagonal (high-temperature) modification down to lower temperatures by the introduction of structural disorder via high-energy ball milling. This approach is concomitant with a significant reduction of crystallite size. Indeed, the genera-

tion of a large volume fraction of hetero-interfaces in the nano-composite  $\text{LiBH}_4:\text{Al}_2\text{O}_3$  results in improved Li dynamics as probed by  $^7\text{Li}$  NMR line-shape measurements and SLR NMR experiments. A comparison is made to the single-phase nanocrystalline  $\text{LiBH}_4$ . Here, SLR rate data also points to improved diffusivity, reflected in a metastable behavior slightly below the phase-transition temperature. In the second paper NMR and impedance spectroscopy was used to comprehensively investigate a gas-phase synthesized non-stoichiometric amorphous Li-Al-Si-oxide, prepared in the group of Prof. Dr. Binnewies (Hannover, Germany). This system served as a model for materials exhibiting high structural disorder. While the compound was found to display only moderate Li diffusivity, the work itself shows how complementary methods—being sensitive to diffusion processes on different time and length scales—can be used to thoroughly characterize structurally disordered materials intended for use in Li-ion batteries.

## 3.2 Argyrodite-type Li-ion conductors

### 3.2.1 Long-range Li<sup>+</sup> dynamics in the lithium argyrodite Li<sub>7</sub>PSe<sub>6</sub> as probed by rotating-frame spin-lattice relaxation NMR (pp. 47–56)

Epp, V., Gün, Ö., Deiseroth, H.-J., and Wilkening, M. *Physical Chemistry Chemical Physics* **15**, 7123–7132 (2013).—This article is reproduced by permission of The PCCP Owner Societies. The original article can be found online at <http://pubs.rsc.org/en/Content/ArticleLanding/2013/CP/c3cp44379e#!divAbstract>. ©2013 The PCCP Owner Societies.

## Long-range Li<sup>+</sup> dynamics in the lithium argyrodite Li<sub>7</sub>PSe<sub>6</sub> as probed by rotating-frame spin–lattice relaxation NMR†

Cite this: *Phys. Chem. Chem. Phys.*, 2013, **15**, 7123

V. Epp,<sup>a</sup> Ö. Gün,<sup>b</sup> H.-J. Deiseroth<sup>b</sup> and M. Wilkening<sup>\*a</sup>

Lithium-rich argyrodites belong to a relatively new group of fast ion conducting solids. They might serve as powerful electrolytes in all-solid-state lithium-ion batteries being, from a medium-term point of view, the key technology when safe energy storage systems have to be developed. Spin–lattice relaxation (SLR) nuclear magnetic resonance (NMR) measurements carried out in the rotating frame of reference turned out to be the method of choice to study Li dynamics in argyrodites. When plotted as a function of the inverse temperature, the SLR rates  $\log_{10}(R_{1\rho})$  reveal an asymmetric diffusion-induced rate peak. The rate peak contains information on the Li jump rate, the activation energy of the hopping process as well as correlation effects. In particular, considering the high-temperature flank of the SLR NMR rate peak recorded in the rotating frame of reference, an activation energy of approximately 0.49 eV is found. This value represents long-range lithium jump diffusion in crystalline Li<sub>7</sub>PSe<sub>6</sub>. As an example, at 325 K the Li jump rate determined from SLR NMR is in the order of  $1.4 \times 10^5 \text{ s}^{-1}$ . The pronounced asymmetry of the rate peak  $R_{1\rho}(1/T)$  points to correlated Li motion. It is comparable to that which is typically found for structurally disordered materials showing a broad range of correlation times.

Received 5th December 2012,  
Accepted 15th March 2013

DOI: 10.1039/c3cp44379e

[www.rsc.org/pccp](http://www.rsc.org/pccp)

### 1. Introduction

The development of powerful lithium-ion batteries, which are expected to be the intermediate-term devices to store electrical energy, requires the availability and provision of lithium-ion conductors with a very high Li<sup>+</sup> mobility.<sup>1–7</sup> In particular, compared to *liquid* electrolytes, the use of *solid* ion conductors meets the challenges to design more powerful and highly safe lithium-ion batteries.<sup>7,8</sup> These are expected to show a long lifetime which is, in particular, necessary for large-scale, decentralised stationary energy storage. Thus, research on materials for lithium-ion batteries is in line with the imperative goal to reduce our dependence on fossil fuels if we are to store electrical energy from renewable sources and, hence, to combat climate change. Finding suitable solid electrolytes will certainly provide a leap forward towards the development of safe

all-solid-state lithium-ion batteries being useful for diverse applications of energy storage systems such as portable electronic devices or even (hybrid) electric vehicles.

During the last few years many Li containing solid electrolytes have been screened and also modified for such purposes. However, the number of suitable candidates turns out to be rather rare, see, *e.g.*, ref. 8–14. Essentially, besides chemical inertness, which oxide materials usually show, they have to fulfill the necessary requirement to exhibit an ionic conductivity exceeding, in the ideal case,  $10^{-3} \text{ S cm}^{-1}$  at room temperature.

Quite recently, a new class of Li-rich materials has been investigated, *viz.* crystalline lithium argyrodites, which exhibit such a sufficiently high Li<sup>+</sup> mobility.<sup>9,15</sup> So far, Li dynamics of the compounds belonging to the class of Li<sub>7</sub>PX<sub>6</sub> (X = S, Se) and Li<sub>6</sub>PX<sub>5</sub>X' (X' = Cl, Br, I), which are from a structural point of view closely related to the mineral Ag<sub>8</sub>GeS<sub>6</sub>, have mainly been investigated by impedance spectroscopy.<sup>9,15–19</sup> Apart from first line shape analyses,<sup>9,15</sup> an in-depth Li nuclear magnetic resonance (NMR) spin–lattice relaxation (SLR) study is still missing. It turned out that the highest conductivity was found for the halides rather than for the pure sulfides or selenides.<sup>15</sup> Apart from impedance spectroscopy, Li jump rates and thus Li

<sup>a</sup> Christian Doppler Laboratory for Lithium-ion Batteries, Graz University of Technology, Institute for Chemistry and Technology of Materials, Stremayrgasse 9, 8010 Graz, Austria. E-mail: viktor.epp@tugraz.at, wilkening@tugraz.at

<sup>b</sup> University of Siegen, Inorganic Chemistry I, Adolf-Reichwein-Straße 2, 57068 Siegen, Germany

† Electronic supplementary information (ESI) available. See DOI: 10.1039/c3cp44379e

diffusion coefficients can be studied by time-domain Li NMR spectroscopy.<sup>20–26</sup> Compared to conductivity measurements, diffusion-induced Li NMR SLR rates solely reflect Li<sup>+</sup> diffusivity rather than e<sup>−</sup> dynamics which might also contribute to the total conductivity probed. In the latter case, contributions arising from other charge carriers have to be carefully eliminated which in some cases might be fraught with great experimental difficulties. By using NMR spectroscopy instead, no special post-preparation of the material to be investigated is necessary and a powdered sample is sufficient to study Li dynamics in detail. Usually the powder is sealed in a small glass ampoule in an inert gas atmosphere to protect it from moisture. Therefore, NMR spectroscopy offers a rather direct and non-destructive access to Li self-diffusion parameters which can easily be converted into (solid-state) Li diffusion coefficients.<sup>27–29</sup>

In the present case, the low-temperature modification of Li<sub>7</sub>PSe<sub>6</sub>, whose structure has been well characterized by both X-ray powder diffraction and high-resolution NMR recently,<sup>15</sup> was chosen to study dynamic properties by temperature-variable <sup>7</sup>Li NMR spectroscopy. The material served as a first model substance to enlighten Li ion transport properties of lithium-rich argyrodites by NMR SLR methods. Here, NMR SLR rate measurements performed in the so-called *rotating* frame of reference turned out to be the best choice to study Li self-diffusion processes. The method takes advantage of an oscillating magnetic field  $B_1$  (rather than the ordinary external magnetic field  $B_0$ ), which is used to perturb the <sup>7</sup>Li spin system in the frame of an SLR NMR experiment.<sup>30,31</sup> The associated radio (or locking) frequency  $\omega_1$  is related to  $B_1$  via  $\gamma B_1 = \omega_1$  where  $\gamma$  is the magnetogyric ratio of the nucleus under investigation. Since  $\omega_1$  is in the order of some tens of kHz and  $\omega_0$  is in the upper MHz range, NMR SLR measurements performed in the rotating frame of reference are sensitive to Li jump rates with values in the order of  $10^4$  to  $10^5$  s<sup>−1</sup>, thus, considerable longer correlation times can be probed than it is possible with SLR NMR measurements performed in the laboratory frame of reference being the more common technique to probe ion dynamics by NMR.<sup>25,28</sup>

In general, monitoring the complete diffusion-induced SLR NMR rate peak, which is obtained when the SLR rate  $R_{1p}$  is plotted vs. the inverse temperature  $1/T$ , gives access to both the activation energy  $E_a$  and the pre-exponential factor  $\tau_0^{-1}$  determining the underlying Arrhenius relation (see below). Furthermore, it contains information about correlation effects such as structural disorder and Coulomb interactions.<sup>32</sup> Therefore, it might be useful to roughly evaluate to what extent short-range Li motions influence the  $R_{1p}$  rates measured and, thus, ion transport parameters.

## II. Experiment

Synthesis and characterization of polycrystalline Li<sub>7</sub>PSe<sub>6</sub> with  $\mu\text{m}$ -sized crystallites (as well as the closely related Li<sub>7</sub>PS<sub>6</sub>) are described in great detail by Kong *et al.*<sup>15</sup> Both Li<sub>7</sub>PS<sub>6</sub> and Li<sub>7</sub>PSe<sub>6</sub> exhibit two structural modifications with a fully

reversible phase transition at 483 K and 437 K, respectively. While the high-temperature modification shows the typical argyrodite-type structure (space group  $F\bar{4}3m$ ), the crystal structure of the low-temperature modification is closely related to that of the low-temperature form of  $\alpha$ -Cu<sub>7</sub>PSe<sub>6</sub> crystallizing with orthorhombic symmetry.<sup>15</sup>

<sup>7</sup>Li NMR measurements were conducted on a high performance digital Bruker Avance III spectrometer in connection with a shimmed cryomagnet of a nominal magnetic field of ca. 7 T. This corresponds to a Larmor frequency of  $\omega_0/2\pi = 116$  MHz. A commercial high-temperature probe head (Bruker Biospin) was employed allowing  $\pi/2$  pulse lengths of about 2.9  $\mu\text{s}$ . The measurements were performed at temperatures ranging from 216 K to 416 K, which were monitored using a Eurotherm temperature controller in combination with a type T thermocouple. Measurements at temperatures down to 112 K were carried out using a cryo probe (Bruker) which was operated by evaporating liquid nitrogen. As compared to the standard probe, the  $\pi/2$  pulse length of the cryo probe was ca. 5.2  $\mu\text{s}$ . Prior to the measurements the sample was vacuum dried and fire sealed in a glass NMR tube of 5 mm in diameter and 3 cm in length.

<sup>7</sup>Li NMR SLR rates  $1/T_1 = R_1$  were acquired by means of the saturation recovery pulse sequence  $10 \times \pi/2 - t_d - \pi/2$  which is depicted in Fig. 1(A).<sup>20,33</sup> Here, the initial ten  $\pi/2$  pulses in rapid succession are used to destroy any longitudinal magnetization  $M_z$  before its recovery is recorded as a function of the delay times  $t_d$ . <sup>7</sup>Li NMR SLR rates  $1/T_{1p} = R_{1p}$  were recorded in the rotating frame of reference (SLRp). To this end the spin-locking technique<sup>30–36</sup> was employed (see Fig. 1(B)) where the relaxation of the equilibrium magnetization is probed at rather low magnetic field strengths  $B_1$ . The corresponding locking frequency

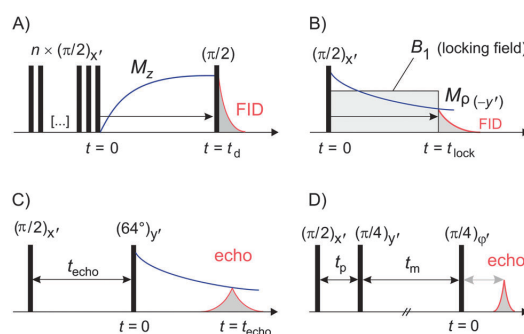


**Fig. 1** (A) The saturation recovery pulse sequence used to probe the SLR NMR rates  $R_1$ : a comb of closely spaced rf-pulses  $(\pi/2)_{x'}$  ( $n \approx 10$ ) destroys the (initial) longitudinal magnetization ( $M_z = M_{eq}$ ) so that  $M_z = 0$  at  $t = 0$ . The subsequent recovery of  $M_z(t)$  is probed with a single  $\pi/2$ -pulse which is sent after a variable relaxation delay  $t = t_d$ . (B) The pulse sequence of the spin-lock technique to record the rotating-frame NMR rates  $R_{1p}$ : immediately after the  $\pi/2$ -pulse the magnetization  $M$  pointing along the  $(-y')$  is locked by the field  $B_1$ . The decay of  $M_{p(-y')}$  is then probed by plotting the height (or area) of the free induction decay (FID) as a function of the locking pulse length  $t_{lock}$ . See also ref. 37. In a simplified manner (C) and (D) depict the pulse sequences to record SSR NMR rates and stimulated echo decay curves. See the text for further explanation.

was chosen to be  $\omega_1/2\pi \approx 45$  kHz with the duration of the locking pulse  $t_{\text{lock}}$  varying between 10  $\mu\text{s}$  and 100 ms. The recycle delay for the SLR experiments was set to at least  $5 \times 1/R_1$ . Both  $R_1$  and  $R_{1p}$  were obtained by parameterizing the magnetic transients  $M_z(t_d)$  and  $M_p(t_{\text{lock}})$ , respectively, by stretched exponentials. In the case of  $R_{1p}$  the exponent  $\gamma$  in  $M_p(t_{\text{lock}}) \propto \exp(-(t_{\text{lock}}/T_{1p})^\gamma)$  ranges from 0.4 to 0.9 ( $210 \text{ K} \leq T \leq 430 \text{ K}$ ). For the sake of completeness, temperature-variable  $^7\text{Li}$  NMR spin-spin relaxation (SSR) rates  $1/T_2 = R_2$  were monitored, which were recorded using a solid-echo pulse sequence<sup>33</sup> optimized for spin-3/2 nuclei (see Fig. 1(C)).  $t_{\text{echo}}$  denotes the variable interpulse delay. The corresponding NMR spectra were either obtained after irradiation with a single  $\pi/2$  pulse or using the solid-echo pulse sequence. In the latter case, echoes were recorded at fixed  $t_{\text{echo}}$  of 20  $\mu\text{s}$ ; spectra were obtained by Fourier transformation beginning from the echo top.

In addition to the SLR and SSR NMR measurements, first  $^7\text{Li}$  NMR stimulated echoes have been recorded by utilizing the Jeener-Broekaert<sup>38</sup> pulse sequence which is in simplified terms shown in Fig. 1(D).<sup>21,39–41</sup> Usually, such stimulated echo measurements are sensitive to slow Li dynamics.<sup>21,42–48</sup> The technique gives access to single-spin two-time correlation functions<sup>21,22,39</sup> and takes advantage of the different electrical environments the Li spins sense during hopping from site to site. Here, so-called  $^7\text{Li}$  sin-sin hopping correlation functions,<sup>21,39</sup> *i.e.*, spin-alignment echo (SAE) decay curves,<sup>24,25,43</sup> were monitored at a fixed preparation time  $t_p$  of 12  $\mu\text{s}$  and a variable mixing time  $t_m$  ranging from 10  $\mu\text{s}$  to 100 s. Appropriate phase cycling is necessary to eliminate unwanted coherences.<sup>39</sup>

### III. Results and discussion

Temperature-variable  $^7\text{Li}$  NMR spectra of crystalline  $\text{Li}_7\text{PSe}_6$  yield first insights into the Li dynamics of the argyrodite. In Fig. 2 various NMR spectra are shown which were recorded at temperatures ranging from 216 to 417 K. They were acquired using a single pulse sequence, thus, quadrupole intensities (see below) are largely suppressed. Typically, at low temperatures, *i.e.* in the so-called rigid-lattice regime, a dipolar broadened NMR (central) line is observed which can be approximated with a Gaussian. Due to the increasing motion of the Li spins at elevated temperatures dipole-dipole interactions are continuously averaged. Hence, the central NMR line width obeys a motional narrowing (MN) from which the Li jump rate can be roughly estimated. In the present case, even at temperatures as low as 200 K MN has already set in. This can be clearly seen when Fig. 3 is considered where the NMR line width (full width at half maximum), directly read out from the NMR spectra recorded, is plotted *vs.*  $T$ . The dashed line is simply drawn to guide the eye; the rigid-lattice regime is reached at temperatures lower than 150 K.

Whereas at the highest temperatures ( $T > 350$  K, that is, the regime of extreme narrowing) the NMR central line, corresponding to the spin-quantum transition  $I = \pm 1/2 \Leftrightarrow I = \mp 1/2$ ,

can be well approximated with a Lorentzian, the NMR line in the intermediate temperature range can be represented by the sum of a Lorentzian line and a Gaussian line. However, a strongly heterogeneous narrowing of the NMR central line, which in many cases is reflected by a pronounced difference in line width of the two components,<sup>50,51</sup> seems to be absent in the present case. Thus, the lack of clearly recognizable two-phase spectra hampers a quantitative analysis according to that, *e.g.*, presented in ref. 52. Nevertheless, the shape of the central transitions shown in Fig. 2(a) points to a distribution of Li jump rates and, therefore, also to a distribution of Li migration pathways in the  $\text{Li}$ -argyrodite studied.

Since the MN curve shown in Fig. 3 is obtained by plotting the overall line widths of the spectra recorded, it is only of limited use for the extraction of dynamic jump parameters. Significant MN is expected when the jump rate  $\tau^{-1}$  reaches the order of the rigid lattice line width. For example, one might take use of the inflexion point of the curve ( $T_{\text{inf}} \approx 235$  K) to estimate  $\tau^{-1}$ . Using  $\nu_{\text{H}} \approx 6.8$  kHz for the NMR line width measured in the rigid lattice regime, the corresponding Li jump rate  $\tau^{-1}$  is approximately given by  $\tau_{\text{MN}}^{-1} \approx 2\pi \times \nu_{\text{H}} \approx 4 \times 10^4 \text{ s}^{-1}$ . Moreover, from the so-called onset temperature ( $T_{\text{onset}} \approx 180$  K) an activation energy  $E_{\text{a,MN}}$  can be roughly estimated according to the expression of Waugh and Fedin,<sup>53</sup>  $E_{\text{a,MN}}/\text{meV} = 1.62 \times T_{\text{onset}}/\text{K}$ . In the present case this yields  $E_{\text{a,MN}} \approx 0.3$  eV. However, considering the analysis of Faske *et al.*,<sup>51</sup> in the case of a distribution of lithium jump rates, this approach is at risk to underestimate the activation energy obtained and to overestimate the jump rate deduced from MN, respectively. In particular, this is the case when motion-induced line narrowing spans a broad temperature range, here this is more than 100 K, and  $T_{\text{onset}}$  is mainly governed by the fraction of fast ions which are presumably subject to, *e.g.*, short-range (or spatially localized) jump processes.<sup>52</sup>

In the present case, a more precise access to Li jump rates is given by SLR NMR. Before discussing the corresponding results, it is useful to have a closer look on the features of the NMR spectra recorded in the rigid-lattice regime and in the limit of extreme narrowing, *i.e.*, at the highest temperatures where the line width is mainly governed by inhomogeneities of the external magnetic field. Interestingly, in the latter regime a well-defined quadrupole powder pattern shows up. Such electric quadrupole intensities are due to the interaction of the quadrupole moment of the 3/2-spin nucleus, which is a result of the non-spherical charge distribution of the nucleus, being immersed in an electronic environment characterized by a non-vanishing electric field gradient (EFG). The latter is produced by the electric charge distribution in the direct neighbourhood of the nucleus under observation. This additional interaction alters the Zeeman levels and thus the associated (angular) Zeeman frequency  $\omega_0$  towards  $\omega_0 \pm \omega_Q$ .<sup>54</sup> The corresponding quadrupole frequency is given by

$$\omega_Q = \pm \delta \pi / 2 (3 \cos^2 \Theta - 1 - \eta_Q \sin^2 \Theta \cos(2\Phi)) \quad (1)$$

with the quadrupole coupling constant  $\delta = e^2 q Q / h$ . Here,  $e$  and  $q$  are the proton charge and the principle component of the

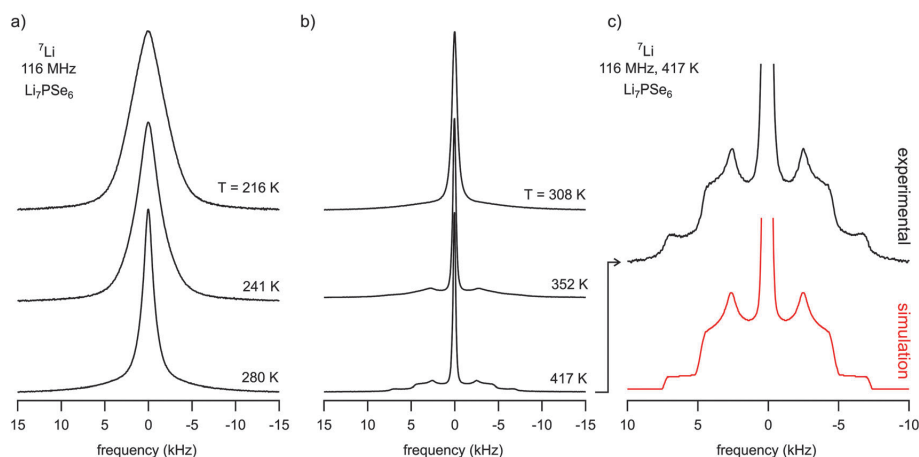


**Fig. 2** (a) and (b)  $^7\text{Li}$  NMR spectra of ternary  $\text{Li}_7\text{PSe}_6$  recorded at the temperatures indicated. The line width steadily decreases reflecting a pronounced motional narrowing which indicates rapid Li exchange on the NMR time scale defined by the rigid lattice line width of  $\text{Li}_7\text{PSe}_6$ . Pronounced and well-defined quadrupole powder patterns emerge at temperatures chosen to be higher than 300 K. It is fully developed at 417 K. (c) Magnification of the quadrupole powder pattern of the  $^7\text{Li}$  NMR recorded at 417 K. The spectrum shown at the bottom displays a simulation of the measured one with the help of WinSolids software<sup>49</sup> using a single set of fitting parameters describing the NMR line shape. See the text for further details.

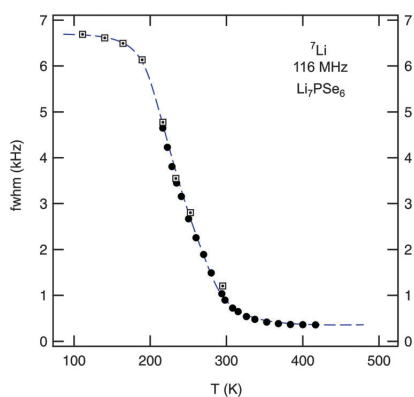


**Fig. 3** Motional narrowing of the  $^7\text{Li}$  NMR linewidth of polycrystalline  $\text{Li}_7\text{PSe}_6$ . While filled symbols (●) represent data points recorded using a standard probe, boxes display the line widths (fwhm) of NMR spectra recorded using a cryo probe. The rigid lattice value,  $\nu_{\text{rl}} \approx 6.8$  kHz, is reached at temperatures below 150 K. The onset of MN is expected when the Li jump rate reaches values in the order of  $10^3 \text{ s}^{-1}$ . See the text for further explanation.

electric field gradient tensor, respectively.  $Q$  is the electric quadrupole moment of the  $^7\text{Li}$  nucleus and  $\hbar$  denotes Planck's constant. The angles  $\Theta$  and  $\Phi$  specify the orientation of the external field  $B_0$  in the principle axis system of the EFG tensor at the site of the  $^7\text{Li}$  spin. The parameter  $\eta_Q$  reflects any asymmetries of the EFG tensor. Here, the  $^7\text{Li}$  NMR line recorded at 417 K can be well represented by a quadrupole powder pattern with  $\delta = 14.6$  kHz and  $\eta_Q = 0.6$ . Certainly, the values should be regarded as mean values characterizing the EFG tensor the Li spins are exposed to due to rapid hopping at

elevated temperatures. In the low-temperature modification of  $\text{Li}_7\text{PSe}_6$  the Li ions occupy electrically (and magnetically) inequivalent crystallographic sites. In general, the absence of a complete averaging of electric quadrupole interactions at high  $T$  has been found for many Li ion conductors and might be regarded as a universal feature.<sup>47,55,56</sup> It is referred to as anisotropic (or inhomogeneous) diffusion which is certainly traced back to the complex crystal structure of the lithium-containing argyrodite under investigation, *cf.* also Fig. 7 in ref. 16.

In the absence of lithium motions on the kHz scale, quadrupole intensities in the rigid-lattice regime can be made visible by recording NMR solid echoes. Owing to receiver dead-time effects, fast decaying components of an FID are difficult to detect. In Fig. 4 an NMR spectrum recorded in the rigid-lattice regime is shown which has been acquired at 190 K with the help of a two-pulse solid-echo sequence. Besides the Gaussian shaped central line, whose area fraction is about 36% of the total area, a broad quadrupole foot (64%) becomes apparent. The width (fwhm) of the latter component is about 54 kHz and points to a mean rigid-lattice quadrupole coupling constant in the order of 100 kHz. This value is comparable with those of other Li ion conductors studied. With increasing temperature, the rigid-lattice quadrupole interactions are partly averaged due to Li motions with rates as high as  $10^5 \text{ s}^{-1}$ . Finally, the well-defined powder pattern, as characterized above, shows up at higher  $T$ .

As mentioned above, straightforward insights into the Li dynamics in the ternary argyrodite are provided by analyzing diffusion-induced  $^7\text{Li}$  NMR SLR rates.<sup>20,21,23–28,37,57,58</sup> In Fig. 5 the  $R_{1\rho}$  rates measured in both the laboratory and rotating frames of reference are shown in an Arrhenius plot. The  $R_1$  rates reveal a

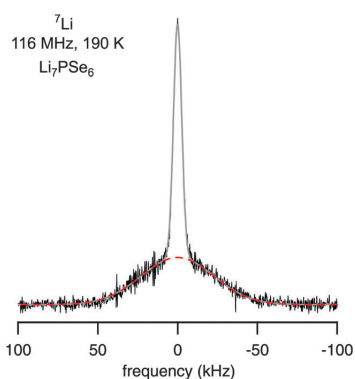


**Fig. 4**  ${}^7\text{Li}$  solid-echo (first-order quadrupolar) NMR spectrum recorded using a two-pulse sequence at 116 MHz and 190 K. The area fractions of the dipolar broadened central and quadrupole contribution are in agreement with the theoretical ratio of 4:6. Upon increasing temperature, the central line and the broad quadrupole signal narrow due to rapid Li exchange.

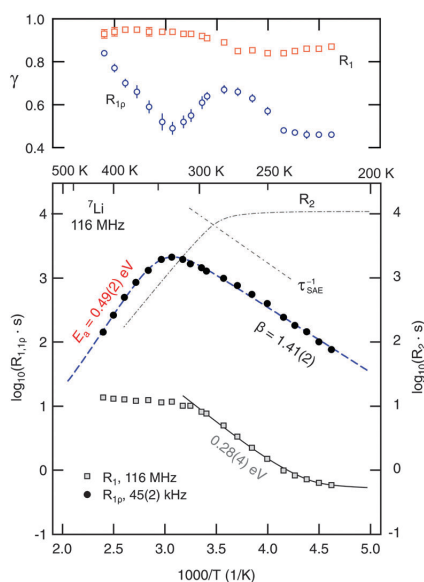


**Fig. 5** Arrhenius plot of the  ${}^7\text{Li}$  NMR SLR rates measured at a Larmor frequency  $\omega_0/2\pi$  of 116 MHz ( $R_1$ ) and a locking frequency  $\omega_1/2\pi$  of 45(2) kHz ( $R_{1p}$ ). The dashed line represents a modified BPP fit taking into account a sub-quadratic frequency dependence of the  $R_{1p}$  rates ( $R_{1p} \propto \omega_1^{-\beta}$ ,  $\beta < 2$ ) in the limit  $\omega_1\tau \gg 1$ . The upper figure shows the temperature dependence of  $\gamma$  used to parameterize the corresponding magnetization transients. For comparison, the temperature behaviour of the  $R_2$  SSR NMR rates and the decay rates deduced from stimulated echo NMR (see the inset of Fig. 7) are also shown. See the text for further explanation.

diffusion-induced low-temperature flank pointing to a relatively small activation energy of only 0.28(1) eV. The so-called low- $T$  regime of NMR SLR is sensitive to short-range rather than to long-range lithium diffusion.<sup>20</sup> Interestingly, the SLR rates

probed in the laboratory frame of reference do not exhibit a  $R_1(1/T)$  rate peak; above 300 K the rates are independent of temperature and amount to be about  $10 \text{ s}^{-1}$ . Note that at  $T < 235 \text{ K}$  the rates are increasingly governed by non-diffusive and weakly temperature-dependent background effects which, most likely, can be ascribed to coupling of the Li spins with paramagnetic impurities. However, in the case of NMR SLR measurements in the rotating frame of reference performed at a locking frequency in the order of 45 kHz the  $R_{1p}$  rates pass through a well-defined maximum showing up at  $T_{\text{max}} = 325 \text{ K}$ . This allows the direct determination of the Li jump rate  $\tau^{-1}$  which can be estimated using the maximum condition  $\omega_1\tau \approx 0.5$ . Note that this estimation is based on an exponential correlation function  $G(t)$  leading to symmetric NMR rate peaks (see below). Here, at  $T_{\text{max}}$  the rate  $\tau^{-1}$  is in the order of  $1.4 \times 10^5 \text{ s}^{-1}$ . Compared to the result from NMR motional narrowing it becomes evident that the rate  $\tau_{\text{MN}}^{-1}$  seems to overestimate the jump process because of the reasons discussed above.

A more detailed analysis is achieved by using an appropriate relaxation model<sup>20,59</sup> to evaluate the SLR NMR rates  $R_{1p}(1/T)$  measured. The dashed line shown in Fig. 5 represents a complete relaxation fit according to

$$R_{1p}(\omega_1, T) \propto J^{3D}(\omega_1, T) \propto \tau_c^{-1} (1 + (2\omega_1\tau_c)^\beta). \quad (2)$$

Note that the correlation rate  $\tau_c^{-1}$  is in the order of the jump rate  $\tau^{-1}$ . In general,  $J^{3D}$  denotes the spectral density function characterizing electric and magnetic field fluctuations due to three-dimensional ion hopping. Here, the expression of the spectral density function, to which  $R_{1p}(\omega_1, T)$  is proportional, is based on the relaxation model of Bloembergen, Purcell and Pound (BPP) introduced for 3D, isotropic diffusion.<sup>60</sup> Originally, the exponent  $\beta$  is given by  $\beta = 2$ , which originates from the assumption of an underlying single exponential motional correlation function  $G(t)$  by Fourier transformation. In the case of  $\beta = 2$  this results in a symmetric (Lorentzian shaped) spectral density function  $J^{3D}$ .<sup>20</sup> Values smaller than two (for  $\beta$  the range  $1 < \beta \leq 2$  is valid) as introduced by Küchler *et al.*<sup>61</sup> lead to asymmetric NMR SLR rate peaks whereby the slope of the low-temperature flank, that is the regime where  $\omega_1\tau \gg 1$  holds, is smaller than that of the corresponding high-temperature side characterized by the limit  $\omega_1\tau \ll 1$ . In particular, asymmetric NMR SLR rate peaks have been observed for structurally disordered ion conductors. Theoretical investigations show that Coulomb interactions of the moving ions and/or structural disorder seem to be responsible for the asymmetries observed in NMR relaxometry.<sup>62–64</sup> A pronounced heterogeneous dynamics, being closely related to structural disorder which can be represented by an irregular formed potential landscape, is expected to include both long-range dynamics as well as localized hopping processes.

In the present case, the  $R_{1p}(\omega_1, T)$  data can be best represented by a fit with  $\beta = 1.41(2)$ . This result certainly points to a non-exponential motional correlation function. It might directly

reflect a heterogeneous potential landscape the Li ions are exposed to. In  $\text{Li}_7\text{PSe}_6$  the Li ions occupy multiple, distinctly connected sites as revealed by high-resolution  $^7\text{Li}$  NMR spectroscopy.<sup>15</sup> A relatively low  $\beta$  value, as found here, is comparable to that recently reported for Li ion hopping in  $\text{Li}_7\text{La}_3\text{Zr}_2\text{O}_{12}$  (LLZ); LLZ also exhibits a highly complex crystallographic structure where the Li ions are distributed among various inequivalent positions. Let us mention that  $\beta < 2$  minimally influences the maximum condition used above to estimate the jump rate at the temperature where the rate peak shows up. Taking into account  $\beta = 1.41(2)$ , the exact maximum condition is given by

$$\omega_1\tau = 0.5(\beta - 1)^{-1/\beta} \approx 0.94 \quad (3)$$

provided  $J^{3D}$  is restricted to a single term as done in eqn (2), which turns out to be a very good approximation.

With  $E_a$  (0.49(2) eV) and  $\tau_{c,0}^{-1} \approx \tau_0^{-1} (1.6(9) \times 10^{13} \text{ s}^{-1})$  available from the relaxation fit,<sup>65</sup> the jump rate following the Arrhenius relation  $\tau^{-1} = \tau_0^{-1} \exp(-E_a/(k_B T))$  can be determined. Here,  $k_B$  denotes Boltzmann's constant. At ambient temperature, this yields  $\tau^{-1} \approx 9.5 \times 10^4 \text{ s}^{-1}$ . Using the Einstein–Smoluchowski equation, which relates  $\tau^{-1}$  with the self-diffusion coefficient  $D_{sd}$  via

$$D_{sd} = a^2/(6\tau) \quad (4)$$

it turned out that  $D_{sd}$  is  $1.3(8) \times 10^{-15} \text{ m}^2 \text{ s}^{-1}$  at  $T = 300 \text{ K}$ . Here, the jump distance  $a$  was estimated to be  $a \approx 2.9 \text{ \AA}$  which is based on the structural data given in ref. 15. With  $D_{sd}$  the corresponding ion conductivity can also be determined via the Nernst–Einstein equation. According to this relation the so-called solid-state diffusion coefficient  $D_{NE}$  is obtained which is given by

$$D_{NE} = \frac{\sigma_{dc} k_B T}{Nq^2} \quad (5)$$

$N$  denotes the charge carrier density and  $q$  represents the charge of the Li ions.  $\sigma_{dc}$  is the ionic dc conductivity. Note that  $D_{NE}$  is directly linked with  $D_{sd}$  according to  $D_{NE} = fH_R D_{sd}$ . Here,  $H_R$  is the Haven ratio and  $f$  denotes the so-called correlation factor. In the present case we assumed  $fH_R \approx 1$  to estimate the ionic conductivity  $\sigma_{dc}$ . Once again,  $N$  has been estimated based on the crystallographic data recently obtained for  $\text{Li}_7\text{PSe}_6$ .<sup>15</sup> With  $D_{sd}$  given above, the ionic conductivity turns out to be in the order of  $2 \times 10^{-6} \text{ S cm}^{-1}$  at 300 K. This is in reasonably good agreement with preliminary conductivity measurements on similar samples.<sup>16</sup> It should be noted that even higher ion conductivities have been probed for some halide-containing Li-argyrodites.<sup>9,16,17</sup>

Identifying  $E_a = 0.49(2) \text{ eV}$  (see above) with the activation energy reflecting long-range Li diffusion in  $\text{Li}_7\text{PSe}_6$ , the slope of the low- $T$  flank of the rate peak of Fig. 5 might be related to Li jump processes taking place on a much shorter length scale. This is expressed by  $\omega_1\tau \gg 1$  being valid in this temperature range. In the present case, the low- $T$  flank is characterized by  $E_{a,\text{low}} = 0.21(1) \text{ eV}$ , thus, fulfilling the relation  $E_{a,\text{low}} = (\beta - 1)E_a$ . It directly links the frequency dependence of  $R_{1\rho} \propto \omega_1^{-\beta}$  to the asymmetry of the diffusion-induced relaxation rate peak  $R_{1\rho}(1/T)$ .

Indeed, the crystallographic structure of Li-containing argyrodites contains structural motifs, viz. Li ions residing in close-by tetrahedral voids, which might help explain the differences between localized, i.e., short-range Li dynamics on the one hand and long-range Li diffusion on the other hand.<sup>15</sup> This is also supported by recent theoretical investigations on halide-containing Li-argyrodites.<sup>16,17</sup>

For comparison with the SLR NMR rates, the  $\gamma$  exponents describing the deviation of the magnetization transients  $M_p(t_{\text{lock}})$ , see Fig. 6, from single-exponential time behaviour are also included in Fig. 5. Whereas a straightforward interpretation of  $\gamma$  is generally not available, one might read out two features showing up in the present case. At very low temperatures the exponent is approximately 0.5 which might point to (diffusion-induced) spin-lattice relaxation due to coupling of the  $^7\text{Li}$  spins primarily to paramagnetic impurities. At even lower temperatures homonuclear spin-diffusion might play an additional role. With increasing diffusivity,  $\gamma$  initially increases before a minimum value is attained at  $T_{\text{max}}$  where the corresponding maximum peak  $R_{1\rho}(1/T)$  shows up. Interestingly, when  $T$  is further increased and Li diffusion becomes rapid the exponent  $\gamma$  steadily increases towards  $\gamma = 1$ , i.e., single-exponential time behaviour. Note that at very high temperatures the various electrical interactions the Li spins are exposed to are greatly averaged resulting in a quadrupole powder pattern which can be simulated with a single set of (mean) parameters. Thus, when considering the underlying motional correlation function, being at least partly reflected by the exponent  $\gamma$ , it might also change as a function of temperature and seems to tend to become a single exponential in the limit  $\omega_1\tau \ll 1$ . Such an observation is in agreement with the predictions of Ngai and co-workers,<sup>66</sup> who have analyzed the shape of motional correlation functions from both NMR and impedance spectroscopy measurements.

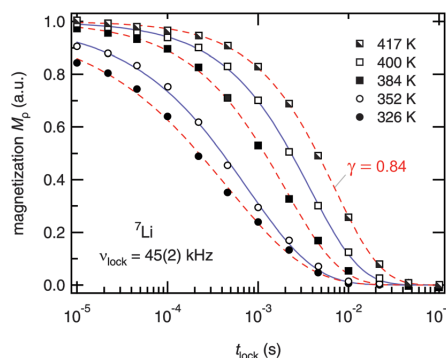


**Fig. 6**  $^7\text{Li}$  NMR magnetization transients  $M_p(t_{\text{lock}})$  of  $\text{Li}_7\text{PSe}_6$  recorded at the temperatures indicated and at  $\omega_0/2\pi = 116 \text{ MHz}$  and  $\omega_1/2\pi = \nu_1 = 45(2) \text{ kHz}$ . Dashed and solid lines represent fits according to  $M_p(t_{\text{lock}}) \propto \exp(-(t_{\text{lock}}/T_1)^\gamma)$ . At high temperatures, i.e. in the limit  $\omega_1\tau \gg 1$ , the stretching exponent  $\gamma$  increases towards single exponential time behaviour. The decay curves recorded above 360 K represent magnetization transients of the high-temperature flank of the  $R_{1\rho}(1/T)$  peak shown in Fig. 5.

For the sake of completeness,  $R_2$  SSR NMR rates were recorded at temperatures down to 190 K. In the rigid-lattice regime,  $T_2$  is approximately 70  $\mu\text{s}$ . This is in good agreement with the second moment, *i.e.*, the line width of the central transition in this temperature range (6.8 kHz), see above. It is worth mentioning that, as expected, the  $^7\text{Li}$  NMR solid echoes are composed of a fast and slowly decaying contribution which mirror quadrupolar and dipolar contributions. Irrespective of what is analyzed in detail, *i.e.*, (i) the complete area under the echo, (ii) the amplitude of the quadrupole part or (iii) the area of the slowly decaying dipolar part, at very low  $T$  the corresponding transients follow single-exponential time behaviour (see Fig. S1 and S2, ESI†). However, the situation changes upon increasing  $T$ . Then, a fast decaying and temperature independent contribution with  $R_{2'} = 30 \mu\text{s}$  shows up (see Fig. S2, ESI†). These rates might reflect a very slow dynamic process. Interestingly, the stimulated echoes, which are presented below, also seem to point to a subset of lithium ions with a very low diffusivity.

For comparison, in Fig. 5 the temperature-dependent  $R_2$  rates of the slowly decaying part of the transients are included. The rates start to decrease at  $T = 260$  K. At this temperature the associated jump rate is in the order of  $10^4 \text{ s}^{-1}$ , which is in good agreement with the Arrhenius parameters deduced from the  $R_{1\rho}(1/T)$  peak. However, the corresponding activation energy, which can be estimated from the linearly decaying part of the  $R_2$  curve, turns out to be only 0.4 eV (see also Fig. S2, ESI†). Moreover, the maximum  $R_{1\rho}$  rate exceeds  $R_2$ . Similarly, this has been observed by, *e.g.*, Bertermann *et al.*<sup>56</sup> who recorded  $R_2$  rates using a Hahn echo pulse sequence. In doing so, Hahn echo decay seems to be determined by dipolar rather than by quadrupolar interactions as expected.

The present difference between  $R_{1\rho}$  and  $R_2$  also indicates that the two rates probed are not necessarily influenced by exactly the same relaxation mechanism and/or the same subset of (differently coupled) Li spins. Considering the pre-factor obtained from the  $R_{1\rho}(1/T)$  fit ( $R_{1\rho} = C' \times J^{3\text{D}}(2\omega_1)$ ), which amounts to  $C' = 2.95(9) \times 10^9 \text{ s}^{-2}$ , thus, being in the order of the square of the rigid-lattice quadrupole coupling constant (see above), we suppose that, besides dipolar ones, fluctuating quadrupolar interactions also play a large role in influencing  $R_{1\rho}$ . However, a conclusive answer to what extent dipolar interactions affect the SLR NMR rates probed might only be possible by future  $^6\text{Li}$  NMR experiments carried out at resonance frequencies comparable to those used for the  $^7\text{Li}$  NMR measurements.

In addition to NMR SLR measurements in the rotating frame of reference, we have recorded  $^7\text{Li}$  spin-alignment echo NMR decay curves which are sensitive to slow Li exchange processes between electrically inequivalent Li sites in the argyrodite. Thus, the method takes advantage of the distinct quadrupolar interactions of the jumping Li ions. The decay curves shown in Fig. 7 were obtained by plotting the intensity of the spin-alignment echo (read out at the echo maximum, *i.e.*, at  $t = t_p$ ) as a function of mixing time. The  $S_2$  curves reflect the probability to find an Li nuclear spin, which initially ( $t_m = 0$ ) resides

on a specific site, on an electrically equivalent site at a later time ( $t = t_m$ ).

Interestingly, echo damping proceeds in two steps.<sup>22,26,67</sup> Most likely, the first decay step directly reflects Li hopping; the second step, however, might be induced by (quadrupolar) spin-lattice relaxation and/or spin-diffusion effects. The latter are expected to be characterized by a decay rate  $\tau''$  being in the order of seconds. The full decay curves were parameterized with a combination of two stretched exponentials according to

$$S_2(t_p, t_m, t = t_p) = \left( A e^{-(t_m/\tau_{\text{SAE}})^{\gamma_{\text{SAE}}}} + B \right) e^{-(t_m/\tau'')^{\gamma''}} \quad (6)$$

Below 270 K, the stretching parameter  $\gamma_{\text{SAE}}$  is approximately 0.5. It decreases with increasing  $T$  reaching  $\gamma_{\text{SAE}} \approx 0.25$  at ambient temperature. The fits yield the decay rates  $\tau_{\text{SAE}}^{-1}$  shown in the inset of Fig. 7. Obviously, the first decay step points to Li jumps which are thermally activated similar to those being responsible for motion-induced SLR NMR in the limit  $\omega_0\tau \gg 1$  (see above). Note that in other cases SAE NMR has been proven to be very successful in characterizing long-range ion transport properties.<sup>25,51,68–70</sup> In the examples studied so far, the corresponding activation energy  $E_{a,\text{SAE}}$  turned out to be very similar to the value  $E_{a,\text{dc}}$  deduced from dc-conductivity measurements. However, in the present case, low-temperature echo damping seems to be mainly influenced by a diffusion process with a much lower thermal activation. This behaviour might change when  $^6\text{Li}$  (spin-1 nucleus) stimulated echoes are recorded instead of  $^7\text{Li}$  (spin-3/2 nucleus) echoes. This is because the latter are exposed to rather large homonuclear dipole-dipole interactions which might strongly influence the generation of a pure spin-alignment state.

Irrespective of this possible influence on the  $^7\text{Li}$  NMR  $S_2$  curves, even at temperatures as low as 220 K the two-step decay behaviour remains. For example, the (normalized) correlation

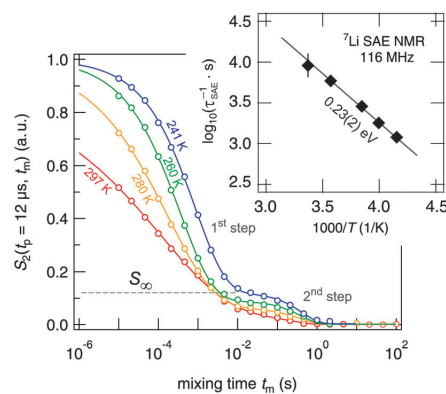


**Fig. 7**  $^7\text{Li}$  NMR (sin-sin) two-time correlation functions recorded using the Jeener-Broekaert<sup>38,39</sup> pulse sequence (116 MHz,  $t_p = 12 \mu\text{s}$ ). While the first decay step of the  $S_2$  decay curve reflects Li hopping between electrically inequivalent Li sites in crystalline  $\text{Li}_7\text{PSe}_6$ , the second one is induced by (quadrupolar) spin-lattice relaxation. Solid lines represent fits with a combination of two stretched exponentials.

function recorded at 241 K is characterized by a so-called plateau value  $S_\infty = B/(A+B)$  (see eqn (6)) which is approximately 0.12. In general,  $1/S_\infty$  is related to the number of electrically inequivalent Li sites the ion visits during self diffusion.<sup>39</sup> The inverse,  $1/S_\infty$ , equals the number of available Li sites provided these are equally populated and visited by the spins with the same probability.  $S_\infty = 0.12$  leads, at first glance, to approximately eight different Li sites. In fact, there are at least seven electrically inequivalent Li sites occupied in Li<sub>7</sub>PSe<sub>6</sub>. It is worth mentioning that, once again, <sup>7</sup>Li-<sup>7</sup>Li dipole-dipole interactions might influence  $1/S_\infty$  which usually point to a larger number of sites than actually present in the crystal structure. Such a situation has also been found for SAE NMR measurements on β-eucryptite, LiAlSiO<sub>4</sub>, single crystals.<sup>71</sup> With increasing temperature  $T$ , the value  $S_\infty$  decreases which might be attributed to the increasing averaging of electric quadrupolar as well as magnetic dipolar interactions due to sufficiently fast Li hopping.

Alternatively, the emergence of a distinct plateau might also be interpreted in terms of a small and decoupled sub-ensemble of very slow Li ions that show up at large mixing times and low temperature. However, since the corresponding decay rates associated with the second step ( $1/\tau''$ ) do not reveal a significant temperature dependence, the above-given explanation, pointing to the averaging of quadrupole interactions, seems to be more suitable to understand the NMR response. Moreover, at higher temperatures the jump process occurring during the evolution period determined by  $t_p$  might also affect the correlation functions probed. This phenomenon is called *motional phase averaging*, see ref. 21 for further details.

In contrast to the diffusion process being responsible for the maximum of  $R_{1\rho}(1/T)$ , the first decay step of the SAE NMR decay curves reflects Li spins diffusing on a rather long time scale. In this context it is worth mentioning once again that, in general, SAE NMR is insensitive to Li<sup>+</sup> jumps between electrically inequivalent sites. This also holds for sufficiently fast exchange processes for which echo formation is not possible or for hopping processes leading to elimination of fluctuating EFGs. The latter means fast jump processes involving a small number of preferred but electrically inequivalent sites. Such a process would lead to an averaged but mixing-time independent EFG and is expected to contribute to SLR NMR but it would be invisible for SAE NMR. This view might help understand the difference found between  $\tau^{-1}$  from  $R_{1\rho}(1/T)$  and  $\tau_{\text{SAE}}^{-1}$ . Such a scenario of fast and slowly diffusing spins,<sup>16</sup> which allow exchange between each other, is also in agreement with a relatively large final state amplitude for the slow process most likely involving the majority of the Li sites available. As mentioned above, exchange between closely adjacent voids in Li<sub>7</sub>PSe<sub>6</sub>, see ref. 15 and 16, might represent such a preferred (spatially localized and fast) hopping process to which SAE NMR is not sensitive, cf. also the illustration of Fig. 7 in ref. 16. The relatively low activation energy deduced from SAE NMR might point to the conclusion that at higher  $T$  further hopping processes come into play which are finally detected by  $R_{1\rho}(1/T)$  in the high-temperature limit.

For comparison with a recent study on Li<sub>4</sub>SnS<sub>4</sub>, let us note that Dehnen and co-workers<sup>72</sup> reported on SAE data which reveal low-temperature echo decay damping pointing to an extremely slow Li motional process. This process is reported to be thermally activated by 0.05 eV only. Very recently, by our own group a similar motion process with an activation energy of 0.09 eV was observed for a structurally disordered ion conductor. In contrast to the SAE NMR response probed here, but in analogy to the well-known *nearly constant loss* (NCL) phenomenon in conductivity spectroscopy, in ref. 73 we interpreted this feature as a result from strictly localized (or caged) motions, see also ref. 74.

Finally, instead of a single (Arrhenius-type) diffusion process we found indications for various motional mechanisms present in Li<sub>7</sub>PSe<sub>6</sub>. This also includes the possibility that diffusion mechanisms change as a function of temperature and dominate others in certain ranges. It also helps understand why it is hardly possible to perform a so-called joint fit, see, e.g., ref. 28, of the temperature-variable and frequency-dependent SLR NMR rates  $R_{1\rho}$  and  $R_1$ . Here, the rates  $R_1$  might be interpreted as the result of a superposition of different processes leading to 0.28 eV (Fig. 5) in the end. In contrast, long-range Li<sup>+</sup> ion dynamics at higher  $T$  seem to be determined by an activation energy of 0.49 eV which can be deduced from the  $R_{1\rho}(1/T)$  peak in the relaxation limit  $\omega_1\tau_c \ll 1$ .

#### IV. Conclusion and outlook

In summary, local electric structures and Li self-diffusion in a polycrystalline sample of Li<sub>7</sub>PSe<sub>6</sub> have been examined by temperature-variable <sup>7</sup>Li NMR spectroscopy. Line shape as well as SLR measurements have been used to get insights into translational Li dynamics present. While the first seem to be mainly governed by local exchange processes, with the help of SLR measurements short- as well as long-range diffusion parameters are accessible. In particular, it turned out that SLR measurements performed in the rotating frame of reference are highly suited to characterize Li hopping motions taking place on different length scales in the Li-containing argyrodite. From the diffusion-induced  $R_{1\rho}$  SLR rate peak probed, both the activation energy (0.49(2) eV) as well as the pre-exponential factor ( $1.6(9) \times 10^{13} \text{ s}^{-1}$ ) of the underlying Arrhenius relation characterizing long-range dynamics (at higher  $T$ ) could be probed. At ambient temperature, the Li self-diffusion coefficient is approximately  $1.3(8) \times 10^{-15} \text{ m}^2 \text{ s}^{-1}$ . This points to an Li ion conductivity in the order of  $2 \times 10^{-6} \text{ S cm}^{-1}$  at 300 K. In contrast, at lower  $T$  Li dynamics seem to be characterized by activation energies ranging from 0.21 eV ( $R_{1\rho}$ ) to 0.28 eV ( $R_1$ ). Most likely, the relevant diffusion processes being valid in this  $T$  range also entail short-range dynamics.

The measurements carried out so far build a helpful basis to be used for the comparison with halide containing Li-argyrodites such as Li<sub>6</sub>PSe<sub>5</sub>Cl revealing even higher Li conductivities.<sup>9,15,17–19,75</sup> Currently, chlorine-containing and bromine-containing argyrodites are investigated in our laboratory. In addition to the first <sup>7</sup>Li SAE NMR measurements presented here, the analysis of

<sup>6</sup>Li NMR hopping correlation functions might be very useful to shed more light on the dynamic processes probed via the generation of stimulated echoes.

## Acknowledgements

We thank G. Schmidt (Bruker, Karlsruhe (Germany)) for his help with setting up the NMR spectrometer at the TU Graz and greatly appreciate the valuable comments of an unknown referee. Financial support from the Austrian Federal Ministry of Economy, Family and Youth, and the Austrian National Foundation for Research, Technology and Development as well as by the Deutsche Forschungsgemeinschaft (DFG) is highly appreciated (DFG Research Unit 1277).

## References

- 1 M. S. Whittingham, *Chem. Rev.*, 2004, **104**, 4271.
- 2 J. M. Tarascon and M. Armand, *Nature*, 2001, **414**, 359.
- 3 M. Armand and J.-M. Tarascon, *Nature*, 2008, **451**, 652.
- 4 J.-M. Tarascon, *ChemSusChem*, 2008, **1**, 777.
- 5 M. Winter and J. O. Besenhard, *Electrochim. Acta*, 1999, **45**, 31.
- 6 A. S. Aricó, P. Bruce, B. Scrosati, J.-M. Tarascon and W. V. Schalkwijk, *Nat. Mater.*, 2005, **4**, 366.
- 7 J. B. Goodenough and Y. Kim, *Chem. Mater.*, 2010, **22**, 587.
- 8 P. Knauth, *Solid State Ionics*, 2009, **180**, 911.
- 9 H.-J. Deiseroth, S.-T. Kong, H. Eckert, J. Vannahme, C. Reiner, T. Zaiss and M. Schlosser, *Angew. Chem., Int. Ed.*, 2008, **47**, 755.
- 10 Y. Zhao and L. L. Daemen, *J. Am. Chem. Soc.*, 2012, **134**, 15042.
- 11 A. Hayashi and M. Tatsumisago, *Electron. Mater. Lett.*, 2012, **8**, 199.
- 12 N. Kamaya, K. Homma, Y. Yamakawa, M. Hirayama, R. Kanno, M. Yonemura, T. Kamiyama, Y. Kato, S. Hama and K. Kawamoto, *et al.*, *Nat. Mater.*, 2011, **10**, 682.
- 13 H. Buschmann, J. Dölle, S. Berendts, A. Kuhn, P. Bottke, M. Wilkening, P. Heitjans, A. Senyshyn, H. Ehrenberg and A. Lotnyk, *et al.*, *Phys. Chem. Chem. Phys.*, 2011, **13**, 19378.
- 14 S. Narayanan, V. Epp, M. Wilkening and V. Thangadurai, *RSC Adv.*, 2012, **2**, 2553.
- 15 S. T. Kong, O. Gün, B. Koch, H. J. Deiseroth, H. Eckert and C. Reiner, *Chem.-Eur. J.*, 2010, **16**, 5138.
- 16 O. Pecher, S.-T. Kong, T. Goebel, V. Nickel, K. Weichert, C. Reiner, H.-J. Deiseroth, J. Maier, F. Haarmann and D. Zahn, *Chem.-Eur. J.*, 2010, **16**, 8347.
- 17 R. P. Rao and S. Adams, *Phys. Status Solidi A*, 2011, **208**, 1804.
- 18 P. R. Rayavarapu, N. Sharma, V. K. Peterson and S. Adams, *J. Solid State Electrochem.*, 2012, **16**, 1807.
- 19 S. Boulineau, M. Courty, J.-M. Tarascon and V. Viallet, *Solid State Ionics*, 2012, **221**, 1.
- 20 P. Heitjans, A. Schirmer and S. Indris, in *Diffusion in Condensed Matter*, ed. P. Heitjans and J. Kräger, Springer, 2005, ch. 9, p. 367.
- 21 R. Böhmer, K. Jeffrey and M. Vogel, *Prog. Nucl. Magn. Reson. Spectrosc.*, 2007, **50**, 87.
- 22 C. Brinkmann, S. Faske, B. Koch and M. Vogel, *Z. Phys. Chem.*, 2010, **224**, 1535.
- 23 V. Epp and M. Wilkening, *Phys. Rev. B: Condens. Matter Mater. Phys.*, 2010, **82**, 020301.
- 24 M. Wilkening, J. Heine, C. Lyness, A. R. Armstrong and P. G. Bruce, *Phys. Rev. B: Condens. Matter Mater. Phys.*, 2009, **80**, 064302.
- 25 M. Wilkening and P. Heitjans, *ChemPhysChem*, 2012, **13**, 53.
- 26 M. Wilkening and P. Heitjans, *Phys. Rev. B: Condens. Matter Mater. Phys.*, 2008, **77**, 024311.
- 27 M. Wilkening, A. Kuhn and P. Heitjans, *Phys. Rev. B: Condens. Matter Mater. Phys.*, 2008, **78**, 054303.
- 28 A. Kuhn, S. Narayanan, L. Spencer, G. Goward, V. Thangadurai and M. Wilkening, *Phys. Rev. B: Condens. Matter Mater. Phys.*, 2011, **83**, 094302.
- 29 A. Kuhn, J.-Y. Choi, L. Robben, F. Tietz, M. Wilkening and P. Heitjans, *Z. Phys. Chem.*, 2012, **226**, 525.
- 30 D. Ailion and C. P. Slichter, *Phys. Rev. Lett.*, 1964, **12**, 168.
- 31 C. P. Slichter and D. Ailion, *Phys. Rev. Sect. A*, 1964, **135**, A1099.
- 32 E. Fukushima and S. B. W. Roeder, *Experimental Pulse NMR: A Nuts and Bolts Approach*, Addison-Wesley Pub. Co., Advanced Book Program, Reading, Mass., 1981.
- 33 D. C. Ailion and C. P. Slichter, *Phys. Rev. Sect. A*, 1965, **137**, A235.
- 34 D. C. Look and I. J. Lowe, *J. Chem. Phys.*, 1966, **44**, 2995.
- 35 T. J. Rowland and F. Y. Fradin, *Phys. Rev.*, 1969, **182**, 760.
- 36 D. Wolf, *Phys. Rev. B: Solid State*, 1974, **10**, 2724.
- 37 A. Kuhn, M. Kunze, P. Sreeraj, H. D. Wiemhöfer, V. Thangadurai, M. Wilkening and P. Heitjans, *Solid State Nucl. Magn. Reson.*, 2012, **42**, 2.
- 38 J. Jeener and P. Broekaert, *Phys. Rev.*, 1967, **157**, 232.
- 39 R. Böhmer, *J. Magn. Reson.*, 2000, **147**, 78.
- 40 X.-P. Tang, R. Busch, W. Johnson and Y. Wu, *Phys. Rev. Lett.*, 1998, **81**, 5358.
- 41 X.-P. Tang, U. Geyer, R. Busch, W. Johnson and Y. Wu, *Nature*, 1999, **402**, 160.
- 42 R. Böhmer, T. Jörg, F. Qi and A. Titze, *Chem. Phys. Lett.*, 2000, **316**, 419.
- 43 F. Qi, T. Jörg and R. Böhmer, *Solid State Nucl. Magn. Reson.*, 2002, **22**, 484.
- 44 M. Wilkening and P. Heitjans, *J. Phys.: Condens. Matter*, 2006, **18**, 9849.
- 45 B. Koch and M. Vogel, *Solid State Nucl. Magn. Reson.*, 2008, **34**, 37.
- 46 M. Wilkening, W. Küchler and P. Heitjans, *Phys. Rev. Lett.*, 2006, **97**, 065901.
- 47 M. Wilkening, D. Gebauer and P. Heitjans, *J. Phys.: Condens. Matter*, 2008, **20**, 022201.
- 48 M. Wilkening, C. Lyness, A. R. Armstrong and P. G. Bruce, *J. Phys. Chem. C*, 2009, **113**, 4741.
- 49 K. Eichele, *WSolids 1*, Solid-State NMR Spectrum Simulation, Version 1.19.15, University of Tübingen, 2009.
- 50 M. Wilkening, S. Indris and P. Heitjans, *Phys. Chem. Chem. Phys.*, 2003, **5**, 2225.

- 51 S. Faske, H. Eckert and M. Vogel, *Phys. Rev. B: Condens. Matter Mater. Phys.*, 2008, **77**, 104301.
- 52 M. Storek, R. Böhmer, S. W. Martin, D. Larink and H. Eckert, *J. Chem. Phys.*, 2012, **137**, 124507.
- 53 J. Waugh and I. Fedin, *Sov. Phys. Solid State*, 1963, **4**, 1633.
- 54 A. Abragam, *The Principles of Nuclear Magnetism*, Clarendon, Oxford, 1961.
- 55 R. Bertermann and W. Müller-Warmuth, *Z. Naturforsch., A: Phys. Sci.*, 1998, **53**, 863.
- 56 R. Bertermann, W. Müller-Warmuth, C. Jansen, F. Hiltmann and B. Krebs, *Solid State Ionics*, 1999, **117**, 245.
- 57 D. Brinkmann, *Prog. Nucl. Magn. Reson. Spectrosc.*, 1992, **24**, 527.
- 58 A. Kuhn, P. Sreeraj, R. Pöttgen, H.-D. Wiemhöfer, M. Wilkening and P. Heitjans, *J. Am. Chem. Soc.*, 2011, **133**, 11018.
- 59 P. M. Richards, in *Topics in Current Physics*, ed. M. B. Salamon, Springer, Berlin, 1979, vol. 15.
- 60 N. Bloembergen, E. M. Purcell and R. V. Pound, *Phys. Rev.*, 1948, **73**, 679.
- 61 W. Küchler, P. Heitjans, A. Payer and R. Schöllhorn, *Solid State Ionics*, 1994, **70–71**, 434.
- 62 A. Bunde, W. Dieterich, P. Maass and M. Meyer, in *Diffusion in Condensed Matter – Methods, Materials, Models*, ed. P. Heitjans and J. Kärger, Springer, Berlin, 2nd edn, 2005, ch. 20, pp. 813–856.
- 63 M. Meyer, P. Maass and A. Bunde, *Phys. Rev. Lett.*, 1993, **71**, 573.
- 64 K. Funke, *Prog. Solid State Chem.*, 1993, **22**, 111.
- 65 Similar values ( $E_a$  (0.49(1) eV) and  $\tau_{c,0}^{-1} = 6(3) \times 10^{12} \text{ s}^{-1}$ ) were obtained by analyzing the rotating-frame SLR NMR data with a Cole–Davidson spectral density function.<sup>76</sup> The distribution parameter  $\alpha$  of the Cole–Davidson function turned out to be  $\alpha = 0.42(2)$ .
- 66 C. Leon, J. Habasaki and K. L. Ngai, *Z. Phys. Chem.*, 2009, **223**, 1311.
- 67 M. Vijayakumar, S. Kerisit, Z. Yang, G. L. Graff, J. Liu, J. A. Sears and S. D. Burton, *J. Phys. Chem. C*, 2009, **113**, 20108.
- 68 M. Wilkening, R. Amade, W. Iwaniak and P. Heitjans, *Phys. Chem. Chem. Phys.*, 2006, **9**, 1239.
- 69 M. Wilkening, C. Mühle, M. Jansen and P. Heitjans, *J. Phys. Chem. B*, 2007, **111**, 8691.
- 70 B. Ruprecht, M. Wilkening, R. Uecker and P. Heitjans, *Phys. Chem. Chem. Phys.*, 2012, **14**, 11974.
- 71 F. Qi, G. Diezemann, H. Böhm, J. Lambert and R. Böhmer, *J. Magn. Reson.*, 2004, **169**, 225.
- 72 T. Kaib, S. Haddadpour, M. Kapitein, P. Bron, C. Schröder, H. Eckert, B. Roling and S. Dehnen, *Chem. Mater.*, 2013, **24**, 2211.
- 73 V. Epp, C. Brüning, M. Binnewies, P. Heitjans and M. Wilkening, *Z. Phys. Chem.*, 2012, **226**, 513.
- 74 F. Qi, C. Rier, R. Böhmer, W. Franke and P. Heitjans, *Phys. Rev. B: Condens. Matter Mater. Phys.*, 2005, **72**, 104301.
- 75 R. Prasado Rao, N. Sharma, V. K. Peterson and S. Adams, *Solid State Ionics*, 2013, **230**, 72.
- 76 P. A. Beckmann, *Phys. Rep.*, 1988, **171**, 85.

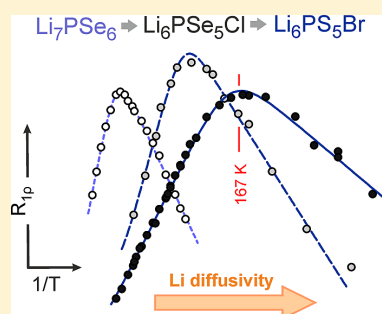
### 3.2.2 Highly mobile ions: Low-temperature NMR directly probes extremely fast Li<sup>+</sup> hopping in argyrodite-type Li<sub>6</sub>PS<sub>5</sub>Br (pp. 58–63)

Epp, V., Gün, Ö., Deiseroth, H.-J., and Wilkening, M. *Journal of Physical Chemistry Letters* **4**, 2118–2123 (2013).—This article is reprinted with the permission of the American Chemical Society. The original article can be found online at <http://pubs.acs.org/doi/abs/10.1021/jz401003a>. ©2013 American Chemical Society.

# Highly Mobile Ions: Low-Temperature NMR Directly Probes Extremely Fast Li<sup>+</sup> Hopping in Argyrodite-Type Li<sub>6</sub>PS<sub>5</sub>Br

Viktor Epp,<sup>\*,†</sup> Özgül Gün,<sup>‡</sup> Hans-Jörg Deiseroth,<sup>‡</sup> and Martin Wilkening<sup>\*,†</sup><sup>†</sup>Christian Doppler Laboratory for Lithium Batteries, and Institute for Chemistry and Technology of Materials, Graz University of Technology, Stremayrgasse 9, 8010 Graz, Austria<sup>‡</sup>Anorganische Chemie, University of Siegen, Adolf-Reichwein-Straße 2, 57068 Siegen, Germany**S** Supporting Information

**ABSTRACT:** The development of safe and long-lasting all-solid-state lithium-ion batteries needs electrolytes with exceptionally good transport properties. Here, we report on the combination of several solid-state nuclear magnetic resonance (NMR) techniques which have been used to precisely probe short-range as well as long-range Li<sup>+</sup> dynamics in Li<sub>6</sub>PS<sub>5</sub>Br from an atomic-scale point of view. NMR data clearly reveal an extraordinary high Li diffusivity. This manifests in so-called diffusion-induced spin–lattice relaxation NMR rate peaks showing up at temperatures as low as 260 K. From a quantitative point of view, at ambient temperature the Li jump rate is of the order of 10<sup>9</sup> s<sup>-1</sup> which corresponds to a Li<sup>+</sup> conductivity in order of 10<sup>-3</sup> to 10<sup>-2</sup> S/cm, thus, indicating “liquid-like” Li<sup>+</sup> diffusion behavior in Li<sub>6</sub>PS<sub>5</sub>Br.

**SECTION:** Kinetics and Dynamics

Since the discovery of ionic conduction in solids many decades ago, the research field, which is frequently known as *solid state ionics* today, has emerged to be one of the most important subdisciplines of physical chemistry, in particular, and materials science, in general. Currently, this ongoing progress is additionally driven by the increasing demand to realize advanced and energy-dense electrochemical storage systems that need fast ion conductors.

Looking toward improved lithium-ion batteries<sup>1–4</sup> for, for example, electric vehicles as well as for storing energy from renewable but intermittent sources, new materials with extraordinary transport properties have to be developed, thoroughly characterized, and tested. To go beyond today's commercially available systems, which mostly rely on flammable liquid electrolytes, more than ever before, *solid* electrolytes<sup>5</sup> are indispensable to guarantee both safety and reliability as well as a long life of a rechargeable battery.

Besides thermal and electrochemical stability, a powerful solid electrolyte, which conducts lithium ions between the negatively charged anode and the positive cathode, needs to have an Li ion conductivity higher than 10<sup>-3</sup> S/cm near room temperature. So far, only a few crystalline solids are known<sup>5–12</sup> that meet these requirements. Once promising candidates are found, Li transport parameters have to be precisely and reliably measured.<sup>13</sup> However, in the case of lithium the pool of methods is rather limited. For example, because there is no suitable long-living isotope known, the well-known radio tracer method cannot be applied. Conductivity spectroscopy needs careful postpreparation of the sample and might suffer from

porosity, grain boundary resistances, and electrode effects.<sup>14</sup> Nuclear magnetic resonance (NMR) spectroscopy,<sup>15–20</sup> however, which takes advantage of the superb receptivity of the <sup>7</sup>Li nucleus (spin-3/2), represents an atomic-scale, nondestructive, and even contactless method to be used for this purpose. Moreover, the combination of complementary time-domain NMR techniques allows probing Li diffusion parameters over a large dynamic range, covering in the best case more than 10 decades.<sup>19,21,22</sup>

We report on an example par excellence where relaxation NMR was used to directly probe Li jump rates  $1/\tau$  and activation energies  $E_a$  in argyrodite-type cubic Li<sub>6</sub>PCh<sub>5</sub>X (Ch = S, Se; X = Cl, Br),<sup>14,23,24</sup> representing a new class of highly conducting solid electrolytes. It turned out that polycrystalline Li<sub>6</sub>PS<sub>5</sub>Br belongs, as yet, to one of the fastest solid Li conductors investigated by Li NMR. The results even exceed those recently reported for an ultrafast jump diffusion process in Li<sub>12</sub>Si<sub>7</sub>.<sup>25</sup> Finally, by systematically comparing the results of different members of the Li<sub>6</sub>PS<sub>5</sub>Br family, the measurements helped us to understand how anion substitution may improve cation diffusivity – a general concept that is extremely advantageous to tailor transport properties. Let us note that, even today, a knowledge-based and target-oriented development of functional materials, in the true sense of the word, has been documented extremely rarely.

**Received:** May 14, 2013**Accepted:** June 11, 2013**Published:** June 11, 2013

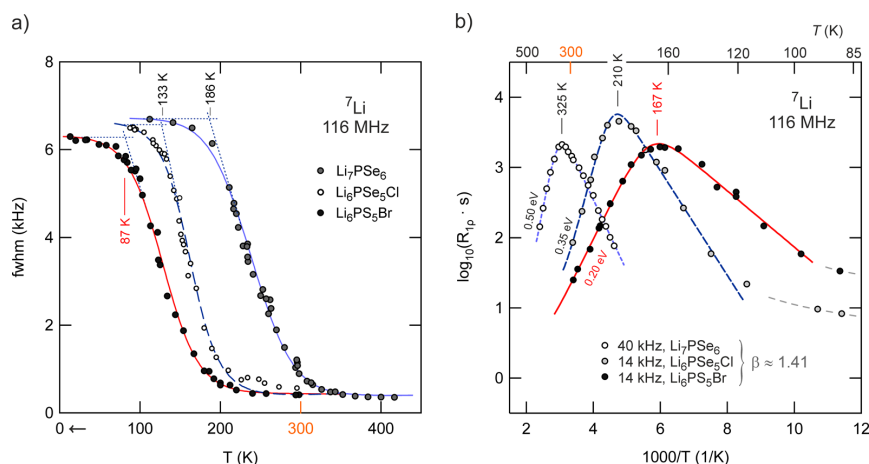


**Figure 1.** (a) Temperature dependence of the  ${}^7\text{Li}$  NMR line widths (full width at half-maximum) of three selected Li-argyrodites. Data for  $\text{Li}_7\text{PSe}_6$  were taken from ref 32. Lines are to guide the eye. Dotted lines indicate the determination of the onset of motion-induced line narrowing. A value of 87 K, which is obtained for  $\text{Li}_6\text{PS}_5\text{Br}$ , indicates extremely fast hopping processes. (b) Arrhenius plot of the corresponding  ${}^7\text{Li}$  SLR  $\rho$  NMR rates recorded at the locking frequencies indicated. Here, at the peak maximum, the Li jump rate is at least  $10^5 \text{ s}^{-1}$ . The lines represent fits according to a modified BPP relaxation model,<sup>13,36,37</sup> taking into account its asymmetry by introducing the parameter  $\beta$ . The farther the diffusion-induced NMR relaxation peak is shifted toward lower  $T$ , the faster the Li exchange and the smaller the activation energy turns out. The latter is directly given by the slope of the respective high-temperature flank. In summary, Li diffusion drastically increases in the following order:  $\text{Li}_7\text{PSe}_6 < \text{Li}_6\text{PSe}_5\text{Cl} < \text{Li}_6\text{PS}_5\text{Br}$ . See the text for further details.

The Li-argyrodites, with natural Li abundance ( ${}^7\text{Li}$  92.5%,  ${}^6\text{Li}$  7.2%), were prepared by solid-state synthesis; details of sample preparation are described elsewhere.<sup>14</sup> To protect the polycrystalline powder samples permanently from any traces of moisture they were carefully fire-sealed in glass ampoules.  ${}^7\text{Li}$  NMR line shapes and spin–lattice relaxation (SLR) measurements in both the laboratory and rotating frame of reference were recorded on a digital Avance III NMR spectrometer that is connected to a shimmed cryo magnet with a nominal magnetic field of 7 T. (See the Supporting Information for further experimental details.) Because of the high diffusivity of the Li ions in  $\text{Li}_6\text{PS}_5\text{Br}$  the NMR measurements had to be partly performed at cryogenic temperatures as low as 13 K. For that purpose a special probe designed by Bruker was employed. While line shapes were recorded with a single pulse, SLR NMR rates were acquired using the saturation recovery technique<sup>17,26</sup> and a spin-lock pulse sequence,<sup>26–28</sup> respectively.

First insights into Li dynamics of crystalline solids can be deduced from the motion-induced narrowing of static Li NMR spectra recorded at different temperatures.<sup>29,30</sup> At sufficiently low  $T$ , that is, in the so-called rigid-lattice regime, the Li jump rate  $1/\tau$  is much smaller than the spectral width of the usually dipolarly broadened Gaussian NMR central line. With increasing temperature, however, Li exchange processes become faster, and  $1/\tau$  reaches values being comparable to the spectral width. The associated averaging of dipole–dipole interactions results in a motionally narrowed, in many cases, Lorentzian NMR central line.<sup>31</sup> This behavior is also observed in the present case. For comparison, in Figure 1a, the NMR line widths (full width at half-maximum) for three selected Li-argyrodites are plotted versus temperature. While onset of motional narrowing (MN) for  $\text{Li}_7\text{PSe}_6$  significantly starts at  $T_{\text{MN}} = 186 \text{ K}$ ,<sup>32</sup> the corresponding curve of  $\text{Li}_6\text{PSe}_5\text{Cl}$  is clearly shifted toward lower temperature yielding  $T_{\text{MN}} = 133 \text{ K}$ . This value is comparable to that found recently for the ultrafast

diffusion process in polycrystalline  $\text{Li}_{12}\text{Si}_7$ . At the onset point of the narrowing curve the jump rate  $1/\tau$  is expected to be on the order of  $10^3 \text{ s}^{-1}$ . Most importantly, a further shift is observed for  $\text{Li}_6\text{PS}_5\text{Br}$ , resulting in an extremely low onset temperature of  $T_{\text{MN}} = 87 \text{ K}$  (Figure 1a). The results nicely corroborate those reported by Eckert and coworkers,<sup>7</sup> who recorded NMR spectra down to 130 K, as well as confirm the data presented by Koch.<sup>33</sup> To verify such ultrafast diffusion processes, we measured diffusion-induced  ${}^6\text{Li}$  and  ${}^7\text{Li}$  SLR NMR rates at different frequencies and over a broad temperature range.

Provided SLR is solely induced by diffusion processes, the NMR SLR rate  $R_{1(\rho)}$  passes through a maximum on a  $\log(R_{1(\rho)})$  versus  $1/T$  plot.<sup>13,17,34</sup> When  $R_{1(\rho)}$  reaches its maximum value the mean correlation rate, being almost identical to the Li jump rate  $1/\tau$ , was on the order of the Larmor ( $\omega_0$ ) or locking frequency ( $\omega_1$ ) used to sample the NMR rates.<sup>13,17</sup> Because  $\omega_0$  is in the megahertz range and  $\omega_1$  is on the order of kilohertz, complementary SLR NMR experiments are sensitive to motional processes covering a quite large time scale. Let us first discuss those carried out at comparable locking frequencies of  $\omega_1/2\pi = 45$  and 14 kHz, respectively (see Figure 1b).<sup>35</sup> While  $\text{Li}_7\text{PSe}_6$  reveals an asymmetric rate peak showing up at  $T_{\text{max}} = 325 \text{ K}$ , that of the Cl-containing argyrodite shows up at 210 K, indicating greatly improved Li diffusion; in the case of rotating frame SLR  $\rho$ , at  $T_{\text{max}}$  the jump rate is given by  $1/\tau$  ( $T_{\text{max}} \approx 2\omega_1$ ),<sup>13,17</sup> thus, being on the order of  $10^6 \text{ s}^{-1}$ . In perfect agreement with the line width measurements (Figure 1a), the rate peak  $R_{1(\rho)}(1/T)$  of  $\text{Li}_6\text{PS}_5\text{Br}$ , which was recorded at  $\omega_1/2\pi = 14 \text{ kHz}$ , is shifted toward even lower  $T$  yielding  $T_{\text{max}} = 167 \text{ K}$  (Figure 2b). For comparison, considering other fast ion conductors studied, a value on the order of  $10^5$  jumps per second is usually found slightly below room temperature.<sup>21</sup> Here the shift of more than 100 K toward lower  $T$  unequivocally classifies  $\text{Li}_6\text{PS}_5\text{Br}$  as an electrolyte with fast Li exchange processes.

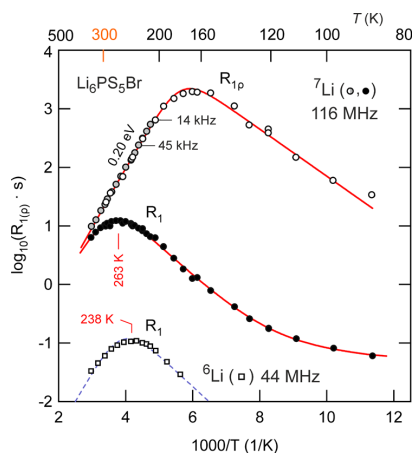


**Figure 2.** Arrhenius plot of the  ${}^7\text{Li}$  NMR relaxation rates  $R_1$  and  $R_{1\rho}$  of polycrystalline  $\text{Li}_6\text{PS}_5\text{Br}$  measured in both the rotating frame (see Figure 1b) and laboratory frame of reference. Solid lines represent a joint fit being based on the BPP model (see text). For comparison, the diffusion-induced  ${}^6\text{Li}$  SLR NMR rates recorded at 44 MHz are also included. Li SLR NMR rate maxima, showing up at 263 and 238 K, that is, well below room temperature, point to extremely fast, translational Li ion motions with jump rates of the order of  $10^9 \text{ s}^{-1}$ , that is, residence times as low as 1 ns.

At room temperature, the jump rate of  $\text{Li}_6\text{PS}_5\text{Br}$  is expected to reach even larger values. Indeed, SLR NMR measurements performed at a resonance frequency of 116 MHz reveal a diffusion-induced rate peak  $R_1(1/T)$  passing through its maximum at  $T_{\text{max}} = 263 \text{ K}$  (Figure 2). This has been corroborated by complementary  ${}^6\text{Li}$  measurements carried out at 44 MHz yielding  $T_{\text{max}} = 238 \text{ K}$  (see also Figure 2). With  $1/\tau(T_{\text{max}}) \approx \omega_1$ , being valid for SLR NMR in the laboratory frame of reference,<sup>17</sup> this yields  $1/\tau(238 \text{ K}) = 2.8 \times 10^8 \text{ s}^{-1}$  and  $1/\tau(263 \text{ K}) = 7.3 \times 10^8 \text{ s}^{-1} \approx 10^9 \text{ s}^{-1}$ , respectively. Thus, well below room temperature the mean residence time of a Li ion is close to 1 ns. To our knowledge this is so far one of the fastest solid-state diffusion processes probed by time-domain  ${}^6\text{Li}$  NMR relaxometry. For comparison, in  $\text{Li}_{12}\text{Si}_7$ , the  $R_1(1/T)$  rate peak shows up at much higher temperatures (viz.  $T_{\text{max}} = 400 \text{ K}$ ) when measured at 77.7 MHz.<sup>25</sup>

The jump rates derived from SLR NMR can be converted into conductivity values according to the Einstein–Smoluchowski equation and the Nernst–Einstein equation.<sup>38</sup> The first interrelates  $1/\tau$  with the self-diffusion coefficient: assuming 3D diffusion and a jump distance of 2.5 Å, which is a very reasonable value in the present case,<sup>39</sup> we obtain  $D_{263\text{K}} = a^2/(6\tau) = 7.6 \times 10^{-8} \text{ cm}^2 \text{ s}^{-1}$  (in a relatively theory-independent way). Disregarding any correlation effects, by means of the Nernst–Einstein equation,  $D_{263\text{K}}$  can roughly be converted into a conductivity value  $\sigma$ . Here a mean residence time of 1 ns corresponds to  $\sigma$  in the order of  $\sigma \approx 10^{-2} \text{ S/cm}$ , clearly illustrating extremely mobile lithium ions in polycrystalline  $\text{Li}_7\text{PS}_5\text{Br}$  (see below). Certainly, this conversion should be regarded as a rough estimate because relaxation NMR and conductivity spectroscopy sense different kinds of correlation functions.<sup>40,41</sup>

To understand the motion-induced  ${}^7\text{Li}$  SLR NMR rates of  $\text{Li}_7\text{PSe}_6$ ,  $\text{Li}_6\text{PSe}_5\text{Cl}$ , and  $\text{Li}_6\text{PS}_5\text{Br}$  in more detail, we used modified BPP-type<sup>42</sup> spectral density functions  $J(\omega_0, \tau_c)$  and

$J(\omega_0, \omega_1, \tau_c)$  that are based on exponential motional correlation functions<sup>17,42</sup>  $G(t')$  to describe the temperature dependence of  $R_1(1/T)$  and  $R_{1\rho}(1/T)$ , respectively.<sup>13,25,34</sup> The correlation time  $\tau_c$  is within a factor of 2<sup>17</sup> identical to the Li residence time  $\tau = \tau_0 \exp(-E_a/(k_B T))$ ; here  $E_a$  denotes the activation energy and  $k_B$  is Boltzmann's constant.

The Lorentzian-shaped function  $J$ , which is directly proportional to  $R_1$  and  $R_{1\rho}$ , can be derived from  $G$  by Fourier transformation.<sup>17,43</sup> In the case of a 3D diffusion process, we have  $J \propto \tau$  at high temperatures, that is, in the limit  $\omega_{0(\rho)}\tau \ll 1$ , and  $J \propto \tau^{-1}\omega_{0(\rho)}^{-\beta}$  (with  $1 < \beta \leq 2$ ) in the low  $T$  limit where  $\omega_{0(\rho)}\tau \gg 1$  holds.<sup>17,34</sup> Original BPP-type behavior<sup>36</sup> does not take into account correlation effects and predicts  $\beta = 2$  leading to symmetric relaxation rate peaks.<sup>17,44</sup> Asymmetric peaks are usually found for structurally complex or even disordered ion conductors.<sup>6,13,34</sup> Such materials reveal a broad range of short-range and long-range motional processes that are affected by correlation effects<sup>45</sup> resulting from, for example, Coulomb interactions.<sup>46</sup> In the present case, the  $R_{1\rho}(1/T)$  fits yield an asymmetry parameter  $\beta_\rho \approx 1.4$  (Figure 1b), while  $\beta \approx 1.5$  is found for the  ${}^7\text{Li}$  NMR (and  ${}^6\text{Li}$  NMR) rates recorded in the laboratory frame of reference (see Figure 2). The small difference in  $\beta$  points to slightly differing correlation effects affecting the SLR NMR rates, which are per se sensitive to Li motions on different time scales.<sup>34</sup>

It is clearly evident from Figure 1b that  $E_a$ , which can be independently deduced from the slope of the high- $T$  flank, decreases from  $\sim 0.5 \text{ eV}$  in steps of 0.15 eV. This result is in excellent agreement with the shift of the rate peaks observed: the smaller  $E_a$ , the faster Li diffusion becomes. Thus, Li exchange drastically increases in the following order:  $\text{Li}_7\text{PSe}_6 (\approx \text{Li}_7\text{PS}_6) < \text{Li}_6\text{PSe}_5\text{Cl} < \text{Li}_6\text{PS}_5\text{Br}$ . Let us note that  $\text{Li}_7\text{PSe}_6$ , investigated in ref 32 in detail, is expected to show very similar diffusion parameters as the S-analogue  $\text{Li}_7\text{PS}_6$ . The value found for  $\text{Li}_6\text{PSe}_5\text{Cl}$  (0.35 eV) is in good agreement with the one calculated by Rao et al. characterizing the 3D long-range pathway network.<sup>23</sup>

The lowest value,  $E_a = 0.20(1) \text{ eV}$  ( $200 \text{ K} < T < 330 \text{ K}$ , see Figure 2), is also found when the NMR peaks  $R_{1\rho}(1/T)$  and  $R_1(1/T)$  of  $\text{Li}_6\text{PS}_5\text{Br}$  are analyzed in terms of a global fit (solid lines in Figure 2), that is, linking the fitting parameters such as  $\omega_0$ , the activation energies, and coupling constants. In the present case, however, the best fit is obtained when  $\beta \neq \beta_\rho$  (see above) and  $1/\tau_0$  of SLR NMR is independent of that used to parametrize the  $R_{1\rho}(1/T)$  peak. It is worth noting that nondiffusive background relaxation, see the SLR NMR rates of Figure 2, which were recorded below 120 K, were taken into account by an appropriate power law:  $R_1 \propto T^\kappa$  with  $\kappa \approx 2$ . Such effects, which are also seen in Figure 1b, presumably represent SLR induced by lattice vibrations or by coupling of the Li spins with traces of paramagnetic impurities. Moreover, from many different runs of the global fit procedure it turned out that it is useful to replace  $\omega_1 = 14 \text{ kHz} \times 2\pi$  with a slightly larger value of  $\omega_{\text{eff}} = 1.4 \omega_1$ . Here the factor of 1.4 takes into account local magnetic fields in the order of the locking field.

For comparison, the fitting results obtained are listed in Table 1. Interestingly, the  $R_{1\rho}$  data seem to underestimate the Arrhenius prefactor, leading to  $\tau_0 = 6(2) \times 10^{-12} \text{ s}$ , while the  $R_1(1/T)$  peak yields  $\tau_0 = 2(1) \times 10^{-13} \text{ s}$ . The latter value, whose inverse agrees with the typical range of phonon frequencies, is corroborated by analyzing the  ${}^6\text{Li}$   $R_1(1/T)$  rate peak, which is best characterized by  $\tau_0 = 3(1) \times 10^{-13} \text{ s}$ .

**Table 1. Results ( $E_a$ ,<sup>b</sup>  $\beta_{(\rho)}$ ,  $\tau_0$ , and the pre-factor  $C^c$ ) of the overall SLR NMR Fit Shown in Figure 2 (solid lines)<sup>a</sup>**

	$E_a^b$	$C^c$	$\beta_{(\rho)}$	$\tau_0$
$R_1$ ( <sup>7</sup> Li)	0.20(1) eV	$5.8(1) \times 10^9 \text{ s}^{-2}$	1.54	$2(1) \times 10^{-13} \text{ s}$
$R_{1\rho}$ ( <sup>7</sup> Li)			1.36	$6(1) \times 10^{-12} \text{ s}$
$R_1$ ( <sup>6</sup> Li)	0.20(3) eV	$2(1) \times 10^7 \text{ s}^{-2}$	1.53	$3(1) \times 10^{-13} \text{ s}$

<sup>a</sup>The fit was carried out using  $\omega_{1,\text{eff}} = 1.4 \omega_1$  with  $\omega_1 = 14 \text{ kHz} \times 2\pi$ ,  $\omega_0$  (<sup>7</sup>Li) = 116 MHz  $\times 2\pi$ , and  $\omega_0$  (<sup>6</sup>Li) = 44 MHz  $\times 2\pi$ . <sup>b</sup>This value refers to the slope of the high- $T$  flank of the SLR NMR peaks. <sup>c</sup>The prefactor  $C$  interrelates  $J(\omega_0, \tau_c)$  with the relaxation rate  $R_1$ . Values ranging from  $10^9$  to  $10^{10} \text{ s}^{-2}$  correspond to the square of typical <sup>7</sup>Li quadrupole coupling constants.<sup>31</sup> Note that the quadrupole moment of <sup>6</sup>Li is by a factor of 50 smaller than that of <sup>7</sup>Li; therefore, for <sup>6</sup>Li NMR, the dipolar contributions play a non-negligible role.

Thus, describing (long-range) Li diffusion in  $\text{Li}_6\text{PS}_5\text{Br}$  with a single Arrhenius relation, the jump rate  $\tau(T)$  is given by  $\tau = 3(1) \times 10^{-13} \text{ s} \cdot \exp(-0.20(2) \text{ eV}/(k_B T))$ . According to that result, at  $T = 125 \text{ K}$ , that is, at the temperature of the inflection point of the NMR motional narrowing curve of  $\text{Li}_6\text{PS}_5\text{Br}$  (see Figure 1b), the jump rate  $1/\tau$  should be on the order of  $3.5 \times 10^4 \text{ s}^{-1}$ . Indeed, with the rigid lattice line width  $\Delta\nu_{\text{fl}} = 6 \text{ kHz}$ , the estimation  $1/\tau \approx \Delta\nu_{\text{fl}} \times 2\pi$  yields  $3.9 \times 10^4 \text{ s}^{-1}$ . Certainly, this agreement does not rule out the presence of other, quite different and temperature-dependent diffusion processes. In particular, while activation energies determined in the limit  $\omega_{0(\rho)}\tau \ll 1$  are generally compared with those from dc-conductivity probing long-range ion transport,<sup>17,34</sup> the low- $T$  flank of the  $R_{1\rho}(1/T)$  rate peak is influenced by short-range motional processes characterized by much smaller activation energies;<sup>34</sup> here, this is 0.08(2) eV for  $\text{Li}_6\text{PS}_5\text{Br}$  and 0.15(2) eV for the Cl-analogue; cf. also results from theoretical studies including also I-containing compounds.<sup>23,39</sup>

Finally, it is highly useful to compare the absolute values of the purely diffusion-induced <sup>6</sup>Li (spin-1) NMR rates in the limit  $\omega_0\tau \ll 1$  with those of the corresponding <sup>7</sup>Li (spin-3/2) NMR rate peak. For dipolar interactions being responsible for SLR NMR, the ratio  $R_1(^6\text{Li})/R_1(^7\text{Li}) = r$  is expected to be on the order of two, while for quadrupolar relaxation  $r$  should be on the order of  $10^{-4}$ .<sup>47</sup> Experimentally we found  $5.3(2) \times 10^{-3}$  pointing to a quadrupolar mechanism influencing <sup>7</sup>Li NMR spin-lattice relaxation here.

In conclusion, among the Li-argyrodites studied here,  $\text{Li}_6\text{PS}_5\text{Br}$  turned out to be a material with an exceptionally high Li diffusivity. The corresponding long-range jump process is characterized by a hopping activation energy of only 0.2 eV as deduced from the various temperature-variable NMR SLR measurements. This extraordinary feature manifests in (laboratory frame) SLR NMR rate peaks showing up at temperatures as low as 260 K. From a quantitative point of view, at room temperature, this yields a Li jump rate of  $10^9 \text{ s}^{-1}$ , which corresponds to an  $\text{Li}^+$  conductivity on the order of  $10^{-3}$  to  $10^{-2} \text{ S/cm}$ , thus indicating “liquid-like” diffusion behavior comparable to, for example, the interlayer process in  $\text{Li}_3\text{N}$ .<sup>48</sup> The activation energy and the estimated ionic conductivity from SLR NMR are in agreement with results deduced from previous and recent conductivity studies.<sup>7,23,49</sup> Let us note that in the limit of  $\omega_{0(\rho)}\tau \ll 1$ , SLR NMR is expected to yield activation energies being comparable to those characterizing long-range ion transport, while on the low- $T$  side of a given NMR relaxation peak, localized, that is, short-range, Li motional processes are probed.<sup>17,34</sup>

The high Li diffusivity found makes the development of safe and long-lasting all-solid-state lithium batteries feasible. It might be understood by comparing the results from the three different samples studied: because Li diffusivity increases from  $\text{Li}_2\text{PSe}_6$  to  $\text{Li}_6\text{PSe}_5\text{Cl}$  (and  $\text{Li}_6\text{PS}_5\text{Br}$ ), the structural mismatch and strain generated by substitution of a large halogen ion for, for example, selenium, seems to be highly relevant when a high Li mobility needs to be achieved. Moreover, the larger Li diffusivity of  $\text{Li}_6\text{PS}_5\text{Br}$  against  $\text{Li}_6\text{PSe}_5\text{Cl}$  might be attributed to the combination of anions with different polarizabilities. In summary, the present example illustrates how anion substitution can be used as a tool to successfully manipulate cation diffusivity in a crystalline solid.

## ■ ASSOCIATED CONTENT

### Supporting Information

Cf. for experimental details including information on the equipment used, the measurement conditions chosen, and the pulse sequences applied to record the SLR NMR data. This material is available free of charge via the Internet at <http://pubs.acs.org>.

## ■ AUTHOR INFORMATION

### Corresponding Author

\*E-mail: [viktor.epp@tugraz.at](mailto:viktor.epp@tugraz.at); [wilkening@tugraz.at](mailto:wilkening@tugraz.at).

### Notes

The authors declare no competing financial interest.

## ■ ACKNOWLEDGMENTS

We thank G. Schmidt (Bruker, Karlsruhe (Germany)) for his help with setting up the NMR spectrometer at the TU Graz. Financial support by the Austrian Federal Ministry of Economy, Family and Youth and the Austrian National Foundation for Research, Technology and Development as well as by the Deutsche Forschungsgemeinschaft (DFG) is highly appreciated (DFG Forschergruppe 1277, grant no.: WI3600 4-1/4-2).

## ■ REFERENCES

- (1) Aricò, A. S.; Bruce, P.; Scrosati, B.; Tarascon, J.-M.; Schalkwijk, W. V. Nanostructured Materials for Advanced Energy Conversion and Storage devices. *Nat. Mater.* **2005**, *4*, 366–377.
- (2) Tarascon, J. M.; Armand, M. Issues and Challenges Facing Rechargeable Lithium Batteries. *Nature* **2001**, *414*, 359–367.
- (3) Bruce, P. G.; Scrosati, B.; Tarascon, J.-M. Nanomaterials for Rechargeable Lithium Batteries. *Angew. Chem., Int. Ed.* **2008**, *47*, 2930–2946.
- (4) Armand, M.; Tarascon, J.-M. Building Better Batteries. *Nature* **2008**, *451*, 652–657.
- (5) Knauth, P. Inorganic Solid Li Ion Conductors: An Overview. *Solid State Ion.* **2009**, *180*, 911–916.
- (6) Buschmann, H.; Dölle, J.; Berendts, S.; Kuhn, A.; Bottke, P.; Wilkening, M.; Heitjans, P.; Senyshyn, A.; Ehrenberg, H.; Lotnyk, A.; Duppel, V.; Kienle, L.; Janek, J. Structure and Dynamics of the Fast Lithium Ion Conductor “ $\text{Li}_7\text{La}_3\text{Zr}_2\text{O}_{12}$ ”. *Phys. Chem. Chem. Phys.* **2011**, *13*, 19378–19392.
- (7) Deiseroth, H.-J.; Kong, S.-T.; Eckert, H.; Vannahme, J.; Reiner, C.; Zaiss, T.; Schlosser, M.  $\text{Li}_6\text{PS}_5\text{X}$ : A Class of Crystalline Li-Rich Solids With an Unusually High  $\text{Li}^+$  Mobility. *Angew. Chem., Int. Ed.* **2008**, *47*, 755–758.
- (8) Hayashi, A.; Tatsumisago, M. Recent Development of Bulk-type Solid-state Rechargeable Lithium Batteries with Sulfide Glass-Ceramic Electrolytes. *Electron. Mater. Lett.* **2012**, *8*, 199–207.
- (9) Murugan, R.; Thangadurai, V.; Weppner, W. Fast Lithium Ion Conduction in Garnet-Type  $\text{Li}_7\text{La}_3\text{Zr}_2\text{O}_{12}$ . *Angew. Chem., Int. Ed.* **2007**, *46*, 7778–7781.

- (10) Kamaya, N.; Homma, K.; Yamakawa, Y.; Hirayama, M.; Kanno, R.; Yonemura, M.; Kamiyama, T.; Kato, Y.; Hama, S.; Kawamoto, K.; Mitsui, A. A Lithium Superionic Conductor. *Nat. Mater.* **2011**, *10*, 682–686.
- (11) Takada, K.; Tansho, M.; Yanase, I.; Inada, T.; Kajiyama, A.; Kouguchi, M.; Kondo, S.; Watanabe, M. Lithium Ion Conduction in  $\text{LiTi}_2(\text{PO}_4)_3$ . *Solid State Ion.* **2001**, *139*, 241–247.
- (12) Hayamizu, K.; Aihara, Y. Lithium Ion Diffusion in Solid Electrolyte  $(\text{Li}_2\text{S})_x(\text{P}_2\text{S}_5)_3$  Measured by Pulsed-Gradient Spin-echo  $^7\text{Li}$  NMR Spectroscopy. *Solid State Ion.* **2013**, *238*, 7–14.
- (13) Kuhn, A.; Narayanan, S.; Spencer, L.; Goward, G.; Thangadurai, V.; Wilkening, M. Li Self-diffusion in Garnet-type  $\text{Li}_7\text{La}_3\text{Zr}_2\text{O}_{12}$  as Probed Directly by Diffusion-induced  $^7\text{Li}$  Spin-lattice Relaxation NMR Spectroscopy. *Phys. Rev. B* **2011**, *83*, 094302/1–094302/11.
- (14) Deiseroth, H.-J.; Maier, J.; Weichert, K.; Nickel, V.; Kong, S.-T.; Reiner, C.  $\text{Li}_7\text{PS}_6$  and  $\text{Li}_6\text{PS}_5\text{X}$  (X: Cl, Br, I): Possible Three-dimensional Diffusion Pathways for Lithium Ions and Temperature Dependence of the Ionic Conductivity by Impedance Measurements. *Z. Anorg. Allg. Chem.* **2011**, *637*, 1287–1294.
- (15) Brinkmann, D. NMR-Studies of Superionic Conductors. *Prog. Nucl. Magn. Reson. Spectrosc.* **1992**, *24*, 527–552.
- (16) Böhmer, R.; Jeffrey, K.; Vogel, M. Solid-state Li NMR with Applications to the Translational Dynamics in Ion Conductors. *Prog. Nucl. Magn. Reson. Spectrosc.* **2007**, *50*, 87–174.
- (17) Heitjans, P.; Schirmer, A.; Indris, S. In *Diffusion in Condensed Matter - Methods, Materials, Models*, 2nd ed.; Heitjans, P., Kärger, J., Eds.; Springer: Berlin, 2005; p 367.
- (18) Wilkening, M.; Lyness, C.; Armstrong, A. R.; Bruce, P. G. Diffusion in Confined Dimensions:  $\text{Li}^+$  Transport in Mixed Conducting  $\text{TiO}_2$ -B Nanowires. *J. Phys. Chem. C* **2009**, *113*, 4741–4744.
- (19) Wilkening, M.; Küchler, W.; Heitjans, P. From Ultra-slow to Fast Lithium Diffusion in the 2D Ion Conductor  $\text{Li}_x\text{TiS}_2$  - Probed Directly by Stimulated-Echo NMR and Nuclear Magnetic Relaxation. *Phys. Rev. Lett.* **2006**, *96*, 065901/1–065901/4.
- (20) Wilkening, M.; Mühle, C.; Jansen, M.; Heitjans, P. Microscopic Access to Long-Range Diffusion Parameters of the Fast Lithium Ion Conductor  $\text{Li}_7\text{BiO}_6$  by Solid State  $^7\text{Li}$  Stimulated Echo NMR. *J. Phys. Chem. B* **2007**, *111*, 8691–8694.
- (21) Wilkening, M.; Heitjans, P. Li Jump Process in  $h\text{-Li}_{0.7}\text{TiS}_2$  Studied by Two-time  $^7\text{Li}$  Spin-alignment Echo NMR and Comparison with Results on Two-dimensional Diffusion from Nuclear Magnetic Relaxation. *Phys. Rev. B* **2008**, *77*, 024311/1–024311/13.
- (22) Wilkening, M.; Kuhn, A.; Heitjans, P. Atomic-scale Measurement of Ultraslow Li Motions in Glassy  $\text{LiAlSi}_2\text{O}_6$  by Two-time  $^6\text{Li}$  Spin-alignment Echo NMR. *Phys. Rev. B* **2008**, *78*, 054303/1–054303/9.
- (23) Rao, R. P.; Adams, S. Studies of Lithium Argyrodite Solid Electrolytes for All-solid-state Batteries. *Phys. Status Solidi A*. **2011**, *208*, 1804–1807.
- (24) Boulineau, S.; Courty, M.; Tarascon, J.-M.; Viallet, V. Mechanochemical Synthesis of Li-argyrodite  $\text{Li}_6\text{PS}_5\text{X}$  (X = Cl, Br, I) as Sulfur-based Solid Electrolytes for all Solid State Batteries Application. *Solid State Ionics* **2012**, *221*, 1.
- (25) Kuhn, A.; Sreeraj, P.; Pöttgen, R.; Wiemhöfer, H.-D.; Wilkening, M.; Heitjans, P. Li Ion Diffusion in the Anode Material  $\text{Li}_{12}\text{Si}_7$ : Ultrafast Quasi-1D Diffusion and Two Distinct Fast 3D Jump Processes Separately Revealed by  $^7\text{Li}$  NMR Relaxometry. *J. Am. Chem. Soc.* **2011**, *133*, 11018–11021.
- (26) Fukushima, E.; Roeder, S. B. W. *Experimental Pulse NMR*; Addison-Wesley: Reading, 1981.
- (27) Ailion, D.; Slichter, C. P. Study of Ultraslow Atomic Motions by Magnetic Resonance. *Phys. Rev. Lett.* **1964**, *12*, 168–171.
- (28) Slichter, C. P.; Ailion, D. Low-Field Relaxation and the Study of Ultraslow Atomic Motions by Magnetic Resonance. *Phys. Rev. B* **1964**, *135*, A1099–A1110.
- (29) Wilkening, M.; Epp, V.; Feldhoff, A.; Heitjans, P. Tuning the Li Diffusivity of Poor Ionic Conductors by Mechanical Treatment: High Li Conductivity of Strongly Defective  $\text{LiTaO}_3$  Nanoparticles. *J. Phys. Chem. C* **2008**, *112*, 9291–9300.
- (30) Wilkening, M.; Bork, D.; Indris, S.; Heitjans, P. Diffusion in Amorphous  $\text{LiNbO}_3$  Studied by  $^7\text{Li}$  NMR — Comparison with the Nano- and Microcrystalline Material. *Phys. Chem. Chem. Phys.* **2002**, *4*, 3246–3251.
- (31) Bertermann, R.; Müller-Warmuth, W.; Jansen, C.; Hiltmann, F.; Krebs, B. NMR Studies of the Lithium Dynamics in Two Thioborate Superionic Conductors:  $\text{Li}_9\text{B}_{19}\text{S}_{33}$  and  $\text{Li}_{4-2x}\text{Sr}_{2+x}\text{B}_{10}\text{S}_{19}$  ( $x \approx 0.27$ ). *Solid State Ionics* **1999**, *117*, 245–255.
- (32) Epp, V.; Gün, O.; Deiseroth, H.-J.; Wilkening, M. Long-range  $\text{Li}^+$  Dynamics in the Lithium Argyrodite  $\text{Li}_7\text{PSe}_6$  as Probed by Rotating-frame Spin-lattice Relaxation NMR. *Phys. Chem. Chem. Phys.* **2013**, *15*, 7123–7132.
- (33) Koch, B. Festkörper-NMR-Studien zur Struktur und Kationenmobilität in kristallinen Lithiumionenleitern. Ph.D. Thesis, University of Münster, Münster, 2009.
- (34) Wilkening, M.; Heitjans, P. From Micro to Macro: Access to Long-Range  $\text{Li}^+$  Diffusion Parameters in Solids via Microscopic  $^6\text{Li}$  Spin-Alignment Echo NMR Spectroscopy. *ChemPhysChem* **2012**, *13*, 53–65.
- (35) Note that with the NMR cryo probe employed we could not reach locking frequencies lower than 40 kHz. As can be seen from Figure 2, in the case of 3D BPP-type behavior a slight decrease in the locking frequency does influence the low-T flank only. The peak maximum is expected to shift only slightly towards lower T. Even in the case of 45 kHz it is still expected to show up well below 200 K.
- (36) Bloembergen, N.; Purcell, E. M.; Pound, R. V. Relaxation Effects in Nuclear Magnetic Resonance Absorption. *Phys. Rev.* **1948**, *73*, 679–712.
- (37) Küchler, W.; Heitjans, P.; Payer, A.; Schöllhorn, R.  $^7\text{Li}$  NMR Relaxation by Diffusion in Hexagonal and Cubic  $\text{Li}_x\text{TiS}_2$ . *Solid State Ionics* **1994**, *70*, 434–438.
- (38) Mehrer, H. *Diffusion in Solids: Fundamentals, Methods, Materials, Diffusion-Controlled Processes*; Springer: Berlin, 2007.
- (39) Pecher, O.; Kong, S.-T.; Goebel, T.; Nickel, V.; Weichert, K.; Reiner, C.; Deiseroth, H.-J.; Maier, J.; Haarmann, F.; Zahn, D. Atomistic Characterisation of  $\text{Li}^+$  Mobility and Conductivity in  $\text{Li}_{1-x}\text{PS}_{6-x}\text{I}_x$  Argyrodites from Molecular Dynamics Simulations, Solid-State NMR, and Impedance Spectroscopy. *Chem.—Eur. J.* **2010**, *16*, 8347–8354.
- (40) *Diffusion in Condensed Matter - Methods, Materials, Models*, 2nd ed.; Heitjans, P., Kärger, J., Eds.; Springer: Berlin, 2005.
- (41) Winter, R.; Siegmund, K.; Heitjans, P. Nuclear Magnetic and Conductivity Relaxations by Li Diffusion in Glassy and Crystalline  $\text{LiAlSi}_2\text{O}_6$ . *J. Non-Cryst. Solids* **1997**, *212*, 215–224.
- (42) Bloembergen, N.; Purcell, E. M.; Pound, R. V. Relaxation Effects in Nuclear Magnetic Resonance Absorption. *Phys. Rev.* **1948**, *73*, 679–712.
- (43) Abragam, A. *The Principles of Nuclear Magnetism*; Clarendon: Oxford, U.K., 1961.
- (44) Wilkening, M.; Iwaniak, W.; Heine, J.; Epp, V.; Kleinert, A.; Behrens, M.; Nuspl, G.; Bensch, W.; Heitjans, P. Microscopic Li Self-diffusion Parameters in the Lithiated Anode Material  $\text{Li}_{4+x}\text{Ti}_5\text{O}_{12}$  ( $0 < x < 3$ ) Measured by  $^7\text{Li}$  Solid State NMR. *Phys. Chem. Chem. Phys.* **2007**, *9*, 6199–6202.
- (45) Meyer, M.; Maass, P.; Bunde, A. Spin-Lattice Relaxation: Non-Bloembergen-Purcell-Pound Behavior by Structural Disorder and Coulomb Interactions. *Phys. Rev. Lett.* **1993**, *71*, 573.
- (46) Bunde, A.; Dieterich, W.; Maass, P.; Meyer, M. In *Diffusion in Condensed Matter - Methods, Materials, Models*; Heitjans, P., Kärger, J., Eds.; Springer: Berlin, 2005; p 813.
- (47) Pietrass, T.; Taulelle, F.; Lavela, P.; OlivierFourcade, J.; Jumas, J. C.; Steuernagel, S. Structure and Dynamics of Lithium-intercalated  $\text{SnS}_2$ .  $^6\text{Li}$ ,  $^7\text{Li}$  and  $^{119}\text{Sn}$  Solid State NMR. *J. Phys. Chem. B* **1997**, *101*, 6715–6723.
- (48) Wang, Z.; Gobet, M.; Sarou-Kanian, V.; Massiot, D.; Bessada, C.; Deschamps, M. Lithium Diffusion in Lithium Nitride by Pulsed-field Gradient NMR. *Phys. Chem. Chem. Phys.* **2012**, *14*, 13535–13538.

(49) Prasada Rao, R.; Sharma, N.; Peterson, V. K.; Adams, S. Formation and Conductivity Studies of Lithium Argyrodite Solid Electrolytes Using *in-situ* Neutron Diffraction. *Solid State Ion.* **2013**, *230*, 72–76.

### 3.3 Garnet-type Li-ion conductors

#### 3.3.1 Spin-alignment echo NMR: Probing Li<sup>+</sup> hopping motion in the solid electrolyte Li<sub>7</sub>La<sub>3</sub>Zr<sub>2</sub>O<sub>12</sub> with garnet-type tetragonal structure (pp. 65–72)

Kuhn, A., Epp, V., Schmidt, G., Narayanan, S., Thangadurai, V., and Wilkening, M. *Journal of Physics: Condensed Matter* **24**, 35901 (2012).—This article is reproduced by permission of IOP Publishing Ltd. The original article can be found online at <http://iopscience.iop.org/0953-8984/24/3/035901>. ©2012 IOP Publishing Ltd.

# Spin-alignment echo NMR: probing $\text{Li}^+$ hopping motion in the solid electrolyte $\text{Li}_7\text{La}_3\text{Zr}_2\text{O}_{12}$ with garnet-type tetragonal structure\*

A Kuhn<sup>1</sup>, V Epp<sup>1</sup>, G Schmidt<sup>2</sup>, S Narayanan<sup>3</sup>, V Thangadurai<sup>3</sup> and M Wilkening<sup>1,4,5</sup>

<sup>1</sup> Institute of Physical Chemistry and Electrochemistry, and Centre for Solid State Chemistry and New Materials (ZFM), Gottfried Wilhelm Leibniz University Hannover, Callinstraße 3a, D-30167 Hannover, Germany

<sup>2</sup> Bruker BioSpin GmbH, Silberstreifen, D-76287 Rheinstetten, Germany

<sup>3</sup> Department of Chemistry, University of Calgary, 2500 University Drive NW, Calgary, Alberta, T2N 1N4, Canada

<sup>4</sup> Institute for Chemistry and Technology of Materials, Graz University of Technology, A-8010 Graz, Austria

E-mail: [epp@pci.uni-hannover.de](mailto:epp@pci.uni-hannover.de), [wilkening@pci.uni-hannover.de](mailto:wilkening@pci.uni-hannover.de) and [wilkening@tugraz.at](mailto:wilkening@tugraz.at)

Received 19 July 2011, in final form 14 November 2011

Published 19 December 2011

Online at [stacks.iop.org/JPhysCM/24/035901](http://stacks.iop.org/JPhysCM/24/035901)

## Abstract

<sup>7</sup>Li spin-alignment echo (SAE) nuclear magnetic resonance (NMR) spectroscopy has been used to measure single-spin hopping correlation functions of polycrystalline  $\text{Li}_7\text{La}_3\text{Zr}_2\text{O}_{12}$ . Damping of the echo amplitude  $S_2(t_m, t_p)$ , recorded at variable mixing time  $t_m$  but fixed preparation time  $t_p$ , turns out to be solely controlled by slow Li jump processes taking place in the garnet-like structure. The decay rates  $\tau_{\text{SAE}}^{-1}$  directly obtained by parametrizing the curves  $S_2(t_m, t_p)$  with stretched exponential functions show Arrhenius behaviour pointing to an activation energy of approximately 0.5 eV. This value, probed by employing an atomic-scale NMR method, is in very good agreement with that deduced from impedance spectroscopy used to measure macroscopic Li transport parameters. Most likely, the two methods are sensitive to the same hopping correlation function although Li dynamics are probed in a quite different manner.

(Some figures may appear in colour only in the online journal)

## 1. Introduction

The precise microscopic measurement of Li jump rates, which can be directly transformed into self-diffusion coefficients via the Einstein–Smoluchowski equation (see below), increasingly attracts materials scientists working in the field of clean energy storage systems [1–7]. In

rechargeable batteries, Li ion conductors serve as anodes and cathodes as well as (solid) electrolytes [2–6, 8]. Besides chemical resistance, guaranteeing the safety of an all-solid-state battery, the prerequisites of a promising electrolyte are a high Li ion conductivity and a vanishing electronic one. Among a large number of pure ion conductors, garnet-type oxides [9–13], in particular, have attracted great attention during the past few years. Due to their structural complexity a number of possibilities are offered to control the influence on their ion transport properties, e.g. by changing the overall chemical composition (full replacement of a cation

\* Dedicated to Professor Dr Paul Heitjans on the occasion of his 65th birthday.

<sup>5</sup> [www.wilkening.pci.uni-hannover.de](http://www.wilkening.pci.uni-hannover.de).

species), by knowledge-based doping with isovalent and non-isovalent cations as well as by manipulating the lithium or oxygen stoichiometry. In particular, the latter might be greatly affected by the preparation route chosen to synthesize an oxidic garnet. A thorough understanding of the impact of these changes on Li dynamics requires deep insights into the Li jump processes present in the undoped garnets serving as internal reference materials.

Solid-state nuclear magnetic resonance (NMR) spectroscopy offers a rich portfolio of highly sophisticated techniques which can be used to measure Li jump processes on quite different timescales and length scales [14–28], respectively. In particular, the analysis of stimulated (spin-alignment) echoes [15, 16, 18, 29–42] turned out to be well suited to trace slow motions of spin-1 and spin-3/2 probes such as  ${}^6\text{Li}$  and  ${}^7\text{Li}$  (as well as  ${}^9\text{Be}$  [43–45]) in a rather straightforward way which is comparable to that of magic angle spinning (MAS) NMR exchange spectroscopy [20–24, 27, 46–48]. While exchange spectroscopy requires well-resolved NMR spectra, NMR spin-alignment echoes (SAE) are recorded under static conditions. This makes the technique an attractive alternative when amorphous materials have to be investigated [31, 33, 38].

${}^7\text{Li}$  as well as  ${}^6\text{Li}$  SAE NMR [15], using the three-pulse sequence of Jeener and Broekaert [49] (see section 2), takes advantage of temporal fluctuations of the electric field gradients (EFGs) the jumping ions experience during diffusing. The interaction of the quadrupole moment of the Li nucleus with an EFG, which is caused by the electric charge distribution in its neighborhood, leads to the well-known alteration of the Zeeman frequency [15, 18, 35, 50]. The corresponding orientation-dependent (angular) quadrupole frequency  $\omega_q$ , which is determined by the quadrupole coupling constant  $\delta_q$  as well as the asymmetry parameter of the interaction  $\eta_q$ , is used to label the electrically inequivalent Li sites. The diffusive jump process of the ions is coded in terms of a change in  $\omega_q$ . Thus, the spin-alignment technique allows the measurement of a single-spin correlation function [15, 16]. The intensity of the spin-alignment echo is given by [15, 51]

$$S_2(t_p, t_m) = \frac{9}{20} \langle \sin[\omega_q(t_m = 0)t_p] \sin[\omega_q(t_m)t_p] \rangle. \quad (1)$$

Here,  $t_m$  denotes the mixing time and  $t_p$  the preparation time while  $\langle \dots \rangle$  means powder average. In order to obtain dynamic information of the jump process,  $S_2(t_p, t_m)$  is recorded for fixed  $t_p$  and variable  $t_m$ . The decay curve can be approximated with stretched exponential functions containing a decay rate  $\tau_{\text{SAE}}^{-1}$  which, in the ideal case, might be identified with the mean jump rate  $\tau^{-1}$  of the ion [18, 33, 38, 40]. In the case of three-dimensional diffusion,  $\tau^{-1}$  is related via the well-known Einstein–Smoluchowski equation with the self-diffusion coefficient  $D$  according to  $D = a^2/6\tau$ , see, e.g., [28, 52] for an introduction into solid-state diffusion phenomena.  $a$  is the (mean) jump distance which can be easily deduced from the crystallographic structure of the material [53]. Certainly, in analogy to  ${}^2\text{H}$  as well as  ${}^9\text{Be}$  SAE NMR, the technique is applicable if a non-selective excitation of the Li NMR spectrum is possible. For the two stable

Li isotopes,  ${}^6\text{Li}$  (spin-1) and  ${}^7\text{Li}$ , the quadrupole moments are small enough, resulting in quadrupole coupling constants in the kHz range so that this pre-requirement is perfectly fulfilled [33, 41].

Quite recently, we have investigated Li dynamics in a polycrystalline sample of  $\text{Li}_7\text{La}_3\text{Zr}_2\text{O}_{12}$ , crystallizing with tetragonal symmetry at room temperature, complementarily by diffusion-induced NMR spin–lattice relaxation and electrical impedance spectroscopy [54]. In good agreement with previous impedance spectroscopy results reported by Awaka *et al* [53], slightly above room temperature the Li jump rate amounts to approximately  $10^4 \text{ s}^{-1}$  pointing to an Li self-diffusion coefficient in the order of  $10^{-16} \text{ m}^2 \text{ s}^{-1}$ . Therefore, the material is suitable to be studied with Li-stimulated echo NMR which has proven to be a tool giving direct access to Li motions with rates smaller than  $10^5 \text{ s}^{-1}$  [16, 37, 40, 45, 55]. The upper and lower limits of SAE NMR are given by the spin–spin and spin–lattice relaxation NMR rates of the Li ion conductor under investigation [15].

## 2. Experimental details

${}^7\text{Li}$  NMR spin-alignment echoes (see figure 1) were recorded using an Avance III NMR spectrometer (Bruker BioSpin, Rheinstetten (Germany)) in connection with a shimmed cryomagnet (Bruker) operating at a fixed field of 7 T. The corresponding resonance frequency was 116 MHz. Additionally, some measurements were also carried out at 77 MHz using a Bruker MSL 100 spectrometer in combination with an unshimmed cryomagnet. NMR echoes were acquired with the Jeener–Broekaert pulse sequence [49] which is

$$\beta_{1\phi_1} - t_p - \beta_{2\phi_2} - t_m - \beta_{3\phi_3} - t_{\text{acq}}. \quad (2)$$

where  $\beta_1 = 90^\circ$  and  $\beta_2 = \beta_3 = 45^\circ$ .  $\phi_i$  denotes the phases of the rf pulses  $\beta_i$ . A suitable phase cycling with 32 entries ensures the elimination of unwanted coherences so that dipolar contributions to the echo are, as far as possible, suppressed. The  $90^\circ$  pulse length was  $2.4(1) \mu\text{s}$ . If not stated otherwise the preparation time  $t_p$  was chosen to be  $10 \mu\text{s}$  and the mixing time  $t_m$  was varied from  $10 \mu\text{s}$  to 10 s.  $t_{\text{acq}}$  denotes the acquisition time. The temperature in the sample chamber was controlled with an accuracy of  $\pm 0.5 \text{ K}$ .

The recycle delay  $t_d$  between each scan was chosen to be sufficiently long so that any influence on the echo amplitudes due to short repetition times can be excluded. For this purpose the temperature- and frequency-dependent  ${}^7\text{Li}$  NMR spin–lattice relaxation time  $T_1$  was measured independently by the use of the saturation recovery pulse sequence, see, e.g., [28, 56], before each SAE NMR experiment.  $T_1$  measurements were carried out at various temperatures ranging from 283 to 333 K with a commercial solid-state NMR probe (Bruker). Let us note that the corresponding NMR spin–lattice relaxation transients, which can be represented by a stretched exponential, reveal a two-component behaviour. The amplitude of the main component, which is characterized by the rate  $T_1^{-1}$ , is about 85%. In the  $T$  range covered here  $T_1$  is of the order of 10 s. The

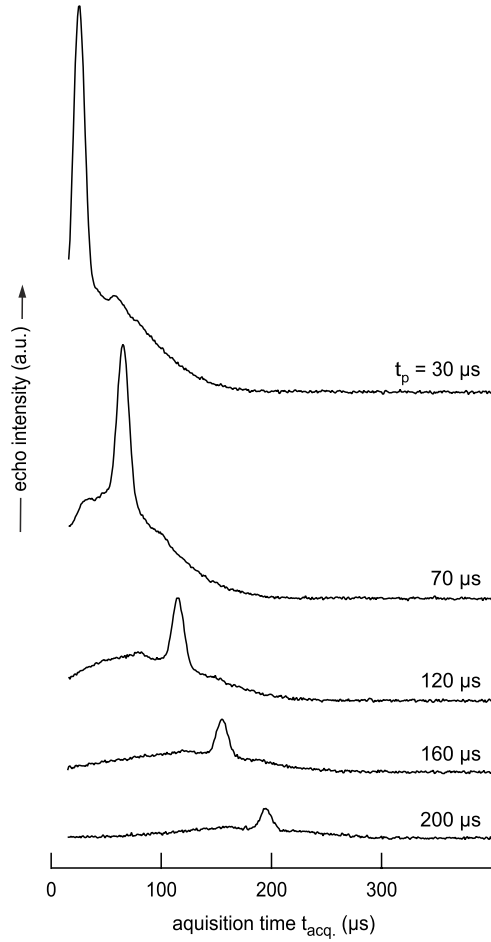


**Figure 1.**  ${}^7\text{Li}$  NMR spin-alignment echoes of tetragonal  $\text{Li}_7\text{La}_3\text{Zr}_2\text{O}_{12}$  recorded at 116 MHz and 294 K with the Jeener–Broekaert pulse sequence. The mixing time was chosen as short as possible to ensure that the echoes are not affected by Li motions. Each echo is composed of a sharply decaying quadrupole intensity and a broad dipolar echo.

second contribution does show up only at much larger delay times. It is characterized by an NMR spin–lattice relaxation time  $T_{1s}$ , which is of the order of a few hundreds seconds. As will be shown below, the relevant part of the SAE decay curves from which the Li diffusion parameters have been deduced is measured at mixing times  $t_m$  ranging from 10  $\mu\text{s}$  to 0.1 s. Thus, from a dynamic point of view the slowly relaxing component has a negligible effect on the echo amplitudes analysed.

The powder sample was fire-sealed in a quartz tube with a diameter of 4 mm and a length of 3 cm. The details of sample preparation and characterization can be found in [54]. X-ray powder diffraction (XRPD) measurements reveal the typical powder pattern of phase-pure  $\text{Li}_7\text{La}_3\text{Zr}_2\text{O}_{12}$  crystallizing with tetragonal symmetry. *In situ* XRPD shows that up to 353 K no phase transformation of the sample occurs. Note that at higher

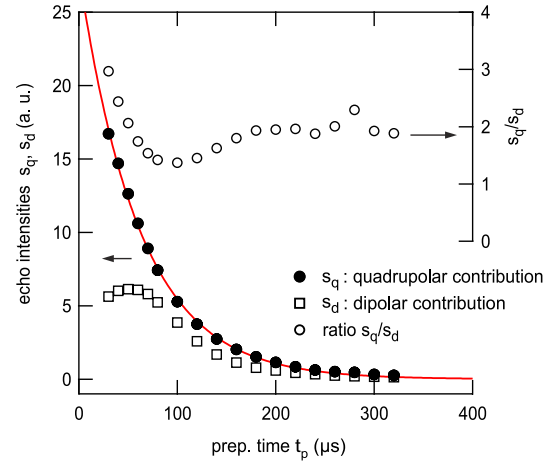


**Figure 2.** Echo intensities  $s_q$  and  $s_d$  versus preparation time, i.e. evolution of the two contributions to the  ${}^7\text{Li}$  spin-alignment echoes in figure 1 with increasing  $t_p$  which is the delay time between the first two pulses of the Jeener–Broekaert echo sequence. The solid line represents a fit using an exponential function  $s_q \propto \exp(-t_{\text{acq.}}/T_{2,q})$ . For comparison, the ratio  $s_q/s_d$  is also shown.

temperatures the space group reversibly changes towards cubic symmetry. However, as is shown in detail in [54], these slight structural changes have no impact on the Li diffusion parameters probed by impedance as well as NMR spin–lattice relaxation measurements.

### 3. Results

In figure 1 a set of typical  ${}^7\text{Li}$  SAE NMR echoes, which have been recorded at ambient temperature using preparation times ranging from 10 to 325  $\mu\text{s}$ , is shown. The recycle delay used was  $5T_1$ . The echoes are composed of two contributions. The sharp echo appearing at  $t_{\text{acq.}} = t_p$  refers to the spin-alignment (quadrupolar) echo whose intensity, when recorded as a function of  $t_m$ , leads to a single spin hopping correlation function (see below). It superimposes a broad echo most likely owing to strong  ${}^7\text{Li}$  homonuclear dipole–dipole interactions [30]. In the ideal case these interactions are completely absent, because for symmetry reasons this contribution should not show up in sin–sin quadrupolar spin-alignment echoes [15].

As expected, owing to transverse dephasing effects, the intensities of the two contributions,  $s_q$  and  $s_d$ , change individually with increasing preparation time (see figure 2). The transverse decay rate of the  ${}^7\text{Li}$  spin-alignment echo, referring to the quadrupolar information stored during  $t_p$ , turns out to be of the order of  $T_{2,q}^{-1} = 62(3) \mu\text{s}$  (see the solid line in figure 2 representing a fit according to a single exponential function). The broad echo representing the weaker dipolar contribution reaches its maximum intensity at  $t_p \approx 50 \mu\text{s}$ . At preparation times larger than  $t_p \approx 80 \mu\text{s}$  it starts to decay exponentially with a decay rate  $T_{2,d}^{-1} \approx 55 \mu\text{s}$

being very similar to  $T_{2,q}^{-1}$ . The ratio  $s_q/s_d$  tends to two at a sufficiently long preparation time. This is in agreement with the calculations presented by Tang and Wu [44]. They analysed the possibility to separate dipolar from quadrupolar contributions to the spin-alignment echo of spin-3/2 nuclei by proper choosing of the interpulse delay  $t_p$ .

Note that in the range  $10 \mu\text{s} < t_p < 300 \mu\text{s}$  the spin-alignment echo precisely appears at  $t' = t_p + t_a$  with  $t_a = 5.5 \mu\text{s}$  reflecting receiver dead time effects as well as the influence of the rf pulses with lengths of a few  $\mu\text{s}$ . This behaviour is in contrast to the broader dipolar echo showing up at  $t' < t_p$  when preparation times  $t_p > 50 \mu\text{s}$  are regarded. The corresponding shift  $t_a$  turns out to be larger and to depend slightly on  $t_p$ .

Fourier transformation starting from the top of the alignment echoes shown in figure 1 yields NMR spectra certainly being composed of two contributions (see figure 3). In a sample with various electrically inequivalent Li sites, which is the case here, the quadrupolar spin-alignment contribution is a superposition of distinct site-specific quadrupole powder patterns. At short  $t_p$  a substructure of the powder pattern can be recognized. From the outer wings a mean quadrupole coupling constant  $\delta_q$  is estimated to be approximately 108 kHz. Note that, due to phase errors, in some cases distorted spin-alignment spectra are obtained. Possible origins of undershoots near the central intensities are explicitly worked out and discussed in [57]. It is beyond the scope of the present paper to analyse the shape of the echoes in detail. Additional echoes and anti-echoes with low intensity and appearing at  $t = t_p \pm t_e$  might contribute to the total echo signal. In the following we will restrict the analysis on the mixing-time-dependent evolution of the intensity of the quadrupolar alignment echo showing up at  $t = t_p$ .

In general, damping of the stimulated echo as a function of mixing time but constant preparation time, that is, recording the curve  $S_2(t_m, t_p)$ , is caused by Li motional processes as well as NMR spin-lattice relaxation effects [15, 32]. Moreover, spin diffusion might influence the echo intensity  $S_2$ , particularly at sufficiently low temperatures where jump rates of the order of  $1 \text{ s}^{-1}$  are expected. Thus, the single-spin correlation function  $S_2'(t_m, t_p)$ , which in many cases can be parametrized with a stretched exponential  $S_2'(t_m, t_p) \propto \exp(-(t_m/\tau_{\text{SAE}})^\gamma)$  with  $0 < \gamma \leq 1$ , is additionally damped by the terms  $\exp(-(t_m/T_{1,q})^{\gamma_q})$  and  $\exp(-(t_m/T_{1,\text{sd}})^{\gamma_{\text{sd}}})$ , respectively. Here,  $T_{1,q}^{-1}$  denotes the quadrupolar spin-lattice relaxation rate (see [32]) and  $T_{1,\text{sd}}^{-1}$  the corresponding decay rate of spin diffusion which is temperature-independent. While the latter decay terms lead to  $S_2 \rightarrow 0$  for  $t_m \rightarrow \infty$ , the single-particle correlation function  $S_2'$ , containing the dynamic information of the diffusion process, generally shows a so-called final-state amplitude  $S_\infty$ . Thus, the complete decay curve  $S_2(t_m, t_p)$  can be written as

$$S_2(t_m, t_p) \propto S_2' \exp(-(t_m/T_{1,q})^{\gamma_q}) \exp(-(t_m/T_{1,\text{sd}})^{\gamma_{\text{sd}}}) \quad (3)$$

with

$$S_2'(t_m, t_p) = (A \exp(-(t_m/\tau_{\text{SAE}})^\gamma) + B) \quad (4)$$

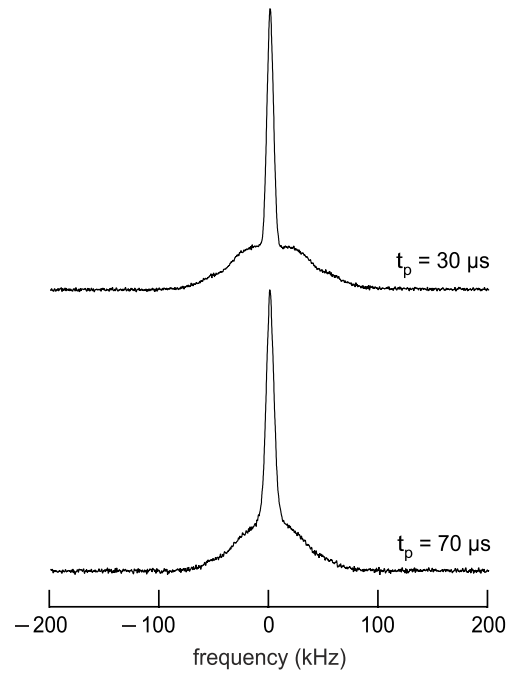


**Figure 3.**  ${}^7\text{Li}$  SAE NMR spectra obtained by Fourier transformation of the echoes shown in figure 1. The spectra are composed of a spin-alignment powder pattern and central intensities due to homonuclear dipole-dipole couplings.

and  $S_\infty = B/(A + B)$ . In the case of normalized curves, meaning the echo intensity ranges from 1 to 0,  $S_\infty = B$  because  $A = 1 - B$ . If  $S_\infty \neq 0$  usually a two-step decay behaviour is observed and the second decay step is characterized by an effective decay rate  $T_{1,\text{eff}}^{-1}$  replacing the product  $\exp(-(t_m/T_{1,q})^{\gamma_q}) \exp(-(t_m/T_{1,\text{sd}})^{\gamma_{\text{sd}}})$  by a single damping term  $\exp(-(t_m/T_{1,\text{eff}})^{\gamma_{\text{eff}}})$ .

In figure 4 normalized echo decay curves  $S_2$  are shown which have been recorded at  $t_p = 12 \mu\text{s}$  and a resonance frequency of 116 MHz. Solid lines show fits according to a stretched exponential function. The stretching exponent  $\gamma$  turns out to be difficult to determine at temperatures higher than 300 K because the decay curves are only partly accessible. This is due to the increase of the Li jump rate  $\tau^{-1}$  being responsible for the shift of the inflection points towards shorter mixing times. Satisfactory results are obtained at lower temperatures. As an example, at 273 K the decay rate  $\tau_{\text{SAE}}^{-1}(T)$ , which might be comparable with the Li jump rate, turned out to be approximately  $1.4 \times 10^3 \text{ s}^{-1}$  and the stretching exponent  $\gamma$  is 0.52(3).

The SAE NMR decay curves in figure 4 were recorded using a recycle delay  $t_d$  of  $5T_1$ . In that case the amplitude  $S_\infty$ , which slightly depends on temperature, is approximately 0.05 ( $300 \text{ K} < T < 333 \text{ K}$ ). Interestingly,  $S_\infty$  increases if  $t_d$  is increased to a few hundred seconds. As an example, in figure 5 an echo decay curve is shown which was recorded at 294 K and a delay time  $t_d = 400 \text{ s}$ . The curve clearly reflects

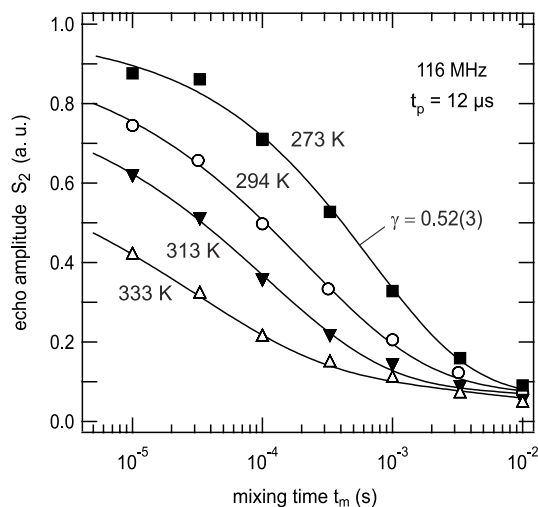


**Figure 4.** Two-time spin-alignment echo NMR correlation functions reflecting diffusive Li motions in the tetragonal garnet-like oxide  $\text{Li}_7\text{La}_3\text{Zr}_2\text{O}_{12}$ . Data points have been recorded at 116 MHz. The recycle delay  $t_d$  was  $5T_1$ . Solid lines show fits according to equation (4) which has been combined with an additional damping term  $\exp(-(t_m/T_{1,\text{eff}})^{\gamma_{\text{eff}}})$  taking into account the echo intensities at  $t_p > 10$  ms.

the two-step behaviour of the spin-alignment echo decay. For comparison, at  $t_d = 400$  s the corresponding effective rate characterizing the second decay step is of the order of  $1 \text{ s}^{-1}$ . It is worth mentioning that the first  $S_2$ -decay step, which proceeds on a much shorter timescale ( $t_m \ll 0.1$  s), is unaffected by the additional increase of  $t_d$ . Thus, for a reliable determination of  $\tau_{\text{SAE}}^{-1}$  the condition  $t_d \approx 5T_1$  is absolutely sufficient.

Usually the residual correlation  $S_\infty$  directly reflects the inverse number of Li sites equivalently participating in the diffusion process. Certainly, this interpretation holds only if these Li sites are equally populated. Assuming that  $T_1$  is of the order of  $T_{1,q}$ , the residual amplitude  $S_\infty = 0.05$  obtained at  $t_d = 5T_1$  might be interpreted in such a way. However,  ${}^7\text{Li}$  dipole–dipole couplings generally lead to an additional decrease of  $S_\infty$  than expected from the crystallographic structure. However, the fact that  $S_\infty$  largely increases with increasing  $t_d$  might be interpreted differently. Presumably, the additional echo intensity originates from a separate spin ensemble characterized by a much slower diffusivity, see also [13, 35]. The same ensemble does also show up in the corresponding  ${}^7\text{Li}$  NMR spin–lattice relaxation transients (see figure 6) as already mentioned in section 2, see also [35] for a very similar observation in the case of the garnet  $\text{Li}_5\text{La}_3\text{Nb}_2\text{O}_{12}$ . The echo amplitude measured at  $t_m = 0.1$  s (cf figure 5) shows that approximately 15% of the Li ions present in the sample turn out to be much less mobile than those being responsible for the first SAE NMR decay step. This value is in good agreement with that obtained from a brief analysis of the NMR spin–lattice relaxation transients also recorded

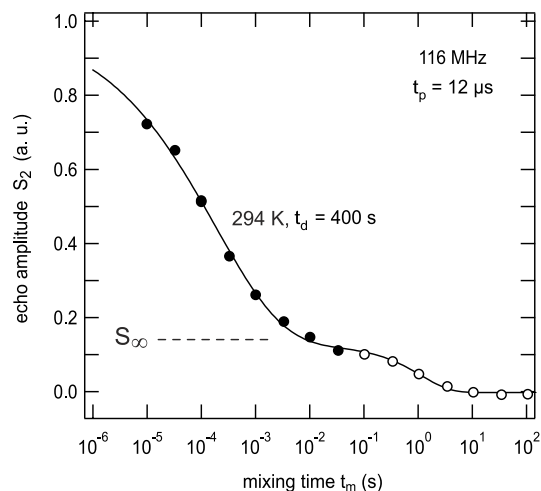


**Figure 5.**  ${}^7\text{Li}$  SAE NMR two-time correlation function (116 MHz) of tetragonal  $\text{Li}_7\text{La}_3\text{Zr}_2\text{O}_{12}$  which has been recorded at 294 K,  $t_p = 12 \mu\text{s}$  and a recycle delay of 400 s. The first decay step (filled symbols) reflects extremely slow Li motions in the garnet structure. A fit similar to those shown in figure 4 yields  $6.3 \times 10^3 \text{ s}^{-1}$ . See text for further details.

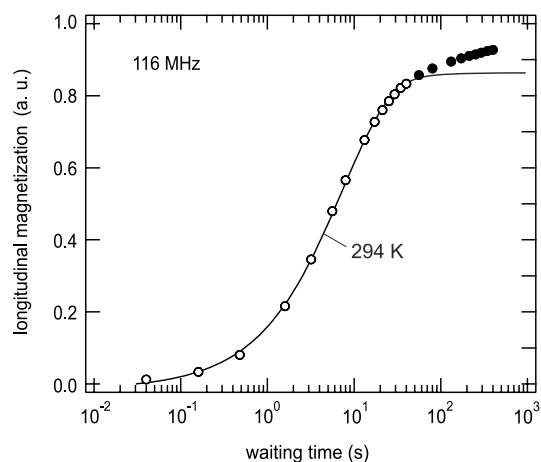


**Figure 6.**  ${}^7\text{Li}$  spin–lattice relaxation NMR transient of a powder sample of  $\text{Li}_7\text{La}_3\text{Zr}_2\text{O}_{12}$  crystallizing with tetragonal symmetry. Data have been measured at 116 MHz and 294 K. The largest waiting time used in the saturation recovery experiment was 400 s. The solid line shows a fit to the main component of the transient (o) using a stretched exponential. The fit yields  $T_1 \approx 7.1$  s and a stretching factor of approximately 0.79. At larger delay times a second contribution shows up (●) which is characterized by a much larger spin–lattice relaxation time  $T_1$ . This component reflects extremely slow Li spins which presumably lead to the second decay step of the corresponding  $S_2$  curve shown in figure 5.

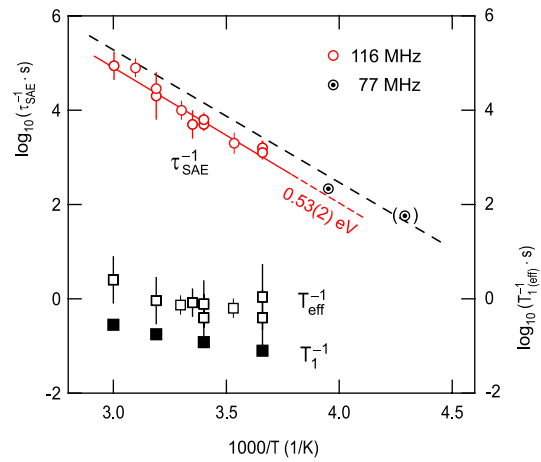
at  $t_d = 400$  s. It is worth noting that, in the present case, it cannot be excluded that the slower spin reservoir stems from a spatially separated second phase which is

*a priori* characterized by its individual  ${}^7\text{Li}$  NMR spin–lattice relaxation rates  $T_1^{-1}$  and  $T_{1,\text{eff}}^{-1}$ , respectively.

Judging from the x-ray powder diffraction pattern of the present sample, already presented in [54], such a minor phase, coexisting with the highly pure garnet one, ought to be x-ray amorphous to a great extent. Recent investigations on other garnet-type oxides have indeed revealed that the presence of a small amount of lithium carbonate cannot be excluded [58]. Its amount might be reduced by post-treatment of the sample with acids as well as by subsequent thermal treatment. It might also be expected that it affects Li transport across grain boundaries. These turned out to block through-going Li transport as compared to long-range transport taking place solely in the bulk of  $\text{Li}_7\text{La}_3\text{Zr}_2\text{O}_{12}$  [54]. Along with these considerations one might think about (re-)interpreting the  ${}^6\text{Li}$  MAS NMR spectra of the garnets, which have been presented in the literature so far, in an alternative way. In the present case, cf [54], the  ${}^6\text{Li}$  MAS NMR spectrum reveals two well-separated spectral components: a fast relaxing main signal appears at a chemical shift of 1 ppm and a slowly relaxing minor intensity shows up at 0 ppm. The latter does only emerge at an extraordinarily large recycle delay time. Thus, when compared with that of the main signal, it is characterized by a very large  ${}^6\text{Li}$  NMR spin–lattice relaxation time. This observation is in agreement with the two-component shape of the  ${}^7\text{Li}$  magnetization transient shown in figure 6. The difference in NMR spin–lattice relaxation rates of the two spectral components might be diagnostic for two magnetically decoupled spin reservoirs. Hence, this could also serve as an argument that the two spin ensembles are also spatially greatly divided. Certainly, further measurements are needed to answer the question whether the minor  ${}^6\text{Li}$  NMR signal, as well as the residual correlation measured here, simply reflects a small amount of a second Li-containing phase (for comparison, see also [59]) rather than much less mobile Li ions in the garnet. Recently, the latter, i.e. the presence of an Li sub-ensemble with very low diffusivity, has been reported on the basis of  ${}^6\text{Li}$  2D exchange NMR spectroscopy for similar garnet-like oxides [13, 24].

Irrespective of the nature of the two spin ensembles, from a dynamic point of view the two spin reservoirs are well separated. Hence, the dynamic parameters of the Li ions in phase-pure  $\text{Li}_7\text{La}_3\text{Zr}_2\text{O}_{12}$  can be studied very well. The first decay step of the measured  $S_2$  curves clearly reflects successful translational Li jumps between electrically inequivalent sites in the garnet structure. The corresponding decay rates  $\tau_{\text{SAE}}^{-1}$  are shown in the Arrhenius plot of figure 7. As an example, the rate deduced from the curve at 294 K is approximately  $6.3 \times 10^3 \text{ s}^{-1}$ . Using  $D = a^2/6\tau$  and  $a \approx 2 \text{ \AA}$ , which is a good approximation for the jump distance, a room-temperature Li self-diffusion coefficient  $D \approx 7 \times 10^{-17} \text{ m}^2 \text{ s}^{-1}$  is obtained.

The  ${}^7\text{Li}$  SAE NMR decay rates shown in figure 7 are in agreement with the Li jump rates estimated from impedance spectroscopy as well as diffusion-induced  ${}^7\text{Li}$  spin–lattice relaxation NMR measurements performed in the rotating frame of reference, see [54]. These rates are indicated in



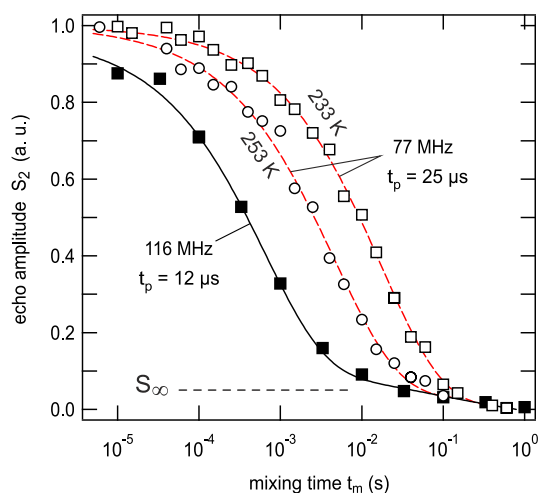
**Figure 7.** Arrhenius plot of the decay rates  $\tau_{\text{SAE}}^{-1}$  obtained from the  $S_2^*(t_m, t_p)$  curves (partly) shown in figures 4 and 5. The solid line is a fit according to  $\tau_{\text{SAE}}^{-1} \propto \exp(-E_a/(k_B T))$  yielding  $E_a \approx 0.53 \text{ eV}$ . For comparison, the rates  $T_1^{-1}$  and  $T_{1,\text{eff}}^{-1}$  are also shown. The dashed line indicates the temperature dependence of Li jump rates estimated from conductivity as well as temperature- and frequency-variable  ${}^7\text{Li}$  NMR spin–lattice relaxation rate measurements [54].

figure 7 by the dashed line. In general, the ionic conductivity  $\sigma$  is related via

$$\tau^{-1} = (H_R/f) \frac{2dk_B T}{Nq^2 a^2} \sigma. \quad (5)$$

with the hopping correlation rate  $\tau^{-1}$ . Equation (5) is a combination of the Einstein–Smoluchowski and the Nernst–Einstein equations, see, e.g., [52]. It takes into account that the self-diffusion coefficient  $D$  (see above) is related to the Nernst–Einstein diffusion coefficient  $D_\sigma$  via  $D = H_R/f D_\sigma$ . The small differences between the rates measured by SAE NMR here and by spin–lattice relaxation in [54] might be explained by the uncertainty of the product  $H_R f$ , which is anticipated to be of the order of unity.

The solid line in figure 7 represents a linear fit also taking into account an SAE NMR decay rate which has been recorded at a lower magnetic field and a slightly larger preparation time. The corresponding  $S_2$  curves are shown in figure 8. For comparison, the one recorded at 116 MHz and 273 K (see figure 7) is also shown. The decay curve recorded at 233 K yields a decay rate  $\tau_{\text{SAE}}^{-1}$  which is slightly larger than expected from the measurements carried out at higher  $T$  (see figure 7). This behaviour is even more pronounced when  $S_2$ -curves measured at 116 MHz are regarded. For the sake of brevity, these are not shown here. Therefore, we excluded data points below 260 K from the Arrhenius fit shown (solid line). Presumably, the correlation functions recorded at lower temperatures start to be increasingly affected by (temperature-independent) spin-diffusion effects. According to the method described by Vogel *et al* [35, 36] the SAE NMR data can be corrected for spin-diffusion effects, see also [42, 50]. Here, however, it turned out that the correction procedure



**Figure 8.** Low-temperature  ${}^7\text{Li}$  SAE NMR correlation functions of polycrystalline  $\text{Li}_7\text{La}_3\text{Zr}_2\text{O}_{12}$  recorded at 77 MHz and  $t_p = 25 \mu\text{s}$ . Echo intensities have been measured at 253 and 233 K. For comparison, the curve shown in figure 5 which has been recorded at 273 K and 116 MHz is also shown. The lines represent fits according to equation (4) which have been combined with an additional damping term, see caption of figure 5. Interestingly, the shape of  $S'_2(t_m, t_p)$ , that is the first decay step, turns out to depend only slightly on  $T$ . The corresponding stretching factor is approximately 0.54 at 253 K. See text for further explanation.

has no significant influence on the decay rates recorded above room temperature. The Arrhenius fit shown in figure 7 yields an activation energy of  $E_a = 0.53(2)$  eV. This value is in good agreement with that probed by impedance spectroscopy, quite recently [53, 54]. This similarity shows that stimulated echo NMR is able to probe long-range Li diffusion from an atomic-scale point of view, that is, taking advantage of the fluctuations of site-specific electric field gradients the mobile Li spins are exposed to. Similar observations have been made for other Li ion conductors studied by both impedance and stimulated echo NMR spectroscopy so far [31, 33, 40, 41, 60, 61].

At sufficiently low temperatures the complete  $S'_2$  decay is accessible. In particular, the curves recorded at 294 and 273 K (see figure 8) are of interest although the influence of spin-diffusion effects might play an increasing role. Starting from  $\gamma = 0.52(3)$  (see the  $S_2$  curve recorded at 273 K and 116 MHz, cf figure 8), the stretching exponent decreases to  $\gamma = 0.48(2)$  (294 K). For comparison, at lower temperatures (233 K) it turns out to be 0.57(2). Thus, most likely the underlying dynamic correlation function probed by  ${}^7\text{Li}$  stimulated echo NMR near ambient temperature is characterized by an exponent  $\gamma$  which is approximately 1/2. Interestingly, impedance as well as  ${}^7\text{Li}$  NMR spin-lattice relaxation measurements, see [54], also indicate a non-exponential hopping correlation function. The corresponding stretching factor deduced from impedance spectroscopy is very similar to the value deduced from SAE NMR. Together with the good agreement of the activation energies probed, this observation indicates that the methods, which *a priori*

probe Li dynamics in different ways, are sensitive to very similar motional correlation functions. Quite recently, the same similarity has also been observed for polycrystalline  $\text{Li}_2\text{C}_2$  complementarily investigated by both impedance as well as SAE NMR spectroscopy by Ruprecht *et al* [60].

#### 4. Conclusions

Alignment echoes of  ${}^7\text{Li}$  spins have been used to trace Li jump processes in the tetragonal modification of  $\text{Li}_7\text{La}_3\text{Zr}_2\text{O}_{12}$ . The method is sensitive to successful translational ionic motions on a relatively long timescale which might be compared with that of dc conductivity measurements. From the diffusion-controlled two-time correlation functions decay rates have been extracted which favourably agree with those probed by impedance spectroscopy and spin-lattice relaxation NMR techniques. Thus, the changes of the site-specific quadrupole frequencies due to diffusive motions of the Li spins result in an echo damping from which the associated jump rate can be deduced in a rather direct way. In the present case this enables the determination of the Li self-diffusion coefficient  $D$  at ambient temperature. The shape of the SAE NMR decay functions probed at room temperature indicates that the underlying motional correlation function can be represented by the term  $\exp(-(t'/\tau)^\gamma)$  with  $\gamma \approx 0.5$ . Finally, we discussed possible origins of a second spin reservoir characterized by much smaller motional correlation rates as reflected by NMR spin-lattice relaxation transients as well as NMR spin-alignment data.

In summary, the example studied here shows once more that spin-alignment echo NMR spectroscopy turns out to be a versatile tool for the investigation of Li jump processes in lithium ion conductors. The information gained from temperature-variable SAE NMR might be helpful to characterize new solid electrolytes urgently needed to develop powerful energy storage systems.

#### Acknowledgments

We thank the Deutsche Forschungsgemeinschaft (DFG) within the research unit 1277 (Mobility of Li ions in solids, projects WI-3600 4-1 and 2-1) as well as the Leibniz University Hannover (Wege in die Forschung II, Dynama) for financial support. AK gratefully acknowledges a grant of the Studienstiftung des Deutschen Volkes eV.

#### References

- [1] Kang K S, Meng Y S, Breger J, Grey C P and Ceder G 2006 *Science* **311** 977
- [2] Winter M and Besenhard J O 1999 *Electrochem. Acta* **45** 31
- [3] Whittingham M S 2004 *Chem. Rev.* **104** 4271
- [4] Poizot P, Laruelle S, Grugeon S, Dupont L and Tarascon J M 2000 *Nature* **407** 496
- [5] Tarascon J M and Armand M 2001 *Nature* **414** 359
- [6] Bruce P G, Scrosati B and Tarascon J-M 2008 *Angew. Chem. Int. Edn* **47** 2930
- [7] Kavan L, Kalbác M, Zúkalová M, Exnar I, Lorenzen V, Nesper R and Grätzel M 2004 *Chem. Mater.* **16** 477

- [8] Aricó A S, Bruce P, Scrosati B, Tarascon J -M and Van Schalkwijk W 2005 *Nature Mater.* **4** 366
- [9] Ramzy A and Thangadurai V 2010 *ACS Appl. Mater. Interfaces* **2** 385
- [10] Murugan R, Weppner W, Schmid-Beurmann P and Thangadurai V 2008 *Mater. Res. Bull.* **43** 2579
- [11] Thangadurai V and Weppner W 2005 *J. Power Sources* **142** 339
- [12] Cussen E J 2010 *J. Mater. Chem.* **20** 5167
- [13] O'Callaghan M P, Powell A S, Titman J, Chen G Z and Cussen E 2008 *Chem. Mater.* **20** 2360
- [14] Brinkmann D 1992 *Prog. Nucl. Magn. Reson. Spectrosc.* **24** 527
- [15] Böhmer R, Jeffrey K and Vogel M 2007 *Prog. Nucl. Magn. Reson. Spectrosc.* **50** 87
- [16] Böhmer R, Jörg T, Qi F and Titze A 2000 *Chem. Phys. Lett.* **316** 419
- [17] Epp V and Wilkening M 2010 *Phys. Rev. B* **82** 020301
- [18] Wilkening M and Heitjans P 2008 *Phys. Rev. B* **77** 024311
- [19] Kuhn A, Sreeraj P, Pöttgen R, Wiemhöfer H-D, Wilkening M and Heitjans P 2011 *J. Am. Chem. Soc.* **133** 11018
- [20] Xu Z and Stebbins J F 1995 *Science* **270** 1332
- [21] Cahill L S, Chapman R P, Britten J F and Goward G R 2006 *J. Phys. Chem. B* **110** 7171
- [22] Verhoeven V W J, de Scheper I M, Nachtegaal G, Kentgens A P M, Kelder E M and Mulder F M 2001 *Phys. Rev. Lett.* **86** 4314
- [23] Cabana J, Dupré N, Rousse G, Grey C P and Palacin M R 2005 *Solid State Ion.* **176** 2205
- [24] van Wüllen L, Echelmeyer T, Meyer H-W and Wilmer D 2007 *Phys. Chem. Chem. Phys.* **9** 3298
- [25] Bräunling D, Pecher O, Trots D M, Senyshyn A, Zherebtsov D A, Haarmann F and Niewa R 2010 *Z. Anorg. Allg. Chem.* **636** 936
- [26] Aatiq A, Ménétrier M, Croguennec L, Suard E and Delmas C 2002 *J. Mater. Chem.* **12** 2971
- [27] Wilkening M, Romanova E E, Nakhla S, Weber D, Lerch M and Heitjans P 2010 *J. Phys. Chem. C* **114** 19083
- [28] Heitjans P, Schirmer A and Indris S 2005 *Diffusion in Condensed Matter—Methods, Materials, Models* 2nd edn, ed P Heitjans and J Kärger (Berlin: Springer) chapter 9, pp 369–415
- [29] Qi F, Jörg T and Böhmer R 2002 *Solid State Nucl. Magn. Reson.* **22** 484
- [30] Qi F, Diezemann G, Böhm H, Lambert J and Böhmer R 2004 *J. Magn. Reson.* **169** 225
- [31] Qi F, Rier C, Böhmer R, Franke W and Heitjans P 2005 *Phys. Rev. B* **72** 104301
- [32] Böhmer R and Qi F 2007 *Solid State Nucl. Magn. Reson.* **31** 28
- [33] Faske S, Eckert H and Vogel M 2008 *Phys. Rev. B* **77** 104301
- [34] Brinkmann C, Faske S, Koch B and Vogel M 2010 *Z. Phys. Chem.* **224** 1535
- [35] Koch B and Vogel M 2008 *Solid State Nucl. Magn. Reson.* **34** 37
- [36] Faske S, Koch B, Murawski S, Kuechler R, Boehmer R, Melchior J and Vogel M 2011 *Phys. Rev. B* **84** 024202
- [37] Wilkening M, Kuechler W and Heitjans P 2006 *Phys. Rev. Lett.* **97** 065901
- [38] Wilkening M, Kuhn A and Heitjans P 2008 *Phys. Rev. B* **78** 054303
- [39] Wilkening M, Lyness C, Armstrong A R and Bruce P G 2009 *J. Phys. Chem. C* **113** 4741
- [40] Wilkening M, Mühle C, Jansen M and Heitjans P 2007 *J. Phys. Chem. B* **111** 8691
- [41] Wilkening M, Gebauer D and Heitjans P 2008 *J. Phys.: Condens. Matter* **20** 022201
- [42] Wilkening M, Lyness C, Armstrong A R and Bruce P G 2009 *J. Phys. Chem. C* **113** 4741
- [43] Tang X -P, Geyer U, Busch R, Johnson W L and Wu Y 1999 *Nature* **402** 160
- [44] Tang X -P and Wu Y 1998 *J. Magn. Reson.* **133** 155
- [45] Tang X -P, Busch R, Johnson W L and Wu Y 1998 *Phys. Rev. Lett.* **81** 5358
- [46] Davis L J M, Heinmaa I and Goward G R 2010 *Chem. Mater.* **22** 769
- [47] Cahill L S, Iriyama Y, Nazar L F and Goward G R 2010 *J. Mater. Chem.* **20** 4340
- [48] Carlier D, Ménétrier M and Delmas C 2001 *J. Mater. Chem.* **11** 594
- [49] Jeener J and Broekaert P 1967 *Phys. Rev.* **157** 232
- [50] Wilkening M, Heine J, Lyness C, Armstrong A R and Bruce P G 2009 *Phys. Rev. B* **80** 064302
- [51] Böhmer R 2000 *J. Magn. Reson.* **147** 78
- [52] Mehrer H 2006 *Diffusion in Solids* (Berlin: Springer)
- [53] Awaka J, Kijima N, Hayakawa H and Akimoto J 2009 *J. Solid State Chem.* **182** 2046
- [54] Kuhn A, Narayanan S, Spencer L, Goward G, Thangadurai V and Wilkening M 2011 *Phys. Rev. B* **83** 18 9849
- [55] Wilkening M and Heitjans P 2006 *J. Phys.: Condens. Matter* **18** 9849
- [56] Fukushima E and Roeder S B W 1981 *Experimental Pulse NMR* (Reading, MA: Addison-Wesley)
- [57] Böhmer R, Faske S and Geil B 2008 *Solid State Nucl. Magn. Reson.* **34** 32
- [58] Galven C, Fourquet J-L, Crosnier-Lopez M-P and Le Berre F 2011 *Chem. Mater.* **23** 1892
- [59] Boulant A, Bardeau J F, Jouanneaux A, Emery J, Buzare J Y and Bohnke O 2010 *Dalton Trans.* **39** 3968
- [60] Ruprecht B, Billetter H, Ruschewitz U and Wilkening M 2010 *J. Phys.: Condens. Matter* **22** 245901
- [61] Wilkening M, Amade R, Iwaniak W and Heitjans P 2006 *Phys. Chem. Chem. Phys.* **9** 1239

**3.3.2 Macroscopic and microscopic Li<sup>+</sup> transport parameters in cubic garnet-type “Li<sub>6.5</sub>La<sub>2.5</sub>Ba<sub>0.5</sub>ZrTaO<sub>12</sub>” as probed by impedance spectroscopy and NMR (pp. 74–82)**

Narayanan, S., Epp, V., Wilkening, M., and Thangadurai, V. *RSC Advances* **2**, 2553–2561 (2012).—This article is reproduced by permission of The Royal Society of Chemistry. The original article can be found online at <http://pubs.rsc.org/en/Content/ArticleLanding/2012/RA/c2ra01042a#divAbstract>. ©2012 The Royal Society of Chemistry.

## Macroscopic and microscopic Li<sup>+</sup> transport parameters in cubic garnet-type “Li<sub>6.5</sub>La<sub>2.5</sub>Ba<sub>0.5</sub>ZrTaO<sub>12</sub>” as probed by impedance spectroscopy and NMR

S. Narayanan,<sup>a</sup> V. Epp,<sup>b</sup> M. Wilkening<sup>b</sup> and V. Thangadurai<sup>\*a</sup>

Received 7th November 2011, Accepted 1st December 2011

DOI: 10.1039/c2ra01042a

The garnet-type “Li<sub>6.5</sub>La<sub>2.5</sub>Ba<sub>0.5</sub>ZrTaO<sub>12</sub>”, crystallizing with cubic symmetry was prepared according to a conventional solid state synthesis method using metal oxides and salt precursors of high purity. The formation of the “single-phase” garnet-type structure was studied by powder X-ray diffraction (PXRD). Electron microprobe analysis (EMPA) coupled with a wavelength-dispersive spectrometer (WDS) showed a rather homogeneous distribution of Ta ions and Zr ions compared to that of Ba ions and La ions in “Li<sub>6.5</sub>La<sub>2.5</sub>Ba<sub>0.5</sub>ZrTaO<sub>12</sub>”. Li ion dynamics were complementarily studied using variable-temperature AC-impedance spectroscopy and <sup>7</sup>Li NMR measurements. The bulk (ion) conductivities probed are in very good agreement with results reported earlier, illustrating the excellent reproducibility of the Li transport properties of “Li<sub>6.5</sub>La<sub>2.5</sub>Ba<sub>0.5</sub>ZrTaO<sub>12</sub>”. In particular, AC impedance and NMR results indicate that the Li transport process studied is of long-range nature. Finally, the chemical compatibility of the electrolyte “Li<sub>6.5</sub>La<sub>2.5</sub>Ba<sub>0.5</sub>ZrTaO<sub>12</sub>” was tested with Li<sub>2</sub>FeMn<sub>3</sub>O<sub>8</sub>, being a high-voltage cathode material. As shown by variable-temperature PXRD measurements, the garnet-type structure (bulk) was found to be stable up to 673 K.

### 1. Introduction

Rechargeable lithium-ion batteries are considered powerful energy storage systems.<sup>1–3</sup> Compared to lead–acid, Ni–Cd or Ni–metal-hydride batteries, for example, commercially available lithium-ion batteries are characterized by a much higher energy density of 650 Wh l<sup>−1</sup> and 150 Wh kg<sup>−1</sup>.<sup>1</sup> Therefore, lithium-ion cells are increasingly used in various portable electronic devices more and more in our daily life. In addition, secondary Li-ion batteries of larger scale are being developed for hybrid electric vehicles, combining an internal combustion engine.<sup>1,2</sup> Certainly, this is driven by the rapid depletion of fossil fuels and growing environmental concerns. The realisation of electric powered vehicles undoubtedly requires the development and investigation of new clean energy storage materials. These are needed to further improve the storage capacity, safety and rate (power) capability of lithium-ion batteries, the most promising energy storage systems in the medium run.

Currently, most conventional lithium-ion batteries utilize an organic polymer electrolyte in combination with a conducting salt such as LiPF<sub>6</sub>. However, these systems suffer from poor chemical as well as electrochemical stability resulting in manifold limitations for high power density applications. Accordingly, the fabrication of completely solid state lithium-ion batteries with

electrochemically stable electrolytes which have high ionic but negligible electronic conductivity appears to be the best solution to overcome the challenges that materials scientists are faced with.<sup>2–5</sup> For example, several solid Li electrolytes based on lithium phosphorous oxynitride (LIPON) ( $2.3 \times 10^{-6}$  S cm<sup>−1</sup>,  $E_a = 0.55 (\pm 0.02)$  eV), sodium superionic conducting (NASICON) phosphates (e.g., LiTi<sub>2</sub>P<sub>3</sub>O<sub>12</sub> ( $2 \times 10^{-6}$  S cm<sup>−1</sup>,  $E_a = 0.30$  eV at 300–470 K), A-site deficient perovskite-type oxides (e.g., (La<sub>(2/3)−x</sub>Li<sub>3x</sub>□<sub>(1/3)−2x</sub>TiO<sub>3</sub>) ( $10^{-3}$  S cm<sup>−1</sup> (bulk)  $E_a = 0.40$  eV) as well as silicates (e.g., Li<sub>4</sub>SiO<sub>4</sub>  $10^{-6}$  S cm<sup>−1</sup> at approximately 330 K,  $E_a = 0.83$  eV) have been investigated for this purpose.<sup>2–9</sup> The room temperature bulk ionic conductivity of most known solid electrolytes ranges from  $10^{-6}$  to  $10^{-3}$  S cm<sup>−1</sup>, while the total ionic conductivity, which is the sum of the bulk and grain-boundary conductivity, in many cases turns out to be a few orders of magnitude lower. Certainly, the values mentioned above depend somewhat on the synthesis methods used. However, in many cases even fast ion conductors offer several problems that limit their use in a lithium-ion battery. For example, the electrochemical instability of Ti-based materials such as La<sub>(2/3)−x</sub>Li<sub>3x</sub>□<sub>(1/3)−2x</sub>TiO<sub>3</sub> is a disadvantage when the material is intended to be used as a solid electrolyte.<sup>5,6,9,10</sup> Thus, new lithium conducting compounds are urgently needed to meet the requirements for completely solid state lithium-ion batteries fulfilling both a sufficient stability and high energy density. In particular, a thorough understanding of their Li<sup>+</sup> transport as well as diffusion properties is expected to be of help for further advancements in clean energy storage research.

Recently, garnet-type<sup>10</sup> oxides with the nominal chemical compositions Li<sub>3</sub>La<sub>3</sub>M<sub>2</sub>O<sub>12</sub> (M = Nb, Ta, Sb), Li<sub>6</sub>La<sub>2</sub>AM<sub>2</sub>O<sub>12</sub> (A = earth alkaline) and Li<sub>7</sub>La<sub>3</sub>Zr<sub>2</sub>O<sub>12</sub> have been developed and

<sup>a</sup>University of Calgary, Department of Chemistry, Calgary, Alberta, T2N 1N4, Canada. E-mail: vthangad@ucalgary.ca;  
Fax: 1 403 210 9364; 1 403 289 9488; Tel: 1 403 210 8649

<sup>b</sup>Graz University of Technology, Institute for Chemistry and Technology of Materials, Stremayrgasse, 9, 8010 Graz, Austria

studied for this purpose. Until now, chemical compositions, crystal structures, and ionic conductivities of many Li-conducting garnets have been investigated in detail by several groups.<sup>10–22</sup> For example,  $\text{Li}_6\text{La}_2\text{BaTa}_2\text{O}_{12}$  is reported to show an electrochemical stability as high as  $6 \text{ V Li}^{-1}$ . Some of these garnets, such as the cubic polymorph of  $\text{Li}_7\text{La}_3\text{Zr}_2\text{O}_{12}$ , are characterized by an extraordinary high ionic (bulk) conductivity of approximately  $10^{-4} \text{ S cm}^{-1}$  at ambient temperature<sup>13,17a</sup> making its use in an all-solid state battery feasible. For comparison, the ionic conductivity of the tetragonal phase of  $\text{Li}_7\text{La}_3\text{Zr}_2\text{O}_{12}$  was found to be two orders of magnitude lower than that of the cubic modification.<sup>18</sup> However, less is known about the details of the conduction mechanisms of Li containing oxide garnets. Complementary impedance spectroscopy measurements and NMR studies might help understand the correlation between crystal structure and Li transport properties. Quite recently, we used variable-temperature NMR spin-lattice relaxation and conductivity measurements to investigate the Li ion dynamics of phase-pure  $\text{Li}_7\text{La}_3\text{Zr}_2\text{O}_{12}$  crystallizing with a tetragonal symmetry.<sup>21</sup> In the present contribution these investigations are extended to another garnet-like oxide, *viz*  $\text{Li}_{6.5}\text{La}_{2.5}\text{Ba}_{0.5}\text{ZrMO}_{12}$  ( $M = \text{Nb, Ta}$ ), whose bulk conductivity<sup>15</sup> is reported to be comparable with those of, *e.g.*, the cubic modification of  $\text{Li}_7\text{La}_3\text{Zr}_2\text{O}_{12}$  and  $\text{Li}_6\text{BaLa}_2\text{Ta}_2\text{O}_{12}$ . Even though the garnet  $\text{Li}_{6.5}\text{La}_{2.5}\text{Ba}_{0.5}\text{ZrMO}_{12}$  is well studied in terms of electrical conductivity, less information is available on Li transport parameters which were probed on different time scales. Here, a combination of several techniques such as variable-temperature  $^7\text{Li}$  NMR spectroscopy, low-temperature AC-impedance measurements as well as electron microprobe analyses are used to characterize structural and dynamic properties of a single-phase sample of polycrystalline “ $\text{Li}_{6.5}\text{La}_{2.5}\text{Ba}_{0.5}\text{ZrTaO}_{12}$ ”.

## 2. Experimental

The compound with the nominal chemical composition “ $\text{Li}_{6.5}\text{La}_{2.5}\text{Ba}_{0.5}\text{ZrTaO}_{12}$ ” was prepared by a conventional solid state synthesis method (ceramic method). The precursors used for the synthesis were  $\text{LiNO}_3$  (99%, Alfa Aesar)  $\text{La}_2\text{O}_3$  (99.99%, Alfa Aesar, pre-heated at 1073 K for 24 h),  $\text{Ba}(\text{NO}_3)_2$  (AR grade, BDH),  $\text{ZrO}_2$  (99%, Alfa Aesar) and  $\text{Nb}_2\text{O}_5$  (99.5%, Alfa Aesar).  $\text{LiNO}_3$  was added in 10 wt% excess to avoid the loss of lithium during the high temperature sintering process. Stoichiometric amounts of the precursors were ball-milled at 200 rpm for 12 h in 2-propanol (Pulverisette ball mill, Fritsch, Germany). Then the mixture was heated for 6 h at 973 K. The resultant powder was ball-milled again to ensure homogenous mixing and then pressed into pellets (Isostatic press, P. O. Weber, Germany). After that the pellets were covered with the mother powder and sintered for 6 h at 1373 K in a clean alumina crucible. The formation of the cubic phase was verified by powder X-ray diffraction (PXRD) using a Bruker D8 diffractometer (Cu-K $\alpha$ , 40 kV, 40 mA). Electron microprobe analysis (EMPA) (Electron Probe Microanalyser, JEOL JXA-8200) coupled with a wavelength-dispersive spectrometer (WDS) was used to characterize morphology and composition (elemental mapping) of the samples. EMPA was carried out under vacuum at an excitation voltage of 15 kV and a current of 11.51 nA. For the electrical conductivity measurements, which were performed in air atmosphere, a Solartron SI 1260 impedance (and gain-phase) analyzer was used (frequencies ranged from 0.01 Hz to 10 MHz).

Prior to the impedance measurements the pellets were cut into small discs using a diamond cutter (Buehler, Isomet 5000). Gold electrodes were pasted on both sides of the pellets and cured for 1 h at 873 K in air.

Variable-temperature  $^7\text{Li}$  nuclear magnetic resonance (NMR) spectra were recorded using an Avance III NMR spectrometer (Bruker BioSpin, Rheinstetten) in combination with a shimmed 7 T cryomagnet (Bruker). The resonance frequency was  $\omega_0/2\pi = 117 \text{ MHz}$ . NMR spectra were acquired with the help of a one-pulse sequence. The recycle delay between each scan was at least  $5 T_1$  where  $T_1$  is the spin-lattice relaxation time in the laboratory frame of reference. NMR  $T_1$  times were recorded with the saturation recovery pulse sequence: a comb of closely spaced  $90^\circ$  pulses destroys longitudinal magnetization and its recovery is probed as a function of delay time with a single detection pulse. A  $^6\text{Li}$  magic angle spinning (MAS) NMR spectrum was recorded at 88 MHz using an Avance 600 Bruker NMR spectrometer connected to a cryomagnet with a nominal field of 14.1 T. We used a standard 2.5 mm MAS NMR probe which was operated at a spinning speed of 30 kHz. Additionally, with the same equipment a  $^{27}\text{Al}$  MAS NMR spectrum was recorded which has been referenced to aqueous  $\text{Al}(\text{NO}_3)_3$ .

Finally, the chemical stability of “ $\text{Li}_{6.5}\text{La}_{2.5}\text{Ba}_{0.5}\text{ZrTaO}_{12}$ ” with respect to a high-voltage cathode material such as  $\text{Li}_2\text{FeMn}_3\text{O}_8$  was tested by heating a mixture of “ $\text{Li}_{6.5}\text{La}_{2.5}\text{Ba}_{0.5}\text{ZrTaO}_{12}$ ” and  $\text{Li}_2\text{FeMn}_3\text{O}_8$  (1 : 1 wt% ratio) at 473 K, 673 K and 873 K for 24 h. PXRD measurements were carried out directly after heat treatment.

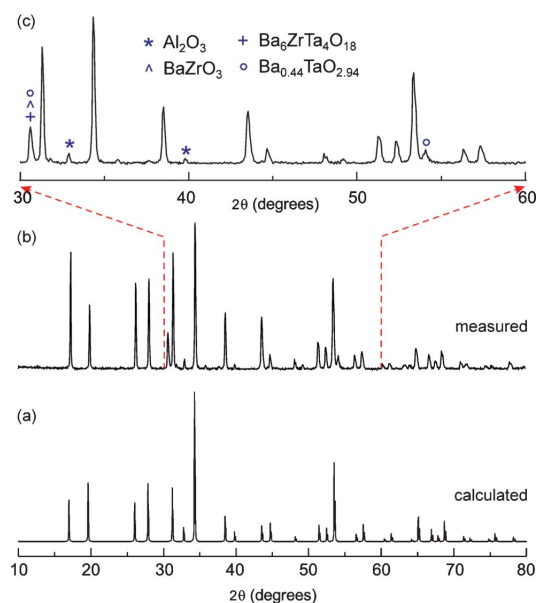


**Fig. 1** Powder X-ray diffraction pattern of (a) the calculated PXRD pattern of cubic  $\text{Li}_5\text{La}_3\text{Nb}_2\text{O}_{12}$  ( $a = 12.80654(11) \text{ \AA}$ ; space group  $Ia-3d$ ,<sup>23</sup> (b) “ $\text{Li}_{6.5}\text{La}_{2.5}\text{Ba}_{0.5}\text{ZrTaO}_{12}$ ” prepared by conventional solid-state synthesis and (c) selected range of the measured PXRD pattern showing the potential impurity phases present.

**Table 1** Indexed parameters obtained from the analyses of the PXRD pattern of “Li<sub>6.5</sub>La<sub>2.5</sub>Ba<sub>0.5</sub>ZrTaO<sub>12</sub>”

<i>h</i>	<i>k</i>	<i>l</i>	<i>d</i> <sub>obs.</sub> (Å)	<i>d</i> <sub>cal.</sub> (Å)	<i>I</i> <sub>obs.</sub> (%)
2	1	1	5.151	5.211	93
2	2	0	4.480	4.513	52
3	2	1	3.405	3.411	69
4	0	0	3.184	3.191	72
4	2	0	2.856	2.854	93
3	3	2	2.720	2.721	10
4	2	2	2.609	2.605	100
5	2	1	2.336	2.330	46
6	1	1	2.077	2.071	43
6	2	0	2.028	2.018	14
6	3	1	1.892	1.882	10
4	4	4	1.850	1.842	6
5	5	1	1.781	1.787	23
7	2	0	1.748	1.753	19
6	4	2	1.716	1.706	73
6	5	0	1.633	1.634	13
8	0	0	1.607	1.596	16
8	2	1	1.537	1.537	6
6	6	0	1.516	1.504	7
6	6	2	1.468	1.464	6
8	3	2	1.452	1.455	6
7	5	2	1.439	1.445	18
9	1	1	1.404	1.401	14
7	6	0	1.388	1.384	9
7	6	1	1.372	1.376	17
8	5	2	1.328	1.324	8
9	3	2	1.313	1.317	6
10	1	0	1.274	1.270	5
10	1	1	1.264	1.264	5
10	2	2	1.229	1.228	8

*a* = 12.764(3) Å

### 3. Results and discussion

#### 3.1 Structural characterization

The PXRD pattern of Fig. 1 clearly shows the formation of cubic “Li<sub>6.5</sub>La<sub>2.5</sub>Ba<sub>0.5</sub>ZrTaO<sub>12</sub>”. In Table 1 the corresponding indexed PXRD data are listed; most of the peaks could be indexed according to the cubic garnet-like parent Li<sub>3</sub>La<sub>3</sub>Nb<sub>2</sub>O<sub>12</sub> crystallizing with the space group *Ia-3d*.<sup>11–16,23</sup> The cell constant *a* is 12.764(3) Å which is comparable to the values reported in the literature.<sup>15</sup> However, there are some impurity peaks which could be attributed to Al<sub>2</sub>O<sub>3</sub>, Ba<sub>6</sub>ZrTa<sub>4</sub>O<sub>18</sub>, BaZrO<sub>3</sub>, and Ba<sub>0.44</sub>TaO<sub>2.94</sub>. They are marked in the selected area PXRD (see Fig. 1 (c)); the major diffractions peaks of these impurity phases are given in Table 2. As well as the separate phases, the incorporation of Al into the garnet structure, which has also been observed in the synthesis of garnet-type Li<sub>7</sub>La<sub>3</sub>Zr<sub>2</sub>O<sub>12</sub> quite recently,<sup>19</sup> is indicated by the <sup>27</sup>Al MAS NMR spectrum shown

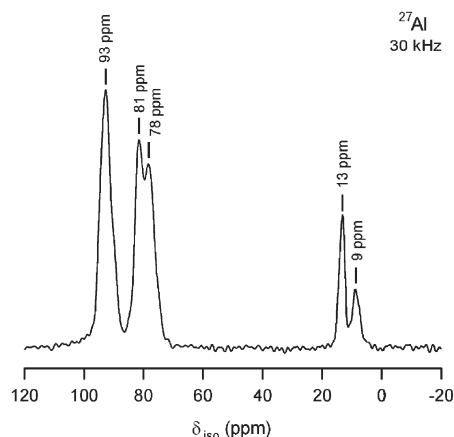


**Fig. 2** <sup>27</sup>Al MAS NMR spectrum (306 K) of “Li<sub>6.5</sub>La<sub>2.5</sub>Ba<sub>0.5</sub>ZrTaO<sub>12</sub>” prepared in an Al<sub>2</sub>O<sub>3</sub> crucible at 1373 K. The spectrum was recorded at 14.1 T using an MAS rotation frequency of 30 kHz.

in Fig. 2. The high-resolution NMR spectrum is composed of several lines at the isotropic chemical shifts ( $\delta_{\text{iso}}$ ) indicated. While the  $\delta_{\text{iso}}$  values at around 15 ppm point to octahedrally coordinated Al ions, chemical shifts larger than 70 ppm can usually be attributed to tetrahedrally coordinated Al. Besides, Al is present in the various separate impurity phases mentioned above, most likely Al cations also occupy multiple sites in the garnet-type structure. In particular, the NMR intensities with peaks at 78 and 81 ppm might reflect Al ions in tetrahedral sites. Additional deshielding (*cf.* the signal located at 93 ppm) might result from cation vacancies in the direct neighbourhood of the Al ions. It can also be an indication of Al ions residing in dodecahedral cages present in the garnet-type structure. For comparison with chemical shifts of known Al-containing oxides (and hydroxides), the NMR line of  $\alpha$ -Al<sub>2</sub>O<sub>3</sub> usually produces a single line with a chemical shift value in the range from 13 to 17 ppm, while the NMR lines of  $\theta$ -Al<sub>2</sub>O<sub>3</sub>, which has an equal number of octahedral and tetrahedral sites, are reported to be centered at 11(1) and 80(1) ppm.<sup>20</sup> Note that the NMR line of  $\gamma$ -AlOOH (boehmite), which transforms into  $\gamma$ -Al<sub>2</sub>O<sub>3</sub> (signals at 12 and 70 ppm) and  $\alpha$ -Al<sub>2</sub>O<sub>3</sub> at sufficiently high temperatures, usually shows up between 5 and 9 ppm.<sup>20</sup> Interestingly, NMR intensities located in the range from 75 to 85 ppm are also visible in the <sup>27</sup>Al NMR spectrum of Al-doped Li<sub>7</sub>La<sub>3</sub>Zr<sub>2</sub>O<sub>12</sub> discussed in detail by Geiger *et al.*<sup>19</sup>

**Table 2** List of possible impurity phases that can be observed in the powder XRD pattern of “Li<sub>6.5</sub>La<sub>2.5</sub>Ba<sub>0.5</sub>ZrTaO<sub>12</sub>”

Compound	Symmetry	Space group (No.)	JCPDS <sup>a</sup> Card No.	Characteristics Diffraction lines 2 $\theta$ /degrees	Intensity (%)	Symbol in Fig. 1
$\theta$ -Al <sub>2</sub> O <sub>3</sub>	Monoclinic	<i>C2m</i> (12)	01-086-1410	32.8	100	*
		<i>C2m</i> (12)	00-023-1009	39.8	62	*
		<i>A2m</i> (12)	00-009-0440			
Ba <sub>6</sub> ZrTa <sub>4</sub> O <sub>18</sub>	Rhombohedral	<i>R-3m</i> (166)	00-044-0563	30.6	100	+
BaZrO <sub>3</sub>	Cubic	<i>Pm-3m</i> (221)	01-089-2486	30.5	100	^
				43.6	54	^
Ba <sub>0.44</sub> TaO <sub>2.94</sub>	Hexagonal	<i>P-62m</i> (189)	00-017-0795	30.7	100	o
				54.1	67	o

<sup>a</sup> Joint Committee on Powder Diffraction Standards (JCPDS)

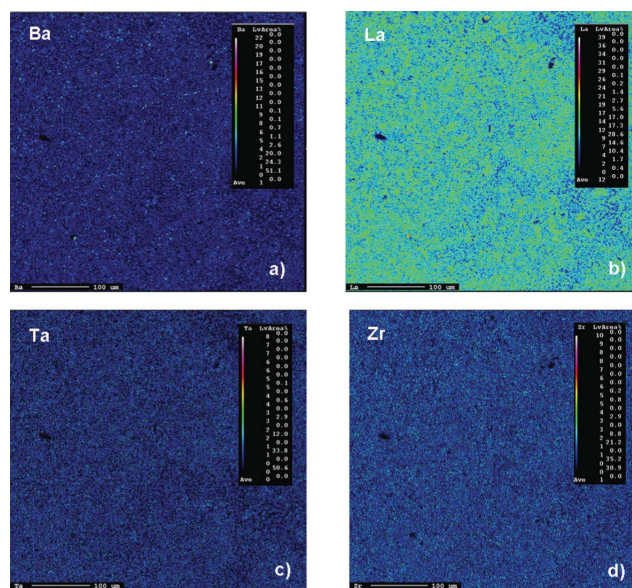


**Fig. 3** Typical elemental mapping analysis of polycrystalline “Li<sub>6.5</sub>La<sub>2.5</sub>Ba<sub>0.5</sub>ZrTaO<sub>12</sub>” prepared by conventional solid state synthesis: (a) Ba, (b) La, (c) Ta and (d) Zr mapping.

Elemental mapping of a large area (in the order of several hundred of micrometre squares) of garnet-type “Li<sub>6.5</sub>La<sub>2.5</sub>Ba<sub>0.5</sub>ZrTaO<sub>12</sub>” prepared at 1373 K is shown in Fig. 3. Let us note that the potential loss of Li during preparation was compensated by adding about 10 wt% excess of LiNO<sub>3</sub>. This is a common procedure to prepare Li-containing garnets *via* solid-state (ceramic) synthesis routes.<sup>10–16</sup> Irrespective of a slight contamination of the garnet phase with Al ions (Figures 1 and 2), the electron microprobe analysis (EPMA) coupled with a wavelength-dispersive spectrometer (WDS) showed a rather homogeneous distribution of Ta ions and Zr ions compared to that of Ba ions and La ions in “Li<sub>6.5</sub>La<sub>2.5</sub>Ba<sub>0.5</sub>ZrTaO<sub>12</sub>”.

### 3.2 Impedance spectroscopy

In Fig. 4 some typical AC-impedance plots (complex plane plots, imaginary part  $-Z''$  of the complex impedance  $Z$  vs the real part  $Z'$ ) of “Li<sub>6.5</sub>La<sub>2.5</sub>Ba<sub>0.5</sub>ZrTaO<sub>12</sub>” are shown which were recorded at 230 K, 252 K and 257 K in air. Besides electrode polarization effects showing up as spikes in the low frequency range, the bulk response can be well separated from the grain-boundary contribution. The frequency dependent data was quantitatively analyzed with a suitable equivalent circuit using individual resistances and constant phase elements (CPEs) representing the electrical bulk, grain-boundary and electrode responses. (see the inset of Fig. 4 (c)). In Table 3 the resulting fitting parameters, which correspond to the solid lines in Fig. 4 (a) to (c), are listed. Among others, these include the bulk and grain-boundary resistances,  $R_b$  and  $R_{gb}$ . The complex impedance  $Z_{CPE}$  of a constant phase element can be simply expressed as:<sup>24</sup>

$$\hat{Z}_{CPE} = \frac{1}{Q(j\omega)^n} \quad (1)$$

where the angular frequency is given by  $\omega = 2\pi \times f$  ( $f$  denotes the technical frequency).  $j$  is equal to  $\sqrt{-1}$ ,  $n$  is an empirical parameter which can take any arbitrary value between 0 and 1.  $Q$  has the numerical value of the admittance  $1/|\hat{Z}|$  at  $\omega = 1 \text{ rad s}^{-1}$ . Accordingly, the capacitance which can be associated with the CPE was calculated using the expression:<sup>24</sup>

$$C = R \left( \frac{1-n}{n} \right) Q \left( \frac{1}{n} \right) \quad (2)$$

Here, the parameter  $n$  was found to be close to one, *i.e.*,  $C \approx Q$ . While the capacitance  $C$  for the high-frequency semicircle turned out to be in the order of  $10^{-11}$  F, the semicircle showing up at intermediate frequencies is characterized by a capacitance ranging from  $10^{-10}$  to  $10^{-9}$  F (see Table 3). These values are typical for capacitances which can be ascribed to bulk and grain-boundary contributions in ion conducting ceramic materials.<sup>25,26</sup> Let us mention that the quality of the fits performed, expressed by the parameter  $\chi^2$  (see Table 3), increases with increasing temperature. As expected, the bulk resistance decreases with increasing  $T$ , clearly indicating a thermally-activated electrical relaxation process.

For comparison, typical impedance spectra, which are obtained by plotting the real part  $\sigma$  of the complex conductivity vs  $\omega$ , are shown in Fig. 5 (a). Depending on temperature, in the range from  $10^3$  to  $10^6$  Hz the spectra reveal an almost frequency independent conductivity plateau. Polarization effects due to ion blocking electrodes show up when  $\omega$  is smaller than approximately  $10^2$  Hz and temperatures ranging from 297 K to 357 K are regarded (Fig. 5). At the highest frequencies the beginning of a dispersive AC-conductivity region can be seen.  $\sigma(\omega)$  seems to follow a power law behaviour according to,<sup>27–34</sup>

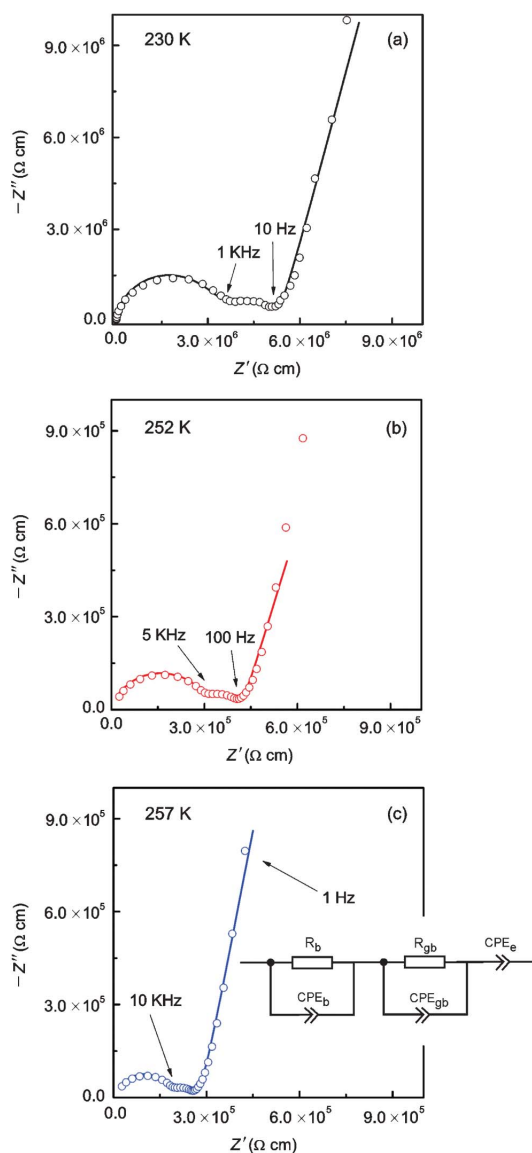


**Fig. 4** Typical AC-impedance plots of “Li<sub>6.5</sub>La<sub>2.5</sub>Ba<sub>0.5</sub>ZrTaO<sub>12</sub>” which were recorded at (a) 230 K, (b) 252 K, and (c) 257 K. Solid lines show fits using the equivalent circuit shown in (c). See text for further details. Bulk, grain boundary and electrode responses can be well separated.

$$\sigma(\omega) - \sigma(0) \propto \omega^p \quad (3)$$

**Table 3** Fitting results of the analysis of the AC-impedance data (Fig. 4 (a) to (c)) by using suitable equivalent circuit elements (see the inset of Fig. 4 (c))

T (K)	R <sub>b</sub> (Ω)	CPE <sub>b</sub> (F)	n <sub>b</sub>	C <sub>b</sub> (F)	R <sub>gb</sub> (Ω)	CPE <sub>gb</sub> (F)	n <sub>gb</sub>	C <sub>gb</sub> (F)	CPE <sub>el</sub> (F)	n <sub>el</sub>	χ <sup>2</sup>
230	8.95 × 10 <sup>5</sup>	4.62 × 10 <sup>-11</sup>	0.90	1.52 × 10 <sup>-11</sup>	6.04 × 10 <sup>5</sup>	1.83 × 10 <sup>-8</sup>	0.65	1.49 × 10 <sup>-9</sup>	5.28 × 10 <sup>-7</sup>	0.83	3 × 10 <sup>-3</sup>
252	8.64 × 10 <sup>4</sup>	2.81 × 10 <sup>-10</sup>	0.79	1.59 × 10 <sup>-11</sup>	3.18 × 10 <sup>4</sup>	4.50 × 10 <sup>-8</sup>	0.74	4.55 × 10 <sup>-9</sup>	9.30 × 10 <sup>-7</sup>	0.81	9 × 10 <sup>-4</sup>
257	3.56 × 10 <sup>4</sup>	7.91 × 10 <sup>-11</sup>	0.91	2.23 × 10 <sup>-11</sup>	4.68 × 10 <sup>4</sup>	4.29 × 10 <sup>-7</sup>	0.38	7.34 × 10 <sup>-10</sup>	8.83 × 10 <sup>-7</sup>	0.88	4 × 10 <sup>-4</sup>

where  $\sigma(0)$  denotes the so-called “DC-conductivity” and  $p$  the power law exponent which, in most cases, shows values between 0.6 and 0.8.<sup>27–34</sup> The corresponding complex plane plots are presented in Fig. 5 (b). Arrows mark the frequency range used for the power law fits which are shown in Fig. 5 (a) by solid lines. Fitting parameters are provided in Table 4. Since the dispersive region was only partly accessible due to experimental limitations, the power law exponents have to be regarded as rough estimations. Nevertheless, the values obtained are in agreement with results which can be found in the literature, particularly with those which have been reported for structurally disordered materials.<sup>32–34</sup> In the Arrhenius plot of Fig. 6 the  $\sigma(0)$  values are shown together with conductivity data which were taken from previous impedance studies. Above 330 K the DC-conductivities,  $\sigma(0)$ , obey an Arrhenius law characterized by an activation energy,  $E_a$ , of approximately 0.34 eV which is consistent with results reported in the literature for other garnet-type electrolytes. Below 300 K the activation energy increases which might indicate a change of the conduction mechanism.<sup>10–17</sup> For comparison, the garnets Li<sub>7</sub>La<sub>3</sub>Zr<sub>2</sub>O<sub>12</sub> (cubic modification), Li<sub>6</sub>BaLa<sub>2</sub>Ta<sub>2</sub>O<sub>12</sub>, Li<sub>6</sub>BaLa<sub>2</sub>Nb<sub>2</sub>O<sub>12</sub>, Li<sub>5.5</sub>La<sub>3</sub>Nb<sub>1.75</sub>In<sub>0.25</sub>O<sub>12</sub> and Li<sub>5</sub>La<sub>3</sub>Nb<sub>2</sub>O<sub>12</sub> show activation energies of 0.31, 0.40, 0.44, 0.51 and 0.43 eV, respectively.<sup>10,13,15,17</sup>

In order to estimate a macroscopic (solid-state) Li diffusion coefficient ( $D$ ), we have converted the  $\sigma(0)$  values according to the Nernst–Einstein relation:

$$\sigma(0) = \frac{q^2 N}{k_B T} \cdot D \quad (4)$$

Here,  $k_B$  is Boltzmann’s constant,  $q$  the elementary charge and  $N$  the number density of charge carriers which can be calculated according to  $N = n_c/V$ .  $n_c$  is the number of Li ions per unit cell and  $V$  the volume of the unit cell calculated from the PXRD analysis. Solid-state diffusion coefficients  $D$  range from 10<sup>-12</sup> to 10<sup>-10</sup> cm<sup>2</sup> s<sup>-1</sup> between 230 K and 280 K, and from 10<sup>-10</sup> to 10<sup>-7</sup> cm<sup>2</sup> s<sup>-1</sup> when temperatures between 320 K and 500 K are regarded. This is in good agreement with results recently reported in the literature.<sup>15</sup>

### 3.3 <sup>7</sup>Li NMR line shape measurements

For comparison with the conductivity results presented, we have recorded variable-temperature <sup>7</sup>Li MAS NMR line shapes to obtain first insights into the Li dynamics from a microscopic point of view. In general, at a sufficiently low temperature the line width of an NMR spectrum acquired under static, *i.e.*, non-rotating conditions, is dipolarly broadened due to the various Li–Li interactions present in a crystalline solid. With increasing temperature, these (homonuclear) dipole–dipole interactions are increasingly averaged due to the onset of (local) rapid Li hopping processes characterized by jump rates in the order of some kHz.

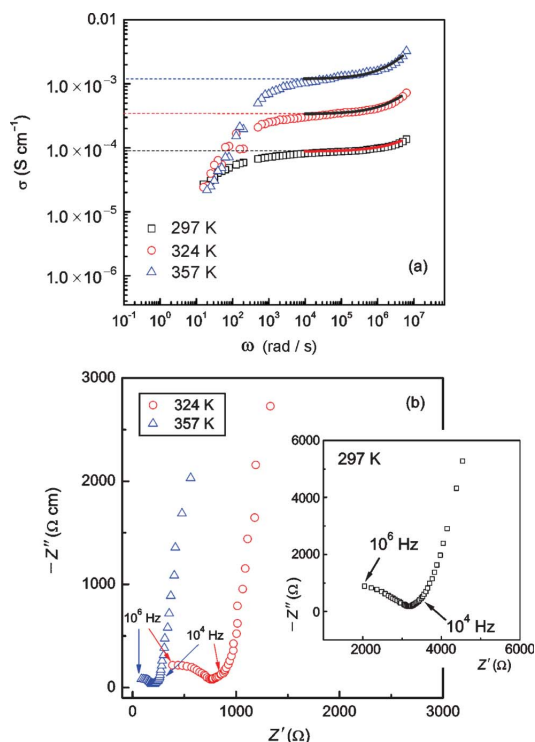


**Fig. 5** (a) Impedance spectra of “Li<sub>6.5</sub>La<sub>2.5</sub>Ba<sub>0.5</sub>ZrTaO<sub>12</sub>” measured at the temperatures indicated. Prior to the measurements the polycrystalline sample was sintered at 1373 K in air. Solid lines in (a) represent a rough analysis of the data using a power law expression (see eqn (3) and Table 3), (b) Corresponding impedance plots of the data shown in (a). The frequency range used for the power law fit is marked by arrows.

Plotting the line width  $\delta$  as a function of temperature  $T$ , a so-called motional narrowing (MN) curve is obtained; see also Ref. 35 for details, which can be used to roughly estimate Li diffusion parameters such as jump rates and activation energies. Starting from  $\delta = \delta_{rl}$ , which is the rigid-lattice line width,  $\delta$  continuously decreases. In the limit of extreme narrowing,  $\delta$  finally reaches  $\delta_{en}$  which is solely governed by the inhomogeneities of the external magnetic field used.

In agreement with the results from impedance spectroscopy (see above), in the case of “Li<sub>6.5</sub>La<sub>2.5</sub>Ba<sub>0.5</sub>ZrTaO<sub>12</sub>” motional

narrowing sets at extremely low temperatures. <sup>7</sup>Li NMR spectra, which were recorded at different temperatures, are shown in Fig. 7 and the corresponding motional narrowing curve is given in Fig. 8. For example, at  $T = 200$  K ( $\approx T_{\text{onset}}$ ) the line width (full width at half maximum) is already decreased from  $\delta_{rl} \approx 8$  kHz to  $\delta = 7$  kHz (see Fig. 8). At this temperature the mean Li jump rate  $1/\tau$  is expected to be in the order of  $10^3$  s<sup>-1</sup>. Using the well known Einstein–Smoluchowski equation:

$$D_{sd} = d_m^2/(6\tau) \quad (5)$$

this yields a self-diffusion coefficient of  $D_{sd} \approx 7 \times 10^{-14}$  cm<sup>2</sup> s<sup>-1</sup>. Here, a mean jump distance  $d_m = 2 \text{ \AA}$  was used to estimate  $D_{sd}$ . The obtained value is in good agreement with those probed by impedance spectroscopy when the  $D$  values plotted in Fig. 6 are extrapolated to lower temperatures.

At  $T = 243$  K the NMR line width is significantly narrowed, revealing a so-called two-component line shape (Fig. 7). In this intermediate temperature range the spectra are composed of a broad Gaussian superimposed by a motional narrowed Lorentzian shaped line. Such a heterogeneous line narrowing has already been observed for other crystalline garnets by Koch *et al.*<sup>36</sup> It points to a distribution of jump rates which are present at least in the range of extremely low temperatures ( $T < 300$  K). This might be the direct consequence of an irregularly shaped potential landscape the hopping ions are exposed to.

In the present case, almost the full motional narrowing curve could be detected (Fig. 8). Thus, the inflexion point of the curve can be accurately determined. Here,  $\delta$  reaches  $\delta_{rl}/2$  when  $T$  is increased to  $T = T_{\text{infl.}} = 230$  K. At this temperature the jump rate  $1/\tau$  can be approximated by  $1/\tau(T_{\text{infl.}}) = 2\pi \times \delta_{rl}$ . Using  $\delta_{rl} = 8$  kHz the corresponding self-diffusion coefficient,  $D_{sd}(T_{\text{infl.}}) = d^2 2\pi\delta_{rl}/6$ , is given by  $D_{sd}(230 \text{ K}) \approx 3.5 \times 10^{-12}$  cm<sup>2</sup> s<sup>-1</sup> confirming the fast ion conduction process presented in Fig. 6. Moreover, the expression introduced by Waugh and Fedin,  $E_{a,MN}/\text{eV} = 1.617 \times 10^{-3} \cdot T_{\text{onset}}/\text{K}$ , can be used to crudely estimate an activation energy from a  $\delta(T)$  curve. Inserting  $T_{\text{onset}} = 200$  K yields  $E_{a,MN} = 0.31$  eV. Almost the same value, *viz.* 0.29 eV, is obtained when the motional narrowing curve is analyzed according to the model of Hendrickson and Bray, see Ref. 21,37,38 for details. Interestingly, the activation energy roughly deduced from NMR line shape measurements is lower than that directly probed by DC-conductivity measurements in the same temperature range. However, it is worth noting that changes in NMR line widths measurements are sensitive to Li dynamics taking place on a shorter length-scale than DC-conductivity measurements. The later are sensitive to long-range Li transport.

**Table 4** DC-conductivity values of “Li<sub>6.5</sub>La<sub>2.5</sub>Ba<sub>0.5</sub>ZrTaO<sub>12</sub>” which were obtained from the frequency-independent plateaus (10<sup>4</sup> to 10<sup>6</sup> Hz) of the impedance spectra shown in Fig. 4 (a). For comparison, data from other ion conductors, partly showing very high ion conductivity, are also listed

solid electrolyte	$T$ (K)	$\sigma_0$ (S cm <sup>-1</sup> )	$p$	$E_a$ (eV)	reference
“Li <sub>6.5</sub> La <sub>2.5</sub> Ba <sub>0.5</sub> ZrTaO <sub>12</sub> ”	297	$9.0 \times 10^{-5}$	$\approx 0.67$	0.57(1) (220 to 290 K)	present work
	324	$3.2 \times 10^{-4}$	$\approx 0.76$	0.37(1) (330 to 500 K)	present work
	357	$1.2 \times 10^{-3}$	$\approx 0.82$	—	present work
Li <sub>4</sub> SiO <sub>4</sub>	396	$4.0 \times 10^{-8}$	0.68	0.83 (333 to 453 K)	32
Li <sub>0.18</sub> La <sub>0.61</sub> TiO <sub>3</sub>	303	$1.0 \times 10^{-4}$	0.60	0.41 (370 to 523 K)	33
Li <sub>7</sub> La <sub>3</sub> Zr <sub>2</sub> O <sub>12</sub> (tetragonal phase)	$\approx 300$	$1.2 \times 10^{-6}$	0.77 (< 135 K)	0.52 (350 to 400 K)	21
Li <sub>7</sub> La <sub>3</sub> Zr <sub>2</sub> O <sub>12</sub> (cubic phase)	$\approx 300$	$\approx 1 \times 10^{-4}$	—	0.32 (290 to 573 K)	17a

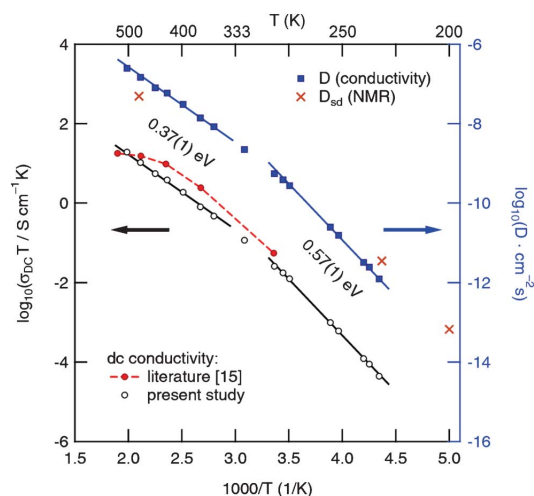


**Fig. 6** Temperature dependence of  $\sigma_{\text{DC}}T$  (as well as  $D$  calculated according to eqn (4)) for polycrystalline “ $\text{Li}_{6.5}\text{La}_{2.5}\text{Ba}_{0.5}\text{ZrTaO}_{12}$ ”. Solid lines represent fits using an Arrhenius law,  $\sigma_{\text{DC}}T \propto \exp(-E_a/k_B T)$ . For comparison, self-diffusion coefficients estimated from  $^7\text{Li}$  NMR spectroscopy are also included. See text for further details.

The rapid Li exchange process is also reflected by the  $^6\text{Li}$  MAS NMR spectrum shown in Fig. 7 (see inset) which was recorded with ambient bearing gas pressure and at a rotation frequency of 30 kHz. The spectrum is composed of a single NMR line whose line width (fwhm) amounts to no more than 20 Hz. Besides external spinning, an extremely fast Li exchange process, as probed by the static variable-temperature NMR line shape recorded, might additionally cause such a narrow NMR signal. Preliminary  $^7\text{Li}$  NMR spin-lattice relaxation measurements performed at  $\omega_0/2\pi = 117$  MHz indicate that the diffusion-induced rate peak  $1/T_1(1/T)$  shows up at approximately  $T = 480$  K. According to the condition  $\omega_0\tau \approx 1$ , which is valid at the temperature where the peak maximum shows up,<sup>21,39,40</sup> at  $T \approx 480$  K the Li jump rate is expected to be in the order of  $7.3 \times 10^8 \text{ s}^{-1}$  which corresponds to  $D_{\text{sd}} \approx 4.9 \times 10^{-8} \text{ cm}^2 \text{ s}^{-1}$  (Fig. 6).

### 3.4 Compatibility with electrode materials

Finally, the compatibility and chemical stability of “ $\text{Li}_{6.5}\text{La}_{2.5}\text{Ba}_{0.5}\text{ZrTaO}_{12}$ ” against the high-voltage cathode material  $\text{Li}_2\text{FeMn}_3\text{O}_8$  was studied by heating a mixture of the two compounds at elevated temperatures. Interestingly, despite of the high Li diffusivity probed, cubic “ $\text{Li}_{6.5}\text{La}_{2.5}\text{Ba}_{0.5}\text{ZrTaO}_{12}$ ” turns out to be stable up to 673 K (Fig. 9) while at 873 K the garnet seems to react with the cathode material. The corresponding PXRD pattern is solely governed by the peaks of the spinel  $\text{Li}_2\text{FeMn}_3\text{O}_8$  (Fig. 8). The chemical stability of “ $\text{Li}_{6.5}\text{La}_{2.5}\text{Ba}_{0.5}\text{ZrTaO}_{12}$ ” in the presence of a commonly used cathode material such as  $\text{Li}_2\text{FeMn}_3\text{O}_8$  makes it a promising candidate for further battery application studies.

## 4. Conclusions

In summary, the garnet-type “ $\text{Li}_{6.5}\text{La}_{2.5}\text{Ba}_{0.5}\text{ZrTaO}_{12}$ ” represents a very promising oxide to be used as highly conducting

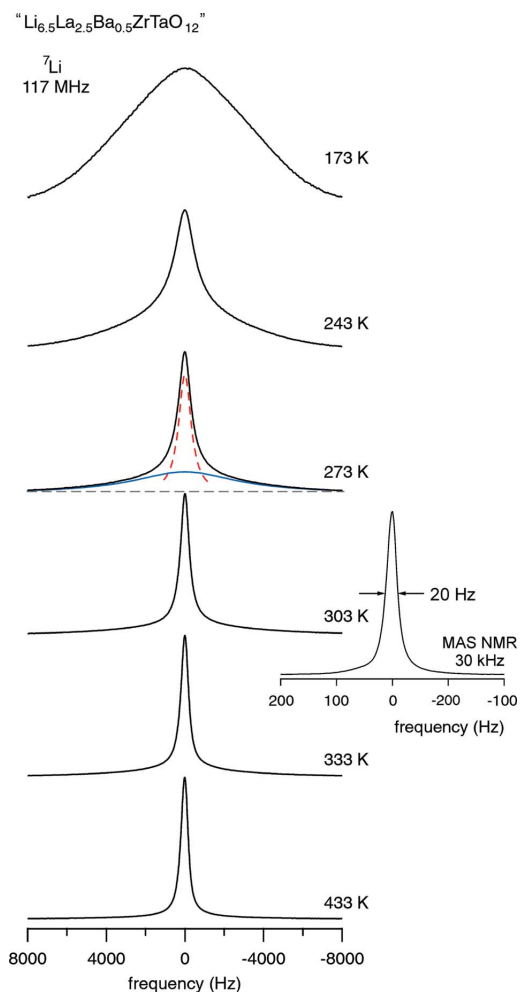


**Fig. 7**  $^7\text{Li}$  NMR spectra (117 MHz) of “ $\text{Li}_{6.5}\text{La}_{2.5}\text{Ba}_{0.5}\text{ZrTaO}_{12}$ ” recorded at the temperatures indicated. At intermediate  $T$  the spectra are composed of two components reflecting fast and slow Li ions in the garnet. As an example, the spectrum recorded at 273 K has been fitted with a sum of a narrow Lorentzian (dashed line) and a broad Gaussian (solid line). The number fraction of fast Li ions turns out to be approximately 50% at this temperature. Inset:  $^6\text{Li}$  MAS NMR spectrum recorded at a spinning speed of 30 kHz and ambient bearing gas.

electrolyte in future all solid state lithium-ion batteries. At room temperature (300 K), the Li conductivity  $\sigma_{\text{DC}}$ , characterizing long-range ion transport, is of the order of  $10^{-4} \text{ S cm}^{-1}$ . Rapid Li diffusivity was confirmed by  $^7\text{Li}$  NMR line shape measurements clearly revealing that motional narrowing of the line width sets in at temperatures as low as 220 K, *i.e.*, well below ambient temperature. Hence, NMR line shape measurements indicate that  $\sigma$  is solely governed by ionic conductivity. Despite of the high  $\text{Li}^+$  conductivity of garnet-type “ $\text{Li}_{6.5}\text{La}_{2.5}\text{Ba}_{0.5}\text{ZrTaO}_{12}$ ”, the oxide shows a remarkably good chemical stability when heated together with a cathode material such as  $\text{Li}_2\text{FeMn}_3\text{O}_8$ ,

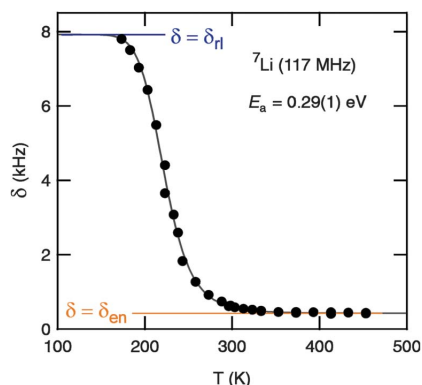


**Fig. 8** Motional narrowing of the  ${}^7\text{Li}$  NMR spectra (117 MHz) of “ $\text{Li}_{6.5}\text{La}_{2.5}\text{Ba}_{0.5}\text{ZrTaO}_{12}$ ”. The (overall) line width  $\delta$  (fwhm, full width at half maximum) is plotted as a function of temperature  $T$ . Starting from a  $\delta_{\text{H}}$  slightly larger than 8 kHz, the line width is reduced to  $\delta_{\text{en}} = 420$  Hz when  $T$  is higher than 300 K. The solid line shows a fit according to the model of Hendrickson and Bray<sup>36,37</sup> yielding an activation energy of 0.29(1) eV. See text for further details.

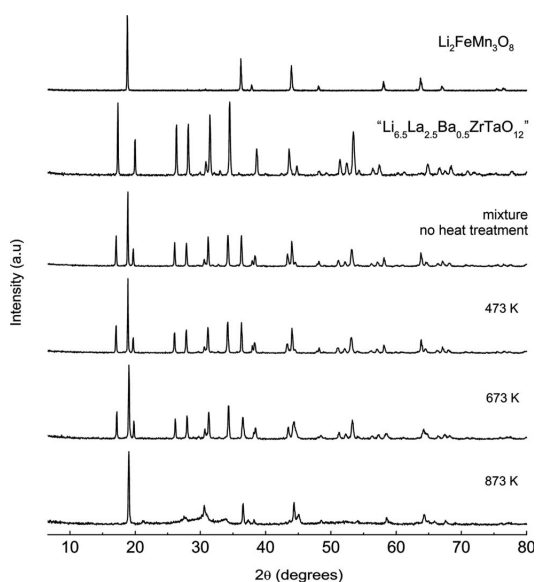


**Fig. 9** PXRD pattern of mixtures of “ $\text{Li}_{6.5}\text{La}_{2.5}\text{Ba}_{0.5}\text{ZrTaO}_{12}$ ” and  $\text{Li}_2\text{FeMn}_3\text{O}_8$  (1 : 1 wt% ratio) illustrating the chemical compatibility of the garnet-like oxide with a high-voltage cathode material. The mixtures have been heated at 473 K, 673 K and 873 K for 24 h in air.

making it a highly suitable candidate for applications in all-solid-state energy systems.

### Acknowledgements

One of us (V. T.) would like to thank the AUTO21 Network of Centres of Excellence, Canada’s national automotive research

and development program, and the Canada Foundation for Innovation (CFI) for their support. We also thank Robert Marr of the Department of Geoscience, University of Calgary for his help with EMPA and WDS measurements.

### References

- (a) B. Scrosati, J. Hassoun and Y.-K. Sun, *Energy Environ. Sci.*, 2011, **4**, 3287–3295; (b) C.-X. Zu and H. Li, *Energy Environ. Sci.*, 2011, **4**, 2614–2624; (c) V. Etacheri, R. Marom, R. Elazari, G. Salitra and D. Aurbach, *Energy Environ. Sci.*, 2011, **4**, 3243–3262; (d) J. M. Tarascon and M. Armand, *Nature*, 2001, **414**, 359–367.
- (a) J. B. Goodenough and Y. Kim, *Chem. Mater.*, 2010, **22**, 587–603; (b) X.-P. Gao and H.-X. Yang, *Energy Environ. Sci.*, 2010, **3**, 174–189.
- X. Xu, J. B. Bates, G. E. Jellison and F. X. Hart, *J. Electrochem. Soc.*, 1997, **144**, 524–532.
- H. Kawai and J. Kuwano, *J. Electrochem. Soc.*, 1994, **141**, L78–L79.
- A. D. Robertson, A. R. West and A. G. Ritchie, *Solid State Ionics*, 1997, **104**, 1–11.
- V. Thangadurai and W. Weppner, *Ionics*, 2006, **12**, 81–92.
- G. Adachi, N. Imanaka and H. Aono, *Adv. Mater.*, 1996, **8**, 127–135.
- P. Knauth, *Solid State Ionics*, 2009, **180**, 911–916.
- J. W. Fergus, *J. Power Sources*, 2010, **195**, 939–954.
- V. Thangadurai, H. Kaack and W. Weppner, *J. Am. Ceram. Soc.*, 2003, **86**, 437–440.
- J. Percival and P. R. Slater, *Solid State Commun.*, 2007, **142**, 355–357.
- E. J. Cussen, *J. Mater. Chem.*, 2010, **20**, 5167–5173.
- V. Thangadurai and W. Weppner, *Adv. Funct. Mater.*, 2005, **15**, 107–112.
- M. P. O’Callaghan and E. J. Cussen, *Chem. Commun.*, 2007, 2048–2050.
- (a) S. Narayanan and V. Thangadurai, *J. Power Sources*, 2011, **196**, 8080–8090; (b) A. Ramzy and V. Thangadurai, *Appl. Mater. Interfaces*, 2010, **2**, 385–390; (c) V. Thangadurai and W. Weppner, *J. Solid State Chem.*, 2006, **179**, 974–984.
- J. Percival, E. Kendrick and P. Slater, *Solid State Ionics*, 2008, **179**, 1666–1669.
- (a) R. Murugan, V. Thangadurai and W. Weppner, *Angew. Chem. Int. Ed.*, 2007, **46**, 7778–7781; (b) K. Kim, Y. Iriyama, K. Yamamoto, S. Kumazaki, T. Asaka, K. Tanabe, C. A. J. Fisher, T. Hirayama, R. Murugan and Z. Ogumi, *J. Power Sources*, 2011, **196**, 764–767; (c) M. Kotobuki, H. Munakata, K. Kanamura, Y. Sato and T. Yoshida, *J. Electrochem. Soc.*, 2010, **157**, A1076–A1079; (d) S. Ohta, T. Kobayashi and T. Asaoka, *J. Power Sources*, 2011, **196**, 3342–3345; (e) Y. Shimonishi, A. Toda, T. Zhang, A. Hirano, N. Imanishi, O. Yamamoto and Y. Takeda, *Solid State Ionics*, 2011, **183**, 48–53; (f) Y. Jin and P. J. McGinn, *J. Power Sources*, 2011, **196**, 8683–8687.
- J. Awaka, N. Kijima, H. Hayakawa and J. Akimoto, *J. Solid State Chem.*, 2009, **182**, 2046–2052.
- C. A. Geiger, E. Alekseev, B. Lazic, M. Fisch, T. Armbruster, R. Langner, M. Fechtelkord, N. Kim, T. Pettke and W. Weppner, *Inorg. Chem.*, 2011, **50**, 1089–1097.
- L. A. O’Dell, S. L. P. Savin, A. V. Chadwick and M. E. Smith, *Solid State Nucl. Magn. Res.*, 2007, **31**, 169–173.
- A. Kuhn, S. Narayanan, L. Spencer, G. Goward, V. Thangadurai and M. Wilkening, *Phys. Rev. B*, 2011, **83**, 094302.
- H. Xie, J. A. Alonso, Y. Li, M. T. Fernandez and J. B. Goodenough, *Chem. Mater.*, 2011, **23**, 3587–3589.
- E. J. Cussen, *Chem. Commun.*, 2006, 412–413.
- Q. Li and V. Thangadurai, *Fuel Cells*, 2009, **9**, 684–698.
- V. Thangadurai, R. A. Huggins and W. Weppner, *J. Power Sources*, 2002, **108**, 64–69.
- J. T. S. Irvine, D. C. Sinclair and A. R. West, *Adv. Mater.*, 1990, **2**, 132–137.
- A. K. Jonscher, *Dielectric Relaxation in Solids*, 1983, Chelsea Dielectric Press, London.
- A. K. Jonscher, *Nature*, 1977, **267**, 673–679.
- K. A. Mauritz, *Macromolecules*, 1989, **22**, 4483–4488.
- D. K. Pradhan, R. N. P. Choudhary and B. K. Samantaray, *Int. J. Electrochem. Sci.*, 2008, **3**, 597–608.
- M. A. Paris and J. Sanz, *Chem. Mater.*, 2000, **12**, 1694–1701.
- D. P. Almond, A. R. West and R. J. Grant, *Solid State Commun.*, 1982, **44**, 1277–1280.
- D. P. Almond, G. K. Duncan and A. R. West, *Solid State Ionics*, 1983, **8**, 159–164.

- 
- 34 I. M. Hodge, M. D. Ingram and A. R. West, *J. Amer. Ceram. Soc.*, 1976, **59**, 360–366.
- 35 M. Wilkening, V. Epp, A. Feldhoff and P. Heitjans, *J. Phys. Chem. C*, 2008, **112**, 9291–9300.
- 36 B. Koch and M. Vogel, *Solid State Nucl. Magn. Reson.*, 2008, **34**, 37–43.
- 37 J. Hendrickson and P. Bray, *J. Magn. Res.*, 1973, **9**, 341–357.
- 38 M. Wilkening, D. Bork, S. Indris and P. Heitjans, *Phys. Chem. Chem. Phys.*, 2002, **4**, 3246–3251.
- 39 V. Epp and M. Wilkening, *Phys. Rev. B*, 2010, **82**, 020301.
- 40 A. Kuhn, P. Sreeraj, R. Pöttgen, H.-D. Wiemhöfer, M. Wilkening and P. Heitjans, *J. Am. Chem. Soc.*, 2011, **133**, 11018–11021.

### 3.4 Layer-structured Li-ion conductors

#### 3.4.1 Fast Li diffusion in crystalline $\text{LiBH}_4$ due to reduced dimensionality: Frequency-dependent NMR spectroscopy (pp. 84–87)

Epp, V. and Wilkening, M. *Physical Review B* **82**, 20301 (2010).—This article is reproduced by permission of The American Physical Society. The original article can be found online at <http://journals.aps.org/prb/abstract/10.1103/PhysRevB.82.020301>. ©2010 The American Physical Society.

## Fast Li diffusion in crystalline $\text{LiBH}_4$ due to reduced dimensionality: Frequency-dependent NMR spectroscopy

V. Epp and M. Wilkening\*

*Institute of Physical Chemistry and Electrochemistry, Gottfried Wilhelm Leibniz University Hannover, Callinstr. 3a, D-30167 Hannover, Germany*

(Received 13 May 2010; published 16 July 2010)

The hexagonal and orthorhombic form of lithium borohydride,  $\text{LiBH}_4$ , are investigated by temperature and frequency-dependent nuclear magnetic resonance (NMR) spectroscopy. The local electronic structure and microscopic diffusion parameters are determined by recording both  $^6,7\text{Li}$  NMR spectra and spin-lattice relaxation (SLR) rates. The rates of the high-temperature flank of the SLR-NMR peaks of hexagonal  $\text{LiBH}_4$  clearly depend on resonance frequency which unequivocally reveals a low-dimensional diffusion process. Due to the very limited number of suitable model substances this makes lithium borohydride an extremely attractive material to study the effect of reduced dimensionality on Li dynamics. Most likely, the spatial confinement of Li hopping is also responsible for the very high ionic conductivity found for the hexagonal polymorph, recently.

DOI: [10.1103/PhysRevB.82.020301](https://doi.org/10.1103/PhysRevB.82.020301)

PACS number(s): 66.30.-h, 76.60.-k, 82.47.Aa

**Introduction.** The hexagonal modification of crystalline lithium borohydride,  $\text{LiBH}_4$ , belongs to one of the fastest Li ion conductors discovered<sup>1</sup> with promising application possibilities as electrolyte in all-solid-state rechargeable batteries.<sup>2-4</sup> Materials with high ionic conductivity are highly required for the development of so-called clean energy storage systems which are indispensable when the problem of global warming has to be addressed. In order to meet these challenges, materials science has to focus on the knowledge-based identification of new as well as on the target-oriented improvement of known ion conductors. Certainly, this includes the detailed, atomic-scale investigation of diffusion pathways giving information about the general rules leading to fast ion conduction in solids. In many studies<sup>5</sup> structural properties such as disorder and defects are discussed to be responsible for enhanced diffusivity. However, the influence of dimensionality is hardly considered to explain transport properties of solids, so far.

Although  $\text{LiBH}_4$  is a long-known reducing agent in organic synthesis and considered as an advantageous material for hydrogen storage, the high ionic conductivity of its hexagonal polymorph and modified forms has been found only recently.<sup>1,6,7</sup> Matsuo *et al.* suggested that Li diffusion is confined to two dimensions (2D) in  $\text{LiBH}_4$ .<sup>1</sup> This conclusion is based on a rough comparison of Li jump rates deduced from temperature-variable Li nuclear magnetic resonance (NMR) spin-lattice-relaxation (SLR) measurements with results from electrical impedance spectroscopy. However, such a comparison is fraught with a lot of difficulties since rigorous assumptions concerning correlation factors and the conversion of SLR-NMR rates ( $T_1^{-1}$ ) into reliable cation jump rates have to be made. Moreover, low-temperature SLR NMR and conductivity measurements probe diffusion and transport parameters, respectively, on quite different length scales. In general, the analysis of diffusion-controlled SLR-NMR rates as a function of the inverse temperature ( $1/T$ ), only, is by far not sufficient to unequivocally find out whether Li migration in  $\text{LiBH}_4$  is restricted to two dimensions or not. Instead, frequency-dependent SLR-NMR measurements have to be carried out for this purpose. To our

knowledge, only few such solid-state NMR studies exist so far<sup>8,9</sup> including an elegant  $^1\text{H}$  NMR study by McDowell *et al.*<sup>10</sup> on the metal hydride  $\text{ZrBe}_2\text{H}_{1.4}$ .

While NMR, when applied to both liquids and solids, offers a large set of techniques widely used to probe diffusion parameters on quite different time and length scales,<sup>11-14</sup> it is far less known that recording SLR-NMR rates as a function of resonance frequency  $\omega_0/2\pi$  can be employed in a unique way to determine the dimensionality of a given diffusion process from an atomic-scale point of view. Fortunately, randomly oriented powder samples are sufficient for such measurements since the method is solely based on the different spectral density functions  $J(\omega)$  controlling diffusion in one dimension, two dimensions, or three dimensions (3D).<sup>5</sup> In

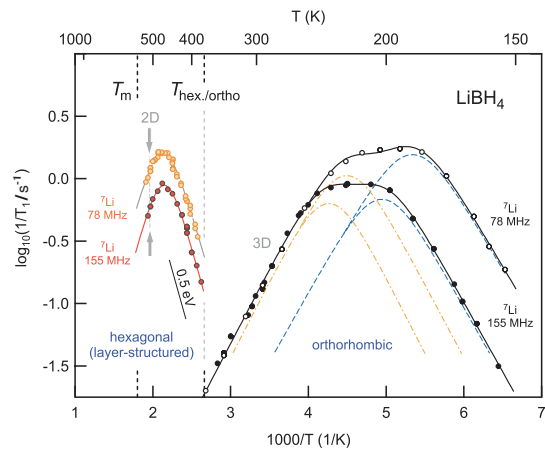


FIG. 1. (Color) Purely diffusion-induced  $^7\text{Li}$  SLR-NMR rates of hexagonal and orthorhombic  $\text{LiBH}_4$ . The rates were measured at the radio frequencies  $\omega_0/2\pi$  indicated. Solid lines in the  $T$  range of hexagonal  $\text{LiBH}_4$  are to guide the eye. Note the nonvanishing frequency dependence at temperatures above the peak maxima (see arrows) of hexagonal  $\text{LiBH}_4$  stable at  $T > T_{\text{hex./ortho}}$ . See text for further explanations.

the present Rapid Communication we will show that besides its application-oriented relevance, hexagonal  $\text{LiBH}_4$  turned out to be one of the very rare materials highly suitable to study the influence of dimensionality on purely diffusion-induced Li SLR-NMR rates. Without any doubt, the frequency dependence of the high-temperature SLR-NMR rates observed here, unequivocally points to a low-dimensional diffusion process in layer-structured  $\text{LiBH}_4$  which might also be the key to understand the very high ion conductivity observed, recently.

**Experiment.** The crystal structure of  $\text{LiBH}_4$  was studied by Soulié *et al.*<sup>15</sup> using synchrotron x-ray powder diffraction. Below  $T_{\text{hex./ortho}}=381$  K lithium borohydride shows orthorhombic symmetry (space group  $Pnma$ ). At temperatures higher than  $T_{\text{hex./ortho}}$  it undergoes a first-order phase transition and becomes hexagonal ( $P6_3mc$ ). The process is fully reversible.  $\text{LiBH}_4$  melts at about  $T_m=553$  K. Because of this we have restricted our NMR measurements to temperatures lower than 515 K.

Nominally pure  $\text{LiBH}_4$  (colorless crystallites with diameters in the micrometer range) was purchased from Alfa Aesar, strictly handled under inert-gas atmosphere and fire sealed in quartz tubes for the NMR measurements.  $^6\text{Li}$  and  $^7\text{Li}$  SLR-NMR rates were recorded using two Bruker spectrometers (MSL 100 and MSL 400) connected to Oxford cryomagnets of 4.9 T and 9.4 T (shimmed magnet), respectively. The saturation recovery pulse sequence<sup>5</sup> was used to measure the diffusion-induced recovery of the longitudinal magnetization  $M$  as a function of waiting time  $t$  after perturbing the equilibrium state,  $M(t)=M_0$ , with a comb of several closely spaced  $\pi/2$  radio-frequency pulses. The corresponding transients  $M(t)$ , which were measured at different temperatures, strictly follow single exponential time behavior  $M(t)=M_0[1-\exp(-t/T_1)]$ . NMR spectra were obtained by Fourier transformation of the free induction decays recorded after excitation the sample with a single radio-frequency pulse.

**Results and discussion.** Before analyzing the SLR-NMR data of hexagonal  $\text{LiBH}_4$  it is worth discussing a few details of  $T_1^{-1}=f(\omega_0, T)$  of its orthorhombic form where the  $^7\text{Li}$  NMR  $T_1^{-1}$  rates are indirectly controlled by rapid rotational motions of the  $\text{BH}_4$  tetrahedra rather than by fast translational Li jumps.<sup>16</sup> Temperature-variable  $^7\text{Li}$  SLR-NMR rates ( $T_1^{-1}$ ) of orthorhombic  $\text{LiBH}_4$ , which were recorded at two different frequencies  $\omega_0/2\pi$  (155 and 78 MHz), are shown in Fig. 1.

$T_1^{-1}(1/T)$  can be fitted with a sum (solid lines) of two rate peaks  $T_{1,i}^{-1}(\omega_0, T) \propto J_i^{3D}(\omega_0, T) \propto \tau_{c,i}/[1+(\omega_0\tau_{c,i})^2]$  ( $i=1, 2$ ), respectively. They incorporate exponential lattice correlation functions  $G_i(t)$ , i.e., Lorentzian-shaped spectral density functions  $J_i^{3D}(\omega_0)$  as assumed by Bloembergen, Purcell, and Pound (BPP) for 3D random jump diffusion.<sup>17</sup> Note that  $J(\omega)$  is the Fourier transform of  $G(t)$ . The fits  $T_{1,i}^{-1}(\omega_0, T)$  were restricted to a single term for a good approximation. The motional correlation time  $\tau_c$  is given by the Arrhenius relation  $\tau_{c,i} = \tau_{c0,i} \times \exp[E_{a,i}/(k_B T)]$  where  $\tau_{c0,i}$  represent the pre-exponential factors,  $E_{a,i}$  the activation energies, and  $k_B$  Boltzmann's constant, respectively. Dashed and dashed-dotted lines in Fig. 1 show the deconvolution of  $T_1^{-1}(1/T)$  into the rate peaks  $T_{1,1}^{-1}(\omega_0, T)$  and  $T_{1,2}^{-1}(\omega_0, T)$ , respectively,

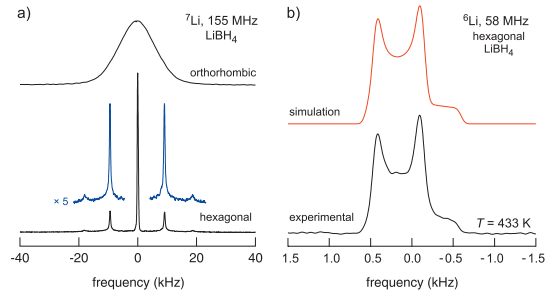


FIG. 2. (Color) (a)  $^7\text{Li}$  NMR spectra of orthorhombic (top) and hexagonal  $\text{LiBH}_4$  (bottom) recorded at  $\omega_0/2\pi=155$  MHz on a nonrotating sample. (b) Static  $^6\text{Li}$  NMR spectrum (referenced to a 1 M LiCl) of hexagonal  $\text{LiBH}_4$  (bottom) and its simulation using  $\delta_q(^6\text{Li})=770$  Hz and  $|\Delta\sigma|=3$  ppm, respectively. See text for further explanations.

depending on  $\omega_0/2\pi$  each. The activation energies turned out to be  $E_{a,1}=0.23(1)$  eV and  $E_{a,2}=0.21(1)$  eV. As expected for 3D diffusion the SLR-NMR rate is independent of frequency in the high- $T$  limit  $\omega_0\tau_c \ll 1$ . At low temperatures, i.e., in the limit  $\omega_0\tau_c \gg 1$ , a frequency dependence shows up. In this regime  $T_1^{-1}$  follows the BPP-type power law  $T_1^{-1} \propto \omega_0^{-2}$  for uncorrelated motion which is already implemented in the above-mentioned spectral density function.

As mentioned above, Li SLR-NMR rates reflect the dynamics of the  $\text{BH}_4$  units. The fact that Li diffusion is slow in orthorhombic  $\text{LiBH}_4$  can be easily verified when  $^7\text{Li}$  NMR line shapes are regarded (Fig. 2). In the orthorhombic phase the  $^7\text{Li}$  NMR spectrum recorded under static conditions is Gaussian shaped and the corresponding line width (full width at half height), which is approximately 16.5 kHz (see Fig. 2 of an NMR spectrum of the so-called rigid lattice regime which is in perfect agreement to those shown by Corey *et al.*<sup>18</sup>), does not change significantly from 155 K up to 380 K. We refer to Ref. 19 for  $^7\text{Li}$  magic angle spinning (MAS) NMR spectra which were used to extract information on local electronic structures in ortho- $\text{LiBH}_4$ . Therefore,  $\tau_c$  is expected to be larger than 1 ms in this  $T$  regime rather than on the order of 1 ns as can be estimated from the maxima positions of the  $T_{1,i}^{-1}(\omega_0, T)$  rate peaks where  $\omega_0\tau_{c,i} \approx 1$  holds. The two rate maxima observed can be attributed to two different rotational jump processes of the  $\text{BH}_4$  units which was rationalized by, e.g.,  $^{11}\text{B}$  and  $^1\text{H}$  SLR-NMR measurements, recently.<sup>16</sup>

However, the situation of extremely slow Li motions in the orthorhombic form changes dramatically when the structure of  $\text{LiBH}_4$  turns into the layered one with hexagonal symmetry. In Fig. 2 the  $^7\text{Li}$  NMR spectrum of layer-structured  $\text{LiBH}_4$  is compared with that of the orthorhombic form. Above 381 K very similar and fully motionally narrowed NMR spectra are obtained indicating very fast Li diffusion with a mean motional correlation time being much smaller than 0.1 ms. In Refs. 1 and 18 similar observations were made. As expected for a spin-3/2 nucleus such as  $^7\text{Li}$ , a well-defined quadrupole powder pattern shows up in this  $T$  range revealing distinct inner singularities and outer wings

from which the quadrupole coupling constant  $\delta_q(^7\text{Li})$  can be determined.  $\delta_q(^7\text{Li})$  turns out to be about 37.06(2) kHz which is in good agreement with results obtained when  $^7\text{Li}$  MAS NMR spectra are analyzed.<sup>19</sup>  $\delta_q(^7\text{Li})$  characterizes the strength of the electric interaction of the  $^7\text{Li}$  quadrupole moment  $q$  with the electric field gradient (EFG) produced by the electric charge distribution in the neighborhood of the Li site. The EFG is found to be almost axially symmetric here so that it can be deduced from the quadrupole singularities in a straightforward way<sup>20</sup> without invoking a simulation of the spectrum. In principle, this is also possible for the  $^6\text{Li}$  NMR spectrum recorded. However, due to the much smaller quadrupole moment of  $^6\text{Li}$  compared to  $^7\text{Li}$  the relative influence of chemical shift anisotropy  $\Delta\sigma$  on the line shape is much larger. Hence, we have simulated the spectrum shown in Fig. 2(b) to determine both  $\delta_q(^6\text{Li})$  and  $|\Delta\sigma|$  using the program WSOLIDS.<sup>21</sup> Once again the EFG turned out to be almost axially symmetric and  $\delta_q(^6\text{Li})$  and  $|\Delta\sigma|$  amount to be about 770 Hz and 3 ppm, respectively. Thus, the ratio  $\delta_q(^6\text{Li})/\delta_q(^7\text{Li})=q(^6\text{Li})/q(^7\text{Li})$  is about 0.02, which is in good agreement with a previously reported value obtained in the same way on an Li<sub>3</sub>N single crystal.<sup>22</sup>

The observed chemical-shift anisotropy as well as the fact that the quadrupole interactions are not averaged by rapid Li hopping on the hexagonal lattice point to a highly anisotropic Li diffusion process. Its low-dimensional nature can be unequivocally verified when the high-temperature flanks ( $\omega_0\tau_c \ll 1$ ) of the corresponding Li NMR  $T_1^{-1}(1/T)$  rate peaks recorded at different  $\omega_0/2\pi$  values are regarded (Figs. 1 and 3). In the high- $T$  limit a characteristic frequency dependence shows up which can only be interpreted in terms of Li diffusion taking place in confined dimensions. As mentioned above, in the case of 3D diffusion no such frequency dependence shows up in this limit. Note that the high- $T$  flank of a SLR-NMR rate peak is solely influenced by the dimensionality of the diffusion process. This is in contrast to the slope of the low- $T$  flank which can be additionally affected by correlation effects such as Coulomb interactions and/or structural disorder.<sup>5,23–25</sup> Usually this leads to a reduced slope in the limit  $\omega_0\tau_c \gg 1$  resulting in a subquadratic dependence  $T_1^{-1} \propto \omega_0^\beta$  with  $1 < \beta \leq 2$ .<sup>5</sup> Quite recently, Solonin *et al.* reported on  $^7\text{Li}$  NMR relaxation rates in the limit  $\omega_0\tau_c \ll 1$ ; however, they did not analyze their data with respect to dimensionality effects.<sup>26</sup>

Relaxation models developed for 2D diffusion of dipolarly coupled spins predict a logarithmic frequency dependence of  $T_1^{-1}$  on the high- $T$  side of the rate peak.<sup>27</sup> The spectral density function  $J^{2D}(\omega_0, \tau_c) \propto \tau_c \ln[1 + 1/(\omega_0\tau_c)^2]$  introduced by Richards combines the two limiting cases for low and high temperatures of a 2D system.<sup>28</sup> For uncorrelated 2D motion the rate peak is expected to be asymmetric in shape exhibiting a slightly reduced slope in the limit  $\omega_0\tau_c \ll 1$  compared to that of the low- $T$  side. In the case of  $^7\text{Li}$  SLR NMR this might be masked due to the larger homonuclear and heteronuclear couplings of the  $^7\text{Li}$  spins so that an almost symmetric rate peak is observed (see Fig. 1). Note that also in hexagonal LiBH<sub>4</sub> the BH<sub>4</sub> units are expected to perform fast rotational motions. Interestingly, the special characteristics of  $J^{2D}(\omega_0, \tau_c)$  can be observed in the case of  $^6\text{Li}$  subjected to much smaller coupling mechanisms. In the

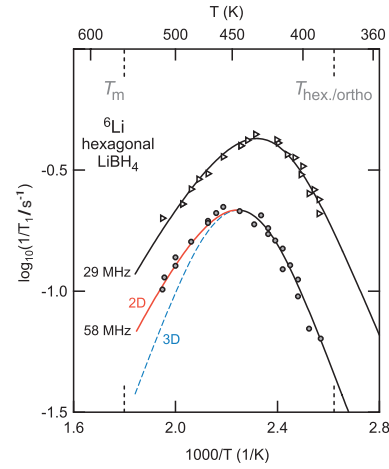


FIG. 3. (Color) Arrhenius representation of the  $^6\text{Li}$  SLR-NMR rates of hexagonal LiBH<sub>4</sub> recorded at  $\omega_0/2\pi=58$  MHz and 29 MHz, respectively. Solid lines represent fits according to a spectral density function  $J^{2D}(\omega_0, T)$  proposed for 2D diffusion (see text) revealing the characteristic asymmetry of the rate peaks  $T_1^{-1}(1/T)$ . The slope on the high- $T$  flank of the rate peaks is by about a factor of 3/4 smaller than that of the low- $T$  side. Symmetric rate peaks would be obtained in the case of 3D diffusion (indicated by the dashed line).

present study a sample with natural abundance (7.5%  $^6\text{Li}$ ) was investigated. Therefore, interfering interactions are additionally largely reduced due to the spatial separation of the  $^6\text{Li}$  spins (quasispin-1/2 nuclei). In contrast to  $^7\text{Li}$  NMR, the smaller frequencies of the  $^6\text{Li}$  SLR-NMR measurements allow the detection of larger ranges of the high- $T$  flanks of the rate peaks (see Fig. 3) which shift to lower  $T$  when  $\omega_0/2\pi$  is decreased. Solid lines in Fig. 3 show fits according to Richards' spectral density function  $J^{2D}(\omega_0, \tau_c)$  based on  $T_1^{-1}(\omega_0, \tau_c) \propto \tau_c \ln(1/\omega_0\tau_c)$  for  $\omega_0\tau_c \ll 1$  and a BPP-type frequency dependence  $T_1^{-1}(\omega_0, \tau_c) \propto \omega_0^{-2}\tau_c^{-1}$  for  $\omega_0\tau_c \gg 1$  (vide supra). It is worth mentioning that in the case of LiBH<sub>4</sub> the recorded SLR-NMR rates are purely induced by diffusion. Any nondiffusive background effects, see, e.g., Ref. 14, are completely absent, i.e., no correction procedures are necessary to obtain reliable Li  $T_1^{-1}$  rates. From the fits shown in Fig. 3 a pre-exponential factor  $\tau_{c0}$  on the order of  $10^{-15}$  s is obtained being in agreement with values typically found for phonon frequencies. The activation energy turns out to be  $E_a=0.54(2)$  eV and characterizes long-range Li diffusion in LiBH<sub>4</sub>. It is in good agreement with that deduced from electrical impedance spectroscopy (0.53 eV), recently.<sup>1</sup>

Let us note that the same values for  $E_a$  and  $\tau_{c0}$  are obtained when the four-parameter spectral density function is used which was proposed by MacDonald *et al.*<sup>29</sup> for like-spin magnetic dipolar interactions between spins undergoing 2D diffusion. In the temperature range covered here the corresponding fits are very similar to those shown in Fig. 3. Analyzing just the rates on the low- $T$  flank of the  $^6\text{Li}$  SLR-NMR rate peaks leads to  $E_a \approx 0.5$  eV as well. In the limit  $\omega_0\tau_c \gg 1$  the  $T_1^{-1}$  rates are sensitive to localized motions. This

indicates that no difference between short-range and long-range motions in  $\text{LiBH}_4$  can be observed by NMR. The same result has been found for layer-structured  $\text{Li}_x\text{TiS}_2$ , recently.<sup>11,14</sup>

A singular  $T_1^{-1}(1/T)$  rate peak recorded at one resonance frequency only, restricts the possibilities to extract information about the dimensionality of ion dynamics solely to the analysis of the shape of the peak. This necessarily requires highly precise measurements certainly carried out over a large temperature range in order to reveal the small differences between the two slopes on either sides of the maximum, see, e.g., Ref. 14. Even more, an exact model is needed being capable to predict  $T_1^{-1}(1/T)$  with respect to structural details of the material under investigation. Let us note that the observed asymmetry highlighted in Fig. 3 might not be observed if the low- $T$  side of the peak is influenced by correlation effects ( $\beta < 2$ ). In such cases symmetric rate peaks may show up masking the information about dimensionality effects in the limit  $\omega_0\tau_c \ll 1$ . Therefore, frequency-dependent SLR-NMR measurements are by far the best choice to confirm low-dimensional diffusion. The nonvanishing frequency dependence of the  $T_1^{-1}$  rates in the limit  $\omega_0\tau_c \ll 1$  (see Figs. 1 and 3) also shows up when SLR-NMR rates  $T_{1e}^{-1}(1/T)$  are recorded in the rotating frame of reference. Preliminary,  $T_{1e}^{-1}(1/T)$  NMR measurements have been performed at three locking frequencies  $\omega_1/2\pi$  ranging from 4.5 to 18 kHz. The data are consistent with a linear dependence of  $T_{1e}^{-1}(1/T)$  on  $\ln(1/\omega_1)$ .

*Conclusion and outlook.* Interestingly, layered-structured Li ion conductors such as  $\text{Li}_3\text{N}$ ,<sup>30,31</sup> Li containing  $\beta''$  alumina,<sup>32</sup>  $\text{Li}_x\text{CoO}_2$ ,<sup>33</sup>  $\text{Li}_x\text{MoO}_3$ ,<sup>34,35</sup> or  $\text{Li}_x\text{TiS}_2$ ,<sup>14</sup> for which (dominating) 2D diffusion is already proved or strongly anticipated, often exhibit a high Li diffusivity. Together with the results presented here one might recall the assumption that materials providing diffusion pathways with confined dimensions, i.e., where the mobile ions are guided by structural restrictions, are beneficial for fast diffusion of small cations such as  $\text{Li}^+$ . Of course, this might not hold for one-dimensional ionic motion which can be easily blocked by a small concentration of crystal imperfections or impurities. Let us note that Matsuo *et al.* successfully stabilized the hexagonal structure of  $\text{LiBH}_4$  down to 340 K by adding binary halides such as  $\text{LiI}$ ,<sup>6</sup> see also Ref. 19. Certainly, more investigations are needed in order to develop further rules being helpful in the design of new materials as well as in the controlled manipulation of their diffusion parameters.

We gratefully acknowledge P. Heitjans for many fruitful discussions and for access to the NMR equipment in Hannover. We thank A. Düvel and J. Heine for their technical help. Financial support by the Leibniz University Hannover (Wege in die Forschung II, Dynamia) as well as the Deutsche Forschungsgemeinschaft [research unit 1277 (molife), Grants No. WI 3600 2-1 and No. WI 3600 4-1] is highly acknowledged.

\*Author to whom correspondence should be addressed; wilkening@pci.uni-hannover.de; www.wilkening.pci.uni-hannover.de

<sup>1</sup>M. Matsuo, Y. Nakamori, S.-i. Orimo, H. Maekawa, and H. Takamura, *Appl. Phys. Lett.* **91**, 224103 (2007).

<sup>2</sup>J. M. Tarascon and M. Armand, *Nature (London)* **414**, 359 (2001).

<sup>3</sup>M. S. Whittingham, *Chem. Rev.* **104**, 4271 (2004).

<sup>4</sup>P. Novák, K. Müller, K. Santhanam, and O. Haas, *Chem. Rev.* **97**, 207 (1997).

<sup>5</sup>P. Heitjans, A. Schirmer, and S. Indris, in *Diffusion in Condensed Matter—Methods, Materials, Models*, 2nd ed., edited by P. Heitjans and J. Kärger (Springer, Berlin, 2005), Chap. 9, pp. 369–415.

<sup>6</sup>H. Maekawa *et al.*, *J. Am. Chem. Soc.* **131**, 894 (2009).

<sup>7</sup>M. Matsuo *et al.*, *J. Am. Chem. Soc.* **131**, 16389 (2009).

<sup>8</sup>W. Küchler, P. Heitjans, A. Payer, and R. Schöllhorn, *Solid State Ionics* **70-71**, 434 (1994).

<sup>9</sup>K. Metcalfe *et al.*, *Solid State Ionics* **26**, 209 (1988).

<sup>10</sup>A. F. McDowell, C. F. Mendelsohn, M. S. Conradi, R. C. Bowman, and A. J. Maeland, *Phys. Rev. B* **51**, 6336 (1995).

<sup>11</sup>M. Wilkening, W. Küchler, and P. Heitjans, *Phys. Rev. Lett.* **97**, 065901 (2006).

<sup>12</sup>M. Wilkening *et al.*, *Phys. Chem. Chem. Phys.* **9**, 6199 (2007).

<sup>13</sup>M. Wilkening, A. Kuhn, and P. Heitjans, *Phys. Rev. B* **78**, 054303 (2008).

<sup>14</sup>M. Wilkening and P. Heitjans, *Phys. Rev. B* **77**, 024311 (2008).

<sup>15</sup>J. Soulié, G. Renaudin, R. Černý, and K. Yvon, *J. Alloys Compd.* **346**, 200 (2002).

<sup>16</sup>A. V. Skripov, A. V. Soloninin, Y. Filinchuk, and D. Chernyshov,

*J. Phys. Chem. C* **112**, 18701 (2008).

<sup>17</sup>N. Bloembergen, E. M. Purcell, and R. V. Pound, *Phys. Rev.* **73**, 679 (1948).

<sup>18</sup>R. L. Corey *et al.*, *J. Phys. Chem. C* **112**, 18706 (2008).

<sup>19</sup>L. M. Arbjerg *et al.*, *Chem. Mater.* **21**, 5772 (2009).

<sup>20</sup>T. Bredow, P. Heitjans, and M. Wilkening, *Phys. Rev. B* **70**, 115111 (2004).

<sup>21</sup>K. Eichele, WSOLIDS 1 (2009), Solid-State NMR Spectrum Simulation, Version 1.19.15, University of Tübingen.

<sup>22</sup>M. Wilkening, D. Gebauer, and P. Heitjans, *J. Phys.: Condens. Matter* **20**, 022201 (2008).

<sup>23</sup>M. Meyer, P. Maass, and A. Bunde, *Phys. Rev. Lett.* **71**, 573 (1993).

<sup>24</sup>K. Funke, *Prog. Solid State Chem.* **22**, 111 (1993).

<sup>25</sup>K. L. Ngai, *Comments Solid State Phys.* **9**, 141 (1980).

<sup>26</sup>A. V. Soloninin, A. V. Skripov, A. L. Buzlukov, and A. P. Stepanov, *J. Solid State Chem.* **182**, 2357 (2009).

<sup>27</sup>A. Avogadro and M. Villa, *J. Chem. Phys.* **66**, 2359 (1977).

<sup>28</sup>P. M. Richards, *Solid State Commun.* **25**, 1019 (1978).

<sup>29</sup>D. H. MacDonald *et al.*, *J. Phys.: Condens. Matter* **10**, 417 (1998).

<sup>30</sup>D. Brinkmann, M. Mali, J. Roos, R. Messer, and H. Birli, *Phys. Rev. B* **26**, 4810 (1982).

<sup>31</sup>B. Bader *et al.*, *J. Phys.: Condens. Matter* **4**, 4779 (1992).

<sup>32</sup>G. C. Farrington and J. L. Briant, *Science* **204**, 1371 (1979).

<sup>33</sup>A. Van der Ven, G. Ceder, M. Asta, and P. D. Tepsch, *Phys. Rev. B* **64**, 184307 (2001).

<sup>34</sup>C. Julien and G. Nazri, *Solid State Ionics* **68**, 111 (1994).

<sup>35</sup>T. Brezesinski, J. Wang, S. H. Tolbert, and B. Dunn, *Nature Mater.* **9**, 146 (2010).

### 3.4.2 Two-dimensional diffusion in $\text{Li}_{0.7}\text{NbS}_2$ as directly probed by frequency-dependent $^7\text{Li}$ NMR (pp. 89–95)

Epp, V., Nakhal, S., Lerch, M., and Wilkening, M. *Journal of Physics: Condensed Matter* **25**, 195402 (2013).—This article is reproduced by permission of IOP Publishing Ltd. The original article can be found online at <http://iopscience.iop.org/0953-8984/25/19/195402/>. ©2013 IOP Publishing Ltd.

# Two-dimensional diffusion in $\text{Li}_{0.7}\text{NbS}_2$ as directly probed by frequency-dependent $^7\text{Li}$ NMR

V Epp<sup>1,3</sup>, S Nakhal<sup>2</sup>, M Lerch<sup>2</sup> and M Wilkening<sup>1,4</sup>

<sup>1</sup> Graz University of Technology, Institute for Chemistry and Technology of Materials, Stremayrgasse 9, A-8010 Graz, Austria

<sup>2</sup> Berlin University of Technology, Institute for Chemistry, Straße des 17. Juni 135, D-10623 Berlin, Germany

E-mail: [viktor.epp@tugraz.at](mailto:viktor.epp@tugraz.at) and [wilkening@tugraz.at](mailto:wilkening@tugraz.at)

Received 13 February 2013, in final form 27 March 2013

Published 19 April 2013

Online at [stacks.iop.org/JPhysCM/25/195402](http://stacks.iop.org/JPhysCM/25/195402)

## Abstract

Li ion diffusion in layer-structured  $\text{Li}_{0.7}\text{NbS}_2$  has been complementarily investigated by nuclear magnetic resonance (NMR) spectroscopy from an atomic scale point of view. In the present case,  $^7\text{Li}$  NMR spin–lattice relaxation (SLR) rates  $R_{1\rho}$  probed in the rotating frame of reference proved very informative in characterizing the Li self-diffusion process in the van der Waals gap between the  $\text{NbS}_2$  layers. While temperature-variable SLR $_{\rho}$  measurements were used to determine dynamic parameters such as jump rates ( $\tau^{-1}$ ) and the activation energy ( $E_a$ ), frequency-dependent measurements were used to specify the dimensionality of the diffusion process. In particular, the effect of annealing, i.e., the distribution of Li ions between the layers, on overall Li dynamics has been studied. When plotted in an Arrhenius diagram, the  $R_{1\rho}$  rates of an annealed sample, which were recorded at a locking frequency of 20 kHz, pass through a diffusion-induced relaxation peak whose maximum shows up at 320 K. Employing an appropriate diffusion model and appropriately accounting for a non-diffusive background relaxation, a Li jump rate  $\tau^{-1}$  (300 K)  $\approx 1.3 \times 10^5 \text{ s}^{-1}$  and an activation energy  $E_a$  of 0.43(2) eV can be deduced. Most importantly, in the high- $T$  limit of the diffusion-induced rate peak, i.e., when  $\omega_1 \tau \ll 1$  holds, the rates follow a logarithmic frequency dependence. This points to a diffusion process of low dimensionality and is in good agreement with predictions of relaxation models developed for 2D diffusion.

(Some figures may appear in colour only in the online journal)

## 1. Introduction

Layer-structured materials, into which small ions such as lithium can be reversibly inserted in a facile way, play a major role as electrode materials in current battery technology [1–3]. In particular, rechargeable batteries taking advantage of lithium ions as charge carriers are expected to serve as powerful electrochemical energy storage systems in the future [4–7]. However, experimental studies reporting on the

atomic scale investigation of lithium diffusion mechanisms are relatively rare [8–14].

Lithium nuclear magnetic resonance (NMR) spectroscopy has proved to be a very powerful tool for this purpose [9–11, 15–27]. By using time-domain NMR spin–lattice relaxation (SLR) measurements it is possible to gather information on both short-range as well as long-range translational ion dynamics [16, 18]. Furthermore, when carried out as a function of (angular) frequency,  $\omega_0$ , in a certain temperature limit, the diffusion-induced SLR NMR rate is also sensitive to the dimensionality of the diffusion process [28–31]. So far, only a few such experimental studies

<sup>3</sup> Author to whom any correspondence should be addressed.

<sup>4</sup> [www.lithium.tugraz.at](http://www.lithium.tugraz.at).

can be found in the literature, see, e.g., [14, 32–34]. An elegant and comprehensive example is that of McDowell *et al.*, who investigated 2D motion of hydrogen in  $\text{ZrBe}_2\text{H}_{1.4}$  [34].

Here, layer-structured  $\text{Li}_{0.7}\text{NbS}_2$  served as a lithium-containing model substance to enlighten in which way the spatially confined environment affects  $\text{Li}^+$  diffusion in the van der Waals gap of  $\text{NbS}_2$ . It turned out that such diffusion mechanisms are particularly well suited to be studied by frequency-dependent SLR NMR measurements carried out in the rotating frame [18, 35, 36]. Relaxation models developed for low-dimensional diffusion in solids predict a characteristic frequency dependence of the SLR rates  $R_{1(\rho)}$  probed in the high-temperature limit of the corresponding diffusion-induced relaxation peak  $R_{1(\rho)}(1/T)$  [16, 28, 37]. Notably, the spectral density function  $J^{2\text{D}}(\omega_0, \tau_c) \propto \tau_c \ln(1 + 1/(1 + \omega_0\tau_c)^\beta)$ , introduced by Richards [28, 29, 37] to approximate [31] 2D diffusion (see below), predicts a logarithmic frequency dependence  $R_1 \propto -\tau_c \ln(\omega_0\tau_c)$  in the limit  $\omega_0\tau_c \ll 1$ . Thus, it can be used to verify spatially confined, two-dimensional self-diffusion. Any inter-layer hopping processes present would sensitively influence this frequency dependence. Taken together, besides probing dynamic parameters such as jump rates ( $\tau^{-1} \approx \tau_c^{-1}$ ) and activation energies ( $E_a$ ), frequency-dependent SLR NMR also enables one to collect information on the prevailing Li diffusion mechanism [32].

Besides studying dimensionality effects on Li diffusion, we also put emphasis on the importance of ‘structural homogenization’, that is, the thermally assisted uniform distribution of Li ions between the  $\text{NbS}_2$  layers. Here, NMR SLR rates of an annealed and a virgin sample, i.e., a sample shortly investigated after chemical Li intercalation of  $\text{NbS}_2$ , were comparatively studied. It turned out that the mean Li jump rate of the sample obtained after the homogenizing annealing step, which was also used for the laborious frequency-dependent measurements, was improved by more than two orders of magnitude.

## 2. Experiment

Polycrystalline niobium disulfide, 3R- $\text{NbS}_2$  (space group  $R3m$ ), was prepared by reaction of  $\text{Nb}_2\text{O}_5$  (Sigma Aldrich 99.9%) with  $\text{H}_2\text{S}$  gas (Messer, 2.0) for 3 h at 107 K in a conventional tube furnace. Chemical Li intercalation was carried out with *n*-butyllithium (1.6 M in hexane) to yield a composition of  $\text{Li}_{0.7}\text{NbS}_2$ . The suspension was stirred under inert gas atmosphere for 24 h. At all stages phase purity was checked by powder x-ray diffraction. In order to prevent de-lithiation at elevated temperatures and to avoid any reaction or decomposition with moisture, the sample was always kept under Ar atmosphere. For the NMR measurements the powder sample was fire sealed in a glass tube under vacuum. Directly after lithiation it might be reasonable to assume that the structure of the intercalation compound is at least slightly distorted. For example, the Li ions are likely to aggregate close to the crystallite interfaces exposed to the solution of *n*-butyllithium, possibly even occupying intra-layer sites. Their occurrence on sites deep inside the crystal structure might be relatively rare. Thus,

in order to study structural homogenization effects, the first investigations were performed on an ‘as-prepared’ sample, i.e., without prior temperature treatment. Subsequently, the glass tube containing the sample was placed in an oven to anneal the intercalation compound at 773 K for 10 days. This so-called ‘annealed’ sample was investigated in greater detail for the dimensionality study.

Temperature-variable and frequency-dependent  $^7\text{Li}$  NMR measurements were carried out on a Bruker Avance III spectrometer in connection to a shimmed cryomagnet. A ceramic high-temperature NMR probe (Bruker BioSpin) was used, allowing  $\pi/2$  pulse lengths of about 2.5  $\mu\text{s}$ . The nominal magnetic field was  $B_0 = 7.04$  T, corresponding to a resonance frequency of  $\omega_0/2\pi = 116.5$  MHz. The measurements were performed at temperatures ranging from 200 to 570 K.

$^7\text{Li}$  NMR spectra of lithiated niobium disulfide were obtained by Fourier transformation of the free induction decays (FIDs). These were acquired under static, i.e., non-rotating conditions, as a function of temperature with a single pulse experiment using sufficiently long recycle delays of up to 100 s at the lowest temperature accessible.  $^7\text{Li}$  SLR NMR rates in the laboratory frame of reference  $1/T_1 = R_1$  were recorded by means of the classical saturation recovery pulse sequence [38]  $10 \times \pi/2 - t_d - \pi/2$  at 116.5 MHz. Here, the first ten  $\pi/2$  pulses in rapid succession are used to destroy any longitudinal contributions to the magnetization  $M_z$ . The recovery of  $M_z$  is then recorded as a function of the delay time  $t_d$ . The resulting magnetization transients  $M_z(t_d)$  were parameterized by stretched exponentials of the form  $M_z(t_d) = M_{z,\text{eq}}\{1 - \exp[-(t_d/T_1)^\gamma]\}$ , with the stretching exponent  $\gamma$  ranging from 0.7 to 0.9.  $M_{z,\text{eq}}$  denotes the magnetization in thermal equilibrium.

SLR NMR measurements in the rotating frame of reference (SLR $\rho$ ) [38–41] are performed at very low magnetic field strengths  $B_1$ , i.e., at angular frequencies of  $\omega_1$  of the order of some kHz (see below). Because of  $\omega_1 \ll \omega_0$ , SLR $\rho$  measurements are sensitive to much slower diffusion processes as compared to SLR NMR measurements in the laboratory frame. Here,  $^7\text{Li}$  NMR SLR $\rho$  rates  $1/T_{1\rho} = R_{1\rho}$  were recorded using the spin-lock technique. To this end, the equilibrium magnetization is rotated in the direction of the  $Y'$  axis of the rotating frame by a  $\pi/2_{Y'}$  pulse along the  $X'$  axis. This is followed immediately by a  $90^\circ$  phase-shifted locking pulse pointing in the same direction as the magnetization, thus locking the spins in the effective (locking) field  $B_1$ . Here, the magnetization  $M_\rho$  tends to its new equilibrium value, which is virtually zero for the applied magnetic field strengths.  $M_\rho$  is measured by recording the FID after switching off the locking field. The SLR $\rho$  rates  $R_{1\rho}$  at a given locking frequency  $\nu_1 = \gamma B_1/2\pi$  (and temperature) were obtained by varying the duration  $t_{\text{lock}}$  of the locking pulse from 100  $\mu\text{s}$  to 10 s. The recycle delay was chosen to be at least  $5 \times T_1$ . As in the laboratory frame of reference, a stretched exponential was fitted to the magnetization transients  $M_\rho(t_{\text{lock}})$  recorded; the stretching exponent  $\gamma$  ranged from 0.3 to 0.9.

NMR measurements over the complete accessible temperature range were performed at two different locking frequencies  $\nu_1$ , namely, at 20 and at 5 kHz. Additionally,

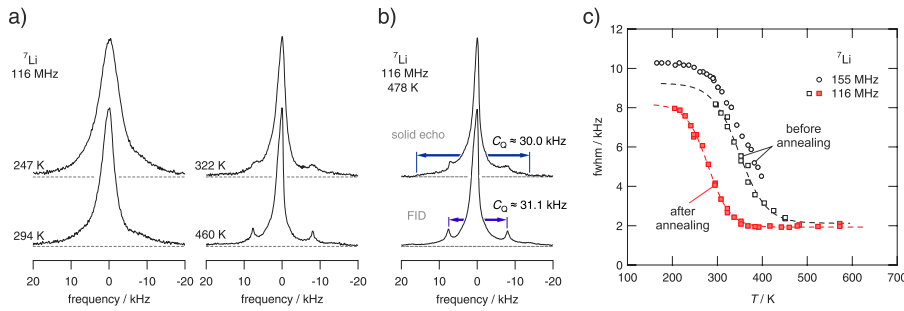


**Figure 1.** (a)  ${}^7\text{Li}$  NMR spectra of annealed, layer-structured  $\text{Li}_{0.7}\text{NbS}_2$  (3R) recorded at  $\omega_0/2\pi = 116$  MHz and at the temperatures indicated. With increasing  $T$  the line width of the slightly anisotropically broadened central line exhibits narrowing due to motional averaging of dipole–dipole interactions. At  $T > 320$  K a distinct quadrupole powder pattern emerges which is fully developed at  $T > 450$  K. (b)  ${}^7\text{Li}$  NMR spectra recorded at 116 MHz and 478 K. Bottom: single pulse spectrum, top: solid-echo spectrum. The electric quadrupole coupling constant  $C_Q$  can be directly read out from the  $90^\circ$  singularities. (c) NMR line width (full width at half maximum, fwhm) as a function of temperature. While the unfilled data points refer to the sample before annealing, filled squares represent the line width after homogenization by soft heat treatment of  $\text{Li}_{0.7}\text{NbS}_2$  at 773 K for ten days. Data were recorded at 116 MHz ( $\blacksquare$ ) and 155 MHz ( $\bullet$ ), respectively. See text for further explanation.

frequency-dependent NMR  $\text{SLR}_\rho$  rates were recorded at two selected temperatures on both sides of the diffusion-induced SLR NMR rate peak where the conditions  $\omega_1 \tau_c \ll 1$  and  $\omega_1 \tau_c \gg 1$  approximately hold, i.e., in the high- $T$  and low- $T$  relaxation limit, respectively.

### 3. Results and discussion

#### 3.1. Static ${}^7\text{Li}$ NMR spectra, motional narrowing, and local electronic structures

In figure 1(a) various  ${}^7\text{Li}$  NMR spectra of annealed  $\text{Li}_{0.7}\text{NbS}_2$  are shown. At low temperatures (rigid lattice regime) the spectra are composed of a single, slightly asymmetric and dipolarly broadened central line with a width  $\Delta\nu = \Delta\nu_{\text{RL}}$  (full width at half maximum, fwhm) of approximately 8 kHz. The NMR line undergoes pronounced motional narrowing (MN) [42] with increasing temperature due to averaging of dipole–dipole interactions because of increasing Li motions. An asymmetric shape, i.e., a non-zero chemical shift anisotropy, is expected for those Li ions located between the  $\text{NbS}_2$  layers and, thus, subject to a highly anisotropic environment [43].

At  $T \gtrsim 320$  K so-called satellite intensities emerge, see also [44], which are fully developed at temperatures above approximately 450 K. The complete NMR powder pattern obtained originates from the electric interaction of the quadrupole moment of the  ${}^7\text{Li}$  nucleus (spin-quantum number  $I = 3/2$ ) with a non-vanishing electric field gradient (EFG) produced by the electric charge distribution in the neighborhood of the spin. From the first-order quadrupolar satellite singularities the nuclear quadrupole coupling constant  $C_Q = e^2 q Q / h$  can be easily determined [45]. Here,  $e$  is the elementary charge,  $eq$  the principal component of the EFG tensor,  $Q$  the electric quadrupole moment, and  $h$  is Planck’s constant. Assuming an axially oriented EFG, [45] from the distance of the satellite lines  $\Delta\nu_Q$ , indicated in

figure 1(b) (bottom), an electric quadrupole coupling constant of  $C_Q({}^7\text{Li}, 478 \text{ K}) = 2\Delta\nu_Q \approx 31$  kHz can be estimated for annealed  $\text{Li}_{0.7}\text{NbS}_2$ . In order to examine the matter more closely, a  ${}^7\text{Li}$  NMR solid echo was recorded at the same temperature; the corresponding NMR spectrum was derived by Fourier transformation, starting at the echo maximum (figure 1(b)), (top). Analyzing the resulting spectrum yields a somewhat smaller value of  $C_Q({}^7\text{Li}) \approx 30$  kHz.

For comparison, the NMR spectra of the virgin, i.e., non-annealed, sample are composed of a broader central transition which shows a less pronounced asymmetry. Even when the temperature is increased to 480 K no (well-defined) quadrupole satellites emerge. Quadrupole signals seem to be of very low intensity and *smear out* over a relatively large frequency range, as is usually found for structurally disordered materials. This clearly points to a rather broad distribution of EFGs, which can be directly ascribed to a non-homogeneous distribution or clustering of Li spins in non-annealed  $\text{Li}_{0.7}\text{NbS}_2$ , as obtained right after Li intercalation. On the other hand, the well-defined single quadrupole powder pattern of the annealed sample, which is revealed by averaging of dipole–dipole interactions due to sufficiently fast Li hopping, points to a single crystallographic site the Li ions occupy in the van der Waals gap. Most likely, this is the intra-layer octahedral site in  $\text{Li}_x\text{NbS}_2$ .

Plotting the width  $\Delta\nu$  of the central transition as a function of temperature allows a more quantitative analysis of the annealing effect found. In figure 1(c) the data sets after (red, filled symbols) and before (black, unfilled symbols) annealing the  $\text{Li}_{0.7}\text{NbS}_2$  sample are shown. In addition to the NMR spectra recorded at 116 MHz, spectra were also recorded at 155 MHz. The difference of about 1 kHz in line width reflects the field dependence of the chemical shift anisotropy affecting the central line. Expectedly, the same effect is observed for the annealed sample when NMR lines recorded at 116 MHz and 194 MHz, respectively, are compared.

The dashed lines in figure 1(c) are drawn to guide the eye; they indicate that the line width in the rigid lattice regime  $\Delta\nu_{\text{RL}}$  is expected to be about 9 kHz and 8 kHz for non-annealed and annealed  $\text{Li}_{0.7}\text{NbS}_2$ , respectively. Since dipolar coupling is proportional to  $1/\bar{r}^3$  (cf. also van Vleck's formula [41, 46, 47]), where  $\bar{r}$  is the mean distance between two Li spins, the decrease in line widths directly reflects the homogenization process, that is, the uniform distribution of  $\text{Li}^+$  in the van der Waals gap which leads to a decrease of  $\bar{r}$ .

More importantly, after the annealing step the onset of MN decreases from  $T_{\text{onset}} \approx 300$  K to about 200 K. This clearly points to improved Li ion dynamics in the heat-treated niobium sulfide. At the inflexion point of the MN curve a jump rate of  $\tau_{\text{MN}}^{-1} \approx 2\pi \times \Delta\nu_{\text{RL}}$  can be estimated [42]. Thus,  $\tau_{\text{MN}}^{-1}(280 \text{ K}) \approx 5 \times 10^4 \text{ s}^{-1}$  is derived for annealed  $\text{Li}_{0.7}\text{NbS}_2$ . Assuming a similar thermal activation for both samples, this results in an improvement of about two orders of magnitude of  $\tau_{\text{MN}}^{-1}(300 \text{ K})$  as compared to the non-annealed state.

The empirical expression introduced by Waugh and Fedin [48] is helpful to roughly estimate the activation energy of the hopping process; according to  $E_a^{\text{MN}}(\text{meV}) = 1.62 \times T_{\text{onset}}(\text{K})$  a value of about 0.32 eV is found. A very similar result (0.30(2) eV) is obtained when the MN curve is analyzed by taking advantage of the semi-empirical approach of Hendrickson and Bray [49, 50]. Even so, those values have to be taken as a rough estimation only. SLR NMR (see below) is known to deliver more precise results when activation energies have to be determined.

### 3.2. $^7\text{Li}$ NMR SLR measurements

In figure 2 the  $^7\text{Li}$  NMR SLR rates ( $R_1$  and  $R_{1\rho}$ ) of as-prepared (black, unfilled symbols) and annealed (red, filled symbols (see also key))  $\text{Li}_{0.7}\text{NbS}_2$  are shown in an Arrhenius plot. While  $R_1$  rates were recorded in the laboratory frame at a resonance frequency of  $\omega_0/2\pi = 116$  MHz, the corresponding  $R_{1\rho}$  rates were measured in the rotating frame of reference using a locking frequency of  $\omega_1/2\pi = 20$  kHz. By comparing the NMR SLR rates measured before and after annealing, the effect of homogenization on  $R_1$  and  $R_{1\rho}$  can be enlightened. First, we will consider the effect on the  $R_1$  rates.

Before heat treatment, the Arrhenius diagram reveals that  $R_1$  of the as-prepared sample increases linearly with temperature; from the slope of a linear fit an apparent activation energy of 0.2 eV is obtained. Usually, the low- $T$  activation energy of SLR NMR measurements is ascribed to short-range Li dynamics. Its value might be additionally affected by correlation effects (see below) leading to a smaller value than expected. Interestingly, after the homogenization step the overall relaxation process slows down and the rates are increasingly governed by a non-diffusive background relaxation rate  $R_{1,\text{nd}}$ , which can be described using a simple power law [14]. This contribution shows up below room temperature.

A fit of  $R_{1,\text{nd}} \propto T^\kappa$  (dashed line) to the sub-range of the data, indicated by the small arrows in figure 2, yields  $\kappa = 1.14(5)$ . Purely diffusion-induced rates  $R_{1,\text{diff}}$  (open squares) are obtained by subtracting this non-diffusive

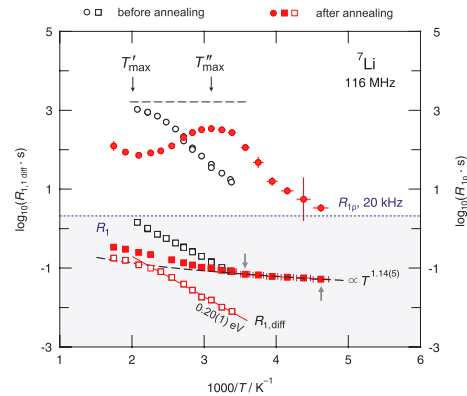


**Figure 2.** Arrhenius plot of the  $^7\text{Li}$  NMR SLR rates of  $\text{Li}_{0.7}\text{NbS}_2$  recorded in the laboratory frame ( $R_1$  (■), see bottom part of the figure) and in the rotating frame of reference ( $R_{1\rho}$  (●), cf. upper part of the figure) measured at  $\omega_0/2\pi = 116$  MHz and  $\omega_1/2\pi = 20$  kHz. Unfilled symbols refer to the situation before annealing, while filled symbols denote data points acquired after the annealing step. After heat treatment  $R_1$  decreases due to the weakening of dipole–dipole interactions with increasing spatial separation of the interacting spins. In order to obtain purely diffusion-induced rates ( $R_{1,\text{diff}}$ ) the non-diffusive background showing up at  $T < 290$  K can be taken into account by an appropriate power law  $R_{1,\text{nd}} \propto T^{1.14}$ . The pronounced shift of the SLR $_{\rho}$  rate peak towards lower  $T$  clearly indicates an increase of Li diffusivity after annealing. The decrease of the absolute values of  $R_{1\rho}$  at  $T_{\text{max}}$  is consistent with a decrease of dipolar interactions. See text for further details.

contribution from the overall rates  $R_1$ . Compared to the non-annealed sample, the absolute values of the  $R_{1,\text{diff}}$  rates of the homogenized one are reduced by one order of magnitude. This points to a weakening of homonuclear dipole–dipole interactions due to an increased average Li–Li distance which is induced by the temperature treatment and the associated structural relaxation. The same effect is observed for  $R_{1\rho}$  when the rates near the peak maxima are compared (see figure 2). Interestingly, the rates  $R_{1,\text{diff}}$  exhibit essentially the same activation energy of 0.2 eV as those of the sample prior to the temperature treatment. In addition, they hint at the onset of a relaxation maximum at  $T \gtrsim 660$  K. This feature, which points to an enhancement of Li diffusivity, is even clearer seen in the case of our  $R_{1\rho}$  measurements.

In the present case, measuring  $R_{1\rho}$  rates allows a more direct and quantitative observation of the effects of temperature treatment on  $\text{Li}^+$  dynamics. Before annealing, the rates recorded above ambient temperature might be interpreted as the low- $T$  flank of a diffusion-induced NMR rate peak most probably having its maximum at  $T'_{\text{max}} \gtrsim 500$  K. Soft heat treatment  $\text{Li}_{0.7}\text{NbS}_2$  does shift this peak towards a much lower temperature so that the complete relaxation rate peak can be observed. Compared to the as-prepared sample, we found  $T'_{\text{max}} \approx 320$  K (see figure 2). Disregarding dimensionality and correlation effects [16, 18, 32], influencing the slope on the low- $T$  side (correlation effects) and high- $T$  side (dimensionality effects), by using the condition  $\omega_1 \tau \approx 0.5$ , which is valid at  $T = T'_{\text{max}}$ , an Li jump rate  $\tau^{-1}$  can be estimated. Here,  $\tau^{-1}(T'_{\text{max}})$  is of the

order of  $2.5 \times 10^5 \text{ s}^{-1}$ . This value is in excellent agreement with that derived from MN at 280 K and shows that the same diffusion processes is probed by the line shape analysis performed. As will be shown below, when referred to 300 K, this corresponds to an increase of Li diffusivity by about 2.5 orders of magnitude when going from the as-prepared to the annealed sample. The enhancement found by SLR $\rho$  NMR mirrors the findings gained through the NMR line analysis presented above.

Note that, just as in the laboratory frame of reference, after annealing the  $^7\text{Li}$  NMR SLR $\rho$  rate,  $R_{1\rho}$  also reveals a distinct non-diffusive background contribution which increasingly influences the overall rate when  $T$  is chosen lower than 250 K. The total rate  $R_{1\rho}$  can be described in terms of a sum of a diffusion-induced relaxation peak  $R_{1\rho, \text{diff}}$  and a non-diffusive background contribution represented by  $R_{1\rho, \text{nd}}$

$$R_{1\rho} = R_{1\rho, \text{diff}} + R_{1\rho, \text{nd}}. \quad (1)$$

In general, non-diffusive longitudinal relaxation is assumed to be caused by a combination of different types of relaxation, most prominent being spin fluctuations due to paramagnetic impurities and phonons, as well as interactions of Li nuclei with conduction electrons. Usually, the superposition

$$R_{1\rho, \text{nd}} = aR_{1\rho}^{\text{para}} + bR_{1\rho}^{\text{phonon}} + cR_{1\rho}^{\text{elec}} + \dots$$

is reasonably well described by a power law, as is also used here:

$$R_{1\rho, \text{nd}} \propto T^\kappa. \quad (2)$$

For a more detailed analysis, in particular with regard to dimensionality, an appropriate NMR relaxation model has to be used to evaluate the NMR SLR $\rho$  data probed on powder samples. In analogy to  $R_{1, \text{diff}}$  the rotating-frame rate  $R_{1\rho, \text{diff}}$  is related to the spectral density  $J(n\omega)$  at multiples of the Larmor frequency  $\omega_0$  and locking frequency  $\omega_1$  via

$$R_{1\rho, \text{diff}} = C_\rho \left( J(2\omega_1) + \frac{5}{3}J(\omega_0) + \frac{2}{3}J(2\omega_0) \right). \quad (3)$$

For two-dimensional (2D) diffusion Richards [28, 37] introduced a logarithmic spectral density function  $J^{2D}(\tau, \omega) \propto \tau \ln(1 + 1/(\omega\tau)^\beta)$ . For uncorrelated motion  $\beta$  equals 2 and assumes smaller values ( $1 < \beta \leq 2$ ) when correlation effects owing to structural disorder and/or Coulomb interactions [51] come into play. Since  $\omega_0 \gg \omega_1$ , only the first term of equation (3) significantly contributes to  $R_{1\rho, \text{diff}}$  in the temperature range covered here, yielding

$$R_{1\rho, \text{diff}}^{2D} \approx C_\rho \tau_c \ln(1 + 1/(2\omega_1 \tau_c)^\beta). \quad (4)$$

The jump rate  $\tau^{-1}$  associated with the 2D diffusion process is of the order of the correlation rate  $\tau_c^{-1}$ . In the easiest case, it can be replaced by an Arrhenius relation containing the pre-exponential factor  $\tau_{c,0}^{-1}$  and the activation energy  $E_a$  governing long-range Li diffusion.

$$\tau^{-1} \approx \tau_c^{-1} = \tau_{c,0}^{-1} \exp(-E_a/k_B T). \quad (5)$$

From equation (4) the behavior of the SLR $\rho$  rates in both temperature limits can be derived. In the low-temperature limit, being characterized by  $\omega_1 \tau \gg 1$ , the

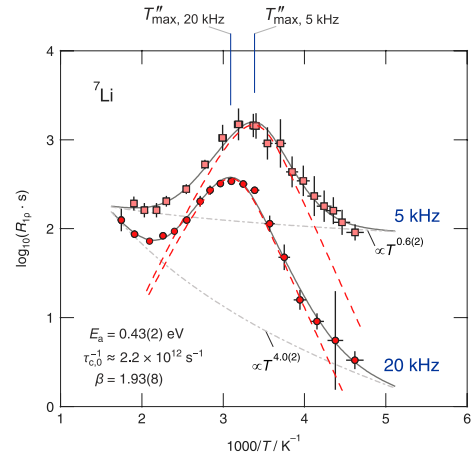


**Figure 3.** Arrhenius plot of the  $^7\text{Li}$  NMR SLR $\rho$  rates of annealed  $\text{Li}_{0.7}\text{NbS}_2$  (3R) measured at a locking frequency  $\omega_1/2\pi$  of 20 kHz (●) and 5 kHz (■), respectively. The rates can be fitted by a superposition (solid line) of a diffusion-induced relaxation rate peak (dashed lines) and a non-diffusive background contribution (dashed-dotted lines). The latter shows a weaker-than-activated temperature dependence, which is here described by a power law  $R_{1\rho, \text{nd}} \propto T^\kappa$ , with  $\kappa_{20 \text{ kHz}} = 4.0$  and  $\kappa_{5 \text{ kHz}} = 0.6$ , respectively. The diffusion-induced relaxation rates are in agreement with an NMR model taking into account both 2D diffusion and a sub-quadratic frequency dependence on the low- $T$  side, see equations (4) and (5). The joint fit (solid lines) represents an overall fit, i.e., it takes into account both data sets simultaneously.

frequency (and temperature) dependence  $R_{1\rho, \text{diff}} \propto \omega_1^{-\beta} \tau_c^{1-\beta}$  is obtained, which is common to diffusion processes in this limit irrespective of the underlying dimensionality, 2D or 3D [16]. The treatment of the equation in the high-temperature range, that is, in the limit  $\omega_1 \tau \ll 1$ , results in a logarithmic frequency dependence  $R_{1\rho, \text{diff}} \propto -\tau_c \ln(\omega_1 \tau_c)$ . In contrast, 3D (isotropic) diffusion would result in frequency-independent  $R_{1\rho, \text{diff}}$  rates [16]. Thus, frequency-dependent SLR measurements serve as a suitable tool to differentiate 2D from 3D hopping motion.

To this end, SLR $\rho$  NMR rates were measured at different locking frequencies  $\omega_1/2\pi$ . As an example, in the Arrhenius plot of figure 3 the SLR $\rho$  NMR rates recorded at  $\omega_1/2\pi = 20 \text{ kHz}$  (see also figure 2) are compared with those acquired at a much lower locking frequency of only 5 kHz. The latter rates also represent the sum of a diffusion-induced contribution and a non-diffusive background according to equation (1), albeit a much smaller exponent  $\kappa \approx 0.6$ , and thus a much weaker temperature dependence, of  $R_{1\rho, \text{nd}}$  is found.

As explicitly shown in figure 3, the two data sets can be evaluated simultaneously by a joint fit of equations (1), (2), (4) and (5), linking the parameters  $C_\rho$ ,  $\tau_{c,0}$ ,  $E_a$ , and  $\beta$  recorded at the two different locking frequencies  $\omega_1 = 5 \text{ kHz}$  and  $\omega_1 = 20 \text{ kHz}$ , respectively. The result is represented by the solid lines in figure 3. While the dashed lines show the purely diffusion-induced relaxation rates  $R_{1\rho, \text{diff}}$ , the non-diffusive background contributions ( $R_{1\rho, \text{nd}}$ ) are represented by dashed-dotted lines. The joint fit yields an

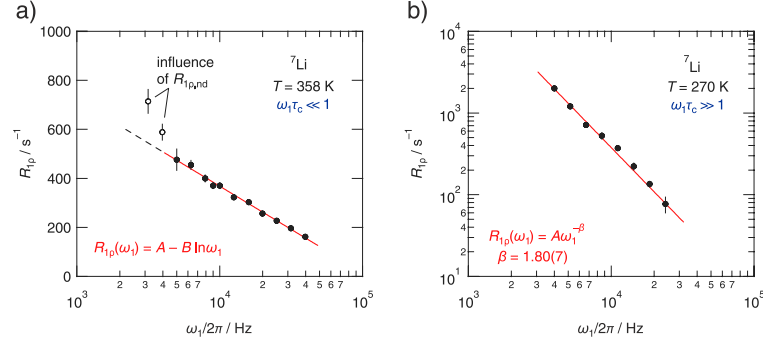


**Figure 4.**  ${}^7\text{Li}$  NMR SLR rates of annealed  $\text{Li}_{0.7}\text{NbS}_2$  (3R) as a function of locking frequency. (a)  $R_{1\rho}$  recorded at 358 K, i.e., on the high-temperature flank of the corresponding relaxation rate peak, where  $\omega_1\tau_c \ll 1$  approximately applies. According to Richards’ semi-empirical model for 2D diffusion [28] ( $R_{1\rho} \propto -\tau_c \ln(\omega_1\tau_c)$ ), a logarithmic frequency dependence is observed. At  $\omega_1/2\pi < 5$  kHz non-diffusive background relaxation ( $R_{1\rho,nd}$ ) becomes significant enough to cause deviation from linearity. (b)  $R_{1\rho}$  rates recorded at 270 K, i.e., on the low-temperature flank of the relaxation rate peak; at this temperature the condition  $\omega_1\tau_c \gg 1$  approximately holds. Here, a (slightly) sub-quadratic ( $\beta = 1.80(7)$ ) frequency dependence  $R_{1\rho} \propto \omega_1^{-\beta}$  is observed.

activation energy  $E_a$  of 0.43(2) eV and a pre-exponential factor  $\tau_0^{-1} \approx \tau_{c,0}^{-1}$  of approximately  $2.2 \times 10^{12} \text{ s}^{-1}$ . According to equation (5), with these values an Li jump rate of  $\tau^{-1}(300 \text{ K}) \approx 1.3 \times 10^5 \text{ s}^{-1}$  is obtained. This value is smaller but still comparable to the analogous 2D Li diffusion process in layer-structured  $\text{Li}_x\text{TiS}_2$  (about 0.41 eV), see [14]. For comparison, polycrystalline layer-structured  $\text{Li}_x\text{TiS}_2$ , which represents one of the first anode insertion hosts for Li ions [52], has been studied recently in detail by both temperature-variable relaxation NMR and stimulated echo NMR. The results clearly point to a solitary diffusion process spanning a dynamic range of ten orders of magnitude [14].

Interestingly, as in the case of  $\text{Li}_x\text{TiS}_2$ , correlation effects, which are accounted for by the exponent  $\beta \approx 1.9$ , turned out to be almost negligible. Instead, the SLR NMR rates in the low- $T$  limit seem to follow the classical BPP-type [53] relaxation behavior given by  $R_{1\rho} \propto \omega_1^{-2}\tau_c^{-1}$  for  $\omega_1\tau_c \gg 1$ .

In order to corroborate whether the diffusion process probed via SLR NMR measurements is restricted to two dimensions, that is, taking place solely in the van der Waals gap of  $\text{Li}_x\text{NbS}_2$ , diffusion-induced  $R_{1\rho}$  rates were directly recorded as a function of locking frequency  $\omega_1/2\pi$  at fixed temperatures  $T_{LT/HT}$  in both temperature limits. The temperatures were chosen to be  $T_{HT} = 358$  K and  $T_{LT} = 270$  K, thus, approximately satisfying the conditions  $\omega_1\tau_c \ll 1$  and  $\omega_1\tau_c \gg 1$ , respectively. The results of the high-temperature measurements are presented in figure 4(a); SLR rates were recorded at frequencies ranging from 3 to 40 kHz. They indeed exhibit a logarithmic temperature dependence  $R_{1\rho} \propto -\ln \omega_1$ , see also [33], as expected from Richards’ semi-empirical model developed for a 2D diffusion process [28]. Note that at frequencies below 5 kHz a deviation from linear behavior is observed, which is most likely due to the increasing influence of the non-diffusive contribution  $R_{1\rho,nd}$  exceeding  $R_{1\rho,diff}$  at high temperatures and sufficiently low locking frequencies.

Similarly, the relaxation rates measured in the low-temperature limit exhibit a slightly sub-quadratic frequency

dependence  $R_{1\rho} \propto \omega_1^{-\beta}$ , as calculated from equation (4) for  $\omega_1\tau_c \gg 1$ . Finally, the parameter  $\beta = 1.80(7)$  obtained is in good agreement with the value of the joint fit shown in figure 3.

#### 4. Conclusion and outlook

Among the various NMR techniques, frequency-dependent SLR measurements represent a unique tool to identify low-dimensional diffusion processes. The analysis is based on the evaluation of diffusion-induced SLR NMR rates recorded in the so-called high-temperature limit of a given diffusion-induced relaxation rate peak  $R_{1\rho,diff}(1/T)$ . In the present case,  $\text{Li}_x\text{NbS}_2$  served as one of very rare model substances to study spatially confined Li hopping processes in the van der Waals gap of the host material  $\text{NbS}_2$ . SLR NMR measurements in the rotating frame of reference turned out to be highly useful to thoroughly characterize the diffusion process and to compare the results with the NMR model introduced by Richards for 2D diffusion [28, 29]. The rates  $R_{1\rho}$  of a homogenized sample clearly reveal a logarithmic frequency dependence in the limit  $\omega_1\tau_c \ll 1$ , which agrees with the theoretical prediction for a two-dimensionally restricted diffusion process.

Long-range Li diffusion in the 3R modification of  $\text{Li}_x\text{NbS}_2$  with  $x = 0.7$  can be characterized by an activation energy of 0.43 eV and a pre-exponential factor of  $2.2 \times 10^{12} \text{ s}^{-1}$ , which lies in the typical range of phonon frequencies. At ambient temperature the Li jump rate is in the order of  $10^5 \text{ s}^{-1}$ , thus, being comparable to Li dynamics in other layer-structured transition metal disulphides such as  $\text{Li}_x\text{TiS}_2$  [14, 27]. The  $R_{1\rho}$  rates of  $\text{Li}_x\text{NbS}_2$  reveal that, at least for a sufficiently well homogenized sample with  $x = 0.7$ , strong correlation effects due to Coulomb interactions of the  ${}^7\text{Li}$  spins seem to be absent. However, annealing, which facilitates a uniform distribution of Li ions, turns out to have a crucial influence on  $\text{Li}^+$  self-diffusivity. As we

could clearly show,  $^7\text{Li}$  diffusion parameters of  $\text{Li}_{0.7}\text{NbS}_2$  are significantly improved after the soft annealing step has been carried out. Compared to the situation before homogenization, the room-temperature Li jump rate has increased by approximately 2.5 orders of magnitude.

## Acknowledgments

We thank G Schmidt (Bruker BioSpin, Rheinstetten (Germany)) for his technical assistance and our colleagues at the Leibniz University Hannover for fruitful discussions. Financial support by the *Deutsche Forschungsgemeinschaft* (DFG) within the framework of the Research Unit FOR 1277 ‘*Mobilität von Li-Ionen in Festkörpern*’ (molife) as well as by the Graz University of Technology (Austria) is greatly appreciated (grant no. WI3600/2-2 and 4-2).

## References

- [1] Whittingham M S 2004 *Chem. Rev.* **104** 4271
- [2] Fergus J W 2010 *J. Power Sources* **195** 939
- [3] Xu B, Qian D, Wang Z and Meng Y S 2012 *Mater. Sci. Eng. R* **73** 51
- [4] Tarascon J M and Armand M 2001 *Nature* **414** 359
- [5] Aricó A S, Bruce P, Scrosati B, Tarascon J-M and Van Schalkwijk W 2005 *Nature Mater.* **4** 366
- [6] Bruce P G, Scrosati B and Tarascon J-M 2008 *Angew. Chem. Int. Edn* **47** 2930
- [7] Park M, Zhang X, Chung M, Less G B and Sastry A M 2010 *J. Power Sources* **195** 7904
- [8] Xu Z and Stebbins J F 1995 *Science* **270** 1332
- [9] Verhoeven V W J, de Scheper I M, Nachtegaal G, Kentgens A P M, Kelder E M, Schoonman J and Mulder F M 2001 *Phys. Rev. Lett.* **86** 4314
- [10] Cahill L S, Chapman R P, Britten J F and Goward G R 2006 *J. Phys. Chem. B* **110** 7171
- [11] Cahill L S, Iriyama Y, Nazar L F and Goward G R 2010 *J. Mater. Chem.* **20** 4340
- [12] Wilkening M, Romanova E, Nakhil S, Weber D, Lerch M and Heitjans P 2010 *J. Phys. Chem. C* **114** 19083
- [13] van Wüllen L, Sofina N, Hildebrandt L, Mühle C and Jansen M 2006 *Solid State Ion.* **177** 1665
- [14] Wilkening M and Heitjans P 2008 *Phys. Rev. B* **77** 024311
- [15] Brinkmann D 1992 *Prog. Nucl. Magn. Reson. Spectrosc.* **24** 527
- [16] Heitjans P, Schirmer A and Indris S 2005 *Diffusion in Condensed Matter—Methods, Materials, Models* 2nd edn, ed P Heitjans and J Kärger (Berlin: Springer) pp 369–415 chapter 9
- [17] Böhmer R, Jeffrey K and Vogel M 2007 *Prog. Nucl. Magn. Reson. Spectrosc.* **50** 87
- [18] Wilkening M and Heitjans P 2012 *ChemPhysChem* **13** 53
- [19] van Wüllen L, Echelmeyer T, Meyer H-W and Wilmer D 2007 *Phys. Chem. Chem. Phys.* **9** 3298
- [20] Grey C P and Dupré N 2004 *Chem. Rev.* **104** 4493
- [21] Tang X-P, Busch R, Johnson W L and Wu Y 1998 *Phys. Rev. Lett.* **81** 5358
- [22] He X J, Davis L J M, Bain A D and Goward G R 2012 *Solid State Nucl. Magn. Reson.* **42** 26
- [23] Qi F, Jörg T and Böhmer R 2002 *Solid State Nucl. Magn. Reson.* **22** 484
- [24] Cabana J, Dupré N, Rouse G, Grey C P and Palacín M R 2005 *Solid State Ion.* **176** 2205
- [25] Faske S, Eckert H and Vogel M 2008 *Phys. Rev. B* **77** 104301
- [26] Wilkening M, Gebauer D and Heitjans P 2008 *J. Phys.: Condens. Matter* **20** 022201
- [27] Wilkening M, Kuchler W and Heitjans P 2006 *Phys. Rev. Lett.* **97** 065901
- [28] Richards P M 1979 *Topics in Current Physics* vol 15, ed M B Salamon (Berlin: Springer)
- [29] Avogadro A and Villa M 1977 *J. Chem. Phys.* **66** 2359
- [30] McDowell A F, Fedders P A and Conradi M S 1998 *Phys. Rev. B* **58** 248
- [31] MacDonald D H, Sholl C A and Stephenson P C L 1998 *J. Phys.: Condens. Matter* **10** 417
- [32] Epp V and Wilkening M 2010 *Phys. Rev. B* **82** 020301
- [33] Kuchler W, Heitjans P, Payer A and Schöllhorn R 1994 *Solid State Ion.* **70/71** 434
- [34] McDowell A F, Mendelsohn C F, Conradi M S, Bowman R C and Maeland A J 1995 *Phys. Rev. B* **51** 6336
- [35] Wilkening M, Iwaniak W, Heine J, Epp V, Kleinert A, Behrens M, Nuspl G, Bensch W and Heitjans P 2007 *Phys. Chem. Chem. Phys.* **9** 6199
- [36] Kuhn A, Sreeraj P, Pöttgen R, Wiemhöfer H-D, Wilkening M and Heitjans P 2011 *J. Am. Chem. Soc.* **113** 11018
- [37] Richards P M 1978 *Solid State Commun.* **25** 1019
- [38] Fukushima E and Roeder S B W 1981 *Experimental Pulse NMR* (Reading, MA: Addison-Wesley)
- [39] Ailion D and Slichter C P 1964 *Phys. Rev. Lett.* **12** 168
- [40] Slichter C P and Ailion D 1964 *Phys. Rev.* **135** A1099
- [41] Wolf D 1974 *Phys. Rev. B* **10** 2724
- [42] Wilkening M, Kuhn A and Heitjans P 2008 *Phys. Rev. B* **78** 054303
- [43] Prigge C, Müller-Warmuth W and Schöllhorn R 1995 *Z. Phys. Chem.* **189** 153
- [44] Bertermann R and Müller-Warmuth W 1998 *Z. Naturf. a* **53** 863
- [45] Bredow T, Heitjans P and Wilkening M 2004 *Phys. Rev. B* **70** 115111
- [46] Van Vleck J H 1948 *Phys. Rev.* **74** 1168
- [47] Abragam A 1961 *The Principles of Nuclear Magnetism* (Oxford: Clarendon)
- [48] Waugh J S and Fedin I 1963 *Sov. Phys.—Solid State* **4** 1633
- [49] Hendrickson J and Bray P 1973 *J. Magn. Reson.* **9** 341
- [50] Wilkening M, Bork D, Indris S and Heitjans P 2002 *Phys. Chem. Chem. Phys.* **4** 3246
- [51] Bunde A, Dieterich W, Maass P and Meyer M 2005 *Diffusion in Condensed Matter—Methods, Materials, Models* 2nd edn, ed P Heitjans and J Kärger (Berlin: Springer) pp 813–856, chapter 20
- [52] Whittingham M S 1978 *Prog. Solid State Chem.* **12** 41
- [53] Bloembergen N, Purcell E M and Pound R V 1948 *Phys. Rev.* **73** 679

### 3.4.3 Lithium motion in the anode material $\text{LiC}_6$ as seen via time-domain $^7\text{Li}$ NMR (pp. 97–105)

Langer, J., Epp, V., Heitjans, P., Mautner, F.-A., and Wilkening, M. *Physical Review B* **88**, 94304 (2013).—This article is reproduced by permission of The American Physical Society. The original article can be found online at <http://journals.aps.org/prb/abstract/10.1103/PhysRevB.88.094304>. ©2013 The American Physical Society.

Lithium motion in the anode material  $\text{LiC}_6$  as seen via time-domain  $^7\text{Li}$  NMRJ. Langer,<sup>1,\*</sup> V. Epp,<sup>1,†</sup> P. Heitjans,<sup>2</sup> F. A. Mautner,<sup>1</sup> and M. Wilkening<sup>1,‡</sup><sup>1</sup>Christian Doppler Laboratory for Lithium Batteries, and Institute for Chemistry and Technology of Materials, Graz University of Technology, Stremayrgasse 9, 8010 Graz, Austria<sup>2</sup>Institute of Physical Chemistry and Electrochemistry, Leibniz University Hannover, Callinstraße 3-3a, 30167 Hannover, Germany

(Received 28 June 2013; revised manuscript received 28 August 2013; published 16 September 2013)

Since the commercialization of rechargeable lithium-ion energy storage systems in the early 1990s, graphite intercalation compounds (GICs) have served as the number one negative electrode material in most of today's batteries. During charging the performance of a battery is closely tied with facile Li insertion into the graphite host structure. So far, only occasionally time-domain nuclear magnetic resonance (NMR) measurements have been reported to study Li self-diffusion parameters in GICs. Here, we used several NMR techniques to enlighten Li hopping motions from an atomic-scale point of view. Li self-diffusion in the stage-1 GIC  $\text{LiC}_6$  has been studied comparatively by temperature-variable spin-spin relaxation NMR as well as (rotating frame) spin-lattice relaxation NMR. The data collected yield information on both the relevant activation energies and jump rates, which can directly be transformed into Li self-diffusion coefficients. At room temperature the Li self-diffusion coefficient turns out to be  $10^{-15} \text{ m}^2 \text{ s}^{-1}$ , thus, slightly lower than that for layer-structured cathode materials such as  $\text{Li}_{x \approx 0.7} \text{TiS}_2$ .

DOI: 10.1103/PhysRevB.88.094304

PACS number(s): 66.30.-h, 76.60.-k, 82.56.-b

## I. INTRODUCTION

The stage-1 graphite intercalation compound,  $\text{LiC}_6$ , belongs to one of the most fascinating application-oriented materials which is widely used as an anode in secondary lithium-ion batteries.<sup>1-3</sup> Most of the various electronic devices of our daily life such as notebooks or cell phones rely on the insertion and deinsertion of lithium ions into graphite-based negative electrodes.<sup>4</sup> In particular, the charge/discharge performance and thus the rate capability of an anode is closely related to self-diffusion of lithium ions inside the crystalline host. Moreover, if models are to succeed in simulation of the electrochemical processes in batteries, precisely measured data such as diffusion parameters are required.

Surprisingly, only a few studies can be found in the literature which directly deal with the in-depth investigation of Li diffusion parameters in crystalline, phase-pure  $\text{LiC}_6$ . Despite the relatively simple, but fascinating, structure of  $\text{LiC}_6$  research is yet far away from drawing a comprehensive picture on diffusive Li motion. Apart from earlier studies<sup>5</sup> applying quasielastic neutron scattering (QENS)<sup>6</sup> or taking advantage of  $\beta$ -radiation detected nuclear magnetic resonance ( $\beta$ -NMR) measurements of spin-polarized  $^8\text{Li}$  ( $t_{1/2} = 0.8 \text{ s}$ ) nuclei produced *in situ* by polarized neutron capture,<sup>7-9</sup> classical NMR measurements<sup>9-13</sup> on the stable Li isotope  $^7\text{Li}$  have rarely been utilized for this purpose. *En passant*, the results obtained from  $^7\text{Li}$  pulsed NMR as yet turned out to be less conclusive with respect to Li diffusion parameters.<sup>14</sup> This is because mainly spin-lattice relaxation (SLR) measurements in the so-called laboratory frame of reference have been performed. Compared to other time-domain NMR techniques, those measurements are sensitive to Li jump rates with values in the MHz range.<sup>10</sup> However, in order to probe Li motional processes in the temperature range where the structurally ordered  $\text{LiC}_6$  phase does exist, i.e., at ambient temperature, alternative NMR techniques have to be applied which are able to access much slower Li motions. For example, this is possible by recording SLR rates  $R_1$  in the rotating ( $\rho$ ) frame of reference via the so-called spin-lock technique introduced by Ailion and Slichter.<sup>11,13,15-18</sup> If  $^7\text{Li}$  SLR takes

solely place in the presence of a controllable magnetic field with resonance frequencies on the order of a few kHz instead of some MHz,<sup>19</sup> the desirable diffusion-induced rate peak  $R_1(1/T)$  shows up at much lower temperatures  $T$ .<sup>11,18</sup> In general, the peak entails valuable information on both short-range and long-range motions<sup>9,13,18</sup> as well as correlation effects.<sup>20,21</sup>

Here, layer-structured  $\text{LiC}_6$  (see Fig. 1) served as an excellent model system to probe Li dynamics with spatially confined migration pathways; it is the most prominent anode host material with applications in energy storage technology. The stage-1 compound consists of commensurate layers of carbon and lithium; Li resides in the central site below and above each third hexagon formed by C atoms. The stacking sequence is  $A\alpha A\alpha$  with a periodicity of 3.71 Å; A denotes the graphite basal plane and  $\alpha$  the intercalate layer. The carbon host structure of  $\text{LiC}_6$  allows in-plane jump diffusion and, because of the open channels parallel to the hexagonal  $c$

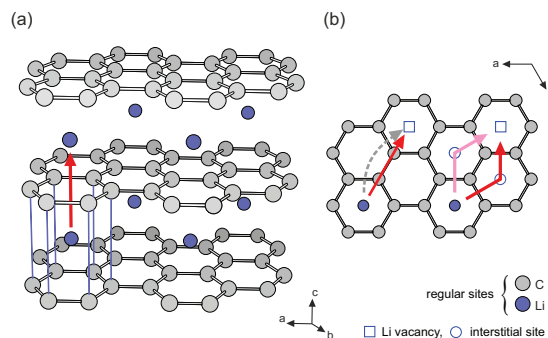


FIG. 1. (Color online) Illustration of the crystal structure of ordered  $\text{LiC}_6$  with  $A\alpha A\alpha$  stacking sequence. (a) View along the  $ab$  plane; (b) view along the  $c$  axis. Arrows roughly indicate possible  $\text{Li}^+$  migration pathways, that is, in-plane diffusion (b) vs motion along the open channels parallel to the hexagonal axis (a). A detailed description of possible migration pathways can be found in Ref. 22.

axis and the small size of the Li ion, it has been argued that also diffusion normal to the graphite plane cannot be ruled out *a priori* as in the case of the heavy alkalis.<sup>23</sup> In the present contribution, the results from various  $^7\text{Li}$  NMR measurements investigating both (local electronic) structure and Li ion dynamics of polycrystalline  $\text{LiC}_6$  will be presented and compared with those deduced from previous  $\beta$ -NMR<sup>7,8</sup> and QENS studies,<sup>5</sup> in particular. While  $\beta$ -NMR results were obtained on highly oriented pyrolytic graphite (HOPG) at temperatures around 373 K, results from QENS being sensitive to Li correlation times in the ns to ps range, were collected at much higher  $T$ , i.e., in a range with sufficiently fast Li motion.

## II. EXPERIMENT

The synthesis procedure to obtain polycrystalline stage-1  $\text{LiC}_6$ , shining like gold, is described in the classical paper by Guérard and Hérold.<sup>24</sup> After preparation, the sample (approximately 300 mg) was sealed in a quartz ampoule (3 cm in length, 5 mm in diameter) and stored for several months at room temperature; we anticipate almost full lithium homogenization, i.e., a homogenous distribution of the Li ions between the layers. The sample consists of  $\text{LiC}_6$  crystallites with diameters less than 500  $\mu\text{m}$ . Phase purity was checked by x-ray powder diffraction (XRPD). XRPD revealed a small volume fraction of the stage-2 compound  $\text{LiC}_{12}$  formed. By NMR, however, it was very difficult to detect this minor phase (see below and Fig. 2). The same sample was used for all measurements presented below.

$^7\text{Li}$  NMR measurements were carried out using two different high-performance digital Bruker Avance III spectrometers in connection with shimmed cryomagnets with nominal magnetic fields of 7 T and 11 T, respectively. This corresponds to  $^7\text{Li}$  Larmor frequencies of  $\omega_0/2\pi = 116$  MHz and  $\omega_0/2\pi = 194$  MHz, respectively. Both a commercial high-temperature probe (Bruker Biospin) and a probe designed for temperatures up to 453 K were employed to measure line shapes and NMR relaxation rates. Typically, the  $\pi/2$  pulse lengths ranged from 6 to 9  $\mu\text{s}$ . The measurements were performed at temperatures ranging from 203 K to 450 K; here, a Eurotherm temperature controller in combination with a type T thermocouple was used.

$^7\text{Li}$  NMR SLR rates  $1/T_1 = R_1$  were acquired with the saturation recovery pulse sequence  $10 \times \pi/2 - t_d - \pi/2 - \text{acq.}$ <sup>9,19</sup> An initial pulse train, consisting of ten  $\pi/2$  pulses separated by 80  $\mu\text{s}$ , was used to destroy any longitudinal magnetization  $M_z$  prior to recording its temperature and frequency dependent recovery as a function of the delay time  $t_d$ . Rotating-frame  $^7\text{Li}$  NMR SLR rates  $1/T_{1e} = R_{1e}$  were recorded with the spin-lock technique,  $\pi/2 \text{p}(t_{\text{lock}}) - \text{acq.}$ <sup>15,16,19,25-28</sup> The corresponding (angular) locking frequency  $\omega_1$  was chosen to be as low as possible. Here,  $\omega_1/2\pi \approx 10$  kHz was used and the duration of the locking pulse  $t_{\text{lock}}$  was varied from 100  $\mu\text{s}$  to 100 ms. Note that the recycle delay for the SLR experiments was set to at least  $5 \times 1/R_1$  in order to guarantee full longitudinal relaxation between each scan. Both  $R_1$  and  $R_{1e}$  were obtained by parameterizing the magnetic transients  $M_z(t_d)$  and  $M_e(t_{\text{lock}})$ , respectively, by stretched exponentials (see below):  $M_z(t_d) \propto 1 - \exp[-(t/T_1)^\nu]$  and  $M_e(t_{\text{lock}}) \propto \exp[-(t_{\text{lock}}/T_{1e})^\nu]$ , respectively.

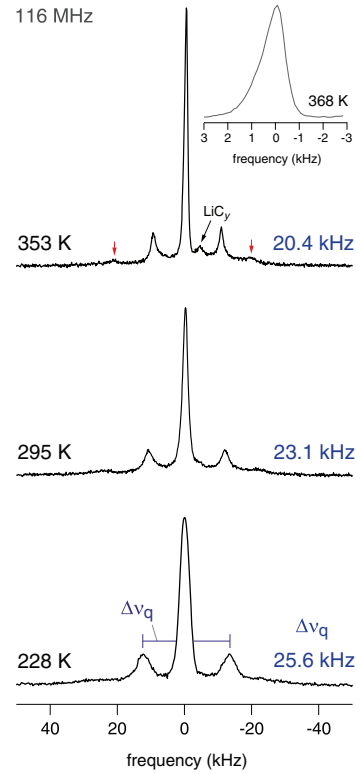


FIG. 2. (Color online) Static  $^7\text{Li}$  NMR spectra of polycrystalline  $\text{LiC}_6$  (116 MHz) recorded at the temperatures indicated. With increasing  $T$  homonuclear dipole-dipole interactions are averaged owing to  $\text{Li}^+$  hopping which results in narrowing of the linewidths. The quadrupole coupling constant  $C_q = 2\Delta\nu_q$  decreases with increasing temperature. The slight anisotropy of the central line (see inset) is due to the layered structure of the sample.

In addition, temperature-variable  $^7\text{Li}$  NMR spin-spin relaxation (SSR) rates  $1/T_2 = R_2$  were recorded by taking advantage of a (two-pulse) solid-echo pulse sequence,<sup>19</sup> that had been optimized for spin-3/2 nuclei such as  $^7\text{Li}$ .  $t_{\text{echo}}$  in  $\pi/2 - t_{\text{echo}} - (64^\circ) - \text{acq.}$  denotes the variable interpulse delay. The transients obtained can be satisfactorily described with single exponentials. Static  $^7\text{Li}$  NMR spectra were either obtained after Fourier transformation (FT) of the free induction decay, which were recorded by nonselective irradiation with a single  $\pi/2$  pulse, or by FT of the solid echo beginning from the top of the signal.

## III. RESULTS AND DISCUSSION

### A. NMR spectra and motional narrowing

Before discussing our SLR NMR results in detail, we call the reader's attention to the static  $^7\text{Li}$  NMR spectra shown in Fig. 2 which were recorded at different temperatures  $T$ . Let us first discuss the central line of the spectrum which is also determined by a distinct powder pattern because of electric

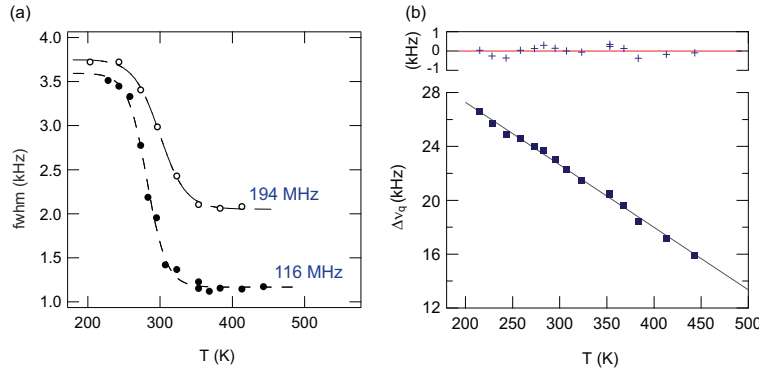


FIG. 3. (Color online) (a) Motional narrowing of the  ${}^7\text{Li}$  NMR central line of polycrystalline  $\text{LiC}_6$ . Linewidths (FWHM, full width at half maximum) were recorded at 116 and 194 MHz. Most likely, the field-dependent final width in the regime of extreme narrowing reflects both the effect of chemical shift anisotropy and, more importantly, the influence of local magnetic field gradients on the spin-spin-relaxation time; see also Ref. 29. (b) Temperature dependence of  $\Delta\nu_q$ ; the upper graph shows the deviations from the linear fit used to describe  $\Delta\nu_q(T)$ .

quadrupolar interactions (see below). At sufficiently low  $T$ ,  $\text{Li}^+$  translational motion is slow compared to the spectral width determined by the central transition. This results in dipolarly broadened NMR spectra. Motion-induced averaging of dipolar interactions causes line narrowing at elevated  $T$  [see Fig. 3(a)]. Expectedly, its overall width (full width at half maximum) in the rigid-lattice regime slightly depends on the strength  $B_0$  of the external magnetic field applied [Fig. 3(a)]. The relatively low, absolute value is compatible with lithium ions lying in planes with six nearest Li neighbors at a distance of approximately 4.3 Å. With increasing  $T$  mainly Li-Li dipolar interactions are averaged due to diffusive motion of the spins. From the motional narrowing (MN) curve an activation energy for Li hopping can be roughly estimated with the relation introduced by Waugh and Fedin. Line narrowing sets in at  $T_n \approx 260$  K which translates into  $E_{a,\text{MN}}/\text{meV} \approx 1.62 \times T_n/\text{K} \hat{=} 0.42$  eV. This value is comparable with the one deduced from the low- $T$  flank of the NMR relaxation rate peaks analyzed below; see also Ref. 30. An analysis according to the Abragam formalism<sup>31</sup> yields an even lower activation energy ( $\leq 0.2$  eV). Possible shortcomings of such analyses have recently been outlined in the study of Faske *et al.* and Storek *et al.*<sup>32,33</sup>

At high temperatures the central line reveals a slight anisotropic broadening which reflects the Li ions exposed to the layer structure of  $\text{LiC}_6$ . Furthermore, in this high- $T$  range, the NMR linewidths of the two-pulse spectra are presumably affected by internal inhomogeneous magnetic fields<sup>29</sup> that arise from the nonzero susceptibility of the  $\text{LiC}_6$  particles (see also below, Sec. III B2).

The spectrum recorded at 353 K (see Fig. 2) revealed a small amount of impurities as indicated by the arrow. Fortunately, such a small amount has negligible influence on the SLR NMR rates recorded. The signal with low intensity, that becomes visible at elevated temperatures only, might be ascribed to stage- $n$  graphite intercalation compounds (GICs) such as  $\text{LiC}_{18}$ ,  $\text{LiC}_{27}$ , or  $\text{LiC}_{36}$ .<sup>34</sup> These might be formed because of Li loss during preparation. Small amounts of the stage-2 GIC  $\text{LiC}_{12}$ , as found by XRPD (see above), could hardly be detected by NMR. In particular,  $\text{LiC}_{12}$  should be distinguishable by its different quadrupole powder pattern characterized by a smaller coupling constant<sup>34</sup> (see also below). Note that the spectra

shown in Fig. 2 are plotted such that the central lines show up at  $\nu = 0$  kHz. When referenced to an aqueous solution of  $\text{LiCl}$  (0.1 M), the NMR shift, i.e., the isotropic Knight shift, turns out to be about 41.6 ppm. This is in perfect agreement with results reported and discussed in the literature<sup>14</sup> for  $\text{LiC}_6$  (about 42.6 ppm),<sup>34</sup> previously.

Owing to the interaction of the quadrupole moment of  ${}^7\text{Li}$  (spin-quantum number 3/2) with a nonvanishing electric field gradient (EFG) at the nuclear site,<sup>31,35,36</sup> the NMR spectra are composed of satellite intensities forming a well-defined quadrupole powder pattern. Since the Li sites are electrically equivalent, a single pattern is observed. From the inner singularities (the outer ones are marked in Fig. 2 by vertically drawn arrows) the site-specific quadrupole coupling constant  $C_q = 2\Delta\nu_q$  can be estimated; see the NMR spectrum recorded at 228 K (Fig. 2). Assuming axial symmetry ( $\eta = 0$ ), as expected from the crystal structure, the quadrupole splitting  $\Delta\nu_q$  is given by  $\Delta\nu_q = |e^2qQ/(2h)|[3\cos^2(\theta) - 1]$  where  $\theta$  denotes the angle between the  $c$  axis and the external magnetic field (in the principal axis system).  $e$  is the elemental charge,  $eq$  represents the EFG at the Li site,  $Q$  is the quadrupole moment of  ${}^7\text{Li}$ , and  $h$  denotes Planck's constant. At the position of the  $90^\circ$  singularities we obtain  $\Delta\nu_q = |e^2qQ/(2h)|$  leading to  $2\Delta\nu_q = |e^2qQ/h| = C_q$ . This yields 46.2 kHz for the quadrupole coupling constant at 295 K. Note once again that the values given in Fig. 2, and those shown as a function of  $T$  in Fig. 3 as well, were obtained for an axially oriented EFG with respect to the principal axis system. The absolute values are consistent with those from  ${}^7\text{Li}$ -NMR and  ${}^8\text{Li}$ - $\beta$ -NMR measurements in the literature.<sup>34,37</sup> As an example, Letellier *et al.*<sup>34</sup> found  $\Delta\nu_q = 22.6$  kHz at ambient temperature which is in good agreement with our value (23.1 kHz). Using an oriented sample, Roth *et al.*<sup>38</sup> report a value of 22 kHz; in an early work of Conard *et al.*<sup>39</sup> a splitting of 24 kHz is found.  $\text{LiC}_{12}$ ,  $\text{LiC}_{18}$ ,  $\text{LiC}_{27}$ , and  $\text{LiC}_{36}$  show smaller quadrupole splittings  $\Delta\nu_q$  ranging from 17 to 19 kHz.<sup>34</sup>

It is worth noting that the decrease of the quadrupole splitting  $\Delta\nu_q$  with increasing  $T$  cannot simply be ascribed to changes of the lattice parameters. Owing to the narrower temperature range covered we were not able to reveal the  $T^{3/2}$  dependence found by  $\beta$ -NMR on an oriented  $\text{LiC}_6$  sample.<sup>37</sup> Here,  $\Delta\nu_q$  (200 K  $< T < 450$  K) changes linearly with  $T$ .

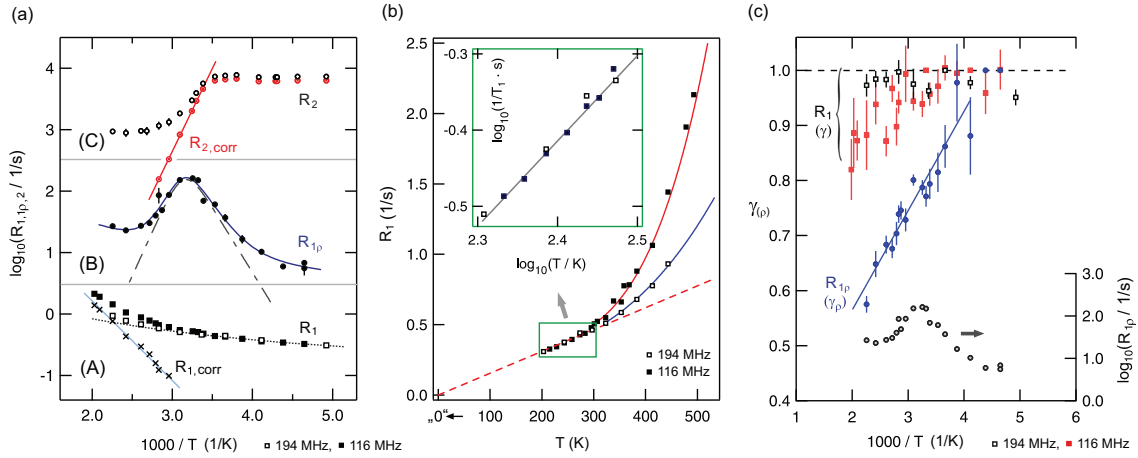


FIG. 4. (Color online) (a) Arrhenius plot illustrating the temperature dependence of the  $^{7}\text{Li}$  NMR relaxation rates  $R_1$  (A) and  $R_{1e}$  (B) measured at 116 and 194 MHz, respectively;  $R_2$  (C) rates were recorded at 116 MHz. (b)  $R_1$  of  $\text{LiC}_6$  plotted as  $R_1$  vs  $T$  and  $\log_{10} R_1$  vs  $\log_{10} T$  (inset). (c) Temperature dependence of the stretching factors  $\gamma$  obtained from the various temperature-variable NMR relaxation transients; exemplarily, selected transients  $M_e$  are depicted in Fig. 5(b). For comparison,  $R_{1e}(1/T)$  is also shown. See text for further explanations.

## B. Diffusion-induced relaxation NMR

### 1. $^{7}\text{Li}$ SLR NMR in the laboratory and rotating frame of reference

In the Arrhenius presentation of Fig. 4(a) an overview of the  $^{7}\text{Li}$  NMR relaxation rates measured is given. At first we will briefly discuss the SLR NMR rates recorded at 116 MHz and 194 MHz, i.e., in the laboratory frame of reference. At low temperatures  $R_1$  seems to be independent of the Larmor frequency applied. Combined with a linear dependence of  $R_1$  on temperature, this is expected for SLR being mainly induced by coupling of the Li spins with conduction electrons. Indeed, a power-law fit

$$R_1 \propto T^\kappa, \quad (1)$$

indicated by the dotted line shown in Fig. 4(a), yields  $\kappa = 1.1(1)$ . This can be even better illustrated by plotting  $R_1$  vs  $T$ : The dashed line in Fig. 4(b) represents ideal linear behavior according to  $R_1 = s'T^\kappa$  with  $\kappa = 1$ . The inset uses the representation  $\log_{10} R_1$  vs  $\log_{10} T$  to calculate  $\kappa$  in the low-temperature regime with a linear fit. The latter yields  $s' = 7.9(3) \times 10^{-4} \text{ s}^{-1} \text{ K}^{-1}$  and  $\kappa = 1.12(4)$  (cf. the power-law analysis shown above). The product  $T_1 T$  turns out to be approximately  $650 \pm 15 \text{ s} \cdot \text{K}$ , which is in very good agreement with the  $^{7}\text{Li}$  NMR result reported by Estrade *et al.*<sup>14</sup> ( $600 \pm 120 \text{ s} \cdot \text{K}$ ).

Above 300 K the rates  $R_1$  increasingly deviate from  $R_1 = S_0 T$  which points to the influence of other relaxation mechanisms owing to  $\text{Li}^+$  hopping processes or (anharmonic) lattice vibrations. A two-phonon Raman process would give  $R_1 \propto T^2$  at temperatures  $T$  larger or similar to the Debye temperature  $\Theta$ . In order to separate such background effects from diffusion-induced processes, we extrapolated the power-law fit of Fig. 4(a) to higher temperatures and subtracted the rates from the overall ones measured; i.e.,

$$R_{1,\text{corr}} = R_1 - R_{1,e} \quad (2)$$

with  $R_{1,e} \approx S_0 T^\kappa$ . If we assume that the background-corrected rates obtained are mainly influenced by Li hopping, an activation energy can be roughly estimated. Note that the rates were recorded in the regime  $\omega_0 \tau \gg 1$ ; i.e., the activation energy  $E_{a,T_1}$  should be characteristic of short-range (or localized) Li motions in  $\text{LiC}_6$ . These might include translational processes in  $\text{LiC}_6$  with a short jump distance.<sup>5</sup> Here, we obtain  $0.25(2) \text{ eV}$  which is very similar to the result previously estimated from NMR line narrowing.<sup>14</sup>

Ion dynamics proceeding on a longer length scale, however, can only be probed when the so-called high- $T$  flank of the diffusion-induced rate peak is reached. In the present case, this needs very high temperatures. Fortunately, the spin-lock technique can be used which is *per se* sensitive to slower Li motions covering a longer time scale. Therefore, we recorded diffusion-induced SLR NMR rate peaks at frequencies  $\omega_1$  on the order of some kHz instead of using  $\omega_0$  with values in the MHz range. Doing so, by formally replacing  $\omega_0$  with  $\omega_1$  the SLR NMR rate peak shifts towards lower temperature so that both the maximum and the high- $T$  flank become accessible. The corresponding rates  $R_{1e}$ , which have been extracted from the stretched magnetization transients recorded, are shown in Fig. 4(a) as a function of the inverse temperature. At low temperatures, that is, below 250 K, they are increasingly governed by nondiffusive background effects. Note that the ratio  $R_{1e}/R_1$  turns out to be approximately 1.5 orders of magnitude. Thus, besides interactions of the Li spins with conduction electrons in the case of  $R_1$  measurements (see above), the low- $T$   $R_{1e}$  rates seem to be influenced by additional processes (see below). For comparison, the corresponding stretching factors of the various transients measured are shown in Fig. 4(c). In Fig. 5 selected magnetization transients of the  $R_{1e}$  NMR measurements are shown.

Finally, with increasing  $T$  the overall rates  $R_{1e}$  pass through a maximum located at  $T = 314 \text{ K}$ . At even higher

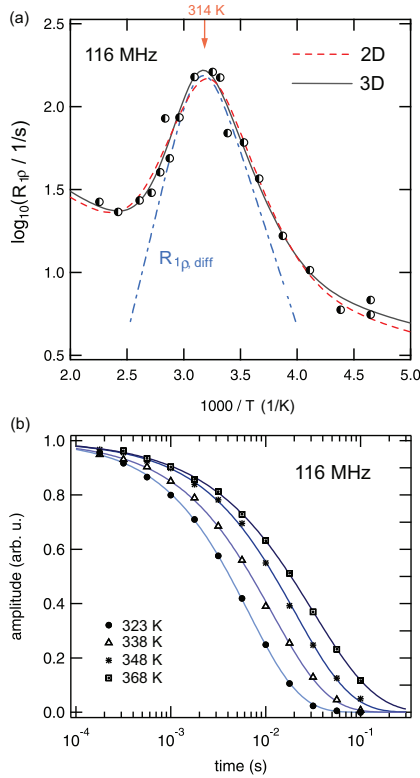


FIG. 5. (Color online) (a)  ${}^7\text{Li}$  SLR  $\rho$  NMR rates of polycrystalline LiC<sub>6</sub> (see Fig. 4), plotted in an Arrhenius diagram. For comparison with the fit according to Eqs. (3) and (4) (solid line), the dashed line represents the 2D fit by means of Eq. (6). The dashed-dotted line shows the purely Li<sup>+</sup> diffusion-induced contribution when the rates are analyzed in terms of a modified BPP-type spectral density function yielding 0.57(2) eV and  $\beta = 1.7(2)$ . (b) Selected temperature-variable magnetization transients  $M_e(t_{\text{lock}})$  containing the  ${}^7\text{Li}$  SLR NMR rates in the rotating frame of reference. The transients illustrate the behavior of  $M_e$  on the high- $T$  flank of the diffusion-induced rate peak shown above. Solid lines show fits with stretched exponentials  $M_e(t_{\text{lock}}) \propto \exp[-(t_{\text{lock}}/T_{1e})^{\gamma_e}]$ ; in this  $T$  range the stretching factor  $\gamma_e$ , also shown in Fig. 4(c), scatters around 0.7 [see Fig. 4(c)].

temperatures, i.e., when  $R_{1e}$  decreases, the nondiffusive relaxation background shows up again. In order to separate unwanted background effects from diffusion-induced contributions, the overall rates  $R_{1e}$  were, in the first place, approximated with a sum of a modified BPP-type relaxation function and a power-law expression:

$$\begin{aligned} R_{1e}^{3D} &= R_{1e,\text{diff}}^{3D} + R_{1e,\text{bgr}} \\ &= C_e (J(2\omega_1) + \frac{5}{3}J(\omega_0) + \frac{2}{3}J(2\omega_0)) + BT^{\kappa'} \end{aligned} \quad (3)$$

with  $J(\omega_{1(0)})$  being here a Lorentzian-shaped spectral density function according to

$$J(\alpha \cdot \omega_{1(0)})_{\alpha=1,2} = C' \tau_c / [1 + (\alpha \cdot \omega_{1(0)} \tau_c)^\beta]. \quad (4)$$

Note that the correlation rate  $\tau_c^{-1}$  is on the order of the jump rate  $\tau^{-1}$ . In many cases it can be described by an Arrhenius relation containing the pre-exponential factor  $\tau_0^{-1}$  and the activation energy  $E_a$  determining long-range Li diffusion

$$\tau_c^{-1} \approx \tau^{-1} = \tau_0^{-1} \exp(-E_a/k_B T); \quad (5)$$

$k_B$  denotes Boltzmann's constant. Here, the best fit yields  $\kappa' = 2.0(4)$ , thus indicating that lattice vibrations become the main origin of background relaxation (see above). The parameter  $\beta$  reflects any asymmetry of the rate peak  $R_{1e}(1/T)$  which may arise from correlation effects such as structural disorder and/or Coulomb interactions.<sup>20,21</sup> In general, uncorrelated motion should result in a symmetric NMR rate peak; any correlation effects, for comparison, are expected to reduce the slope on the low- $T$  side compared to the situation in the limit  $\omega_1 \tau \ll 1$ , that is, the high- $T$  regime. In the present case we found  $\beta = 1.7(2)$ ; thus, the diffusion-induced rate peak, indicated by the dashed-dotted line in Fig. 4(a), is slightly asymmetric.

The activation energy  $E_a$  turned out to be 0.57(2) eV; the prefactor  $\tau_0^{-1}$  is approximately  $1.6 \times 10^{14} \text{ s}^{-1}$ . The latter is in very good agreement with values typically expected for phonon frequencies. Moreover,  $E_a \approx 0.57 \text{ eV}$  is consistent with the prediction of Freiländer *et al.*<sup>7</sup> The value obtained from Eq. (3) also equals the activation energy which can be directly obtained from the high- $T$  side of the rate peak. Moreover, in the limit  $\omega_1 \tau \gg 1$ , where  $J(\omega_1, \tau) \propto \omega^{-\beta} \tau^{1-\beta}$  holds, the corresponding slope yields  $E_{a,\text{low}} = 0.42(2) \text{ eV}$ . In the present case,  $E_{a,\text{low}}$  and  $E_a$  obey the relation  $E_{a,\text{low}} = (\beta - 1)E_a$ . Note that the same result is obtained when Eq. (3) is restricted to the first term:  $R_{1e,\text{diff}} \propto J(2\omega_1)$ .

It is worth noting that  $J(\omega)$  in Eq. (4) represents a spectral density function which describes diffusive motion in three dimensions (3D). Frequency-dependent  $\beta$ -NMR measurements,<sup>7,8</sup> however, indicate a low-dimensional diffusion process in LiC<sub>6</sub>. Additionally, at temperatures higher than 630 K, a 2D motional process was claimed based on QENS measurements.<sup>5</sup> Therefore, we also tried to analyze our SLR NMR data with a semiempirical spectral density function for 2D diffusion. In concrete terms, we used the expression by Richards<sup>40,41</sup> which is based on a function introduced by Avogadro and Villa taking account of a logarithmic frequency dependence in the high-temperature limit  $\omega_{(1)} \tau_c \ll 1$ .<sup>42,43</sup> Following K uchler *et al.*,<sup>44</sup> who first incorporated the effect of correlation via the parameter  $\beta$  also for 2D diffusion, it reads

$$\begin{aligned} R_{1e}^{2D} &= R_{1e,\text{diff}}^{2D} + R_{1e,\text{bgr}} \\ &\approx C'_e \tau_c \ln[1 + 1/(2\omega_1 \tau_c)^\beta] + B'T^{\kappa''}. \end{aligned} \quad (6)$$

This ansatz worked well for other layer-structured materials showing 2D diffusion.<sup>10,12,13,18</sup> The fit, indicated in Fig. 5 by the dashed line, yields  $B \approx B'$  and  $\kappa' \approx \kappa''$ . Moreover,  $E_a^{2D}$  is given by approximately 0.62 eV and, thus, at least comparable to the result obtained by Eqs. (3) and (4). However, in the present case, the prefactor  $\tau_0^{-1}$  turns out to be unusually high; it would be approximately  $1.8 \times 10^{16} \text{ s}^{-1}$ . This is by about two orders of magnitude larger than that obtained from the modified-BPP fit used to describe the temperature dependence of the NMR rates (*vide supra*). Hence, based on the results obtained it seems that the semiempirical Richards model (represented by the dashed line in Fig. 5) is less appropriate to

describe Li dynamics in LiC<sub>6</sub>. Certainly, this fact might also be explained by nonnegligible Li hopping processes taking place via defects perpendicular to the layers, that is, channel-like diffusion, influencing the NMR response of a pure 2D process.

## 2. <sup>7</sup>Li NMR spin-spin relaxation

The results obtained from SLR NMR are corroborated by the analysis of complementary spin-spin relaxation (SSR) data. In agreement with the results of Eqs. (3) and (4), temperature-variable SSR measurement yield an activation energy of 0.53(2) eV. This value can be extracted from the rates measured as follows. Below 285 K, that is, in the so-called rigid lattice regime,  $R_2^{-1}$  is almost independent of temperature and amounts to approximately 125  $\mu$ s. Owing to averaging of dipole-dipole interactions, because of increasing of the Li<sup>+</sup> hopping, the rates significantly start to decrease indicating long-range Li translational motion. Interestingly, at 400 K they reach a plateau value characterized by  $R_{2,\text{high}}^{-1} \approx 1$  ms. This feature is very similar to the one observed by McDowell *et al.*<sup>29</sup> previously in the 2D H<sup>+</sup> ion conductor ZrBe<sub>2</sub>H<sub>1.4</sub> (ZBH). In ZBH the deviation is ascribed to long-range H motion in the presence of a magnetic field gradient which is due to the nonzero magnetic susceptibility of the metal hydride. The mean-field gradient in ZBH is directly proportional to the magnitude  $B_0$  of the external magnetic field applied. As a result, the lower the Larmor frequency used the farther the beginning of the plateau is shifted towards higher temperature resulting in a decrease of  $R_{2,\text{high}}$ . Hence, the residual NMR (central) linewidth in the regime of extreme motional narrowing is expected to be smaller for measurements carried out at 116 MHz compared to those performed at 194 MHz [see Fig. 3(a)].

Subtracting  $R_{2,\text{high}}$  from the overall rates measured yields  $R_{2,\text{corr}}$ . From the linear fit shown in Fig. 4(a) the above-mentioned activation energy [0.53(2) eV] can be deduced. Lastly, with the help of both  $R_{1e}$  and  $R_2$  measurements it is possible to probe Li diffusion in LiC<sub>6</sub> at temperatures ranging from 270 K to 360 K. This regime coincides with the operating range for most battery applications.

### C. Li jump rates and self-diffusion coefficients

Considering the maximum of the  $R_{1e}(1/T)$  peak probed, it is possible to precisely determine the mean Li jump rate irrespective of the spectral density function  $J$  chosen to parametrize the data. At  $T = 314$  K, that is the temperature where the peak shows up [see Fig. 5(a)], for SLR NMR in the rotating frame of reference the condition  $\omega_1 \tau_c \approx 0.5$  holds.<sup>9</sup> Identifying  $\tau_c$  with the motional residence time of an Li spin and inserting  $\omega_1 = 2\pi \times 10(1)$  kHz, we obtain  $\tau_c \approx \tau = 8 \mu$ s. According to the Einstein-Smoluchowski equation,<sup>46</sup>

$$D_{dD} = a^2 / (2d \cdot \tau), \quad (7)$$

this corresponds to  $D_{2D}(314\text{K}) \approx 1.9 \times 10^{-11} \text{ cm}^2 \text{ s}^{-1}$  and  $D_{3D}(314 \text{ K}) \approx 1.3 \times 10^{-11} \text{ cm}^2 \text{ s}^{-1}$ . Here, we used  $a \approx 3 \text{ \AA}$  as a good approximation for a mean jump distance and calculated the diffusion coefficient for both spatially restricted and nonrestricted motion, i.e., for  $d = 2$  or  $d = 3$ , whereby  $d$  represents the dimensionality of the diffusion process.

In Fig. 6(a) the jump rate determined by means of the Li<sup>+</sup> diffusion-induced  $R_{1e}(1/T)$  rate peak is shown in an Arrhenius plot and compared with those values which can be estimated from (analogous) <sup>8</sup>Li  $\beta$ -NMR measurements of Freiländer *et al.*<sup>7</sup> Although <sup>8</sup>Li NMR was carried out on oriented (HOPG) LiC<sub>6</sub> samples good agreement is found. For comparison, the solid line represents an Arrhenius line characterized by an activation energy of 0.55 eV, which represents the mean value when the results from  $R_{1e}$  and  $R_2$  are considered. The gray area indicates the temperature range covered by Li<sup>+</sup> diffusion-induced  $R_{1e}$  measurements. From the Arrhenius line indicated a prefactor  $\tau_0^{-1}$  can be estimated ( $\approx 1 \times 10^{14} \text{ s}^{-1}$ ) which is consistent with that obtained from the analysis of the  $R_{1e}(1/T)$  NMR peak with a BPP-type expression (*vide supra*).

Besides  $R_{1e}$  measurements also  $R_2$  (and motional line narrowing as well) is suitable to estimate Li jump rates. At the temperature where the rates  $R_2$  start to decrease [ $T \approx 294$  K; see Fig. 4(a)] the Li jump rate is expected to be on the order of  $\tau^{-1} \approx 2\pi R_{20}$  with  $R_{20}^{-1} = T_{20} = 140 \mu$ s being the rigid-lattice SLR NMR rate. This yields  $\tau = 22 \mu$ s. Even slower motions can be estimated from the onset of motional line narrowing; in the present case NMR central lines significantly start to decrease in linewidth at  $T \approx 250$  K. Roughly spoken, this is expected when  $\tau$  reaches values on the order of a few ms. Additionally, the inflexion point ( $T_{\text{infl.}} \approx 275$  K at 116 MHz) of the whole motional narrowing (MN) curve (see above, Fig. 3) can be used to estimate  $\tau$  according to  $\tau^{-1}(T_{\text{infl.}}) \approx 2\pi \nu_0$  with  $\nu_0$  being the rigid-lattice linewidth ( $\approx 3.5$  kHz). For comparison, the values estimated from SSR NMR and MN are also included in Fig. 6(a).

It is worth noting that in the presence of a broad distribution of jump rates [note that such a feature would also be reflected in a deviation of  $\beta$  from BPP-type behavior ( $\beta = 2$ )], the NMR line narrowing would be predominantly influenced by that fraction of ions diffusing faster compared to others. Hence, as indicated above, the interpretation of MN NMR data can easily lead to an overestimation of the mean lithium jump rate and an underestimation of the activation energy; see, e.g., Refs. 32 and 33. For comparison, activation barriers ranging from 0.1 and 0.3 eV have been calculated for different types of interstitialcy diffusion mechanisms in LiC<sub>6</sub>.<sup>22</sup>

Finally, considering the rates shown in Fig. 6(a), at room temperature (293 K) the Li jump rate turns out to be  $4.5 \times 10^4 \text{ s}^{-1}$ . This corresponds to a self-diffusion coefficient on the order of  $5 \times 10^{-12} \text{ cm}^2 \text{ s}^{-1}$  at 293 K. Decreasing the temperature from 293 to 268 K ( $-5^\circ\text{C}$ ), Li self-diffusivity is slowed down by a factor of 10. Such key figures are crucial for the safe and efficient operation of graphite-based ion batteries. In particular, at freezing temperatures the performance of a battery is then additionally limited and controlled to a large extent by slow Li diffusion within the host material. It is noteworthy that room-temperature self-diffusion coefficients ranging from  $10^{-16} \text{ m}^2 \text{ s}^{-1}$  to  $10^{-15} \text{ m}^2 \text{ s}^{-1}$ , as found for LiC<sub>6</sub> here, are comparable to those recently obtained by NMR also for layer-structured cathode materials such as Li<sub>1-x $\approx$ 0.7</sub>TiS<sub>2</sub>.<sup>10</sup> Thus, regarding Li *self-diffusion* in fully intercalated stage-1 LiC<sub>6</sub>, Li ion mobility does not exceed that of conventional cathode materials.

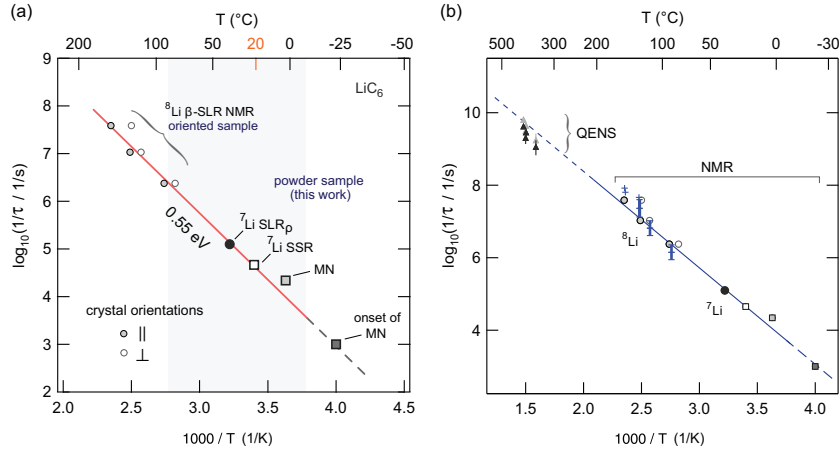


FIG. 6. (Color online) (a) Arrhenius plot of Li jump rates in LiC<sub>6</sub> deduced from various NMR techniques being sensitive to translational ion jumps on quite different time scales, here, covering up to five decades. SLR NMR rate peaks provide a relatively theory-independent determination of jump rates. The rates determined by  $\beta$ -NMR were deduced from Ref. 7. See text for further explanation. (b) Comparison of the rates shown in (a) with those obtained from QENS (Ref. 5). The diffusion coefficients from QENS reported by Magerl *et al.* (Ref. 5) have been roughly converted into jump rates  $\tau^{-1}$  (triangles in black) via the Einstein-Smoluchowski equation [see Eq. (7)] assuming, as suggested in Ref. 5, 2D diffusion and a relatively long jump distance  $a$  of approximately 4.26 Å. Using  $a \approx 3$  Å, which is close to the average of possible jump distances in LiC<sub>6</sub>, yields the rates shown by gray triangles.  $a = 2.5$  Å, which is the jump distance for an interstitial migration mechanism (Refs. 22 and 45), yields an even better agreement. The crosses represent jump rates from  $\beta$ -NMR presented in Ref. 8.

Strictly speaking, the results presented here should not be mixed with *chemical* diffusion coefficients which have been experimentally probed via (solid-state) electrochemical macroscopic method as well as calculated ( $4 \times 10^{-12} \text{ m}^2 \text{ s}^{-1}$ ,  $E_a \approx 0.4 \text{ eV}$ ) recently for 2D (in-plane) Li<sup>+</sup> motion in LiC<sub>6</sub>.<sup>47</sup> Interestingly, the results of the theoretical work by Toyoura *et al.*<sup>45</sup> on ordered LiC<sub>6</sub> agree well with the present findings. Activation barriers for Li migration, which were calculated separately for the vacancy and interstitial Li migration process, turned out to be approximately 0.5 eV; see also Ref. 22. The corresponding (in-plane) diffusion coefficients are  $10^{-14} \text{ m}^2 \text{ s}^{-1}$  and  $10^{-15} \text{ m}^2 \text{ s}^{-1}$ , respectively. Apart from this good agreement, the present results are in line with those from earlier experimental studies; see, e.g., Ref. 48 for an overview of Li (chemical) diffusion coefficients determined for various carbon anode materials. Note that by the application of NMR spectroscopy we were able to study Li ion dynamics separately from electron dynamics in mixed conducting LiC<sub>6</sub>. While the latter influences the SLR NMR rates recorded at low temperatures, with increasing  $T$  diffusive motions significantly govern spin-lattice relaxation while other interactions relatively lose ground. These show up once again at temperatures higher than 400 K.

As a last comparison, in Fig. 6(b) data from the QENS study of Magerl *et al.*,<sup>5</sup> pointing to an in-plane 2D jump-type diffusion mechanism, are included. The self-diffusion coefficients deduced from QENS have been roughly converted into jump rates according to Eq. (7). Here, we used both  $a \approx 4.26$  Å as found by QENS for the 2D diffusion process and  $a \approx 3$  Å, which is a good approximation for the average of possible jump distances. Considering the error limits and the narrow temperature range covered by the earlier study,<sup>5</sup>

in our opinion, a relatively good agreement is found with the results obtained from NMR. The solid line is to guide the eye and refers to an Arrhenius law with  $E_a = 0.54 \text{ eV}$  and  $\tau_0^{-1} = 5 \times 10^{13} \text{ s}^{-1}$  which is very similar to that shown in Fig. 6(a). To sum up, over a relatively broad dynamic range a single Arrhenius relation seems to be appropriate to describe Li diffusion in ordered LiC<sub>6</sub>.

#### IV. CONCLUSIONS AND OUTLOOK

Spin-lattice relaxation NMR using the stable isotope <sup>7</sup>Li was applied to probe room-temperature Li dynamic parameters in polycrystalline, mixed conducting LiC<sub>6</sub> being the most widely used anode material. As deduced from atomic-scale NMR measurements Li hopping in the bulk is characterized by an activation energy of approximately 0.55 eV and an Li self-diffusion coefficient of  $10^{-15} \text{ m}^2 \text{ s}^{-1}$  (295 K), thus, comparable to Li self-diffusivity in layer-structured transition metal sulfides and oxides serving as positive electrodes in lithium-ion batteries.

The results obtained from the different NMR techniques employed are in good agreement with previous studies<sup>7,8</sup> using <sup>8</sup>Li  $\beta$ -NMR to probe diffusion parameters at elevated temperatures. Most importantly, the jump rates can be well approximated with a *single* Arrhenius law which is determined by an activation energy of approximately 0.55 eV and a pre-factor on the order of typical phonon frequencies, viz.,  $10^{14} \text{ s}^{-1}$ . On that note the present study updates our knowledge on Li self-diffusion in LiC<sub>6</sub>. It is noteworthy that the activation energy probed by NMR is in fair agreement with calculated barrier heights ( $\approx 0.5 \text{ eV}$ ) by Toyoura *et al.*<sup>45</sup> for both the in-plane vacancy and interstitial Li migration mechanism. Even the

chemical diffusion coefficients reported by Toyoura *et al.*<sup>45</sup> (viz.,  $10^{-14}$  m<sup>2</sup> s<sup>-1</sup> and  $10^{-15}$  m<sup>2</sup> s<sup>-1</sup> for the interstitial and vacancy mechanism, respectively) agree with the present findings.

Considering solely <sup>7</sup>Li NMR rates, it is difficult to judge whether the diffusion process probed is strictly governed by 2D diffusion. The present results are in very good agreement with those probed by orientation-dependent and frequency-dependent SLR <sup>8</sup>Li  $\beta$ -NMR measurements on highly oriented pyrolytic graphite. The  $\beta$ -NMR results indeed gave strong evidence for low-dimensional lithium diffusion.<sup>7,8</sup> Fair agreement is also found with results from QENS probing in-plane diffusion in the ordered phase of LiC<sub>6</sub>.<sup>5</sup> Recent theoretical investigations also strongly point to high lithium-ion diffusivity in the direction parallel to the graphene layers and to much slower interlayer hopping, that is, motion across the basal plane.<sup>47</sup>

However, though there are convincing reasons to claim even microscopic Li diffusion as purely low-dimensional in LiC<sub>6</sub>, the semiempirical SLR NMR model introduced by Richards for 2D motion seem to be less adequate to satisfactorily describe the temperature dependence of the <sup>7</sup>Li NMR  $R_{1\rho}(1/T)$  rate peak probed here. The applicability of a modified BPP-type relaxation model, see, e.g., the

previous work by Küchler *et al.*,<sup>44</sup> might indicate a small, but nonnegligible, influence of interlayer hopping process on the diffusion-induced SLR NMR rates.

To shed further light on the Li dynamics in LiC<sub>6</sub>, the application of NMR techniques being able to directly record motional correlation functions might be beneficial. For instance, considering the temperature range below 300 K, this should be possible via the generation of Jeener-Broekaert NMR echoes<sup>49</sup> with the so-called spin-alignment echo (SAE) technique.<sup>50-53</sup> In general, SAE (or stimulated echo) NMR is sensitive to extremely slow translational and rotational jump processes.<sup>54-60</sup>

#### ACKNOWLEDGMENTS

We thank our colleagues at the TU Graz and at the Leibniz University Hannover for valuable discussions. Financial support by the Deutsche Forschungsgemeinschaft (DFG) is highly appreciated (DFG Research Unit 1277, Grant No. WI3600/2-2 and 4-1 and Grant No. HE1574/13-2), and by the Austrian Federal Ministry of Economy, Family, and Youth and the Austrian National Foundation for Research, Technology, and Development is greatly appreciated.

\*The authors were equally involved in experimental work, data analysis, and project planning. Corresponding author: julia.langer@tugraz.at

<sup>†</sup>See also for correspondence: viktor.epp@tugraz.at

<sup>‡</sup>See also for correspondence: wilkening@tugraz.at

<sup>1</sup>M. S. Whittingham, *Chem. Rev.* **104**, 4271 (2004).

<sup>2</sup>J. M. Tarascon and M. Armand, *Nature (London)* **414**, 359 (2001).

<sup>3</sup>M. Wakihara and O. Yamamoto, eds., *Lithium Ion Batteries* (Wiley-VCH, Weinheim, 1998).

<sup>4</sup>M. Winter and J. O. Besenhard, *Electrochem. Acta* **45**, 31 (1999).

<sup>5</sup>A. Magerl, H. Zabel, and I. S. Anderson, *Phys. Rev. Lett.* **55**, 222 (1985).

<sup>6</sup>T. Springer and R. E. Lechner, in *Diffusion in Condensed Matter—Methods, Materials, Models*, 2nd ed, edited by P. Heitjans and J. Kärger (Springer, Berlin, 2005), Chap. 3, pp. 91–164.

<sup>7</sup>P. Freiländer, P. Heitjans, H. Ackermann, B. Bader, G. Kiese, A. Schirmer, H.-J. Stöckmann, C. V. der Marel, A. Magerl, and H. Zabel, *Z. Phys. Chem.* **151**, 93 (1987).

<sup>8</sup>A. Schirmer and P. Heitjans, *Z. Naturforsch.* **50a**, 643 (1995).

<sup>9</sup>P. Heitjans, A. Schirmer, and S. Indris, in *Diffusion in Condensed Matter*, edited by P. Heitjans and J. Kärger (Springer, Berlin, 2005), Chap. 9, p. 367.

<sup>10</sup>M. Wilkening and P. Heitjans, *Phys. Rev. B* **77**, 024311 (2008).

<sup>11</sup>M. Wilkening, A. Kuhn, and P. Heitjans, *Phys. Rev. B* **78**, 054303 (2008).

<sup>12</sup>V. Epp and M. Wilkening, *Phys. Rev. B* **82**, 020301 (2010).

<sup>13</sup>V. Epp, O. Gün, H.-J. Deiseroth, and M. Wilkening, *Phys. Chem. Chem. Phys.* **15**, 7123 (2013).

<sup>14</sup>H. Estrade, J. Conard, P. Lauginie, P. Heitjans, F. Fujara, W. Buttler, G. Kiese, H. Ackermann, and D. Guérard, *Physica B* **99**, 531 (1980).

<sup>15</sup>D. Ailion and C. P. Slichter, *Phys. Rev. Lett.* **12**, 168 (1964).

<sup>16</sup>C. P. Slichter and D. Ailion, *Phys. Rev.* **135**, A1099 (1964).

<sup>17</sup>M. Wilkening, W. Iwaniak, J. Heine, V. Epp, A. Kleinert, M. Behrens, G. Nusspl, W. Bensch, and P. Heitjans, *Phys. Chem. Chem. Phys.* **9**, 6199 (2007).

<sup>18</sup>V. Epp, S. Nakhal, M. Lerch, and M. Wilkening, *J. Phys.: Condens. Matter* **25**, 195402 (2013).

<sup>19</sup>E. Fukushima and S. B. W. Roeder, *Experimental Pulse NMR: A Nuts and Bolts Approach* (Addison-Wesley Pub. Co., Advanced Book Program, Reading, MA, 1981).

<sup>20</sup>M. Meyer, P. Maass, and A. Bunde, *Phys. Rev. Lett.* **71**, 573 (1993).

<sup>21</sup>A. Bunde, W. Dieterich, P. Maass, and M. Meyer, in *Diffusion in Condensed Matter—Methods, Materials, Models*, 2nd ed, edited by P. Heitjans and J. Kärger (Springer, Berlin, 2005), Chap. 20, pp. 813–856.

<sup>22</sup>K. Toyoura, Y. Koyama, A. Kuwabara, and I. Tanaka, *J. Phys. Chem. C* **114**, 2375 (2010).

<sup>23</sup>A. Herold, *Synth. Met.* **23**, 27 (1988).

<sup>24</sup>D. Guérard and A. Hérol, *Carbon* **13**, 337 (1975).

<sup>25</sup>D. C. Ailion and C. P. Slichter, *Phys. Rev.* **137**, A235 (1965).

<sup>26</sup>D. C. Look and I. J. Lowe, *J. Chem. Phys.* **44**, 2995 (1966).

<sup>27</sup>T. J. Rowland and F. Y. Fradin, *Phys. Rev.* **182**, 760 (1969).

<sup>28</sup>D. Wolf, *Phys. Rev. B* **10**, 2724 (1974).

<sup>29</sup>A. F. McDowell, C. F. Mendelsohn, M. S. Conradi, R. C. Bowman, and A. J. Maeland, *Phys. Rev. B* **51**, 6336 (1995).

<sup>30</sup>M. Wilkening, D. Bork, S. Indris, and P. Heitjans, *Phys. Chem. Chem. Phys.* **4**, 3246 (2002).

<sup>31</sup>A. Abragam, *The Principles of Nuclear Magnetism* (Clarendon, Oxford, 1961).

<sup>32</sup>S. Faske, H. Eckert, and M. Vogel, *Phys. Rev. B* **77**, 104301 (2008).

- <sup>33</sup>M. Storek, R. Böhmer, S. W. Martin, D. Larink, and H. Eckert, *J. Chem. Phys.* **137**, 124507 (2012).
- <sup>34</sup>M. Letellier, F. Chevallier, and F. Béguin, *J. Phys. Chem. Solids* **67**, 1228 (2006).
- <sup>35</sup>P. Diehl, E. Fluck, H. Günther, R. Kosfeld, and J. Seelig, eds., *NMR—Basic Principles and Progress*, Vol. 30 (Springer, Berlin, 1994).
- <sup>36</sup>D. Freude and J. Haase, in *NMR—Basic Principles and Progress*, edited by P. Barker and H. Pfeiffer, Vol. 29 (Springer, Berlin, 1993).
- <sup>37</sup>P. Freiländer, P. Heitjans, H. Ackermann, B. Bader, G. Kiese, A. Schirmer, and H.-J. Stöckmann, *Z. Naturforsch. A* **41**, 109 (1986).
- <sup>38</sup>G. Roth, K. Lüders, P. Pflüger, and H.-J. Güntherodt, *Solid State Commun.* **39**, 423 (1981).
- <sup>39</sup>J. Conard and H. Estrade, *Mat. Sci. Eng.* **31**, 173 (1977).
- <sup>40</sup>P. M. Richards, *Solid State Commun.* **25**, 1019 (1978).
- <sup>41</sup>P. M. Richards, in *Topics in Current Physics*, edited by M. B. Salamon, Vol. 15 (Springer, Berlin, 1979).
- <sup>42</sup>A. Avogadro and M. Villa, *J. Chem. Phys.* **66**, 2359 (1977).
- <sup>43</sup>C. A. Sholl, *J. Phys. C* **14**, 447 (1981).
- <sup>44</sup>W. Küchler, P. Heitjans, A. Payer, and R. Schöllhorn, *Solid State Ion.* **70/71**, 434 (1994).
- <sup>45</sup>K. Toyoura, Y. Koyama, A. Kuwabara, F. Oba, and I. Tanaka, *Phys. Rev. B* **78**, 214303 (2008).
- <sup>46</sup>H. Mehrer, *Diffusion in Solids* (Springer, Berlin, 2006).
- <sup>47</sup>K. Persson, V. A. Sethuraman, L. J. Hardwick, Y. Hinuma, Y. S. Meng, A. van der Ven, V. Srinivasan, R. Kostecki, and G. Ceder, *J. Phys. Chem. Lett.* **1**, 1176 (2010).
- <sup>48</sup>M. Park, X. Zhang, M. Chung, G. B. Less, and A. M. Sastry, *J. Power Sources* **195**, 7904 (2010).
- <sup>49</sup>J. Jeener and P. Broekaert, *Phys. Rev.* **157**, 232 (1967).
- <sup>50</sup>R. Böhmer, T. Jörg, F. Qi, and A. Titze, *Chem. Phys. Lett.* **316**, 419 (2000).
- <sup>51</sup>F. Qi, T. Jörg, and R. Böhmer, *Solid State Nucl. Magn. Res.* **22**, 484 (2002).
- <sup>52</sup>M. Wilkening, J. Heine, C. Lyness, A. R. Armstrong, and P. G. Bruce, *Phys. Rev. B* **80**, 064302 (2009).
- <sup>53</sup>M. Wilkening, W. Küchler, and P. Heitjans, *Phys. Rev. Lett.* **97**, 065901 (2006).
- <sup>54</sup>X.-P. Tang, R. Busch, W. L. Johnson, and Y. Wu, *Phys. Rev. Lett.* **81**, 5358 (1998).
- <sup>55</sup>M. Lausch and H. W. Spiess, *J. Magn. Reson.* **54**, 466 (1983).
- <sup>56</sup>H. W. Spiess, *J. Chem. Phys.* **72**, 6755 (1980).
- <sup>57</sup>G. Fleischer and F. Fujara, in *NMR—Basic Principles and Progress*, edited by P. Diehl, E. Fluck, H. Günther, R. Kosfeld, and J. Seelig, Vol. 30 (Springer, Berlin, 1994).
- <sup>58</sup>F. Fujara, S. Wefing, and H. Spiess, *J. Chem. Phys.* **84**, 4579 (1986).
- <sup>59</sup>T. Dries, F. Fujara, M. Kiebel, E. Rössler, and H. Silescu, *J. Chem. Phys.* **88**, 2139 (1988).
- <sup>60</sup>M. Wilkening and P. Heitjans, *Solid State Ion.* **177**, 3031 (2006).

### 3.5 Structurally disordered Li-ion conductors

#### 3.5.1 Motion of Li<sup>+</sup> in nanoengineered LiBH<sub>4</sub> and LiBH<sub>4</sub>:Al<sub>2</sub>O<sub>3</sub> — Comparison with the microcrystalline form (pp. 107–114)

Epp, V. and Wilkening, M. *ChemPhysChem* **14**, 3706–3713 (2013).—This article is reproduced by permission of Wiley-VCH. The original article can be found online at <http://onlinelibrary.wiley.com/doi/10.1002/cphc.201300743/abstract>. ©2013 Wiley-VCH Verlag GmbH & Co. KGaA, Weinheim.

DOI: 10.1002/cphc.201300743

# Motion of Li<sup>+</sup> in Nanoengineered LiBH<sub>4</sub> and LiBH<sub>4</sub>:Al<sub>2</sub>O<sub>3</sub> Comparison with the Microcrystalline Form

Viktor Epp\* and Martin Wilkening<sup>[a]</sup>

The introduction of structural disorder and large volume fractions of different kinds of interfaces enables the manipulation of ion dynamics in solids. Variable-temperature solid-state NMR relaxometry is highly useful to study Li<sup>+</sup> jump processes. If carried out as a function of frequency, the resulting NMR relaxation rates also contain information on the dimensionality (1D, 2D, or 3D) of the diffusion process. Recently, NMR relaxometry has revealed the 2D nature of Li hopping in LiBH<sub>4</sub>, and thus this hydride is an interesting ion conductor for further diffusion

studies on the spatially confined motion of Li spins. Here, nanocrystalline LiBH<sub>4</sub> and the two-phase analogue LiBH<sub>4</sub>:Al<sub>2</sub>O<sub>3</sub>, which are prepared by ball milling, serve as interesting model systems to track the changes in NMR relaxation rates with respect to coarse-grained, thermodynamically stable LiBH<sub>4</sub>. This reveals that interface (nano)engineering influences the hexagonal-to-orthorhombic phase transition and thus alters the ion-transport properties of Li in one- and two-phase LiBH<sub>4</sub> towards higher diffusivities at lower temperatures.

## 1. Introduction

Research on highly conducting solids is a vital topic in materials science. Currently, much effort is put into finding suitable crystalline and amorphous ion conductors which meet the needs for leading-edge energy-storage devices and sensors. In particular, Li-ion conductors are expected to play a major role in this field.<sup>[1,2]</sup> Besides application-driven research, also fundamentally oriented studies are required to shine further light on the structure–property relationships in complex, multiphase solids in order to understand the origins of fast ion transport.

Modifying the diffusion parameters of a known Li-ion conductor can prove as useful as synthesizing a new material. Apart from other possibilities, such as doping, in many cases the transport properties of solid electrolytes can be beneficially influenced by the introduction of different kinds of interfaces and the generation of structural disorder.<sup>[3–6]</sup> In nanocrystalline materials, which are characterized by a large surface area owing to mean crystallite sizes of less than approximately 20 nm, the volume fraction of interfacial regions is sufficiently large that the resulting effects on ion dynamics can be studied by solid-state NMR spectroscopy.<sup>[4,5]</sup> In general, besides the various NMR techniques for studying structural features in both solids and liquids, solid-state NMR is also useful for elucidating translational Li dynamics and studying migration pathways by means of variable-temperature and, in particular, frequency-dependent time-domain methods.<sup>[7–14]</sup>

Herein, Li NMR spectroscopy is used to study the effect of nanostructuring<sup>[15]</sup> on lithium ion dynamics in a polycrystalline solid. Lithium borohydride (LiBH<sub>4</sub>),<sup>[16]</sup> which is known as a promising material for high-capacity hydrogen storage,<sup>[17]</sup> proved to be a promising electrolyte for solid-state batteries<sup>[18]</sup> and an interesting NMR model system<sup>[19,20]</sup> to study the effect of both chemical modifications and interface engineering.<sup>[21–24]</sup> Interestingly, it exists in two different modifications.<sup>[25,26]</sup> Orthorhombic LiBH<sub>4</sub>, which is the stable phase at low temperatures, is a rather poor ionic conductor. However, its layer-structured hexagonal form, which is reversibly formed above 380 K, shows very high Li-ion conductivity<sup>[26]</sup> and diffusivity. The latter is characterized by Li residence times on the order of some nanoseconds at 450 K.<sup>[26,27]</sup> Such extremely fast Li dynamics may be explained by the two-dimensionality of the diffusion process, which was studied by variable-temperature and frequency-dependent spin–lattice relaxation (SLR) NMR measurements.<sup>[27]</sup>

In the present investigation, nanoengineering<sup>[4,15]</sup> was achieved by high-energy ball milling of the coarse-grained starting material. Thus, besides reducing the crystallite size to a few nanometers, structural disorder is introduced during mechanical impact.<sup>[28]</sup> As has been shown previously, ball milling can lead to an enormous increase in Li diffusivity and Li conductivity in single-phase oxides such as LiTaO<sub>3</sub> and LiNbO<sub>3</sub>.<sup>[5,29–32]</sup> Moreover, without changing the chemical composition of the ion conductor, the formation of so-called dispersed ion conductors consisting of the conducting phase and an insulator, such as B<sub>2</sub>O<sub>3</sub> or Al<sub>2</sub>O<sub>3</sub>, is also reported to lead to rather high conductivities.<sup>[4,33–38]</sup> In the case of a nanocrystalline two-phase composite, the large volume fraction of ion conductor/insulator interfaces formed by adjacent crystallites enable the ions to use fast (percolating) migration pathways.<sup>[35,37]</sup> Herein, results for the mechanosynthesized, nanocrystalline LiBH<sub>4</sub>:Al<sub>2</sub>O<sub>3</sub> com-

[a] V. Epp, Prof. Dr. M. Wilkening  
Christian Doppler Laboratory for Lithium Batteries  
Institute for Chemistry and Technology of Materials  
Graz University of Technology  
Stremayrgasse 9, 8010 Graz (Austria)  
Fax: (+43) 316 873 32332  
E-mail: viktor.epp@tugraz.at  
wilkening@tugraz.at

posite are compared with those obtained from microcrystalline  $\text{LiBH}_4$  with micrometer-sized crystallites and single-phase, nanocrystalline  $\text{LiBH}_4$ , that is, a sample without the addition of nanometer-sized insulating  $\text{Al}_2\text{O}_3$  particles.

## Experimental Section

Nanocrystalline  $\text{LiBH}_4$  was prepared by ball milling of the original microcrystalline material (Alfa Aesar, 95%) in a SPEX 8000M high-energy shaker mill together with an alumina vial and a single ball. The ball-to-powder weight ratio was chosen to be 4:1 and the milling time was set to 16 h. The vial was placed inside an air-tight steel container, and thus the  $\text{LiBH}_4$  was kept under an argon atmosphere throughout the milling process. The size of the resulting crystallites was about 20 nm. Similarly, the  $\text{LiBH}_4:\text{Al}_2\text{O}_3$  composite was also prepared by mechanical treatment of microcrystalline  $\text{LiBH}_4$  (Sigma-Aldrich,  $\geq 95\%$ ) and  $\alpha\text{-Al}_2\text{O}_3$  (Alfa Aesar, 99.997%). The materials were ball-milled separately for 5 h under argon atmosphere by using the same setup as for nanocrystalline  $\text{LiBH}_4$ . Subsequently, the nanocrystalline powders of the two materials were mixed in a molar ratio of 1:1, which resulted in the formation of a two-phase  $\text{LiBH}_4:\text{Al}_2\text{O}_3$  characterized by a large number of hetero-interfaces generated between adjacent  $\text{LiBH}_4$  and  $\text{Al}_2\text{O}_3$  crystallites.

Solid-state  $^6\text{Li}$  NMR measurements were performed on an MSL-400 spectrometer (Bruker BioSpin, Germany) in conjunction with a shimmed 9.4 T cryomagnet yielding nominal resonance frequencies of 58.9 and 155.5 MHz for  $^6\text{Li}$  and  $^7\text{Li}$  nuclei, respectively. For additional  $^6\text{Li}$  NMR SLR measurements and frequency-dependent  $^7\text{Li}$  NMR SLR measurements, an MSL-100 spectrometer connected to a variable-field cryomagnet was employed. For each spectrometer setup a standard broadband probe (Bruker) allowing for temperatures of  $143 < T < 515$  K was used, which were monitored with a type K thermocouple and an ICT4 temperature controller. The samples were handled under argon atmosphere at all times to avoid any reaction with moisture. Prior to the measurements, the samples were additionally vacuum-dried and fire-sealed in glass NMR tubes with lengths of about 3 cm and diameters of 5 and 10 mm to accommodate different NMR probe-head configurations.

$^7\text{Li}$  NMR lines were recorded by applying a  $\pi/2$  pulse after a sufficiently long recycle delay to ensure a magnetic equilibrium state of the system under investigation. For the  $^6\text{Li}$  NMR SLR measurements the saturation recovery pulse sequence  $10 \times \pi/2 - t_d - \pi/2$  was employed. Here, the first ten closely spaced  $\pi/2$  pulses are used to destroy any longitudinal magnetization  $M_z$ , which will subsequently tend to return to the equilibrium state. This relaxation of the magnetization is recorded by varying the length of the delay time  $t_d$ . The final  $\pi/2$  pulse creates a detectable FID. The magnetization as a function of  $t_d$  exhibits simple exponential behavior  $M_z(t_d) = M_0 [1 - \exp(-t_d/T_1)]$ .

Conductivity spectroscopic measurements were performed by using a Concept 80 spectrometer system (Novocontrol, Germany). Conductivity spectra at frequencies ranging from 10 MHz to 10 MHz were recorded with an Alpha A frequency analyzer in connection with a ZGS active sample cell. The temperature was varied between 123 and 513 K. Additional measurements were performed in the temperature range of 293–513 K by using an Agilent 4991E rf impedance analyzer together with the BDS2200 rf sample cell at frequencies between 1 MHz and 1 GHz. For the conductivity measurements, the  $\text{LiBH}_4$  powder was pressed into pellets without the use of any binder by applying a uniaxial pressure of about 1 GPa.

The resulting pellets, equipped with ion-blocking Pt electrodes, had a thickness of about 1 mm and a diameter of 8 mm. As described above, the sample material was handled carefully under argon atmosphere in all steps of the sample preparation process, with the exception of placing the  $\text{LiBH}_4$  pellet in the impedance sample cells. Hereby, the pellets were unavoidably exposed to air, though the exposure time was very short ( $< 1$  min), and the sample was kept in a dry argon flow during this procedure.

## 2. Results and Discussion

### 2.1. Low-Dimensional Diffusion in Microcrystalline $\text{LiBH}_4$ Probed by Relaxation NMR: A Brief Overview

As mentioned above,  $\text{LiBH}_4$  exists in a highly conducting layered form above 381 K. Matsuo et al. anticipated 2D Li diffusion governing ion transport in this modification by comparing results from SLR NMR and ac conductivity measurements in the “dc regime”.<sup>[26]</sup> Fortunately, the high Li diffusivity in polycrystalline  $\text{LiBH}_4$  with micrometer-sized crystallites is manifested in well-defined diffusion-induced NMR SLR rate peaks obtainable when the SLR NMR rate, recorded at Larmor frequencies  $\omega_0$  in the megahertz range, is plotted against the reciprocal temperature in an Arrhenius diagram. Despite the low melting temperature of  $\text{LiBH}_4$  it is possible to record the full-rate peak  $1/T_1(1/T)$  and to reach the so-called high-temperature flank, for which  $\omega_0\tau_c \ll 1$  holds, where  $\tau_c$  is the motional correlation, which is on the order of the Li residence time  $\tau$ .

In the case of uncorrelated isotropic motion of the spins, a symmetrical rate peak  $1/T_1(1/T)$  is expected. In the well-known BPP model, introduced by Bloembergen, Purcell, and Pound, a single exponential motional correlation function is used to obtain a Lorentzian-shaped spectral-density function after Fourier transformation.<sup>[7]</sup> For the frequency dependence of  $1/T_1$ , the BPP model predicts  $1/T_1 \propto \omega_0^{-\beta}$  with  $\beta=2$  in the limit  $\omega_0\tau_c \gg 1$  and the rate  $1/T_1$  to be independent of  $\omega_0$  in the limit  $\omega_0\tau_c \ll 1$ . Most importantly, while correlation effects such as Coulomb interactions and structural disorder can reduce the slope of the low- $T$  flank ( $\omega_0\tau_c \gg 1$ ) of  $1/T_1(1/T)$ ,<sup>[39,40]</sup> spatial confinement of the moving NMR spins influences the high- $T$  side. Whereas correlation effects lead to  $\beta < 2$ , the second feature produces a frequency dependence of  $1/T_1$  when  $1/\tau_c$  greatly exceeds  $\omega_0$ , which is set by the applied external magnetic field. Moreover, spatial restrictions cause the  $1/T_1$  rates in the limit  $\omega_0\tau_c \ll 1$  to depend more weakly on  $T$  than expected for 3D diffusion.<sup>[41,42]</sup> In agreement with previous predictions and recent theoretical investigations<sup>[43–45]</sup> on phase-pure hexagonal  $\text{LiBH}_4$ , in the limit  $\omega_0\tau_c \ll 1$  the SLR NMR rates indeed reveal a characteristic frequency dependence. This has been shown by both frequency-dependent, purely diffusion induced  $^7\text{Li}$  as well as  $^6\text{Li}$  NMR SLR rates recorded at the high-temperature limit of NMR relaxation.<sup>[27]</sup>

Such a feature is clear evidence of diffusion processes taking place in reduced dimensions such as layers or tunnel structures.<sup>[41,46,47]</sup> As expected for 2D diffusion, the relaxation-rate peaks exhibit an asymmetry<sup>[27]</sup> such that the slope of the high-temperature flank ( $\omega_0\tau_c \ll 1$ ) is lower than that governing  $1/T_1$  in the low-temperature range ( $\omega_0\tau_c \gg 1$ , see Figure 1 a). This be-

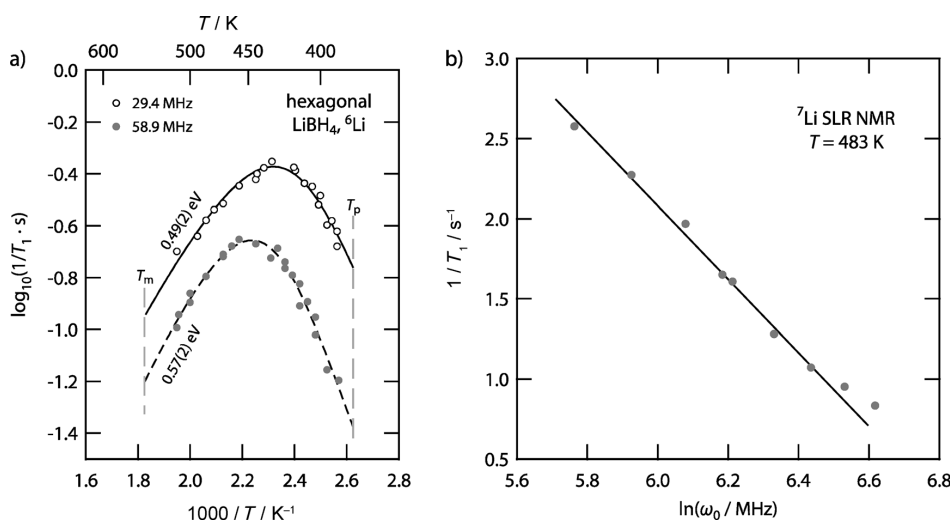


**Figure 1.** a) Arrhenius plot of the <sup>6</sup>Li NMR SLR rates  $1/T_1$  of hexagonal LiBH<sub>4</sub> recorded at the resonance frequencies  $\omega_0/2\pi = 29.4$  and 58.9 MHz, respectively.<sup>[27]</sup> The rates clearly exhibit a frequency dependence in the high-temperature limit, where  $\omega_0\tau_c \ll 1$  approximately holds. The solid lines represent a fit according to Richards' semi-empirical model for 2D diffusion,<sup>[41]</sup> given by Equation (1). b) <sup>7</sup>Li NMR SLR rates recorded at  $T = 483$  K, that is, close to the high-temperature flank of the relaxation peak, as a function of frequency (ca. 50–100 MHz). Here, a logarithmic frequency dependence of the rates is observed, following Richards' expression in this temperature limit:  $1/T_1 \propto -\tau_c \ln(\omega_0\tau_c)$ .

behavior is consistent with the semi-empirical model developed for two-dimensional (2D) jump diffusion by Richards.<sup>[41]</sup> According to this model, the spectral density function  $J(\omega_0, \tau_c)$ , and thus the SLR rate  $1/T_1$ , is given by Equation (1):

$$1/T_1 \propto J^{2D}(\omega_0, \tau_c) \propto \tau_c \ln[1 + 1/(\omega_0\tau_c)^2] \quad (1)$$

Equation (1) combines both characteristics of the <sup>6</sup>Li NMR SLR rate peaks shown in Figure 1a: their asymmetry and the frequency dependence in the limit  $\omega_0\tau_c \ll 1$ . The latter should be a logarithmic dependence, following  $1/T_1 \propto -\tau_c \ln(\omega_0\tau_c)$ . In principle, and apart from field-cycling techniques,<sup>[48–50]</sup> it is possible to elucidate dimensionality effects by measuring diffusion-induced NMR SLR rates as a function of resonance frequency  $\omega_0$  at a fixed temperature.<sup>[11]</sup> Such frequency-dependent SLR NMR measurements are relatively rare.<sup>[51–53]</sup> They can be performed in both the laboratory frame of reference (see also Figure 1a)<sup>[47,52]</sup> and in the so-called rotating frame of reference by using spin-lock techniques. Note that the latter experiments take advantage of locking frequencies  $\omega_1$ , ranging from 5 to 50 kHz and thus extend the time window down to a few kilohertz (e.g. see Küchler et al. for analogous measurements on hexagonal Li<sub>0.7</sub>TiS<sub>2</sub><sup>[47,52]</sup> and a recent study on lithium intercalated 3R-NbS<sub>2</sub><sup>[54]</sup>).

Figure 1b shows the frequency dependence of diffusion-induced <sup>7</sup>Li NMR rates of polycrystalline, monophase LiBH<sub>4</sub>. In general, if recorded at sufficiently high temperatures, the rates follow a logarithmic frequency dependence in agreement with the Richards expression for low-dimensional diffusion.

Closer inspection of the <sup>6</sup>Li NMR relaxation rates shown in Figure 1a reveals a relatively large slope of the rate peak  $1/T_1(1/T)$  in the low- $T$  range. The corresponding activation

energy  $E_a$  is 0.5 eV. This value results from the Richards fit (solid lines); it is similar to that which is obtained when simply the Arrhenius relation [Eq. (2)] is used to analyze the  $T$  dependence of  $T_1$  in the limit  $\omega_0\tau_c \gg 1$ :

$$1/T_1(1/T) \propto \exp[-E_a/(k_B T)] \quad (2)$$

where  $k_B$  is the Boltzmann constant.

To further elucidate the underlying low-dimensional transport process found by NMR spectroscopy and characterized by an activation energy of 0.55 eV, conductivity measurements were performed at temperatures ranging from 123 to 513 K. In Figure 2a the dc conductivities  $\sigma_{dc}T$  are plotted as a function of reciprocal temperature. They were directly read out from the conductivity spectra shown in Figure 2b. The heating step (red) and the cooling step (blue) are plotted separately and the values are compared to those of the above-mentioned study by Matsuo and co-workers.<sup>[26]</sup> As shown by NMR spectroscopy,<sup>[27]</sup> again both modifications are clearly distinguishable; from conductivity spectroscopy the phase-transition temperature is  $T_{PT} \approx 380$  K. In the hexagonal phase, that is, at temperatures  $T > T_{PT}$ ,  $\sigma_{dc}$  is independent of whether the measurements are performed while heating or cooling the sample. Moreover, good agreement with the previous results is found. However, in the orthorhombic form, that is, the low-temperature modification,  $\sigma_{dc}$  recorded while heating is slightly higher than the values measured during cooling. Compared to previous results,<sup>[26]</sup> our sample shows an increase of  $\sigma_{dc}$  by about one order of magnitude. These observations may be due to differences in purity or porosity of the samples. To check whether there is a relation to structural disorder phenomena, further temperature-dependent conductivity experiments are

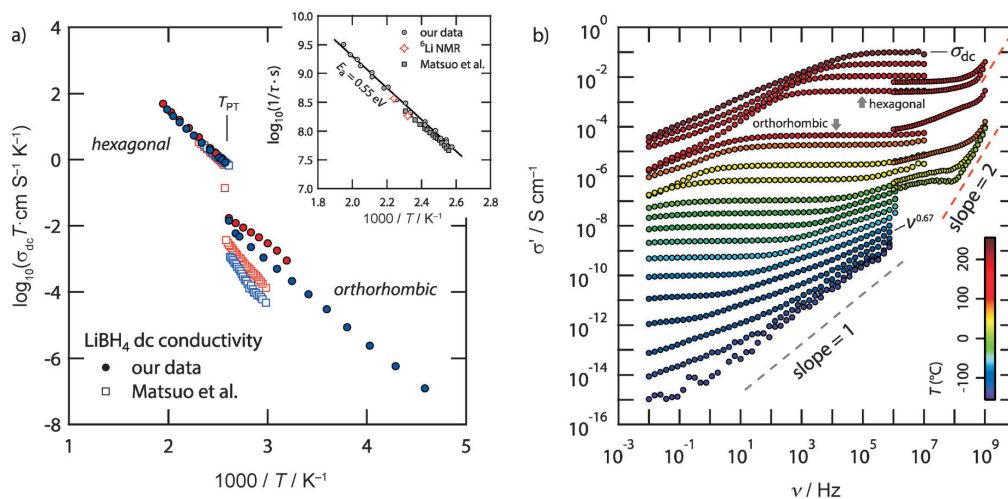


**Figure 2.** a) Arrhenius plot illustrating the temperature dependence of the dc conductivity  $\sigma_{dc}T$  of microcrystalline  $\text{LiBH}_4$  (●). The data were recorded while heating (red) and cooling (blue). For comparison, conductivity data previously published by Matsuo et al.<sup>[26]</sup> are also indicated (□). Inset: Li jump rates  $1/\tau$  of the hexagonal modification of  $\text{LiBH}_4$  versus reciprocal temperature. The rates were obtained from  $^6\text{Li}$  NMR SLR rate maxima by means of the condition  $\omega_0\tau_c \approx 1$  (○) and from dc conductivity by using the Einstein–Smoluchowski and Nernst–Einstein equations (◇, ■) and assuming a 2D diffusion process. See text for further details. b) Selected conductivity spectra from which the data points in (a) were determined. Measurements near  $T_{PT}$  and above were also performed by employing a radio-frequency setup with frequencies ranging from 1 MHz to 1 GHz.

needed. Notworthily, such differences are not revealed by  $^7\text{Li}$  NMR SLR spectroscopy.<sup>[27]</sup>

Most importantly,  $\sigma_{dc}T(1/T)$  of the hexagonal form of  $\text{LiBH}_4$  yields an activation energy of 0.55 eV which is in very good agreement with that deduced from NMR relaxometry. Before discussing this agreement,  $\sigma_{dc}$  values should be converted into Li jump rates for better comparison, and the corresponding conductivity spectra shown in Figure 2b should be inspected in more detail.

In general, by combining the Einstein–Smoluchowski equation<sup>[55,56]</sup> with the Nernst–Einstein expression, that is, connecting the microscopic self-diffusion coefficient with the macroscopic tracer-diffusion coefficient, it is possible to translate the measured  $\sigma_{dc}$  values into jump rates of the diffusing Li ions [Eq. (3)]:

$$1/\tau_\sigma = H_r f (2 dk_B T) / (nq^2 a^2) \sigma_{dc} \quad (3)$$

where the Haven ratio  $H_r$  and the correlation factor  $f$  are both taken to be  $H_r = f = 1$ , assuming uncorrelated jump diffusion of the conducting species,  $n$  and  $q$  are the charge-carrier density and the charge of the ions and can be approximated from structural data,  $d$  is the dimension of the diffusion process, and  $a$  the mean jump distance. The jump rates of hexagonal  $\text{LiBH}_4$  obtained with Equation (3) are shown in the inset of Figure 2a and were calculated for a two-dimensional diffusion process ( $d=2$ ). The assumption seems to be sound, as is evidenced by the excellent agreement with the jump rates  $1/\tau_{\text{NMR}}$  directly deduced from NMR measurements on hexagonal  $\text{LiBH}_4$ . The latter have been derived from the  $^6\text{Li}$  NMR SLR rate maxima, for

which the condition  $\omega_0\tau_c \approx 1$  is satisfied.<sup>[11,57,58]</sup> The good agreement found between  $1/\tau_\sigma$  and  $1/\tau_{\text{NMR}}$  proves that conductivity and NMR probe the same dynamic process in the highly conducting hexagonal phase of  $\text{LiBH}_4$ . This is underpinned by the fact that NMR and conductivity spectroscopy yield the same activation energy of 0.55 eV (see above and the inset of Figure 2a).

The fact that  $E_a = 0.55$  eV was obtained from the low- $T$  flank of the SLR NMR rate peak may indicate that correlation effects, which lead to a smaller slope than expected for uncorrelated motion (see above), play a subordinate role in layer-structured  $\text{LiBH}_4$ . This feature may also show up in frequency-dependent conductivity spectroscopy.

Starting at very low temperatures, that is, with the orthorhombic form of  $\text{LiBH}_4$ , the conductivity spectra show that the slope of the real part  $\sigma'$  of the complex conductivity in the double-logarithmic plot of Figure 2b tends to unity. This is a characteristic of the so-called nearly-constant-loss (NCL) behavior, which can be regarded as one of the universalities in conductivity spectroscopy. It is associated with  $\sigma'$  being independent of temperature and  $\epsilon''$ , the imaginary part of the complex permittivity, being independent of frequency. Although not fully understood as yet, NCL-type conductivity is often related to strictly localized motions which should not be mixed up with “real” translational jumps of the ions.<sup>[59–61]</sup>

With rising temperature deviations from  $\sigma' \propto \nu$  show up and a frequency-independent plateau appears;  $\sigma'$  can be roughly approximated by  $\sigma'(\nu) = \sigma_{dc}(1 + A\nu^p)$ ,<sup>[62]</sup> where  $\sigma_{dc}$  signifies the frequency-independent dc plateau (see above) and the Jonscher exponent  $p$  has a value of approximately 0.67. At intermediate temperatures and particularly in the hexagonal phase, a de-

viation from  $\sigma_{dc}$  is observed at lower frequencies, because the mobility of the Li ions has drastically increased, so that polarization effects at the applied ion-blocking electrodes play a significant role in this frequency range. Apart from such electrode effects, the spectra of hexagonal  $\text{LiBH}_4$  are dominated by a dc plateau up to  $10^7$  Hz. Additional measurements in the radio-frequency range, that is, up to  $10^9$  Hz, revealed further features of the conductivity isotherms of the orthorhombic and hexagonal forms. At the highest frequencies, the isotherms of orthorhombic  $\text{LiBH}_4$  tend to follow a quadratic frequency dependence (see Figure 2b), which points to vibrations affecting  $\sigma'$ . Sidebottom et al.<sup>[63]</sup> reported indications that, for 2D (and 1D, channel-like) diffusion, the Jonscher exponent  $p$  takes on values smaller than those expected for 3D diffusion. In the present case, for an uncorrelated 2D diffusion process, small  $p$  values are expected. A pure Debye response with random motion of the charge carriers would lead to  $p=0$ , that is, the absence of any dispersive contributions leading to  $\sigma' \neq f(\nu)$ . Because of the very high ion conductivity of hexagonal  $\text{LiBH}_4$ , the onset of dispersive regions is shifted towards very high frequencies. Nevertheless, careful inspection of some of the isotherms recorded at very high temperatures may indicate that the dc plateau directly passes into the vibrational regime with  $\sigma'(\nu) \propto \nu^2$ , which suggests a negligible Jonscher-type conductivity.

## 2.2. Comparison with Nanocrystalline, Single-Phase $\text{LiBH}_4$

Before discussing the NMR SLR rates of nanostructured  $\text{LiBH}_4$  prepared by high-energy ball milling, we note that, below the phase-transition temperature  $T_{pt}$ ,  $^7\text{Li}$  (and  $^6\text{Li}$ ) SLR is governed by rotational motion of the  $\text{BH}_4^-$  units rather than by (translational) Li diffusion. This is fully supported by recent variable-temperature  $^7\text{Li}$  NMR line-shape measurements<sup>[26,27]</sup> (see also below).

In the Arrhenius plot of Figure 3a the  $^7\text{Li}$  NMR SLR rates of nanocrystalline  $\text{LiBH}_4$ , recorded at a resonance frequency of  $\omega_0/2\pi = 155.5$  MHz, are shown. The temperature range was chosen such that the regions in which both modifications exist are covered. For comparison, the NMR SLR rates are contrasted with those of microcrystalline  $\text{LiBH}_4$ . The rates of the nanomaterial mostly coincide with those of microcrystalline  $\text{LiBH}_4$  and show deviations only at temperatures ranging from 308 to 380 K, that is, below the hexagonal-to-orthorhombic phase transition. Interestingly, in this regime the rates point to a metastable behavior of the nanocrystalline sample, which is exemplified by the dependence of the  $^7\text{Li}$  NMR SLR rates on whether the measurements are taken during heating ( $\Delta T > 0$ ) or cooling ( $\Delta T < 0$ ) of the sample (as indicated by the arrows in Figure 3a). Coming from the hexagonal form, the  $^7\text{Li}$  NMR SLR rates suggest a smooth transition from the layered modification to the orthorhombic form. However,  $^7\text{Li}$  NMR spectra, shown in Figure 3b, reveal a clear and “sudden” transition at  $T_{pt} \approx 380$  K. Still, the  $^7\text{Li}$  NMR lines in the orthorhombic modification show some kind of motional narrowing setting in at about 300 K. With increasing temperature it becomes apparent that the spectra consist of two contributions, namely, a motion-

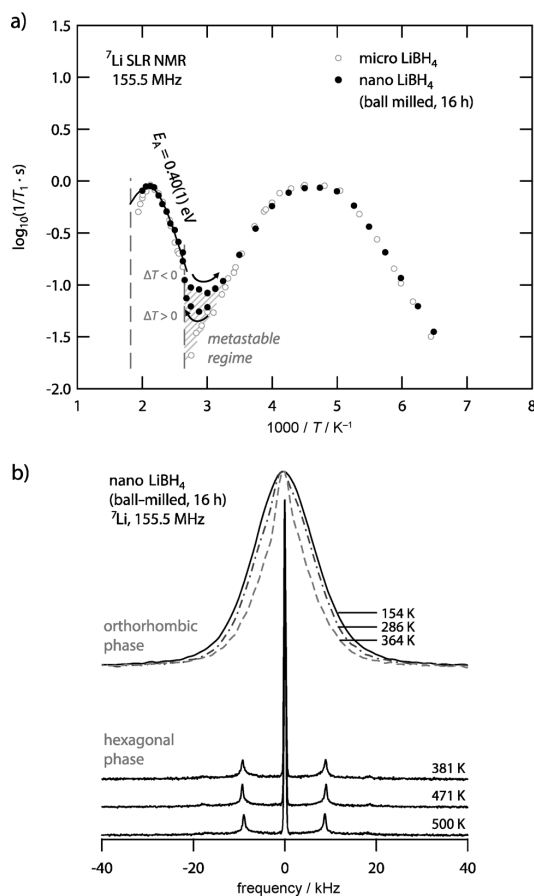


**Figure 3.** a) Plot of the diffusion-induced  $^7\text{Li}$  NMR SLR rates  $1/T_1$  of nanocrystalline  $\text{LiBH}_4$  (●) as a function of reciprocal temperature. Though a phase transition is still observed at the same temperature  $T_{pt}$  as for the microcrystalline material, high-energy ball milling seems to form a metastable material when the temperature range  $308 \leq T \leq 380$  K is considered. The metastable behavior is exemplified by data recorded during heating ( $\Delta T > 0$ ) and cooling ( $\Delta T < 0$ ). In this temperature range, enhanced Li-ion diffusivity is expected compared to microcrystalline  $\text{LiBH}_4$ . Otherwise, the rates are almost indistinguishable from those of the microcrystalline  $\text{LiBH}_4$  (○). b) Selected  $^7\text{Li}$  NMR spectra of nanocrystalline, single-phase  $\text{LiBH}_4$ , recorded at the temperatures indicated. As in the case of microcrystalline  $\text{LiBH}_4$ ,<sup>[26,27]</sup> the hexagonal modification features a well-defined quadrupole powder pattern that shows up immediately at the transition temperature of about 381 K. However, the spectra of orthorhombic  $\text{LiBH}_4$  clearly consist of two contributions: a broad line from which a motionally narrowed line emerges with rising temperature. Though not as pronounced, this behavior is similar to that observed for the nanocrystalline composite  $\text{LiBH}_4:\text{Al}_2\text{O}_3$  (cf. the NMR line recorded at 364 K and see Figure 4b below).

ally narrowed line atop a broad one which does not show any narrowing. The increased NMR SLR rates and the heterogeneous motional narrowing clearly indicate fast Li ions and point to enhanced ion conductivity in nano- $\text{LiBH}_4$ . This feature may be due to possible preservation of the highly conducting hexagonal phase in the interfacial regions of the nanostructured material.

### 2.3. Nanocrystalline Two-Phase $\text{LiBH}_4\cdot\text{Al}_2\text{O}_3$ : The Effect of an Insulating Phase on SLR NMR

Besides single-phase  $\text{LiBH}_4$ , a two-phase composite consisting of nanometer-sized  $\text{LiBH}_4$  in contact with nanocrystalline  $\text{Al}_2\text{O}_3$  acting as an ionic insulator was investigated for comparison.  $^7\text{Li}$  NMR SLR measurements were carried out at temperatures ranging from 140 to 510 K. The diffusion-induced  $^7\text{Li}$  NMR SLR rates of the composite are shown in Figure 4a. While the SLR NMR rate peaks of the orthorhombic form are governed by fast rotational motions of the  $\text{BH}_4^-$  units, those of the hexagonal form solely reflect Li hopping. Careful inspection of the  $^7\text{Li}$ ,

$^1\text{H}$ , and  $^{11}\text{B}$  NMR SLR rates has shown that  $\text{BH}_4^-$  dynamics is governed by two types of rotational motion.<sup>[64–66]</sup>

As can be deduced from the  $^7\text{Li}$  NMR SLR rates of Figure 4a, the  $\text{BH}_4^-$  dynamics is increased compared to that in pure micrometer-sized  $\text{LiBH}_4$ . Unexpectedly, the diffusion-induced  $^7\text{Li}$  NMR SLR rate maximum of the hexagonal phase can no longer be reached.

However, in contrast to the starting material (cf. Figure 3a), the composite no longer shows a sudden phase transition but gradually transforms into the hexagonal phase. Taken together, the  $^7\text{Li}$  NMR SLR rates measured over the whole temperature range can be described by a sum of two sets of SLR rates according to  $1/T_1 = 1/T_1^{(1)} + 1/T_1^{(2)}$ . Interestingly, the rates  $1/T_1^{(1)}$ , which dominate NMR SLR in the orthorhombic regime, follow BBP-type behavior ( $\beta=2$ , see above). However, separation into two different rotational modes is no longer possible. This may be directly related to the structural disorder introduced by ball milling leading to a broad distribution of rotational  $\text{BH}_4^-$  jump rates.

Since the rates  $1/T_1^{(2)}$ , which dominate the NMR SLR of the hexagonal phase, exhibit only the low-temperature flank of a  $1/T_1^{(2)}(1/T)$  rate peak, they can be appropriately described with a single Arrhenius relation. The overall rates are then given by Equation (4):

$$1/T_1 = C\tau_c^{(1)} / [1 + (\omega_0\tau_c^{(1)})^{\beta(-2)}] + A/\tau_c^{(2)} \quad (4)$$

in which  $\tau_c^{(i)} = \tau_{c,0}^{(i)} \exp(E_a^{(i)}/k_B T)$  denotes the respective correlation time, where  $E_a^{(i)}$  is the activation energy ( $i=1, 2$ ). The pre-exponential factor  $\tau_{c,0}^{(1)}$  is approximately  $2 \times 10^{-13}$  s and agrees well with those typically found for phonon frequencies. The activation energies are calculated to be  $E_a^{(1)} = 0.14$  eV and  $E_a^{(2)} = 0.35$  eV. Compared to single-phase  $\text{LiBH}_4$  with micrometer-sized crystallites,<sup>[27]</sup> a decrease in  $E_a$  is observed in both phases.

The gradual phase transformation between the two modifications is also revealed in situ by the  $^7\text{Li}$  NMR spectra shown in Figure 4b. The variable-temperature  $^7\text{Li}$  NMR spectra, recorded under static conditions, provide both structural and further dynamic information. Initially a broad Lorentzian is observed at low temperatures. The line shape gradually changes with increasing  $T$ , but without an abrupt transition to the hexagonal phase. The  $^7\text{Li}$  NMR spectrum of hexagonal  $\text{LiBH}_4$  is composed of a fully motionally narrowed central line and a spin-3/2 quadrupolar powder pattern.<sup>[26,27]</sup> The latter is determined by a single (mean) electric field gradient to which the spins are exposed. With increasing temperature the  $^7\text{Li}$  NMR line of nanocrystalline  $\text{LiBH}_4\cdot\text{Al}_2\text{O}_3$  undergoes a strongly heterogeneous motional narrowing resulting in a two-component NMR line shape, that is, the broad NMR line becomes superimposed by a sharp NMR component. The latter reflects fast Li ions showing up well below the original phase-transition temperature of micrometer-sized, single-phase  $\text{LiBH}_4$ . Compared with results on single-phase nanocrystalline  $\text{LiBH}_4$ , we conclude that these ions do perform translational movements in the regions near to or influenced by the hetero-interfaces between the crystallites of nanocrystalline  $\text{LiBH}_4$  and  $\text{Al}_2\text{O}_3$ . Similar results

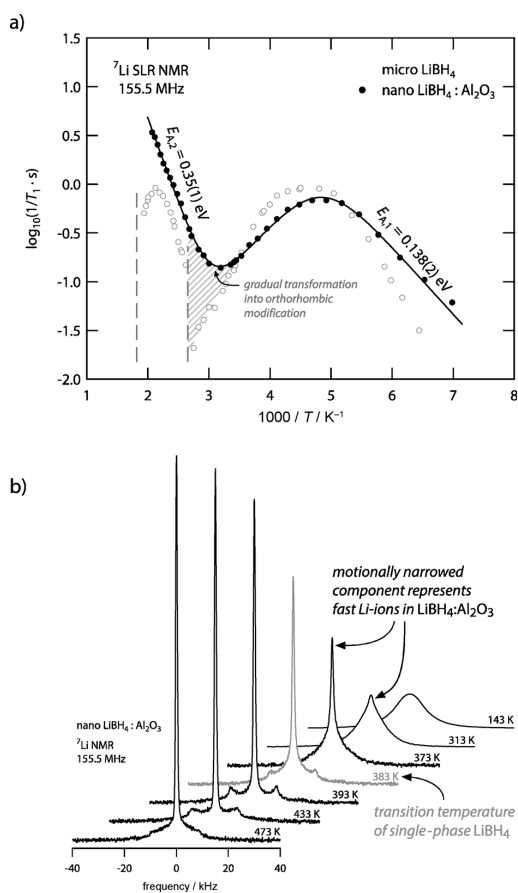


**Figure 4.** a) Arrhenius plot of the  $^7\text{Li}$  NMR SLR rates  $1/T_1$  of nanocrystalline  $\text{LiBH}_4\cdot\text{Al}_2\text{O}_3$  recorded at  $\omega_0/2\pi = 155.5$  MHz (●). Two distinct regimes are clearly distinguishable and correspond to the two modifications of microcrystalline  $\text{LiBH}_4$  (○). However, in the case of  $\text{LiBH}_4\cdot\text{Al}_2\text{O}_3$  there is a gradual transformation from one to the other regime, which also shows up in the corresponding NMR line shapes (see b). The solid line represents a fit according to Equation (4). See text for further details. b)  $^7\text{Li}$  NMR spectra of nanocrystalline  $\text{LiBH}_4\cdot\text{Al}_2\text{O}_3$  recorded at 155.5 MHz and the temperatures indicated. At very low temperature, the spectra consist of a broad Lorentzian; a motionally narrowed component emerges at higher temperatures. The latter is indicative of fast Li-ion motion. At about 380 K, that is, at the transition temperature of single-phase  $\text{LiBH}_4$ , distinct quadrupole satellites show up, which in turn seem to be averaged out for  $T > 470$  K.

have been reported also for  $\text{Li}_2\text{O}:\text{X}_2\text{O}_3$  ( $\text{X}=\text{Al}, \text{B}$ ) composites.<sup>[4, 6, 15, 36]</sup>

In general, motion-induced narrowing of a given NMR line sets in when Li diffusion is fast enough to average dipole–dipole interactions determining the width of the NMR line in the so-called rigid-lattice regime at low temperatures.<sup>[5]</sup> In the present case, the appearance of the sharp NMR line points to Li jump rates on the order of  $10^4 \text{ s}^{-1}$ . The line widths of the two components do not change significantly with temperature; they are about 12.5 and 1.4 kHz. However, the steadily increasing amplitude of the narrow component with rising temperature points to an increase in the amount of very fast Li ions. For instance, at  $T=373 \text{ K}$  the number fraction  $A_f$  of fast-diffusing spins has reached about 25%. At  $T=383 \text{ K}$  the well-defined NMR quadrupole intensities of hexagonal  $\text{LiBH}_4$  emerge, which prove the formation of the layered modification. The spectral distance between the  $90^\circ$  singularities of the quadrupole powder pattern is in agreement with that found for micrometer-sized  $\text{LiBH}_4$ ; however, the whole pattern is somewhat smeared out, once again reflecting (local) structural disorder introduced during mechanical treatment.

At even higher temperatures the quadrupole singularities start to vanish. This may point to further structural changes induced at elevated temperatures. Irrespective of this feature, which must be investigated by, for example, in situ X-ray diffraction, the number fraction  $A_f$  of fast-diffusing Li spins does not significantly depend on temperature once the hexagonal phase has been completely formed.

The example investigated shows how mechanical treatment and formation of a mixed composite can be used to tailor dynamic properties of a given ion conductor. In the present case, well below the hexagonal-to-orthorhombic phase transformation, the nanocrystalline, dispersed ion conductor  $\text{LiBH}_4:\text{Al}_2\text{O}_3$  reveals enhanced Li diffusivity, which becomes evident in increased NMR SLR rates below  $T_{\text{PT}}$  and a pronounced two-component line NMR shape reflecting two dynamically different spin reservoirs.

### 3. Conclusions

Frequency- and temperature-dependent  $^7\text{Li}$  and  $^6\text{Li}$  NMR measurements have shown that Li diffusion in hexagonal  $\text{LiBH}_4$ , which is the thermodynamically stable modification above  $T_{\text{PT}} \approx 380 \text{ K}$ , is confined to two dimensions. To a certain degree, nanostructuring helps to preserve the high ion conductivity down to temperatures well below  $T_{\text{PT}}$ . In particular, the introduction of a large volume fraction of hetero-interfaces in the two-phase composite  $\text{LiBH}_4:\text{Al}_2\text{O}_3$  leads to enhanced Li diffusivity, which is manifested in increased SLR rates and a two-component NMR line shape. The latter is composed of a broad and a motionally narrowed NMR line reflecting heterogeneous dynamics of slow- and fast-diffusing Li spins. Most likely, the highly mobile ions are located near the interfaces between adjacent  $\text{LiBH}_4$  and  $\text{Al}_2\text{O}_3$  crystallites, that is, engineering interfaces in nanocrystalline, dispersed ion conductors is a promising concept to design further ion conductors.

### Acknowledgements

Financial support by the Austrian Federal Ministry of Economy, Family and Youth, and the Austrian National Foundation for Research, Technology and Development as well as by the Deutsche Forschungsgemeinschaft (DFG) is highly appreciated (grant no.: WI3600 4-1/4-2). M.W. thanks the Leibniz University Hannover for the grant "Wege in die Forschung II". We thank the workgroup of Paul Heitjans (Hannover) for access to the NMR lab at the Institute of Physical Chemistry and Electrochemistry.

**Keywords:** conducting materials · hydrides · lithium · nanostructured materials · NMR spectroscopy

- [1] P. Knauth, *Solid State Ionics* **2009**, *180*, 911–916.
- [2] J. B. Goodenough, Y. Kim, *Chem. Mater.* **2010**, *22*, 587–603.
- [3] J. Maier, *Nat. Mater.* **2005**, *4*, 805–815.
- [4] P. Heitjans, M. Wilkening, *MRS Bull.* **2009**, *34*, 915–922.
- [5] M. Wilkening, V. Epp, A. Feldhoff, P. Heitjans, *J. Phys. Chem. C* **2008**, *112*, 9291–9300.
- [6] P. Heitjans, S. Indris, M. Wilkening in *Nanocomposites* (Eds.: P. Knauth, J. Schoonman), Springer, New York, **2007**, pp. 227–246.
- [7] N. Bloembergen, E. M. Purcell, R. V. Pound, *Phys. Rev.* **1948**, *73*, 679–712.
- [8] A. Abragam, *The Principles of Nuclear Magnetism*, Oxford University Press, Oxford, **1961**.
- [9] J. R. Hendrickson, P. J. Bray, *J. Magn. Reson.* **1973**, *9*, 341–357.
- [10] C. A. Sholl, *J. Phys. C* **1981**, *14*, 447.
- [11] P. Heitjans, A. Schirmer, S. Indris in *Diffusion in Condensed Matter* (Eds.: P. Heitjans, J. Kärger), Springer, Berlin, **2005**, pp. 367–415.
- [12] M. Wilkening, P. Heitjans, *ChemPhysChem* **2012**, *13*, 53–65.
- [13] R. Böhmer, K. R. Jeffrey, M. Vogel, *Prog. Nucl. Magn. Reson. Spectrosc.* **2007**, *50*, 87–174.
- [14] D. Brinkmann, *Prog. Nucl. Magn. Reson. Spectrosc.* **1992**, *24*, 527–552.
- [15] P. Heitjans, S. Indris, *J. Phys. Condens. Matter* **2003**, *15*, R1257–R1289.
- [16] M. Matsuo, S. Orimo, *Adv. Energy Mater.* **2011**, *1*, 161–172.
- [17] C. Li, P. Peng, D. W. Zhou, L. Wan, *Int. J. Hydrogen Energy* **2011**, *36*, 14512–14526.
- [18] K. Takahashi, K. Hattori, T. Yamazaki, K. Takada, M. Matsuo, S. Orimo, H. Maekawa, H. Takamura, *J. Power Sources* **2013**, *226*, 61–64.
- [19] R. L. Corey, D. T. Shane, R. C. Bowman, M. S. Conradi, *J. Phys. Chem. C* **2008**, *112*, 19784–19790.
- [20] A. V. Soloninin, A. V. Skripov, A. L. Buzlukov, A. P. Stepanov, *J. Solid State Chem.* **2009**, *182*, 2357–2361.
- [21] H. Maekawa, M. Matsuo, H. Takamura, M. Ando, Y. Noda, T. Karahashi, S. Orimo, *J. Am. Chem. Soc.* **2009**, *131*, 894–895.
- [22] A. V. Skripov, A. V. Soloninin, L. H. Rude, T. R. Jensen, Y. Filinchuk, *J. Phys. Chem. C* **2012**, *116*, 26177–26184.
- [23] M. Matsuo, H. Takamura, H. Maekawa, H.-W. Li, S. Orimo, *Appl. Phys. Lett.* **2009**, *94*, 084103.
- [24] L. M. Arnbjerg, D. B. Ravnsbæk, Y. Filinchuk, R. T. Vang, Y. Cerenius, F. Besenbacher, J.-E. Jørgensen, H. J. Jakobsen, T. R. Jensen, *Chem. Mater.* **2009**, *21*, 5772–5782.
- [25] J. P. Soulié, G. Renaudin, R. Cerný, K. Yvon, *J. Alloys Compd.* **2002**, *346*, 200–205.
- [26] M. Matsuo, Y. Nakamori, S. Orimo, H. Maekawa, H. Takamura, *Appl. Phys. Lett.* **2007**, *91*, 224103.
- [27] V. Epp, M. Wilkening, *Phys. Rev. B* **2010**, *82*, 20301.
- [28] V. Šepelák, A. Düvel, M. Wilkening, K.-D. Becker, P. Heitjans, *Chem. Soc. Rev.* **2013**, *42*, 7507–7520.
- [29] D. Bork, P. Heitjans, *J. Phys. Chem. B* **1998**, *102*, 7303–7306.
- [30] D. Bork, P. Heitjans, *J. Phys. Chem. B* **2001**, *105*, 9162–9170.
- [31] M. Wilkening, D. Bork, S. Indris, P. Heitjans, *Phys. Chem. Chem. Phys.* **2002**, *4*, 3246–3251.
- [32] P. Heitjans, M. Masoud, A. Feldhoff, M. Wilkening, *Faraday Discuss.* **2007**, *134*, 67–82.
- [33] C. C. Liang, *J. Electrochem. Soc.* **1973**, *120*, 1289–1292.

- [34] N. F. Uvarov, V. P. Isupov, V. Sharma, A. K. Shukla, *Solid State Ionics* **1992**, *51*, 41–52.
- [35] S. Indris, P. Heitjans, H. E. Roman, A. Bunde, *Phys. Rev. Lett.* **2000**, *84*, 2889–2892.
- [36] M. Wilkening, S. Indris, P. Heitjans, *Phys. Chem. Chem. Phys.* **2003**, *5*, 2225–2231.
- [37] S. Indris, P. Heitjans, M. Ulrich, A. Bunde, *Z. Phys. Chem.* **2005**, *219*, 89–103.
- [38] G. Albinet, J. M. Debierre, P. Knauth, C. Lambert, L. Raymond, *Eur. Phys. J. B* **2001**, *22*, 421–427.
- [39] M. Meyer, P. Maass, A. Bunde, *Phys. Rev. Lett.* **1993**, *71*, 573–576.
- [40] A. Bunde, W. Dieterich, P. Maass, M. Meyer in *Diffusion in Condensed Matter* (Eds.: P. Heitjans, J. Kärger), Springer, Berlin, **2005**, pp. 813–856.
- [41] P. M. Richards, *Solid State Commun.* **1978**, *25*, 1019–1021.
- [42] P. M. Richards in *Physics of Superionic Conductors* (Ed.: M. Ben Salomon), Springer, Berlin, **1979**, pp. 141–174.
- [43] T. Ikeshoji, E. Tsuchida, K. Ikeda, M. Matsuo, H.-W. Li, Y. Kawazoe, S. Orimo, *Appl. Phys. Lett.* **2009**, *95*, 221901–221903.
- [44] T. Ikeshoji, E. Tsuchida, T. Morishita, K. Ikeda, M. Matsuo, Y. Kawazoe, S. Orimo, *Phys. Rev. B* **2011**, *83*, 144301.
- [45] J. S. G. Myrdal, D. Blanchard, D. Sveinbjörnsson, T. Vegge, *J. Phys. Chem. C* **2013**, *117*, 9084–9091.
- [46] A. Avogadro, M. Villa, *J. Chem. Phys.* **1977**, *66*, 2359–2367.
- [47] W. Küchler, PhD thesis, Universität Hannover (Germany), **1992**.
- [48] A. F. Privalov, S. V. Dvinskikh, F. Fujara, H. M. Vieth, *Appl. Magn. Reson.* **1998**, *15*, 353–361.
- [49] R. Kimmich, E. Anoardo, *Prog. Nucl. Magn. Reson. Spectrosc.* **2004**, *44*, 257–320.
- [50] D. Kruk, F. Fujara, P. Gumann, W. Medycki, A. F. Privalov, C. Tacke, *Solid State Nucl. Magn. Reson.* **2009**, *35*, 152–163.
- [51] R. L. Kleinberg, B. G. Silbernagel, *Solid State Commun.* **1980**, *33*, 867–871.
- [52] W. Küchler, P. Heitjans, A. Payer, R. Schöllhorn, *Solid State Ionics* **1994**, *70/71*, 434–438.
- [53] A. F. McDowell, C. F. Mendelsohn, M. S. Conradi, R. C. Bowman, Jr., A. J. Maeland, *Phys. Rev. B* **1995**, *51*, 6336–6342.
- [54] V. Epp, S. Nakhai, M. Lerch, M. Wilkening, *J. Phys. Condens. Matter* **2013**, *25*, 195402.
- [55] A. Einstein, *Ann. Phys.* **1905**, *322*, 549–560.
- [56] A. Einstein, M. von Smoluchowski, *Untersuchungen über die Theorie der Brownschen Bewegung*, Harri Deutsch, Frankfurt am Main, **1997**.
- [57] A. Kuhn, S. Narayanan, L. Spencer, G. R. Goward, V. Thangadurai, M. Wilkening, *Phys. Rev. B* **2011**, *83*, 94302.
- [58] A. Kuhn, M. Kunze, P. Sreeraj, H.-D. Wiemhöfer, V. Thangadurai, M. Wilkening, P. Heitjans, *Solid State Nucl. Magn. Reson.* **2012**, *42*, 2–8.
- [59] K. Funke, C. Cramer, D. Wilmer in *Diffusion in Condensed Matter* (Eds.: P. Heitjans, J. Kärger), Springer, Berlin, **2005**, pp. 857–893.
- [60] K. Funke, R. D. Banhatti, D. M. Laughman, L. G. Badr, M. Mutke, A. Šantić, W. Wrobel, E. M. Fellberg, C. Biermann, *Z. Phys. Chem.* **2010**, *224*, 1891–1950.
- [61] K. L. Ngai, S. Capaccioli, N. Shinyashiki, M. S. Thayyil, *J. Non-Cryst. Solids* **2010**, *356*, 535–541.
- [62] A. K. Jonscher, *Nature* **1977**, *267*, 673–679.
- [63] D. L. Sidebottom, *Phys. Rev. Lett.* **1999**, *83*, 983–986.
- [64] T. Tsang, T. C. Farrar, *J. Chem. Phys.* **1969**, *50*, 3498–3502.
- [65] A. V. Skripov, A. V. Soloninin, Y. Filinchuk, D. Chernyshov, *J. Phys. Chem. C* **2008**, *112*, 18701–18705.
- [66] K. Jimura, S. Hayashi, *J. Phys. Chem. C* **2012**, *116*, 4883–4891.

Received: August 13, 2013

Published online on October 24, 2013

### 3.5.2 Studying Li dynamics in a gas-phase synthesized amorphous oxide by NMR and impedance spectroscopy (pp. 116–127)

Epp, V., Brüning, C., Binnewies, M., Heitjans, P., and Wilkening, M. *Zeitschrift für Physicalische Chemie* **226**, 513–524 (2012).—This article is reproduced by permission of De Gruyter. The original article can be found online at <http://www.degruyter.com/view/j/zpch.2012.226.issue-5-6/zpch.2012.0224/zpch.2012.0224.xml>. ©2012 Walter de Gruyter GmbH.

# Studying Li Dynamics in a Gas-Phase Synthesized Amorphous Oxide by NMR and Impedance Spectroscopy

By Viktor Epp<sup>1,3,\*</sup>, Christian Brünig<sup>2</sup>, Michael Binnewies<sup>2</sup>, Paul Heitjans<sup>3</sup>, and Martin Wilkening<sup>1,3</sup>

<sup>1</sup> Graz University of Technology, Institute for Chemistry and Technology of Materials, Stremayrgasse 9, A-8010 Graz, Austria

<sup>2</sup> Leibniz University Hannover, Institute of Inorganic Chemistry, Callinstr. 9, D-30167 Hannover, Germany

<sup>3</sup> Leibniz University Hannover, Institute of Physical Chemistry and Electrochemistry, Callinstr. 3-3A, D-30167 Hannover, Germany

(Received February 9, 2012; accepted in revised form April 16, 2012)

(Published online May 14, 2012)

## *Li Diffusion / Solid State NMR / Impedance Spectroscopy / Non-Stoichiometric Compounds*

Li diffusion parameters of a structurally disordered Li-Al-Si-oxide prepared by gas-phase synthesis were complementarily investigated by both time-domain NMR techniques and impedance spectroscopy. The first include <sup>7</sup>Li NMR spin-lattice relaxation (SLR) measurements in the laboratory as well as in the rotating frame of reference. An analysis of variable-temperature NMR line widths point to an activation energy  $E_a$  of approximately 0.6 eV. The value is confirmed by rotating-frame SLR NMR data recorded at approximately 11 kHz. Above room temperature the low-temperature flank of a diffusion-induced rate peak shows up which can be approximated by an Arrhenius law yielding  $E_a = 0.56(1)$  eV. This is in very good agreement with the result obtained from <sup>7</sup>Li spin-alignment echo (SAE) NMR being sensitive to even slower Li dynamics. For comparison, dc-conductivity measurements, probing long-range motions, yield  $E_a = 0.8$  eV. Interestingly, low-temperature SAE NMR decay rates point to localized Li motions being characterized with a very small activation energy of only 0.09 eV.

## 1. Introduction

The precise measurement of diffusion parameters in solids is a vital topic in materials science [1–4]. In particular, the investigation of Li dynamics over a wide length scale turns out to be highly important to understand the underlying structure-property relationships governing ion transport in materials being relevant for battery applications [5–15]. For instance, fast ion conductors are needed to develop powerful all-solid-state

---

\* Corresponding author. E-mail: epp@pci.uni-hannover.de

lithium-ion batteries which are regarded to play a key role in the development of new energy storage systems [16–18].

In many cases the introduction of structural disorder leads to an improvement of the diffusion parameters. For example, Li diffusion in nanocrystalline  $\text{LiNbO}_3$  (and  $\text{LiTaO}_3$ ), [19–21] which was prepared by high-energy ball milling, is enhanced by several orders of magnitude compared to its structurally ordered crystalline counterpart. Especially in the case of amorphous materials, offering both local movement modes and long-range migration pathways, diffusion parameters such as jump rates and activation energies might differ from each other when probed on different length scales and time scales, respectively [20,22–24]. In order to draw a complete picture of the different motions taking place in structurally disordered materials, dynamic parameters should preferably be probed by complementary techniques being sensitive to Li dynamics occurring on different time scales [10,13,25,26]. Here, exemplarily a gas-phase synthesized (metastable) non-stoichiometric amorphous oxide composed of Li, Si and Al served as a highly disordered model substance which was comprehensively investigated by both variable-temperature NMR and impedance spectroscopy.

The present study aims at the comparison of diffusion and transport parameters, respectively, obtained from quite different methods which are sensitive to short-range and long-range Li motions. In particular, besides NMR line shape measurements, variable-temperature  $^7\text{Li}$  NMR spin-lattice relaxation (SLR) rates in both the laboratory and rotating frame of reference [24] have been measured. Whereas the first are sensitive to very fast Li motions with jump rates in the order of the Larmor frequency used, which is in the MHz range here, SLR rates probed in the rotating frame of reference are usually sampled at locking frequencies in the order of some kHz. Thus, the latter measurements are *per se* sensitive to much slower Li dynamic processes with jump rates in the order of  $10^4 \text{ s}^{-1}$ . Even slower Li jump processes were probed by the so-called NMR spin-alignment echo (SAE) technique [22,23,27–32].  $^7\text{Li}$  SAE NMR two-time correlation functions were recorded at different temperatures by the use of the Jeener–Broekaert pulse sequence. In this way, the method is sensitive to Li jump rates with values down to  $10^1 \text{ s}^{-1}$  [7,28]. Finally, impedance spectroscopy measurements covering a frequency range from 10 Hz to 1 MHz complement the study.

## 2. Experimental

The non-equilibrium oxide studied was synthesized *via* a gas-phase reaction in a three-zone tube furnace resulting in a metastable, highly non-stoichiometric powder containing Li, Al, Si, and O. The precursors used for the studied sample were pure lithium chloride (Sigma-Aldrich, > 99%), aluminum chloride (Sigma-Aldrich, 98%), and silicon tetrachloride (Riedel-de-Haen, > 99%). A detailed description of the procedure including the setup of the apparatus used for the gas-phase synthesis employed can be found in Refs. [33,34]. Let us remark that the synthesis route chosen has the great advantage of providing a very easy way to adjust the sample stoichiometry. Up to now, we were able to synthesize a series of non-stoichiometric samples with quite different compositions. These are included in Fig. 1a; here, exemplarily the sample numbered “57” (marked with a cross) was studied. For comparison, the stoichiometric aluminosilicates

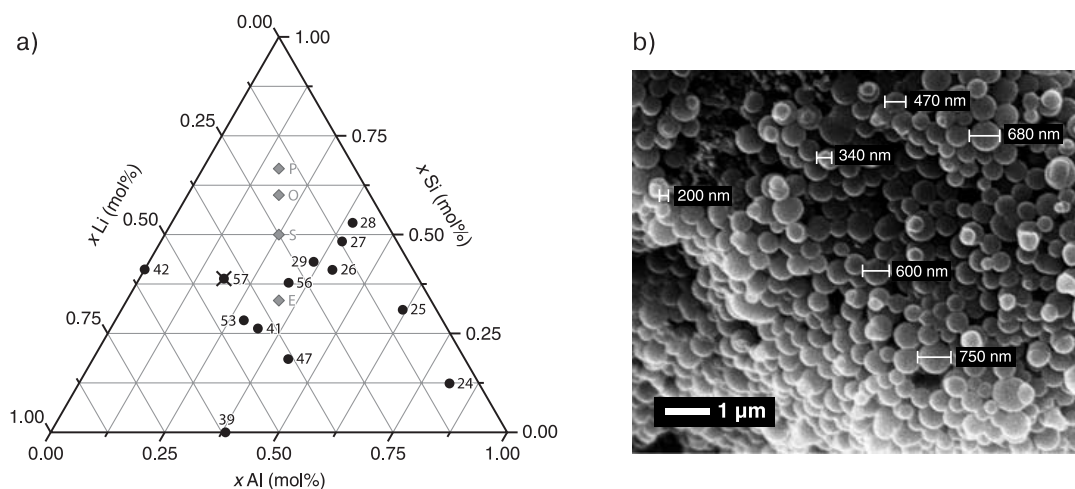


**Fig. 1.** (a) Li-Al-Si-O-phase diagram; so far, a series of non-stoichiometric samples, labelled with numbers, have been prepared in our laboratory. P, O, S, and E highlight the compounds petalite, lithium orthoclase, spodumene and eucryptite. (b) SEM image of sample “57”, see (a).

petalite  $\text{LiAlSi}_4\text{O}_{10}$  (P), lithium orthoclase  $\text{LiAlSi}_3\text{O}_8$  (O), spodumene  $\text{LiAlSi}_2\text{O}_6$  (S) and eucryptite  $\text{LiAlSiO}_4$  (E) are also included. Sample “57” is characterized by an Al:Li:Si ratio of approximately 1:2.3:2.1 (see Fig. 1a). This ratio was determined by inductively coupled plasma atomic emission spectroscopy (ICP-AES). The sample was found to be X-ray amorphous; scanning electron microscopy (SEM) images show that it consists of globular particles with diameters ranging from 200 nm to 750 nm (see Fig. 1b).

Solid-state  $^7\text{Li}$  NMR measurements, carried out to get insights into the Li dynamics of the amorphous oxide, were performed by using a modified Bruker MSL-100 equipped with a Kalmus 400 W amplifier. The spectrometer is connected to a field-variable Oxford cryomagnet which is operated at a (nominal) resonance frequency  $\omega_0/2\pi$  of 77.7 MHz. A standard broadband probe (Bruker) was used to sample NMR spectra and spin-lattice relaxation rates. The temperature in the direct neighbourhood of the sample was monitored with an ITC4 temperature controller (Oxford) using a Ni-CrNi thermocouple. All measurements were performed at temperatures ranging from 173 K to 453 K. The temperature was either adjusted by a stream of heated air ( $T > 300$  K) or by freshly evaporated nitrogen ( $T < 300$  K). Prior to the NMR measurements the sample was extensively vacuum dried and then fire-sealed in a glass tube (4 mm in diameter and 4 cm in length).

$^7\text{Li}$  NMR spin-lattice relaxation rates  $1/T_1$  were acquired with the saturation recovery pulse sequence:  $10 \times \pi/2 - t_i - \pi/2$  [24,35]. The  $\pi/2$  pulse length was approximately 7  $\mu\text{s}$ ; the first 10 pulses, separated by a delay time of 50  $\mu\text{s}$ , are used to destroy longitudinal spin magnetization  $M_z(t)$ . The subsequent recovery of  $M_z(t)$  is recorded as a function of 14 different delay times  $t_i$  ( $i = 1 \dots 14$ ). Similarly,  $^7\text{Li}$  NMR relaxation rates  $1/T_{1\rho}$  in the rotating frame of reference were measured. For this purpose the spin-lock technique [35–41] was used to record  $M_\rho(t_{\text{lock}})$  transients. The duration of the locking pulse  $t_{\text{lock}}$  was varied from 1 ms up to 40 s. The corresponding locking frequency  $\omega_1/2\pi$  was estimated to be of the order of  $\nu_{\text{lock}} = 11$  kHz.

As already mentioned above,  $^7\text{Li}$  NMR spin-alignment echoes were recorded using the pulse sequence introduced by Jeener and Broekaert [42,43]:  $\pi/2_X - t_p - \pi/4_Y - t_m - \pi/4_X - t_p - \text{echo}$ , where  $X$  and  $Y$  denote the phase shifts of the radio frequency (rf) pulses used. In the ideal case, the first two rf pulses, separated by the preparation time  $t_p$  which has to be chosen as short as possible [30,44–48] (here  $t_p = 10 \mu\text{s}$  was used), create (quadrupolar) spin-alignment order. Li motions affecting quadrupole spin-order take place during the mixing period determined by  $t_m$  ( $1 \mu\text{s} < t_m < 100 \text{s}$ ). The third or reading rf pulse of the Jeener–Broekaert pulse sequence transforms spin-alignment back into an observable transverse coherent magnetization giving rise to a stimulated echo at  $t = t_p$ . Damping of the echo intensity  $S_2$  with increasing mixing time leads to a two-time correlation function containing, in general, information on the dynamics [49,50] as well as geometry [51] of the diffusion process studied. The recycle delay was set to at least  $5 \times T_1$ .

Impedance measurements were carried out at frequencies ranging from 5 Hz to 13 MHz with a home-built impedance cell connected to an HP 4192A RF impedance analyzer. The cell was placed in a tube furnace controlled by an OMRON E5CK temperature unit. For the impedance measurements, the powder sample was pressed into a pellet without any binder by applying a uniaxial pressure of about 1 GPa. Pt electrodes were applied by using platinum powder of high purity (Merck, 99.9%). The resulting pellet had a thickness of about 1 mm and a diameter of 8 mm. In order to exclude the influence of water upon the measurements, the sample was heated above 400 K in a dry nitrogen atmosphere for several hours. Subsequently, the impedance spectra were recorded between room temperature and 670 K in the same atmosphere using a home-built impedance cell with a four-terminal configuration.

## 2.1 Results and discussion

### 2.1.1 $^7\text{Li}$ NMR measurements

In many cases, a  $^7\text{Li}$  NMR line-shape analysis provides first insights into the short time-scale Li ion dynamics of a given (diamagnetic) Li ion conductor. In Fig. 2a four selected NMR spectra recorded under static conditions at the temperatures indicated are shown. In the so-called *rigid lattice* regime of the sample, *i. e.*, here at temperatures below 320 K, the  $^7\text{Li}$  NMR spectra consist of a single dipolarly broadened, almost purely Gaussian shaped line. At this temperature Li diffusion is too low to affect the line width of the spectrum. This drastically changes when the Li jump rate reaches the order of the NMR line width. As a result of rapid Li exchange processes taking place at elevated temperatures, (homonuclear) dipole–dipole interactions are increasingly averaged leading to the typical motional narrowing of the line. Here, with rising temperature the shape of the NMR line gradually changes into a pure Lorentzian. At intermediate temperatures the NMR lines seem to show the characteristics of a two-component line shape indicating distinctly mobile Li ions. As expected for an amorphous solid this might point to a heterogeneous dynamics present being similar to that found in other structurally disordered, glassy materials [19,22].

Plotting the NMR line width, *i. e.*, the full width at half maximum (FWHM), as a function of  $T$ , it can be seen that motional narrowing sets in at approximately

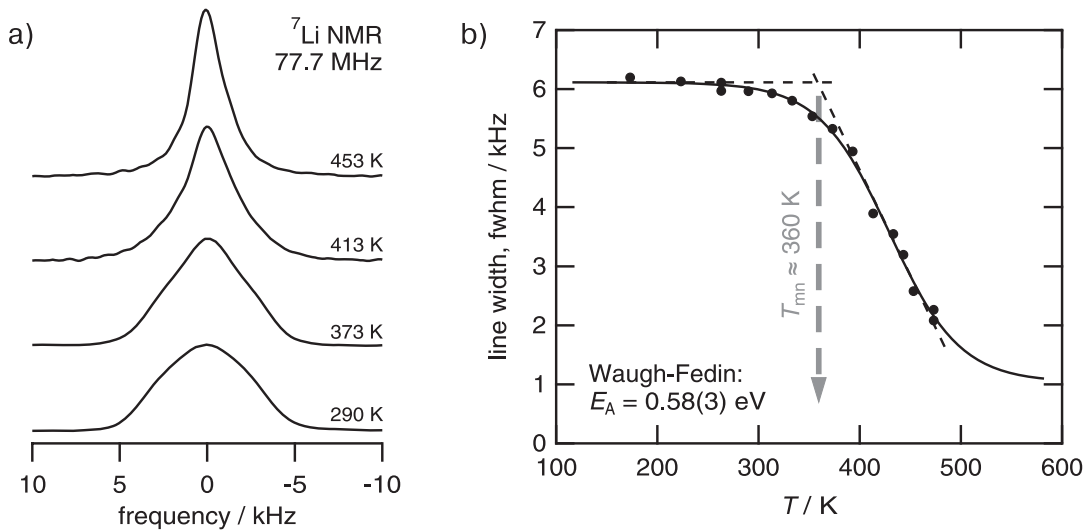


**Fig. 2.** (a) Selected  ${}^7\text{Li}$  NMR spectra of the structurally disordered Li-Si-Al-oxide recorded at 77.7 MHz. (b)  ${}^7\text{Li}$  NMR line width (full width at half maximum, fwhm) as a function of temperature. The onset of motional narrowing is observed at  $T_{\text{mn}} \approx 360$  K and points to an activation energy of approximately 0.6 eV when estimated using the relation introduced by Waugh and Fedin [52]. The solid line is drawn to guide the eye.

$T_{\text{mn}} = 360$  K (see Fig. 2b). Since the rigid-lattice line width is in the order of some kHz, this points to a mean Li jump rate of approximately  $10^3 \text{ s}^{-1}$  at  $T_{\text{mn}}$ . Using the expression introduced by Waugh and Fedin [52], an activation energy of about 0.58 eV can be roughly estimated. The Waugh-Fedin expression relates the onset temperature of motional narrowing with the activation energy of the diffusion process and is given by:  $E_{\text{a,mn}}/\text{eV} = 1.67 \times 10^{-3} \cdot T_{\text{mn}}/\text{K}$ .

In contrast to line shape measurements,  ${}^7\text{Li}$  NMR relaxometry provides a better quantitative access to Li diffusion parameters in solids. In the Arrhenius diagram of Fig. 3a  ${}^7\text{Li}$  NMR SLR rates recorded in the laboratory ( $1/T_1$ ) as well as in the rotating ( $1/T_{1\rho}$ ) frame of reference are shown as a function of inverse temperature. In each case the SLR NMR rate was obtained by fitting the corresponding magnetization transients with stretched exponentials. As an example, in Fig. 3b typical (normalized) magnetization transients  $M_\rho(t_{\text{lock}})$  recorded at different temperatures are shown. The solid lines show fits with  $M_\rho(t_{\text{lock}}) \propto \exp(-(t_{\text{lock}}/T_{1\rho})^\gamma)$ . Interestingly, the stretching exponent  $\gamma$  turned out to scatter around a mean value given by  $\gamma_{\text{m}} = 0.5$ . Hence, all fits were performed with a fixed stretching parameter  $\gamma = \gamma_{\text{m}}$ . Most likely,  $\gamma_{\text{m}} = 0.5$  points to localized relaxation centres such as paramagnetic impurities, see, *e. g.*, Refs. [53,54].

Contrary to the  $\text{SLR}_\rho$  rates in the rotating frame of reference, the  $1/T_1$  rates measured at 77.7 MHz are governed by non-diffusive background relaxation over almost the whole temperature range covered (see Fig. 3a). This manifests in a weak temperature dependence which can be described in terms of a power law  $1/T_{1,\text{nd}} \sim T^\alpha$  with  $\alpha \approx 0.6$  (dotted lines in Fig. 3a). Most likely, it is, to a certain degree, caused by spin-diffusion (*i. e.*, flip-flop processes) due to paramagnetic impurities which are also responsible for the stretching of the corresponding (non-exponential) transients. Furthermore, lattice vibrations or localized (*i. e.*, non-translational) motions, for example,

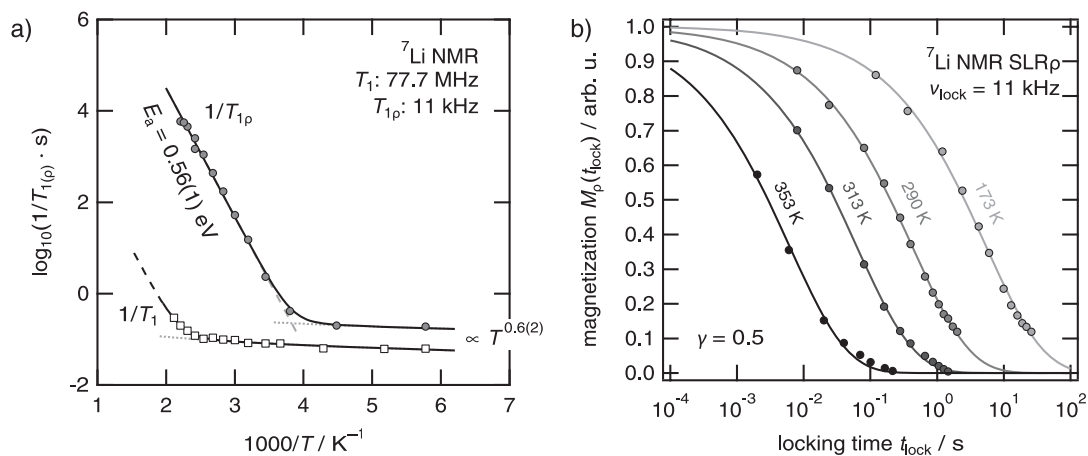


**Fig. 3.** (a)  ${}^7\text{Li}$  NMR SLR rates in the laboratory ( $1/T_1$ ,  $\square$ ) and rotating ( $1/T_{1\rho}$ ,  $\bullet$ ) frame of reference as a function of inverse temperature  $1/T$ . Data have been recorded at a Larmor frequency of 77.7 MHz and a locking frequency of 11 kHz, respectively. The corresponding transients  $M_\rho(t_{\text{lock}})$  are shown in (b). The rates reveal two regimes *viz* the diffusion-controlled flank of a  $1/T_{1(\rho)}(1/T)$  rate peak and a non-diffusive background contribution showing up below 250 K. The latter is characterized by a weaker-than-activated temperature dependence following a power law  $1/T_{1(\rho),\text{nd}} \propto T^{0.6(2)}$  (grey dotted lines). The diffusion-induced low- $T$  flank exhibits Arrhenius behaviour  $1/T_{1(\rho),\text{diff}} \propto \exp(-E_a/k_B T)$  and yields  $E_a = 0.56(1)$  eV (see dashed line). (b)  ${}^7\text{Li}$  NMR SLR $_\rho$  magnetization transients  $M_\rho(t_{\text{lock}})$  for four selected temperatures plotted *vs.* duration of the locking pulse. The locking frequency  $\nu_{\text{lock}}$  was set to  $\omega_1/2\pi = 11$  kHz. The solid lines represent fits of stretched exponentials with a fixed stretching exponent  $\gamma$ . See text for further details.

might contribute to the low-temperature NMR SLR rates  $1/T_1$  and  $1/T_{1\rho}$ , respectively. Whereas for pure spin-diffusion,  $1/T_{1,\text{nd}}$  is expected to be independent of  $T$ , strictly localized motions, in the sense of being the analogy of the well-known nearly constant loss (NCL) phenomenon in dielectric spectroscopy [55–59], would lead to  $1/T_{1,\text{nd}} \sim T^\alpha$  with  $\alpha \rightarrow 1$  [60–62]. For comparison, NMR SLR solely induced by lattice vibrations is expected to yield  $1/T_{1,\text{nd}} \sim T^2$  [63,64].

At temperatures above 410 K the SLR rates shown in Fig. 3a are increasingly influenced by translational Li ion diffusion processes. Therefore, the beginning of the low-temperature flank of the corresponding rate peak shows up. Provided the SLR NMR rates are induced by Li diffusion processes, reducing the Larmor frequency should shift this flank towards lower temperatures. According to the model introduced by Bloembergen, Purcell and Pound [65] the rate  $1/T_1$  on the low- $T$  flank, that is, in the limit  $\omega_0\tau \gg 1$ , is expected to show a quadratic frequency dependence.

The same dependency shows up when  $\omega_0$  is replaced by  $\omega_1$ , *i. e.*, when the resonance frequency in the MHz regime is replaced by a locking frequency being in the order of some kHz [24]. As can be clearly seen in Fig. 3a, at  $T > 265$  K the corresponding NMR SLR $_\rho$  rates probed in the rotating frame of reference exhibit a pronounced diffusion-induced low- $T$  flank following Arrhenius behaviour  $1/T_{1\rho,\text{diff}} \propto \exp(-E_a/k_B T)$  with an activation energy of approximately  $E_a = 0.56$  eV (see the dashed line in Fig. 3a). However, up to  $T = 450$  K no  ${}^7\text{Li}$  NMR SLR $_\rho$  maximum shows up. This might emerge at temperatures higher than 500 K. Below 250 K a non-diffusive background contribution is observed; the corresponding rates  $1/T_{1\rho,\text{nd}}$  depend only weakly on temperature, which

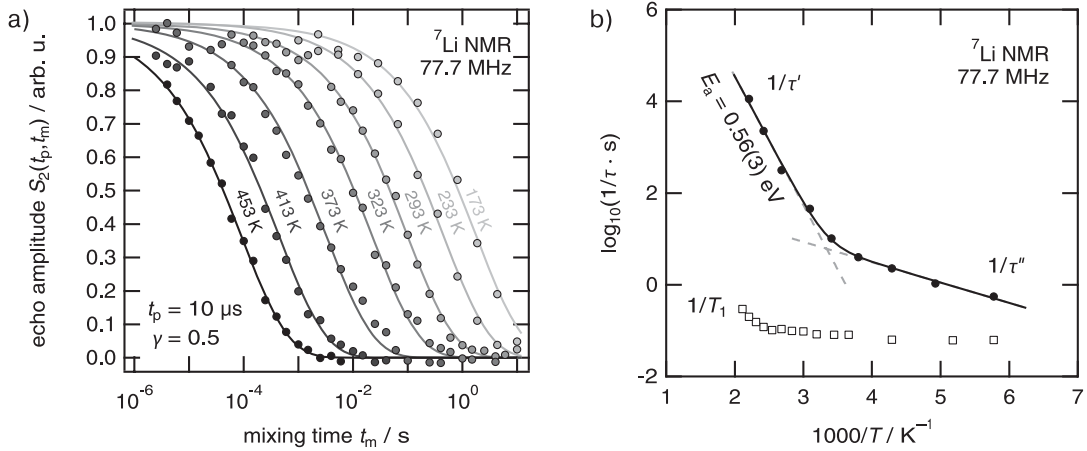


**Fig. 4.** (a)  ${}^7\text{Li}$  NMR SAE decay curves  $S_2(t_p, t_m)$  recorded at the temperatures indicated.  $S_2(t_p, t_m)$  has been plotted in a semi-log representation as a function of  $t_m$ . Data were measured at fixed preparation time,  $t_p = 10 \mu\text{s}$  and at 77.7 MHz. The solid lines are fits according to a stretched exponential using a fixed stretching exponent  $\gamma = 0.5$ . (b) Corresponding  ${}^7\text{Li}$  NMR SAE decay rates ( $\bullet$ ) as a function of the inverse temperature. The rates are a sum of two contributions *viz* a weakly temperature-dependent one showing up at  $T < 280 \text{ K}$  and a strongly thermally-activated one becoming apparent above 290 K. The latter shows Arrhenius behaviour with  $E_a = 0.56 \text{ eV}$ . For comparison, the  ${}^7\text{Li}$  NMR SLR rates  $1/T_1$  ( $\square$ ), see Fig. 3b, are also shown.

is practically the same behaviour as found for the SLR rates recorded in the laboratory frame of reference (see above).

Assuming that the parameters describing the temperature dependencies of the SLR rates found, *viz*  $E_a$  and  $\alpha$ , *i. e.*, of both the diffusion-induced and the non-diffusive contribution, are the same for  $1/T_1$  and  $1/T_{1\rho}$  a joint fit can be applied to the two data sets. The solid lines in Fig. 3a represent such a fit using a sum of the two contributions  $1/T_{1(\rho)} = 1/T_{1(\rho),\text{diff}} + 1/T_{1(\rho),\text{nd}}$ , linking the parameters  $E_a$  and  $\alpha$ . Here, it turned out that  $E_a = 0.57(1) \text{ eV}$  and  $\alpha = 0.6(2)$ . However, since SLR NMR and SLR $_{\rho}$  NMR probe diffusion parameters on different length scales, the slope of the low- $T$  flank of the SLR NMR rates, being sensitive to short-range Li motions, might be smaller than  $E_a$  found for the corresponding flank of the SLR $_{\rho}$  NMR rate peak. Indeed, a dependence of  $E_a$  on the time window used to study Li dynamics has also been found for spodumene ( $\text{LiAlSi}_2\text{O}_6$ ) studied by both NMR and ac impedance spectroscopy [66,67].

In Fig. 4a  ${}^7\text{Li}$  SAE NMR (normalized) decay curves  $S_2(t_p, t_m)$  are presented which have been recorded at fixed preparation time,  $t_p = 10 \mu\text{s}$ . Normalization means that the curves were scaled such that echo intensities range between 0 and 1. The echo amplitudes  $S_2(t_p, t_m)$  recorded at different temperatures can be well described by stretched exponentials according to

$$S_2(t_p, t_m) \propto \exp(-(t_m/\tau)^\gamma) \quad \text{with} \quad \tau = f(T). \quad (1)$$

As in the case of the NMR SLR $_{\rho}$  measurements, the (fractal) stretching exponent turned out to scatter around a mean value  $\gamma_m = 0.5$ . Consequently, we used a fixed (temperature independent) stretching exponent ( $\gamma = \gamma_m$ , see solid lines in Fig. 4a) to extract the echo decay rates  $1/\tau(T)$ . These are shown in Fig. 4b using an Arrhenius representation.

As can be clearly seen, the overall rate  $1/\tau$  is composed of two contributions and can be well described as a sum of the individual rates  $1/\tau'$  and  $1/\tau''$

$$1/\tau = 1/\tau' + 1/\tau'' . \quad (2)$$

$1/\tau'$  as well as  $1/\tau''$  follow Arrhenius behaviour  $1/\tau^i \propto \exp(-E_a^i/k_B T)$ . While  $1/\tau'$  shows a strong temperature dependence characterized by  $E_a = 0.56(3)$  eV which is, within the error given, identical with that probed by  $\text{SLR}_\rho$  NMR (see above), the rates  $1/\tau''$  dominating echo decay at low temperatures point to an activation energy of only  $0.09(1)$  eV. Since an almost temperature independent decay rate would be expected to account for spin-diffusion effects, as mentioned above, one might propose to identify the rate  $1/\tau''$  with a (quadrupolar or dipolar) SLR rate. Although such a rate is expected to be larger than the independently measured rate  $1/T_1$ , the temperature dependencies of these SLR NMR rates should be comparable. Here, however,  $1/T_1$  (as well as  $1/T_{1\rho}$ ) reveals a much weaker temperature dependence (see above). Thus,  $1/\tau''$  seems to contain additional information on the Li dynamics present at low temperatures which are masked in the case of  $1/T_1$  (and  $1/T_{1\rho}$ ). In view of the fact that the associated activation energy is rather low (less than 0.1 eV), (weakly activated) localized (or caged) motions rather than long-range transport might be responsible for the process characterized by  $1/\tau''$ . Interestingly, the activation energy probed is very similar to that of the strictly localized two-site jump processes in crystalline spodumene ( $\text{LiAlSi}_2\text{O}_6$ ) [44]. Further SAE NMR measurements carried out at different resonance frequencies might help to clarify the origin of the low-temperature echo decay.

### 2.1.2 Impedance spectroscopy

Long-range, *i. e.*, end-to-end ion transport can be probed by conductivity measurements. Typical impedance spectra of the gas-phase synthesized amorphous oxide are shown in Fig. 5a where the real part,  $\sigma$ , of the complex conductivity is shown as a function of frequency. Typically, the spectra consist of three regimes. At low frequencies polarisation effects, due to blocking electrodes applied, lead to a decrease of  $\sigma$ , while at high frequencies a dispersive regime is observed. At intermediate frequencies distinct frequency-independent plateaus show up being characteristic of successful ion hops in the oxide studied.

The corresponding conductivity values, depicted in Fig. 5b, were read out at the saddle point of the impedance spectra. In a good approximation they can be identified with the dc-conductivities  $\sigma_{\text{dc}}$ . Let us remark that almost identical values were obtained from an analysis of the corresponding Cole–Cole plots which can be constructed when the (negative) imaginary part of the complex impedance,  $Z''$ , is plotted *vs* the real part,  $Z'$ . The intersection of the semicircle with the real axis is given by  $1/\sigma_{\text{dc}}$ . As can be seen in Fig. 5b,  $\sigma_{\text{dc}}T$  clearly follows Arrhenius behaviour according to

$$\sigma_{\text{dc}}T = \sigma_0 \exp(-E_{a,\sigma}/k_B T) . \quad (3)$$

The fit shown (see the solid line in Fig. 5b) yields an activation energy  $E_{a,\sigma}$  of  $0.80(1)$  eV. Clearly, this value is much larger than those probed by  $\text{SLR}_\rho$  and SAE NMR. Note that  $\text{SLR}_\rho$  rates have been measured at frequencies comparable to those

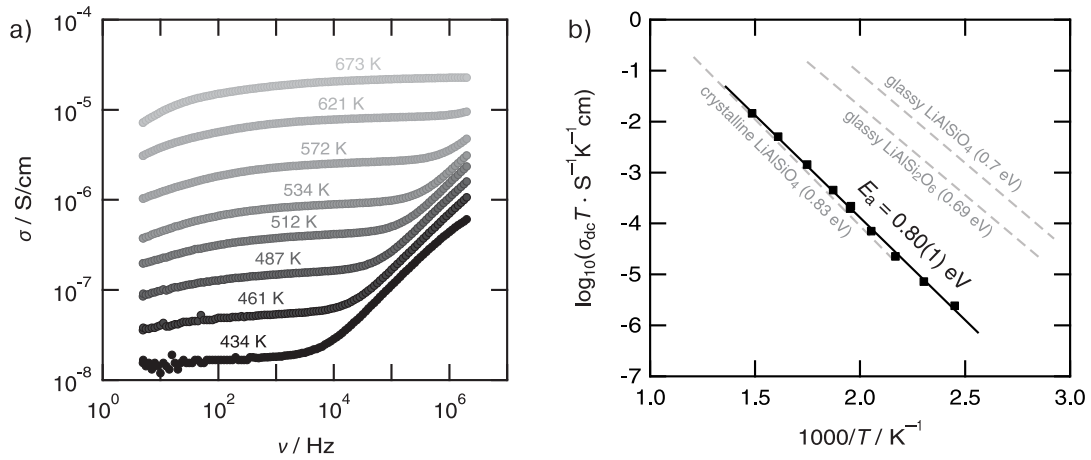


**Fig. 5.** (a) Impedance spectra (normalized to the sample geometry) recorded at the temperatures indicated. The spectra are composed of a “dc-plateau” and a dispersive regime showing up at higher frequencies. At lower frequencies,  $\sigma$  decreases due to ion blocking polarisation effects at the electrodes. (b) The temperature dependence of  $\sigma_{dc}T$  shows Arrhenius behaviour with an activation energy  $E_{a,\sigma} = 0.8$  eV. For comparison, the respective Arrhenius lines of glassy and crystalline eucryptite ( $\text{LiAlSiO}_4$ ) as well as glassy spodumene ( $\text{LiAlSi}_2\text{O}_6$ ) are also indicated (data were taken from Refs. [71,72]).

where the conductivity values have been determined. In the case of SLR NMR one might argue that the rates  $1/T_1$  are influenced by correlation effects caused by Coulomb interactions and/or structural disorder [68–70]. Such effects are known to lead to a reduced slope of the rate peak in the limit  $\omega_0\tau \gg 1$ . This behaviour is accompanied with a sub-quadratic frequency dependence of  $1/T_1$  on the low- $T$  side of the peak  $1/T_1(1/T)$ . However, since no discrepancy between the activation energies found by SLR $_{\rho}$  NMR on the one hand and SAE NMR on the other hand is found, correlation effects seem to play a minor role in affecting SLR NMR rates measured in the low- $T$  limit here. Instead, ion blocking regions of the particle-assembled structure (see Fig. 1b) might contribute to the dc-conductivities probed. In contrast, due to the much lower number density of charge carriers in such near-surface regions, NMR data, even when sensitive to long-range motions as in the case of the SAE technique, is mainly sensitive to Li dynamics taking place in the bulk, *i. e.*, in the interior of the particles.

For comparison, when results from bulk ion conductivities are compared with SAE NMR data, quite often good agreement is found [25]. As an example, this similarity has been shown to be valid for polycrystalline garnet-type  $\text{Li}_7\text{Zr}_2\text{La}_3\text{O}_{12}$  [13,47] investigated quite recently by some of us.

Finally, in Fig. 5b the relatively low Li ion diffusivity and ion conductivity, respectively, found here is compared with results on crystalline and glassy eucryptite  $\text{LiAlSiO}_4$  [71] as well as glassy spodumene  $\text{LiAlSi}_2\text{O}_6$  [72] (see also Refs. [73,74]). Interestingly, although the sample studied turns out to be X-ray amorphous, ion conductivities probed resemble that of crystalline  $\text{LiAlSiO}_4$  rather than that of the glassy counterpart. Once again this might simply be explained by a large influence of ion blocking regions between the globular particles. As indicated by the impedance spectrum recorded at 434 K, a second frequency-independent plateau might show up at larger frequencies reflecting bulk data. Regarding the activation energies deduced from

SLR<sub>p</sub> NMR and SAE NMR, the value of 0.56 eV found for the non-stoichiometric amorphous oxide studied here is reasonably consistent with the trend shown in Fig. 5b.

## 2.2 Conclusion and outlook

Li dynamics in a gas-phase synthesized non-stoichiometric Li-Al-Si-oxide was complementarily investigated by NMR and impedance spectroscopy. The activation energy deduced from <sup>7</sup>Li NMR SLR rates probed in the rotating frame of reference (0.56 eV) is in very good agreement with that probed by mixing-time dependent <sup>7</sup>Li SAE NMR being sensitive to long-range Li motions. Thus, the two methods do obviously probe the same diffusion process in the metastable oxide. Together with results from NMR line shape measurement, the findings reveal moderate Li diffusivity in the structurally disordered oxide investigated. The analysis of variable-temperature impedance spectra point to a Li transport process being characterized by an even higher activation energy of approximately 0.8 eV.

Interestingly, the low temperature SAE NMR decay rates indicate weakly activated localized Li motions characterized by 0.09 eV. Further frequency-dependent SAE NMR measurements as well as the acquisition of low-*T* impedance spectra might help characterize this dynamic process in more detail.

## Acknowledgement

We thank P. Bottke and A. Kuhn for valuable discussions. Financial support by the Deutsche Forschungsgemeinschaft (DFG) within the Research Unit 1277 “Mobilität von Li-Ionen in Festkörpern” (molife) is highly acknowledged.

## References

1. H. Mehrer, *Diffusion in Solids: Fundamentals, Methods, Materials, Diffusion-Controlled Processes*, Springer, Berlin (2007).
2. P. Heitjans and J. Kärger (Eds.), *Diffusion in Condensed Matter: Methods, Materials, Models*, Springer, Berlin (2005).
3. A. V. Chadwick, *Diffus. Fundam.* **2** (2005) 44.
4. P. Heitjans, S. Indris, and M. Wilkening, *Diffus. Fundam.* **2** (2005) 45.
5. V. W. J. Verhoeven, I. M. de Schepper, G. Nachtegaal, A. P. M. Kentgens, E. M. Kelder, J. Schoonman, and F. M. Mulder, *Phys. Rev. Lett.* **86** (2001) 4314.
6. J. Cabana, N. Dupré, G. I. Rousse, C. P. Grey, and M. R. Palacín, *Solid State Ionics* **176** (2005) 2205.
7. M. Wilkening, W. Küchler, and P. Heitjans, *Phys. Rev. Lett.* **97** (2006) 065901.
8. L. S. Cahill, R. P. Chapman, J. F. Britten, and G. R. Goward, *J. Phys. Chem. B* **110** (2006) 7171.
9. L. van Wüllen, T. Echelmeyer, H.-W. Meyer, and D. Wilmer, *Phys. Chem. Chem. Phys.* **9** (2007) 3298.
10. M. Wilkening and P. Heitjans, *Phys. Rev. B* **77** (2008) 024311.
11. B. Koch and M. Vogel, *Solid State Nucl. Mag.* **34** (2008) 37.
12. J. Cabana, J. Shirakawa, G. Chen, T. J. Richardson, and C. P. Grey, *Chem. Mater.* **22** (2010) 1249.
13. A. Kuhn, S. Narayanan, L. Spencer, G. Goward, V. Thangadurai, and M. Wilkening, *Phys. Rev. B* **83** (2011) 094302.

14. H. Hain, M. Scheuermann, R. Heinzmann, L. Wünsche, H. Hahn, and S. Indris, *Solid State Nucl. Mag.* **42** (2012) 9.
15. A. Kuhn, M. Kunze, P. Sreeraj, H. D. Wiemhöfer, V. Thangadurai, M. Wilkening, and P. Heitjans, *Solid State Nucl. Mag.* **42** (2012) 2.
16. M. Armand and J.-M. Tarascon, *Nature* **451** (2008) 652.
17. P. Knauth, *Solid State Ionics* **180** (2009) 911.
18. H. Buschmann, J. Dölle, S. Berendts, A. Kuhn, P. Bottke, M. Wilkening, P. Heitjans, A. Senyshyn, H. Ehrenberg, A. Lotnyk, V. Duppel, L. Kienle, and J. Janek, *Phys. Chem. Chem. Phys.* **13** (2011) 19378.
19. P. Heitjans, M. Masoud, A. Feldhoff, and M. Wilkening, *Faraday Discuss.* **134** (2007) 67.
20. M. Wilkening, V. Epp, A. Feldhoff, and P. Heitjans, *J. Phys. Chem. C* **112** (2008) 9291.
21. M. J. Pooley and A. V. Chadwick, *Radiat. Eff. Defects Solids.* **158** (2003) 209.
22. S. Faske, H. Eckert, and M. Vogel, *Phys. Rev. B* **77** (2008) 104301.
23. M. Wilkening, A. Kuhn, and P. Heitjans, *Phys. Rev. B* **78** (2008) 054303.
24. P. Heitjans, A. Schirmer, and S. Indris, NMR and  $\beta$ -NMR studies of diffusion in interface-dominated and disordered solids, in: *Diffusion in Condensed Matter: Methods, Materials, Models*, P. Heitjans, J. Kärgler (Eds.), Springer, Berlin (2005), pp. 367–415.
25. M. Wilkening and P. Heitjans, *Chem. Phys. Chem.* **13** (2012) 53.
26. M. Wilkening and P. Heitjans, *Solid State Ionics* **177** (2006) 3031.
27. M. Wilkening and P. Heitjans, *Defect Diffus. Forum* **237–240** (2005) 1182.
28. R. Böhmer, T. Jörg, F. Qi, and A. Titze, *Chem. Phys. Lett.* **316** (2000) 419.
29. F. Qi, T. Jörg, and R. Böhmer, *Solid State Nucl. Mag.* **22** (2002) 484.
30. F. Qi, G. Diezemann, H. Böhm, J. Lambert, and R. Böhmer, *J. Magn. Reson.* **169** (2004) 225.
31. R. Böhmer and F. Qi, *Solid State Nucl. Mag.* **31** (2007) 28.
32. S. Faske, B. Koch, S. Murawski, R. Kuchler, R. Böhmer, J. Melchior, and M. Vogel, *Phys. Rev. B* **84** (2011) 024202.
33. T. Giesenberg, S. Hein, M. Binnewies, and G. Kickelbick, *Angew. Chem. Int. Edit.* **43** (2004) 5697.
34. C. Brüning, Ph.D. thesis, Leibniz University Hannover (2010).
35. E. Fukushima and S. B. W. Roeder, *Experimental Pulse NMR: A Nuts and Bolts Approach*, Addison-Wesley Pub. Co., Reading, Mass. (1981).
36. D. Ailion and C. P. Slichter, *Phys. Rev. Lett.* **12** (1964) 16.
37. C. P. Slichter and D. C. Ailion, *Phys. Rev.* **135** (1964) A1099.
38. D. C. Ailion and C. P. Slichter, *Phys. Rev.* **137** (1965) A235.
39. D. C. Look and I. J. Lowe, *J. Chem. Phys.* **44** (1966) 2995.
40. T. J. Rowland and F. Y. Fradin, *Phys. Rev.* **182** (1969) 760.
41. D. Wolf, *Phys. Rev. B* **10** (1974) 2724.
42. J. Jeener and P. Broekaert, *Phys. Rev.* **157** (1967) 232.
43. R. Böhmer, *J. Magn. Reson.* **147** (2000) 78.
44. F. Qi, C. Rier, R. Böhmer, W. Franke, and P. Heitjans, *Phys. Rev. B* **72** (2005) 104301.
45. X.-P. Tang and Y. Wu, *J. Magn. Reson.* **133** (1998) 155.
46. R. Böhmer, K. Jeffrey, and M. Vogel, *Prog. Nucl. Magn. Res. Spectrosc.* **50** (2007) 87.
47. A. Kuhn, V. Epp, G. Schmidt, S. Narayanan, V. Thangadurai, and M. Wilkening, *J. Phys.-Condens. Matter* **24** (2012) 035901.
48. M. Wilkening, J. Heine, C. Lyness, A. R. Armstrong, and P. G. Bruce, *Phys. Rev. B* **80** (2009) 064302.
49. H. W. Spiess, *J. Chem. Phys.* **72** (1980) 6755.
50. M. Lausch and H. W. Spiess, *J. Magn. Reson.* (1969–1992) **54** (1983) 466.
51. F. Fujara, S. Wefing, and H. W. Spiess, *J. Chem. Phys.* **84** (1986) 4579.
52. J. S. Waugh and E. I. Fedin, *Sov. Phys. Solid State* **4** (1963) 1633.
53. D. Tse and S. R. Hartmann, *Phys. Rev. Lett.* **21** (1968) 511.
54. H.-J. Stöckmann and P. Heitjans, *J. Non-Cryst. Solids* **66** (1984) 501.
55. W.-K. Lee, J. F. Liu, and A. S. Nowick, *Phys. Rev. Lett.* **67** (1991) 1559.
56. A. S. Nowick, B. S. Lim, and A. V. Vaysleyb, *J. Non-Cryst. Solids* **172–174** (1994) 1243.
57. H. Jain and S. Krishnaswami, *Solid State Ionics* **105** (1998) 129.

58. A. K. Rizos, J. Alifragis, K. L. Ngai, and P. Heitjans, *J. Chem. Phys.* **114** (2001) 931.
59. K. Funke, R. D. Banhatti, D. M. Laughman, L. G. Badr, M. Mutke, A. Šantić, W. Wrobel, E. M. Fellberg, and C. Biermann, *Z. Phys. Chem.* **224** (2010) 1891.
60. K. L. Ngai, U. Strom, and O. Kanert, *Phys. Chem. Glasses* **33** (1992) 109.
61. O. Kanert, R. Kuchler, J. Dieckhöfer, X. Lu, and H. Jain, *Phys. Rev. B* **49** (1994) 629.
62. O. Kanert, R. Kuchler, P. C. Soares, and H. Jain, *J. Non-Cryst. Solids* **307** (2002) 1031.
63. J. Van Kranendonk, *Physica* **20** (1954) 781.
64. R. L. Mieher, *Phys. Rev.* **125** (1962) 1537.
65. N. Bloembergen, E. M. Purcell, and R. V. Pound, *Phys. Rev.* **73** (1948) 679.
66. A. Kuhn, diploma thesis, Leibniz University Hannover (2008).
67. P. Heitjans, E. Tobschall, and M. Wilkening, *Eur. Phys. J.-Spec. Top.* **161** (2008) 97.
68. M. Meyer, P. Maass, and A. Bunde, *Phys. Rev. Lett.* **71** (1993) 573.
69. A. Bunde, W. Dieterich, P. Maass, and M. Meyer, Ionic transport in disordered materials, in: *Diffusion in Condensed Matter: Methods, Materials, Models*, P. Heitjans, J. Kärger (Eds.), Springer, Berlin (2005), pp. 813–856.
70. K. Funke, *Prog. Solid State Chem.* **22** (1993) 111.
71. P. Bottke, diploma thesis, Leibniz University Hannover (2010).
72. A. Kuhn, M. Wilkening, and P. Heitjans, *Solid State Ionics* **180** (2009) 302.
73. B. Munro, M. Schrader, and P. Heitjans, *Ber. Bunsen. Phys. Chem.* **96** (1992) 1718.
74. A.-M. Welsch, H. Behrens, I. Horn, S. Roß, and P. Heitjans, *J. Phys. Chem. A* **116** (2012) 309.



## 4 Conclusion and outlook

In the course of this dissertation different (classes of) materials have been investigated by various solid-state NMR methods and impedance spectroscopy. The compounds studied were deemed interesting for their potential use in energy storage systems and can be roughly categorized as (i) fast (structurally complex) ion conductors, (ii) structurally disordered ion conductors, and (iii) ion conductors with structurally confined diffusion pathways. Some of the materials turned out to indeed show promise for the usage as solid electrolytes in all-solid-state batteries, *viz.* argyrodite-type  $\text{Li}_6\text{PS}_5\text{Br}$  (Sect. 3.2.2) and garnet-type “ $\text{Li}_{6.5}\text{La}_{2.5}\text{Ba}_{0.5}\text{ZrTaO}_{12}$ ” (Sect. 3.3.2). These show rather high Li diffusivities characterized by DC-conductivities at room temperature in the order of  $10^{-3}$  S/cm\* and  $10^{-4}$  S/cm, respectively. A further highlight of this work can be certainly seen in the unequivocal identification of a low-dimensional diffusion process in hexagonal  $\text{LiBH}_4$  (Sects. 3.4.1 and 3.5.1) and the 3R modification of  $\text{Li}_{0.7}\text{NbS}_2$  (Sect. 3.4.2) via temperature-variable and frequency-dependent  ${}^{6,7}\text{Li}$  SLR NMR experiments. Here, the high-temperature flank of the diffusion-induced SLR maxima shows a logarithmic frequency dependence characteristic for diffusion in two dimensions.

The methods used to characterize diffusion parameters of the potential energy materials can be regarded as very well suited for the task at hand. With the complementary techniques, it was possible to study  $\text{Li}^+$  dynamics in these compounds over a wide range of time scales and temperatures. As such, they certainly form an excellent basis for further measurements, some of which are already underway in our research group.

For example, another structurally complex sulfide was prepared by DI Dominik Wohlmuth and is now being characterized by him. Dominik is also investigating the effect of structural disorder (introduced by high-energy ball milling) on diffusion parameters in  $\text{LiAlO}_2$ .  ${}^7\text{Li}$  NMR SAE experiments following up on the study on  $\text{LiC}_6$  (*cf.* Sect. 3.4.3) have been performed by DI Julia Langer and are currently being evaluated and prepared for publication. Additionally, Julia is also studying the influence of spatially confined structures on Li-ion dynamics in  $\text{Li}_{0.17}\text{SnS}_2$ , a layer-structured lithium intercalation compound. Similarly to Julia’s measurements and to the results presented in Sect. 3.4.2 (3R- $\text{NbS}_2$ ), DI Bernhard Stanje is examining the 2H modification of  $\text{NbS}_2$  at different lithiation states.

After the promising results obtained for the Li argyrodites (notably for  $\text{Li}_6\text{PS}_5\text{Br}$ ), the suitability for their use as solid electrolytes has to be further tested in the form of chemical stability with respect to common cathode materials, see *e. g.* Refs. [148–150]. Such experiments are being currently prepared. A rather “exotic” material for future investigations is found in

---

\* The value for the lithium argyrodite was calculated from NMR-determined Li jump rates making use of both the Einstein-Smoluchowski expression and the Nernst-Einstein equation.

the low-temperature modification of  $\text{Li}_4\text{C}_{60}$ , a fulleride polymer exhibiting a two-dimensional structure. First measurements by Riccò *et al.* not only show it to be a very good ionic conductor ( $10^{-2}$  S/cm at room temperature) but also suggest that the structural dimensionality may also be reflected in SLR NMR data.<sup>[151]</sup> Here, a definitive answer could be given by a comprehensive NMR study.

## A Supplemental material

Below, supplemental material to the articles “Long-range  $\text{Li}^+$  dynamics in the lithium argyrodite  $\text{Li}_7\text{PSe}_6$  as probed by rotating-frame spin–lattice relaxation NMR” (see pp. 47–56) and “Highly Mobile Ions: Low Temperature NMR Directly Probes Extremely Fast  $\text{Li}^+$  Hopping in Argyrodite-type  $\text{Li}_6\text{PS}_5\text{Br}$ ” (see pp. 58–63) is given.

Reproduced by permission of The PCCP Owner Societies. The original article and supplemental material can be found online at <http://pubs.rsc.org/en/Content/ArticleLanding/2013/CP/c3cp44379e#divAbstract>. ©2013 The PCCP Owner Societies.

Reprinted with permission of the American Chemical Society. The original article and supporting information can be found online at <http://pubs.acs.org/doi/abs/10.1021/jz401003a>. ©2013 American Chemical Society.

Supplemental material:

## “Long-range Li<sup>+</sup> dynamics in the lithium argyrodite Li<sub>7</sub>PSe<sub>6</sub> as probed by rotating-frame spin-lattice relaxation NMR”

V. Epp<sup>1,\*</sup>, O. Gün,<sup>2</sup> H.-J. Deiseroth,<sup>2</sup> and M. Wilkening<sup>1</sup>

<sup>1</sup>Christian Doppler Laboratory for Lithium-ion Batteries, Graz University of Technology, Institute for Chemistry and Technology of Materials, Stremayrgasse 9, 8010 Graz, Austria and

<sup>2</sup>University of Siegen, Inorganic Chemistry I, Adolf-Reichwein-Straße 2, 57068 Siegen, Germany

### S1

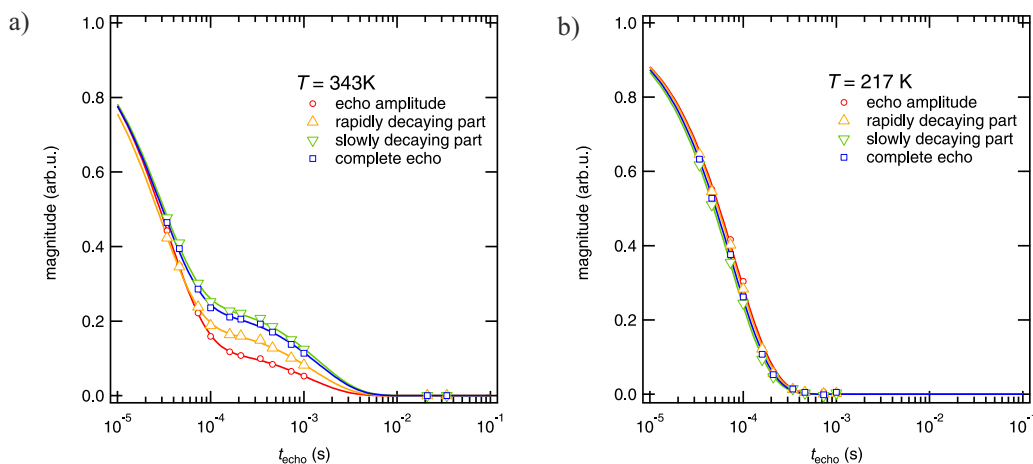


FIG. S1: <sup>7</sup>Li NMR echo decay transients recorded at 116 MHz and at the temperatures indicated. (a) and (b): The decay curves were obtained by evaluating (i) the echo amplitude, (ii) the area under the rapidly decaying part of the echo, (iii) the slowly decaying part, and (iv) the complete echo, respectively. At  $T \geq 295$  K a two-step decay is observed. The first decay step is characterized by a time constant  $T_2'' \approx 3 \times 10^{-5}$  s and is no longer detectable at lower  $T$  (b).

### S2

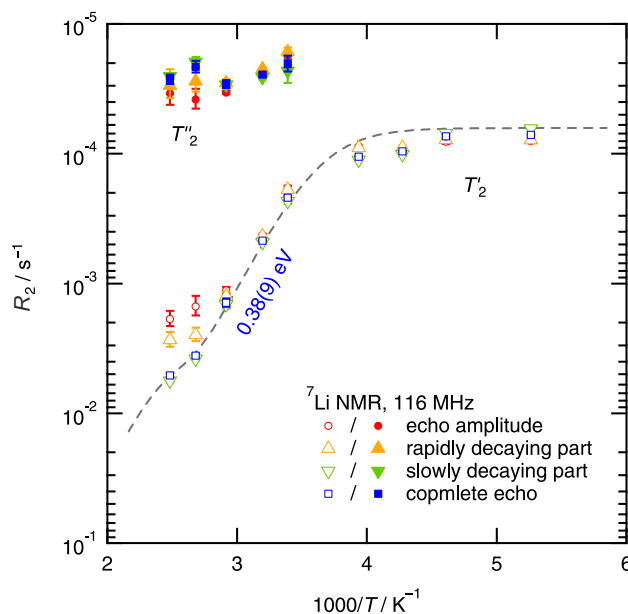


FIG. S2: <sup>7</sup>Li NMR spin-spin relaxation (SSR) rates  $R_2' = 1/T_2'$  and  $R_2'' = 1/T_2''$  as a function of inverse temperature. Both time constants were obtained from double-exponentials  $E(t) = A + B_1 \exp(-t/T_2') + B_2 \exp(-t/T_2'')$  fitted to the corresponding echo decay curves shown in Fig. S1. Applying the BPP model an activation energy of about 0.4 eV is derived from  $T_2''$  data.

Supporting Information

## Highly Mobile Ions: Low Temperature NMR Directly Probes Extremely Fast Li<sup>+</sup> Hopping in Argyrodite-type Li<sub>6</sub>PS<sub>5</sub>Br

Viktor Epp<sup>\*1</sup>, Özgül Gün<sup>2</sup>, Hans-Jörg Deiseroth<sup>2</sup>, and Martin Wilkening<sup>\*1</sup>

<sup>1</sup>Christian Doppler Laboratory for Lithium Batteries ,  
and Institute of Chemistry and Technology of Materials, Graz University of Technology,  
Stremayrgasse 9, 8010 Graz (Austria); e-mail [viktor.epp@tugraz.at](mailto:viktor.epp@tugraz.at); [wilkening@tugraz.at](mailto:wilkening@tugraz.at),  
web: [www.lithium.tugraz.at](http://www.lithium.tugraz.at)

<sup>2</sup>Anorganische Chemie, University of Siegen, Adolf-Reichwein-Straße 2, 57068 Siegen (Germany)

### Experimental

Solid state <sup>7</sup>Li NMR measurements on Li-argyrodite samples with natural isotope abundance (<sup>7</sup>Li: 92.5%, <sup>6</sup>Li 7.2%) were carried out using an Avance III spectrometer connected to a 7 T cryo magnet (Bruker BioSpin GmbH, Germany), resulting in a nominal resonance frequency of  $\omega_0/2\pi = 116.6$  MHz. For experiments at temperatures between 430 K and 210 K a ceramic high temperature probe head was employed, while a cryo probe gave access to temperatures as low as 13 K when using liquid helium (both probes, Bruker BioSpin GmbH). The output power levels of the probes were set so that the  $\pi/2$  pulse length was about 3  $\mu$ s and 4.5  $\mu$ s, respectively. In the case of the ceramic probe the temperature was monitored by a Eurotherm temperature controller connected to a type T thermocouple, while the NMR cryo probe was operated in conjunction with a LakeShore temperature controller and Cernox sensors. Prior to the NMR experiments the powder samples were vacuum dried and fire-sealed in glass NMR tubes of the dimensions 5 mm by 3 cm.

The <sup>7</sup>Li NMR spectra shown here were obtained by Fourier transformation of free induction decay signals (FIDs) recorded by means of a simple one pulse experiment. The recycle delay was chosen to be sufficiently long for the spins to reach equilibrium state after each scan, *e. g.*, at least  $5 \times T_1$ , where  $T_1$  is the spin-lattice relaxation (SLR) time constant.

${}^7\text{Li}$  NMR SLR rates  $R_1 = 1/T_1$  in the laboratory frame of reference were acquired utilizing the saturation recovery pulse sequence:  $n \times \pi/2 - t_d - \pi/2$  (acq.). Here, a train of  $n = 10$  closely timed  $\pi/2$  pulses is used to destroy all contributions to the longitudinal magnetization  $M_z$  prior to the experiment ( $M_z(t = 0) = 0$ ). Subsequently, the relaxation of  $M_z$  towards equilibrium  $M_{z,\text{eq}}$  is recorded as a function of the delay time  $t_d$  ( $M_z(t_d \rightarrow \infty) = M_{z,\text{eq}}$ ), using the last  $\pi/2$  pulse as a detection pulse. The resulting magnetization transients were parameterized employing a stretched exponential of the form  $M_z(t_d) = M_{z,\text{eq}}[1 - \exp(-(R_1 \cdot t_d)^\gamma)]$ . Depending on the sample, the stretching exponent  $\gamma$  was found to be in the range of 0.84 and 1. In addition to  ${}^7\text{Li}$  NMR experiments  ${}^6\text{Li}$  SLR rates were recorded for  $\text{Li}_6\text{PS}_5\text{Br}$  at a Larmor frequency of  $\omega_0/2\pi = 44.2$  MHz at temperatures ranging from 165 K to 353 K.

Similarly,  ${}^7\text{Li}$  NMR spin-lattice relaxation was studied in the rotating frame of reference (SLR<sub>p</sub>). Here, the relaxation is taking place in a much weaker magnetic field  $B_1$  ( $10^4$  Hz) than it is the case in the laboratory frame ( $10^8$  Hz), thus being sensitive to dynamics on longer time and length scales. The relaxation rates  $R_{1p}$  were recorded employing the so-called spin-lock technique, whereby the equilibrium magnetization  $M_{p,\text{eq}} = M_p(0)$  is rotated onto the  $x$ - $y$ -plane and “spin-locked” in the field  $B_1$  by a locking pulse of the duration  $t_{\text{lock}}$ .  $M_p$  is then recorded as a function of  $t_{\text{lock}}$  as it relaxes to its new equilibrium value, which is essentially zero ( $M_p(t_{\text{lock}} \rightarrow \infty) = 0$ ). Here, the magnetization transients took the form  $M_p(t_{\text{lock}}) = M_{p,\text{eq}} \exp(-(R_{1p} \cdot t_{\text{lock}})^\gamma)$ , with stretching exponents  $\gamma$  ranging from 0.46 to 0.94. The experiments were performed at two locking frequencies  $\omega_1/2\pi = 14$  kHz and 45 kHz (see text for further explanations). As for the measurements of the NMR spectra a recycle delay of at least  $5 \times T_1$  was used. Note that with the NMR cryo probe employed we could not reach locking frequencies lower than 40 kHz. As can be seen from figure 2, in the case of 3D BPP-type behavior a slight decrease of the locking frequency does influence the low- $T$  flank only. The peak maximum is expected to shift only slightly towards lower  $T$ . Even in the case of 45 kHz it is still expected to show up well below 200 K.

# B Experimental

## B.1 Apparatus

### B.1.1 Solid-state NMR setup

The main body of the NMR measurements has been performed on Bruker Avance III solid-state NMR spectrometers. These were available in two (essentially same) configurations, differing mainly in the nominal field strength of the shimmed cryomagnets connected to them. While the Avance III 300 is equipped with a 7 T magnet, a 11 T magnet is used in conjunction with the Avance III 500 (see Fig. B.1). This corresponds to  $^7\text{Li}$  resonance frequencies of 116 MHz and 194 MHz, respectively.

The probe heads employed were commercial solid-state broadband probes (Bruker) designed for the operation in different temperature ranges (see Fig. B.2). While the standard teflon probe can be used for measurements between about 180 K and 450 K, the ceramic high-temperature probe can accommodate temperatures up to 620 K. In both cases, a Eurotherm temperature controller in connection with type T thermocouples was used. For measurements at cryogenic temperatures, a cryoprobe was employed. Using liquid nitrogen, this allows for measurements to be performed at temperatures as low as 100 K; with liquid helium, the limit can be pushed down to about 13 K. Here, the temperature is controlled by a LakeShore 331 unit using two Cernox sensors: one in the cryostat and one in the vicinity of the sample.

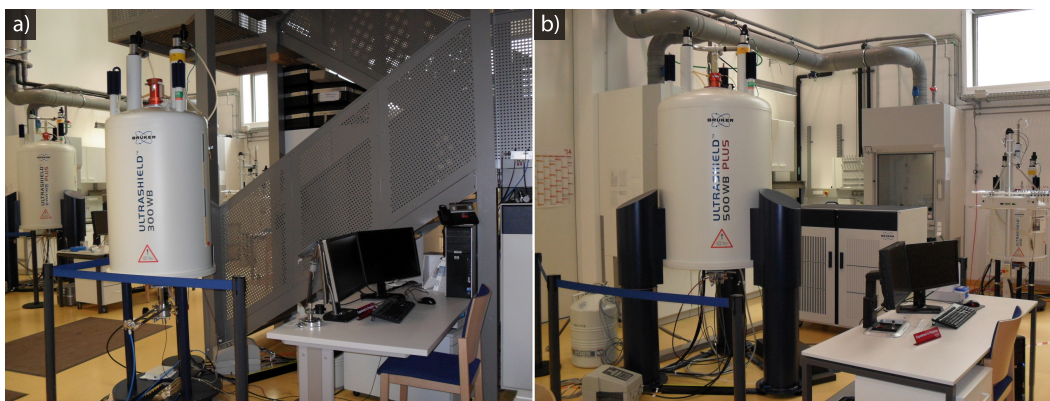


**Figure B.1:** a) Photographs of the solid-state NMR spectrometer workstations: a) Bruker Avance III 300. b) Bruker Avance III 500.

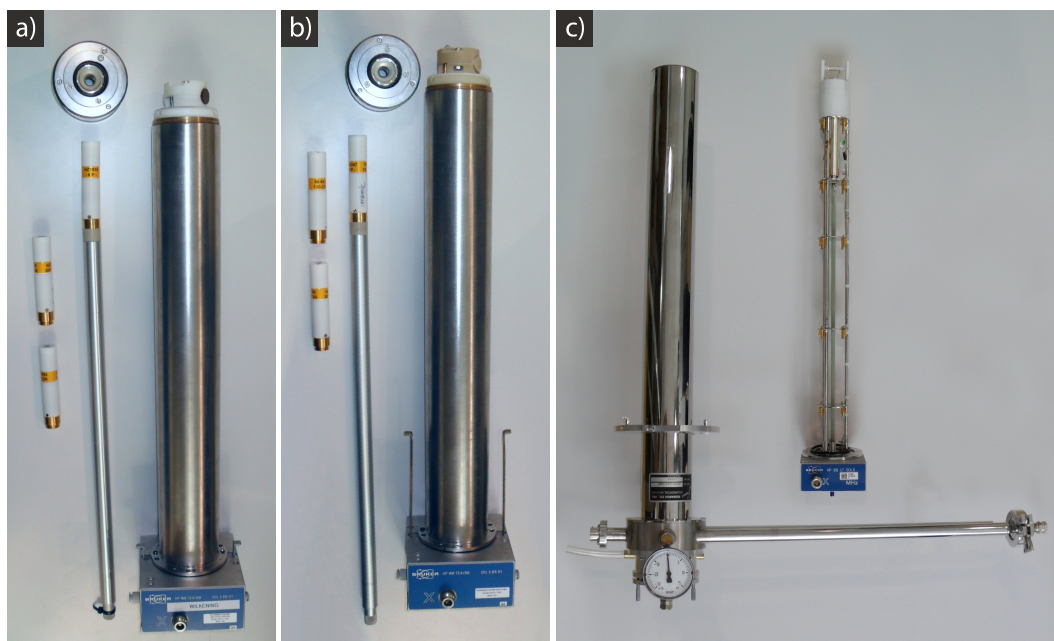


**Figure B.2:** a) Photographs of the solid-state NMR probes used in this work (all commercially available from Bruker): a) Standard solid-state NMR probe (teflon). The accessible temperature ranges from about 180 K to 450 K. b) High-temperature solid-state NMR probe (ceramics). The accessible temperature ranges from about 180 K to 620 K. c) Solid-state NMR cryoprobe. The cryostat is seen on the left, the probe itself on the right. The accessible temperature ranges from RT down to about 13 K.

Some early experiments were conducted on MSL 100 and MSL 400 solid-state NMR spectrometers (Bruker). The MSL 100 was used with a 400 W Kalmus amplifier and an unshimmed field-variable cryomagnet (Oxford) usually operated at 4.9 T, which corresponds to a  ${}^7\text{Li}$  resonance frequency of 78 MHz. The MSL 400 was connected to a shimmed 9.4 T magnet (Oxford), resulting in a  ${}^7\text{Li}$  resonance frequency of 155 MHz. The probes used here were also commercial broadband probe heads (Bruker) accommodating a temperature range of about 130 K ... 470 K. The temperature was monitored with an ITC4 temperature controller (Oxford) and Ni-CrNi thermocouples. More details (as well as pictures) can be found in Refs. [79, 90].

### B.1.2 Impedance spectroscopy setup

Two setups have been used for impedance spectroscopic measurements. The first one was comprised of a HP 4192A RF impedance analyzer. Connected to a home-built impedance cell, it allows the measurements to be performed at frequencies ranging from 5 Hz to 13 MHz. The cell was placed inside a tube furnace and the temperature monitored using an OMRON E5CK controller with Ni-CrNi thermocouples. Here, the experiments can be performed at

temperatures from RT up to about 1200 K. A detailed presentation of this setup (especially of the impedance cell) can be found in Refs. [152, 153].

As the second setup the commercially available “turnkey” Concept 80 system (Novocontrol) has been used; see Fig. B.3. This includes an Alpha-A RF impedance analyzer with an active ZGS sample cell, providing a frequency range of 3  $\mu$ Hz ... 20 MHz. Alternatively, an Agilent 4991E RF impedance analyzer with an RF sample cell can be used, giving access to measurements at frequencies as high as 1 GHz. The temperature is controlled by a Quatro Cryosystem and allows measurements to be performed in the range of 113 K ... 620 K.

## B.2 Software

Listed below is the software used in the acquisition, processing and analysis of data presented in this work.

**TopSpin 3.1** (Bruker BioSpin GmbH): Execution of NMR experiments on the Avance III spectrometers; calculation and phase correction of NMR spectra using the built-in Fourier transformation routine.

**DMFIT Program:**<sup>[154,155]</sup> Conversion of the native Bruker file format into ASCII files.

**WSolids1:**<sup>[156]</sup> Simulation of quadrupolar solid-state NMR spectra.



**Figure B.3:** a) Photograph of the impedance spectroscopy workstation Concept 80 (Novocontrol). Close-ups of the active ZGS sample cell (b) and the RF sample cell (c), respectively.

**WinDETA 5.73** (NOVOCONTROL Technologies GmbH & Co. KG): Execution of all impedance spectroscopy experiments on the Concept 80 system and export of data.

**LabView 6.0:** Execution of the impedance spectroscopy experiments performed with the home-build cell in Hannover.

**IGOR Pro 6.34:** Processing, analysis, and presentation of all data acquired.

**Diamond 3.2:** Visualization of crystal structures.

**CorelDRAW X4:** Graphical post-processing of figures meant for publication.

**TeX Live 2012:** T<sub>E</sub>X typesetting distribution.

**Mendeley Desktop 1.11:** Management of references and generation of bibliographies.

## B.3 NMR pulse sequences

### B.3.1 Saturation recovery pulse sequence

NMR SLR time constants  $T_1$  in the laboratory frame of reference have been recorded employing the saturation recovery pulse sequence shown in Fig. B.4a. Here, a train of usually ten  $\beta_1 = \pi/2$  pulses in rapid succession is used to *saturate* the sample, *i. e.* to destroy the macroscopic longitudinal magnetization  $M_z$ . The subsequent *recovery* of the magnetization is then probed by a detection pulse  $\beta_2 = \pi/2$  after varying delay times  $t_d$ . The amplitude of the resulting FIDs (free induction decays) is proportional to the magnetization and—when plotted as a function of  $t_d$ —gives transients which are usually described by stretched exponentials of the form

$$M_z(t_d) = M_{z,eq} [1 - \exp(-[t_d/T_1]^\gamma)] , \quad (\text{B.1})$$

where  $M_{z,eq}$  is the magnetization at equilibrium and  $\gamma$  the stretching exponent. The phase cycling employed is given in Tab. B.1.\*

In the rotating frame, SLR $\rho$  times  $T_{1\rho}$  have been acquired by the spin-lock technique<sup>[157–160]</sup> depicted in Fig. B.4b. The first pulse  $\beta_1 = \pi/2$  rotates the equilibrium magnetization  $M_{\rho,eq}$  into the  $x$ - $y$  plane, where it is “spin locked” by the locking pulse  $\beta_2$  of variable duration  $t_{lock}$  in a magnetic field  $B_1$ . After switching off the locking pulse the magnetization is recorded in the form of FIDs, as usual. Since  $B_1$  is several orders of magnitude smaller than  $B_0$ , the magnetization will tend to relax towards its new equilibrium value, which is essentially zero. Thus, the transients recorded as a function of  $t_{lock}$  can be parametrized by an appropriate fitting function, *viz.*

$$M_\rho(t_{lock}) = M_{\rho,eq} \exp(-[t_d/T_{1\rho}]^\gamma) . \quad (\text{B.2})$$

---

\* Simple NMR spectra were obtained by Fourier transformation of an FID recorded at a sufficiently long delay time.

In order to ensure that the system reaches its equilibrium state prior to each scan, a recycle delay of at least  $5 \times T_1$  is chosen.

### B.3.2 Solid-state echo pulse sequence

The pulse sequence used to acquire solid-state echoes is shown in Fig. B.4c. The first pulse  $\beta_1 = \pi/2$  rotates the equilibrium magnetization into the  $x$ - $y$  plane, where the spins involved will dephase due to transverse relaxation (SSR) but also due to inhomogeneities (*e. g.* in the static field  $B_0$ ), leading to the usual FID. After some time  $t = t_p$  a refocusing pulse  $\beta_2 = 64^\circ$  is applied, chosen thusly in order to emphasize quadrupolar contributions for spin- $3/2$  nuclei.<sup>[160]</sup> This will reverse the inhomogeneity effects, resulting in an echo at  $t = 2t_p$ , whose time evolution is solely governed by SSR.<sup>[41]</sup> A parametrization of the echo intensity  $M_{x,y}(t_p)$  with an exponential of the form

$$M_{x,y}(t_p) = M_{x,y}^{\text{eq}} \exp(-[2t_p/T_2]^\gamma), \quad (\text{B.3})$$

gives then access to the spin-spin relaxation time  $T_2$ . The transients are usually described by single exponential functions (*i. e.*  $\gamma = 1$ ), though stretched exponentials with  $\gamma < 1$  are also found.\*

### B.3.3 $^7\text{Li}$ NMR SAE pulse sequence

$^7\text{Li}$  NMR stimulated-alignment echoes were recorded employing the Jeener-Broekaert pulse sequence shown in Fig. B.4d and described in Sect. 2.3.4. The appropriate phase cycling used to generate pure quadrupolar spin-alignment states by suppressing unwanted signal contributions is given in Tab. B.4.

The echo amplitudes  $S_2(t_p, t_m)$  have been recorded at a fixed preparation time (usually,  $t_p \approx 10 \mu\text{s}$ ) as a function of mixing time  $t_m$ . In the case of single-spin correlation functions,

\* Solid-state spectra can be derived from the echoes by Fourier transformation starting at the echo maximum.

**Table B.1:** Phase cycling employed in SLR experiments in the laboratory frame of reference as shown in Fig. B.4a.

No.	$\phi_1$	$\phi_2$	Receiver
1	+X	+X	+X
2	+X	-X	-X
3	+X	+Y	+Y
4	+X	-Y	-Y

**Table B.2:** Phase cycling used in the rotating frame to record SLR $\rho$  times  $T_{1\rho}$ . The corresponding pulse sequence is illustrated in Fig. B.4b.

No.	$\phi_1$	$\phi_2$	Receiver
1	+X	+Y	+X
2	-X	-Y	-X

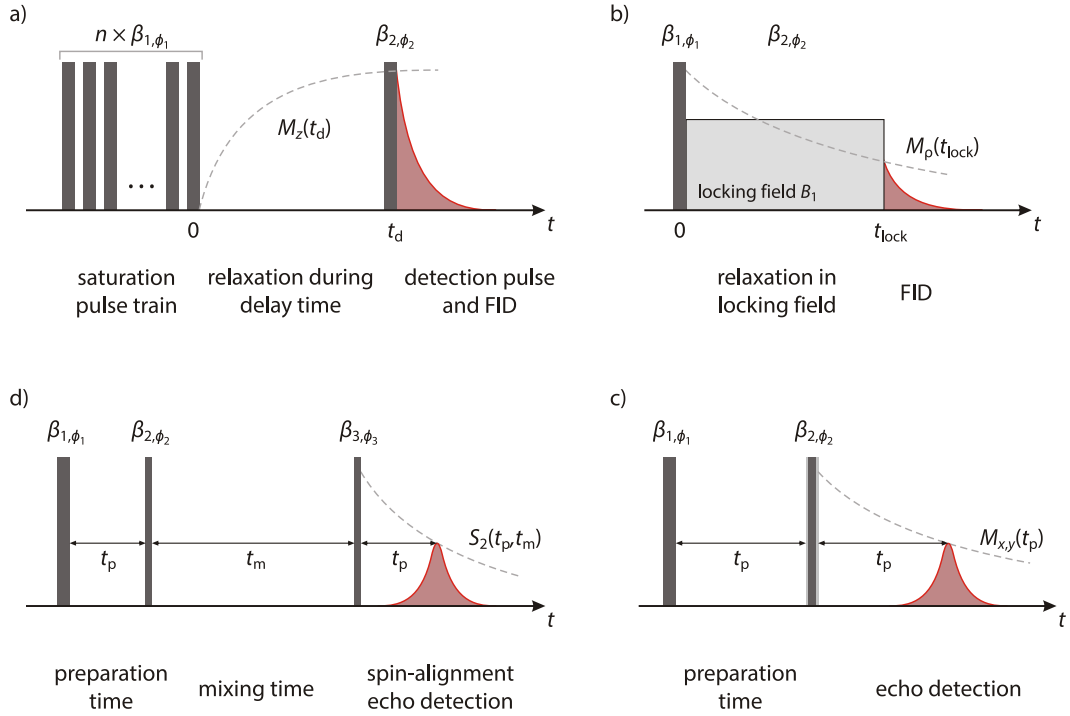


**Figure B.4:** Schematic representation of NMR pulse sequences used in this work (*cf.* also Ref. [99]). a) Saturation recovery pulse sequence used to record SLR times in the laboratory frame. The pulse lengths are  $\beta_1 = \beta_2 = \pi/2$  and the phase cycling is given in Tab. B.1. b) Spin-lock pulse sequence used to study SLR $\rho$  in the rotating frame of reference. The first pulse is chosen as  $\beta_1 = \pi/2$  and the second  $\beta_2$  is used to “spin-lock” the magnetization in the  $x$ - $y$  plane. The corresponding phase cycling can be found in Tab. B.2. c) Solid-state echo pulse sequence employed to record solid-echo spectra and SSR times  $T_2$ . With  $\beta_2 = 64^\circ$ , the length of the second pulse is optimized for spin- $3/2$  nuclei. The phase cycling is given in Tab. B.3. d) Jeener-Broekaert pulse sequence used to record spin-alignment echoes as a function of the mixing time  $t_m$ . The pulse lengths are chosen as  $\beta_1 = \pi/2$ ,  $\beta_2 = \beta_3 = \pi/4$  and the applied phase cycling is reproduced in Tab. B.4.

the resulting decay curves can be commonly parametrized by stretched exponentials of the form

$$S_2(t_p, t_m) = A \exp(-[t_m/\tau_{\text{SAE}}]^\gamma), \quad (\text{B.4})$$

where  $\tau_{\text{SAE}}$  is the SAE correlation time and  $\gamma$  the stretching exponent. However, generally, echo damping is also influenced by relaxation processes and spin-diffusion (*cf.* Sect. 2.3.4), both of which can lead to a second decay step, see *e. g.* Refs. [98, 99] (pages 47ff. and 65ff.).

**Table B.3:** Phase cycling employed in the acquisition of solid-echo spectra and SSR times  $T_2$ .  
See Fig. B.4c.

No.	$\phi_1$	$\phi_2$	Receiver
1	+X	+Y	+X
2	+Y	+Y	-X
3	+X	-X	-Y
4	+Y	-X	+Y
5	+X	-Y	+X
6	+Y	-Y	-X
7	+X	+X	-Y
8	+Y	+X	+Y

**Table B.4:** Phase cycling employed in SAE NMR experiments to record echo amplitudes  $S_2(t_p, t_m)$ ; cf. Fig. B.4d and Sect. 2.3.4.

No.	$\phi_1$	$\phi_2$	$\phi_3$	Receiver	No.	$\phi_1$	$\phi_2$	$\phi_3$	Receiver
1	+X	+Y	+X	-X	17	+X	+Y	-X	+X
2	-X	+Y	+X	+X	18	-X	+Y	-X	-X
3	+X	-Y	+X	+X	19	+X	-Y	-X	-X
4	-X	-Y	+X	-X	20	-X	-Y	-X	+X
5	+Y	+X	+X	+X	21	+Y	+X	-X	-X
6	-Y	+X	+X	-X	22	-Y	+X	-X	+X
7	+Y	-X	+X	-X	23	+Y	-X	-X	+X
8	-Y	-X	+X	+X	24	-Y	-X	-X	-X
9	+X	+Y	+Y	-Y	25	+X	+Y	-Y	+Y
10	-X	+Y	+Y	+Y	26	-X	+Y	-Y	-Y
11	+X	-Y	+Y	+Y	27	+X	-Y	-Y	-Y
12	-X	-Y	+Y	-Y	28	-X	-Y	-Y	+Y
13	+Y	+X	+Y	+Y	29	+Y	+X	-Y	-Y
14	-Y	+X	+Y	-Y	30	-Y	+X	-Y	+Y
15	+Y	-X	+Y	-Y	31	+Y	-X	-Y	+Y
16	-Y	-X	+Y	+Y	32	-Y	-X	-Y	-Y



## C List of publications

### C.1 Journal articles

**Short-range Li diffusion vs long-range ionic conduction in nanocrystalline lithium peroxide  $\text{Li}_2\text{O}_2$  — the discharge product in lithium-air batteries**

Dunst, A., Epp, V., Hanzu, I., Freunberger, S., and Wilkening, M. *Energy Environ. Sci.* **7**, 2739–2752 (2014).

**Motion of  $\text{Li}^+$  in Nanoengineered  $\text{LiBH}_4$  and  $\text{LiBH}_4:\text{Al}_2\text{O}_3$  — Comparison with the Microcrystalline Form**

Epp, V. and Wilkening, M. *ChemPhysChem* **14**, 3706–3713 (2013).

**Lithium motion in the anode material  $\text{LiC}_6$  as seen via time-domain  $^7\text{Li}$  NMR**

Langer, J., Epp, V., Heitjans, P., Mautner, F.-A., and Wilkening, M. *Phys. Rev. B* **88**, 094304-1–9 (2013).

**Highly Mobile Ions: Low-Temperature NMR Directly Probes Extremely Fast  $\text{Li}^+$  Hopping in Argyrodite-Type  $\text{Li}_6\text{PS}_5\text{Br}$**

Epp, V., Gün, Ö., Deiseroth, H.-J., Wilkening, M. *J. Phys. Chem. Lett.* **4**, 2118–2123 (2013).

**Two-dimensional diffusion in  $\text{Li}_{0.7}\text{NbS}_2$  as directly probed by frequency-dependent  $^7\text{Li}$  NMR**

Epp, V., Nakhal, S., Lerch, M., and Wilkening, M. *J. Phys.: Condens. Matter* **25**, 195402-1–7 (2013).

**Long-range  $\text{Li}^+$  dynamics in the lithium argyrodite  $\text{Li}_7\text{PSe}_6$  as probed by rotating-frame spin-lattice relaxation NMR**

Epp, V., Gün, Ö., Deiseroth, H.-J., and Wilkening, M. *Phys. Chem. Chem. Phys.* **15**, 7123–7132 (2013).

**Studying Li Dynamics in a Gas-Phase Synthesized Amorphous Oxide by NMR and Impedance Spectroscopy**

Epp, V., Brüning, C., Binnewies, M., Heitjans, P., and Wilkening, M. *Z. Phys. Chem.* **226**, 513–524 (2012).

**Macroscopic and microscopic  $\text{Li}^+$  transport parameters in cubic garnet-type “ $\text{Li}_{6.5}\text{La}_{2.5}\text{Ba}_{0.5}\text{ZrTaO}_{12}$ ” as probed by impedance spectroscopy and NMR**

Narayanan, S., Epp, V., Wilkening, M., and Thangadurai, V. *RSC Adv.* **2**, 2553–2561 (2012).

**Spin-alignment echo NMR: probing Li<sup>+</sup> hopping motion in the solid electrolyte Li<sub>7</sub>La<sub>3</sub>Zr<sub>2</sub>O<sub>12</sub> with garnet-type tetragonal structure**

Kuhn, A., Epp, V., Schmidt, G., Narayanan, S., Thangadurai, V., and Wilkening, M. *J. Phys: Condens. Matter* **24**, 035901-1–9 (2012).

**Fast Li diffusion in crystalline LiBH<sub>4</sub> due to reduced dimensionality: Frequency-dependent NMR spectroscopy**

Epp, V. and Wilkening, M. *Phys. Rev. B* **82**, 020301-1–4 (2010).

**Tuning the Li Diffusivity of Poor Ionic Conductors by Mechanical Treatment: High Li Conductivity of Strongly Defective LiTaO<sub>3</sub> Nanoparticles**

Wilkening, M., Epp, V., Feldhoff, A., and Heitjans, P. *J. Phys. Chem. C* **112**, 9291–9300 (2008).

**Microscopic Li self-diffusion parameters in the lithiated anode material Li<sub>4+x</sub>Ti<sub>5</sub>O<sub>12</sub> (0 ≤ x ≤ 3) measured by <sup>7</sup>Li solid state NMR**

Wilkening, M., Iwaniak, W., Heine, J., Epp, V., Kleinert, A., Behrens, M., Nuspl, G., Bensch, W., and Heitjans, P. *Phys. Chem. Chem. Phys.* **9**, 6199–6202 (2007).

## C.2 Poster presentations

**Extreme mobility: low-temperature NMR probes highly diffusive Li<sup>+</sup> ions in argyrodite-type Li<sub>6</sub>PSe<sub>5</sub>Cl and Li<sub>6</sub>PS<sub>5</sub>Br**

Epp, V., Gün, Ö., Deiseroth, H.-J., and Wilkening, M. — *Diffusion Fundamentals V*, Leipzig (DE), August 26th–28th, 2013.

**2D Li diffusion in layer-structured Li<sub>x</sub>NbS<sub>2</sub> as probed by frequency-dependent T<sub>1ρ</sub> NMR measurements**

Epp, V., Nakhal, S., Lerch, M., and Wilkening, M. — *GDCh – 16. Vortragstagung der FG Festkörperchemie und Materialforschung*, Darmstadt (DE), September 17th–19th, 2012.

**Li dynamics in the solid electrolyte Li<sub>7</sub>PSe<sub>6</sub> as probed by diffusion-induced <sup>7</sup>Li NMR spin-lattice relaxation**

Epp, V., Gün, Ö., Deiseroth, H.-J., and Wilkening, M. — *III. Tagung der Deutschen Bunsen-Gesellschaft für Physikalische Chemie*, Leipzig (DE), May 17th–19th, 2012.

**Li diffusion in garnet-type Li<sub>6.5</sub>La<sub>2.5</sub>Ba<sub>0.5</sub>ZrTaO<sub>12</sub> crystallizing with cubic symmetry**

Epp, V., Narayanan, S., Thangadurai, V., and Wilkening, M. — *Bunsen Colloquium: Diffusion in Solids – Methods, Models, and Materials*, Hannover (DE), October 27th–28th, 2011.

**Different approaches to improving the Li diffusivity of polycrystalline lithium borohydride**

Epp, V. and Wilkening, M. — *18th International Conference on Solid State Ionics*, Warszawa (PL), July 3rd–8th, 2011.

**Tuning the Li diffusivity of polycrystalline  $\text{LiBH}_4$  by interface engineering**

Epp, V. and Wilkening, M. — 110. *Tagung der Deutschen Bunsen-Gesellschaft für Physikalische Chemie*, Berlin (DE), June 2nd–4th, 2011.

**Investigation of Li dynamics in gas-phase synthesized amorphous oxides by NMR and impedance spectroscopy**

Epp, V., Brünig, C., Wilkening, M., Binnewies, M., and Heitjans, P. — *DPG – Spring meeting of the Division Condensed Matter*, Regensburg (DE), March 21st–26th, 2010.

**Lithium diffusion studies of gas-phase synthesized amorphous oxides – An NMR study**

Epp, V., Brünig, C., Wilkening, M., Binnewies, M., and Heitjans, P. — *Bunsen Colloquium: Spectroscopic Methods in Solid State Diffusion and Reactions*, Hannover (DE), September 24th–25th, 2009.

**Improving the Li diffusivity of poor ionic conductors by high-energy ball milling: High Li conductivity of nanocrystalline  $\text{LiTaO}_3$  and  $\text{LiNbO}_3$** 

Epp, V., Wilkening, M., Feldhoff, A., and Heitjans, P. — 107. *Tagung der Deutschen Bunsen-Gesellschaft für Physikalische Chemie*, Saarbrücken (DE), May 1st–5th, 2008.

**Tuning the Li diffusivity of poor ionic conductors by mechanical treatment: High Li conductivity of nanocrystalline  $\text{LiTaO}_3$** 

Epp, V., Wilkening, M., Feldhoff, A., and Heitjans, P. — *DPG – Spring meeting of the Division Condensed Matter*, Berlin (DE), February 25th–29th, 2008.





# Bibliography

- [1] Solomon, S., Plattner, G.-K., Knutti, R., and Friedlingstein, P. *Proc. Nat. Acad. Sci.* **106**, 1704–1709 (2009).
- [2] *Climate Change 2014: Impacts, Adaptation, and Vulnerability. Part A: Global and Sectoral Aspects*. Field, C. B., Barros, V. R., Dokken, D. J., Mach, K. J., Mastrandrea, M. D., Bilir, T. E., Chatterjee, M., Ebi, K. L., Estrada, Y. O., Genova, R. C., Girma, B., Kissel, E. S., Levy, A. N., MacCracken, S., Mastrandrea, P. R., and White, L. L., editors, Cambridge University Press. Report (2014) • <http://ipcc-wg2.gov/AR5/report/>.
- [3] Dell, R. M. and Rand, D. A. J. *J. Power Sources* **100**, 2–17 (2001).
- [4] Holden, E. and Høyer, K. G. *Transp. Res. D* **10**, 395–403 (2005).
- [5] Doughty, D. and Roth, E. P. *Interface* **21**, 37–44 (2012).
- [6] Roth, E. P. and Orendorff, C. J. *Interface* **21**, 45–50 (2012).
- [7] Golubkov, A. W., Fuchs, D., Wagner, J., Wiltse, H., Stangl, C., Fauler, G., Voitc, G., Thaler, A., and Hacker, V. *RSC Adv.* **4**, 3633–3642 (2014).
- [8] Maier, J. *Nat. Mater.* **4**, 805–815 (2005).
- [9] Heitjans, P., Indris, S., and Wilkening, M. In *Nanocomposites*, Knauth, P. and Schoonman, J., editors, volume 10 of *Electronic Materials: Science and Technology*, 227–246. Springer, New York (2007).
- [10] Wilkening, M., Epp, V., Feldhoff, A., and Heitjans, P. *J. Phys. Chem. C* **112**, 9291–9300 (2008).
- [11] Heitjans, P. and Wilkening, M. *MRS Bull.* **34**, 915–922 (2009).
- [12] Farrington, G. C. and Briant, J. L. *Science* **204**, 1371–1379 (1979).
- [13] Brinkmann, D., Mali, M., Roos, J., Messer, R., and Birli, H. *Phys. Rev. B* **26**, 4810–4825 (1982).
- [14] Bader, B., Heitjans, P., Stockmann, H. J., Ackermann, H., Buttler, W., Freilander, P., Kiese, G., van der Marel, C., and Schirmer, A. *J. Phys.: Condens. Matter* **4**, 4779–4800 (1992).

- [15] Julien, C. and Nazri, G. A. *Solid State Ionics* **68**, 111–116 (1994).
- [16] Van der Ven, A., Ceder, G., Asta, M., and Tepeesch, P. D. *Phys. Rev. B* **64**, 184307 (2001).
- [17] Wilkening, M. and Heitjans, P. *Phys. Rev. B* **77**, 24311 (2008).
- [18] Brezesinski, T., Wang, J., Tolbert, S. H., and Dunn, B. *Nat. Mater.* **9**, 146–151 (2010).
- [19] Borg, R. J. and Dienes, G. J. *An Introduction to Solid State Diffusion*. Academic Press, Boston, San Diego, New York, Berkley, London, Sydney, Tokyo, Toronto (1988).
- [20] Murch, G. E. In *Phase Transformations in Materials*, Kosterz, G., editor, 171–238. Wiley-VCH Verlag GmbH, Weinheim (2001).
- [21] Mehrer, H. In *Diffusion in Condensed Matter*, Heitjans, P. and Kärger, J., editors, 3–63. Springer, Berlin (2005).
- [22] Mehrer, H. *Diffusion in Solids: Fundamentals, Methods, Materials, Diffusion-Controlled Processes*. Springer, Berlin, New York (2007).
- [23] Philibert, J. *Diffusion Fundamentals* **2**, 1.1–10 (2005).
- [24] Fick, A. *Ann. Phys.* **170**, 59–86 (1855).
- [25] Fick, A. *J. Membr. Sci.* **100**, 33–38 (1995).
- [26] Einstein, A. *Ann. Phys.* **322**, 549–560 (1905).
- [27] Einstein, A. *Ann. Phys.* **324**, 371–381 (1906).
- [28] von Smoluchowski, M. *Ann. Phys.* **326**, 756–780 (1906).
- [29] Einstein, A. and von Smoluchowski, M. *Untersuchungen über die Theorie der Brownschen Bewegung*. Verlag Harri Deutsch, Thun/Frankfurt am Main, 3rd edition (1997).
- [30] Kärger, J., editor. *Leipzig, Einstein, Diffusion*. Leipziger Universitätsverlag, Leipzig, 2nd edition (2010).
- [31] Funke, K. *Sci. Technol. Adv. Mater.* **14**, 43502 (2013).
- [32] Brown, R. *Ann. Phys.* **90**, 294–313 (1828).
- [33] Schmalzried, H. *Chemical Kinetics of Solids*. VCH, Weinheim, New York, Basel, Cambridge, Tokyo (1995).
- [34] Kleber, W., Bautsch, H.-J., Bohm, J., and Klimm, D. *Einführung in die Kristallographie*. Oldenbourg Wissenschaftsverlag GmbH, München, 19th edition (2010).

- [35] Wollenberger, H. J. In *Physical Metallurgy*, Cahn, R. W. and Haasen, P., editors, volume 2, 1621–1720. Elsevier Science B. V., Amsterdam, 4th edition (1996).
- [36] Christian, J. W. and Vitek, V. *Rep. Prog. Phys.* **33**, 307–411 (1970).
- [37] Hirth, J. P. In *Physical Metallurgy*, Cahn, R. W. and Haasen, P., editors, volume 3, 1831–1875. Elsevier Science B. V., Amsterdam, 4th edition (1996).
- [38] Heitjans, P. and Indris, S. *J. Phys.: Condens. Matter* **15**, R1257–R1289 (2003).
- [39] Wadhwa, A. S. and Dhaliwal, H. S. *A Textbook of Engineering Material and Metallurgy*. University Science Press, New Delhi (2008).
- [40] Rothman, S. J. In *Diffusion in Materials*, Laskar, A. L., Bocquet, J. L., Brebec, G., and Monty, C., editors, 269–286. Kluwer Academic Publishers, Dordrecht, Boston, London (1990).
- [41] Hahn, E. L. *Phys. Rev.* **80**, 580–594 (1950).
- [42] Stilbs, P. *Prog. Nucl. Magn. Reson. Spectrosc.* **19**, 1–45 (1987).
- [43] Stejskal, E. O. and Tanner, J. E. *J. Chem. Phys.* **42**, 288–292 (1965).
- [44] Blanter, M. S., Golovin, I. S., Neuhäuser, H., and Sinning, H.-R. *Internal Friction in Metallic Materials – A Handbook*. Springer, Berlin, New York (2007).
- [45] Gorsky, W. S. *Phys. Z. Sowjetunion* **8**, 457–471 (1935).
- [46] Alefeld, G., Völkl, J., and Schaumann, G. *phys. status solidi (b)* **37**, 337–351 (1970).
- [47] Schaumann, G., Völkl, J., and Alefeld, G. *phys. status solidi (b)* **42**, 401–413 (1970).
- [48] Völkl, J. *Ber. Bunsenges. Phys. Chem.* **76**, 797–805 (1972).
- [49] Völkl, J. and Alefeld, G. *Il Nuovo Cimento B Series II* **33**, 190–204 (1976).
- [50] Snoek, J. L. *Physica* **6**, 591–592 (1939).
- [51] Snoek, J. L. *Physica* **8**, 711–733 (1941).
- [52] Wert, C. A. *J. Phys. Chem. Solids* **31**, 1771–1783 (1970).
- [53] Zener, C. *Trans. AIME* **152**, 122–126 (1943).
- [54] Zener, C. *Phys. Rev.* **71**, 34–38 (1947).
- [55] Bocquet, J. L., Brebec, G., and Limoge, Y. In *Physical Metallurgy*, Cahn, R. W. and Haasen, P., editors, 535–668. Elsevier Science B. V., Amsterdam, 4th edition (1996).

- [56] Mössbauer, R. L. *Z. Angew. Phys.* **151**, 124–143 (1958).
- [57] Parak, F. *Nature* **478**, 325 (2011).
- [58] *The Nobel Prize in Physics 1961*. Nobel Media AB 2014. Web, 5 August 2014 • [http://www.nobelprize.org/nobel\\_prizes/physics/laureates/1961/](http://www.nobelprize.org/nobel_prizes/physics/laureates/1961/).
- [59] Vogl, G. and Petry, W. In *Festkörperprobleme 25*, Grosse, P., editor, volume 25 of *Advances in Solid State Physics*, 655–667. Springer, Berlin, Heidelberg (1985).
- [60] Vogl, G. and Sepiol, B. In *Diffusion in Condensed Matter*, Heitjans, P. and Kärger, J., editors, 65–91. Springer, Berlin (2005).
- [61] Bée, M. *Quasielastic Neutron Scattering: Principles and Applications in Solid State Chemistry, Biology, and Materials Science*. Adam Hilger, Bristol, Philadelphia (1988).
- [62] Springer, T. In *Springer Tracts in Modern Physics*, volume 64, 1–100. Springer, Berlin, Heidelberg (1972).
- [63] Springer, T. and Lechner, R. E. In *Diffusion in Condensed Matter*, Heitjans, P. and Kärger, J., editors, 93–164. Springer, Berlin (2005).
- [64] Hempelmann, R. *Quasielastic Neutron Scattering and Solid State Diffusion*. Clarendon Press, Oxford (2000).
- [65] *The Nobel Prize in Physics 1952*. Nobel Media AB 2013. Web, 6 May 2014 • [http://www.nobelprize.org/nobel\\_prizes/physics/laureates/1952/](http://www.nobelprize.org/nobel_prizes/physics/laureates/1952/).
- [66] Levitt, M. H. *Spin Dynamics: Basics of Nuclear Magnetic Resonance*. John Wiley & Sons, Hoboken, NJ, 2nd edition (2008).
- [67] Nolting, W. *Grundkurs Theoretische Physik 5/1: Quantenmechanik – Grundlagen*. Springer, Berlin, Heidelberg, 8th edition (2013).
- [68] Schwabl, F. *Quantenmechanik (QM I)*. Springer, Berlin, Heidelberg, New York, 7th edition (2007).
- [69] Scheck, F. *Theoretische Physik 2: Nichtrelativistische Quantenmechanik*. Springer-Lehrbuch. Springer, Berlin, Heidelberg, 3rd edition (2013).
- [70] Scheck, F. *Quantum Physics*. Springer, Heidelberg, New York, Dordrecht, London, 2nd edition (2013).
- [71] Duer, M. J. *Introduction to Solid-State NMR Spectroscopy*. Blackwell Science Ltd, Malden, MA (2004).
- [72] Duer, M. J., editor. *Solid State NMR Spectroscopy: Principles and Applications*. Number 39. Blackwell Science Ltd, Malden, MA (2002).

- [73] Slichter, C. P. *Principles of Magnetic Resonance*. Springer-Verlag, Berlin, New York, 3rd edition (1990).
- [74] Abragam, A. *The Principles of Nuclear Magnetism*. Oxford University Press, Oxford, U.K. (1961).
- [75] Kelly, S. W. and Sholl, C. A. *J. Phys.: Condens. Matter* **4**, 3317–3330 (1992).
- [76] Heitjans, P., Indris, S., and Wilkening, M. *Diffusion Fundamentals* **2**, 45.1–20 (2005).
- [77] Bloembergen, N., Purcell, E. M., and Pound, R. V. *Phys. Rev.* **73**, 679–712 (1948).
- [78] Richards, P. M. In *Physics of Superionic Conductors*, Salamon, M. B., editor, 141–174. Springer-Verlag, Berlin, New York, 1st edition (1979).
- [79] Wilkening, M. *Ultralangsame Ionenbewegungen in Festkörpern*. Logos Verlag Berlin GmbH, Berlin (2005). Dissertation, Universität Hannover.
- [80] Beckmann, P. A. *Phys. Rep.* **171**, 85–128 (1988).
- [81] Bunde, A., Dieterich, W., Maass, P., and Meyer, M. In *Diffusion in Condensed Matter*, Heitjans, P. and Kärger, J., editors, 813–856. Springer, Berlin (2005).
- [82] Küchler, W. *Kernspinresonanz-Untersuchungen zur Diffusion von Li in der schichtstrukturierten und der kubischen Interkalationsverbindung  $\text{Li}_x\text{TiS}_2$* . Dissertation, Universität Hannover (1992).
- [83] Ritter, C., Müller-Warmuth, W., and Schöllhorn, R. *J. Chem. Phys.* **83**, 6130–6138 (1985).
- [84] Heitjans, P., Schirmer, A., and Indris, S. In *Diffusion in Condensed Matter*, Heitjans, P. and Kärger, J., editors, 367–415. Springer, Berlin (2005).
- [85] Avogadro, A. and Villa, M. *J. Chem. Phys.* **66**, 2359–2367 (1977).
- [86] Sholl, C. A. *J. Phys. C: Solid State Phys.* **14**, 447–464 (1981).
- [87] Richards, P. M. *Solid State Commun.* **25**, 1019–1021 (1978).
- [88] Küchler, W., Heitjans, P., Payer, A., and Schöllhorn, R. *Solid State Ionics* **70-71**, 434–438 (1994).
- [89] Qi, F.  *$^2\text{H}$ - und  $^7\text{Li}$ -NMR-Untersuchungen zur Dynamik an Ionenleitern*. Dissertation, Johannes Gutenberg-Universität Mainz (2003).
- [90] Ruprecht, B. *Langsamer Li-Transport in Lithiumübergangsmetalloxiden untersucht mit NMR- und impedanzspektroskopischen Methoden*. Dissertation, Leibniz Universität Hannover (2012).

- [91] Tang, X.-P. and Wu, Y. *J. Magn. Reson.* **133**, 155–165 (1998).
- [92] Wilkening, M., Küchler, W., and Heitjans, P. *Phys. Rev. Lett.* **97**, 65901 (2006).
- [93] Wilkening, M. and Heitjans, P. *ChemPhysChem* **13**, 53–65 (2012).
- [94] Ruprecht, B., Wilkening, M., Uecker, R., and Heitjans, P. *PCCP* **14**, 11974–11980 (2012).
- [95] Jeener, J. and Broekaert, P. *Phys. Rev.* **157**, 232–240 (1967).
- [96] Böhmer, R. *J. Magn. Reson.* **147**, 78–88 (2000).
- [97] Böhmer, R., Jeffrey, K. R., and Vogel, M. *Prog. Nucl. Magn. Reson. Spectrosc.* **50**, 87–174 (2007).
- [98] Kuhn, A., Epp, V., Schmidt, G., Narayanan, S., Thangadurai, V., and Wilkening, M. *J. Phys.: Condens. Matter* **24**, 35901 (2012).
- [99] Epp, V., Gün, O., Deiseroth, H.-J., and Wilkening, M. *PCCP* **15**, 7123–32 (2013).
- [100] Schaefer, D., Leisen, J., and Spiess, H. W. *J. Magn. Reson., Series A* **115**, 60–79 (1995).
- [101] Qi, F., Diezemann, G., Böhm, H., Lambert, J., and Böhmer, R. *J. Magn. Reson.* **169**, 225–239 (2004).
- [102] Spiess, H. W. *J. Chem. Phys.* **72**, 6755–6762 (1980).
- [103] Faske, S., Eckert, H., and Vogel, M. *Phys. Rev. B* **77**, 104301 (2008).
- [104] Wilkening, M., Kuhn, A., and Heitjans, P. *Phys. Rev. B* **78**, 54303 (2008).
- [105] Buschmann, H., Dolle, J., Berendts, S., Kuhn, A., Bottke, P., Wilkening, M., Heitjans, P., Senyshyn, A., Ehrenberg, H., Lotnyk, A., Duppel, V., Kienle, L., and Janek, J. *PCCP* **13**, 19378–19392 (2011).
- [106] Welsch, A.-M., Behrens, H., Horn, I., Roß, S., and Heitjans, P. *J. Phys. Chem. A* **116**, 309–318 (2012).
- [107] Macdonald, J. R. *Ann. Biomed. Eng.* **20**, 289–305 (1992).
- [108] Barsoukov, E. and Macdonald, J. R., editors. *Impedance Spectroscopy – Theory, Experiment, and Applications*. Wiley, Hoboken, N. J., 2nd edition (2005).
- [109] Cole, K. S. and Cole, R. H. *J. Chem. Phys.* **9**, 341–351 (1941).
- [110] Randles, J. E. B. *Discuss. Faraday Soc.* **1**, 11–19 (1947).
- [111] Jaffé, G. *Phys. Rev.* **85**, 354–363 (1952).

- [112] Macdonald, J. R. and Johnson, W. B. In *Impedance Spectroscopy – Theory, Experiment, and Applications*, Barsoukov, E. and Macdonald, J. R., editors, 1–26. Wiley, Hoboken, N. J. (2005).
- [113] Macdonald, J. R. and Garber, J. A. *J. Electrochem. Soc.* **124**, 1022–1030 (1977).
- [114] Macdonald, J. R., Schoonman, J., and Lehnen, A. P. *J. Electroanal. Chem. Interfacial Electrochem.* **131**, 77–95 (1982).
- [115] McKubre, M. C. H. and Macdonald, D. D. In *Impedance Spectroscopy – Theory, Experiment, and Applications*, Barsoukov, E. and Macdonald, J. R., editors, 129–204. Wiley, Hoboken, N. J. (2005).
- [116] Carter, C. W. *Bell Syst. Tech. J.* **4**, 387–401 (1925).
- [117] Orazem, M. E. and Tribollet, B. *Electrochemical Impedance Spectroscopy*. Wiley, Hoboken, N. J. (2008).
- [118] Lvovich, V. F. *Impedance Spectroscopy: Applications to Electrochemical and Dielectric Phenomena*. Wiley, Hoboken, N. J. (2012).
- [119] Epp, V. and Wilkening, M. *ChemPhysChem* **14**, 3706–3713 (2013).
- [120] Kimball, J. C. and Adams, L. W. *Phys. Rev. B* **18**, 5851–5858 (1978).
- [121] Jonscher, A. K. *Nature* **267**, 673–679 (1977).
- [122] Lee, W. K., Liu, J. F., and Nowick, A. S. *Phys. Rev. Lett.* **67**, 1559–1561 (1991).
- [123] Lim, B. S., Vaysleyb, A. V., and Nowick, A. S. *Appl. Phys. A* **56**, 8–14 (1993).
- [124] Sidebottom, D. L., Green, P. F., and Brow, R. K. *Phys. Rev. Lett.* **74**, 5068–5071 (1995).
- [125] Nowick, A. S., Vaysleyb, A. V., and Kuskovsky, I. *Phys. Rev. B* **58**, 8398–8406 (1998).
- [126] Nowick, A. S., Vaysleyb, A. V., and Liu, W. *Solid State Ionics* **105**, 121–128 (1998).
- [127] Rizos, A. K., Alifragis, J., Ngai, K. L., and Heitjans, P. *J. Chem. Phys.* **114**, 931–934 (2001).
- [128] Kanert, O., Küchler, R., Soares, P. C., and Jain, H. *J. Non-Cryst. Solids* **307**, 1031–1038 (2002).
- [129] Funke, K., Cramer, C., and Wilmer, D. In *Diffusion in Condensed Matter*, Heitjans, P. and Kärger, J., editors, 857–893. Springer, Berlin (2005).
- [130] Funke, K., Banhatti, R. D., Laughman, D., Badr, L., Mutke, M., Šantić, A., Wrobel, W., Fellberg, E. M., and Biermann, C. *Z. Phys. Chem.* **224**, 1891–1950 (2010).

- [131] Ngai, K. L., Capaccioli, S., Shinyashiki, N., and Thayyil, M. S. *J. Non-Cryst. Solids* **356**, 535–541 (2010).
- [132] Strom, U., Hendrickson, J. R., Wagner, R. J., and Taylor, P. C. *Solid State Commun.* **15**, 1871–1875 (1974).
- [133] Nernst, W. *Z. Phys. Chem.* **2**, 613–637 (1888).
- [134] Townsend, J. S. *Philos. Trans. R. Soc. London A* **193**, 129–158 (1900).
- [135] Einstein, A. *Z. Elektrochem.* **14**, 235–239 (1908).
- [136] Murch, G. E. *Solid State Ionics* **7**, 177–198 (1982).
- [137] Lidiard, A. B. *Il Nuovo Cimento* **7**, 620–631 (1958).
- [138] Murch, G. E. and Dyre, J. C. *Solid State Ionics* **20**, 203–207 (1986).
- [139] Dyre, J. C. and Murch, G. E. *Solid State Ionics* **21**, 139–142 (1986).
- [140] Isard, J. O. *J. Non-Cryst. Solids* **246**, 16–26 (1999).
- [141] Bychkov, E., Price, D. L., and Lapp, A. *J. Non-Cryst. Solids* **293-295**, 211–219 (2001).
- [142] Feldmann, H., Lechner, R. E., and Wilmer, D. *MRS Proc.* **756**, 81–86 (2002).
- [143] Spaeth, M., Kreuer, K.-D., Maier, J., and Cramer, C. *J. Solid State Chem.* **148**, 169–177 (1999).
- [144] Epp, V., Gün, O., Deiseroth, H.-J., and Wilkening, M. *J. Phys. Chem. Lett.* **4**, 2118–2123 (2013).
- [145] Freiländer, P., Heitjans, P., Ackermann, H., Bader, B., Kiese, G., Schirmer, A., Stöckmann, H. J., der Marel, C. V., Magerl, A., and Zabel, H. *Z. Phys. Chem.* **151**, 93–101 (1987).
- [146] Schirmer, A. and Heitjans, P. *Z. Naturforsch.* **50a**, 643–652 (1995).
- [147] Epp, V. and Wilkening, M. *Phys. Rev. B* **82**, 20301 (2010).
- [148] Whittingham, M. S. *Chem. Rev.* **104**, 4271–4302 (2004).
- [149] Xu, B., Qian, D., Wang, Z., and Meng, Y. S. *Mater. Sci. Eng. R* **73**, 51–65 (2012).
- [150] Chen, J. *Materials* **6**, 156–183 (2013).
- [151] Riccò, M., Belli, M., Mazzani, M., Pontiroli, D., Quintavalle, D., Jánossy, A., and Csányi, G. *Phys. Rev. Lett.* **102**, 145901 (2009).

- [152] Indris, S. *Perkolation von Grenzflächen in nanokristallinen keramischen Kompositen –  $^7\text{Li}$ -NMR-Relaxation*. Cuvillier Verlag, Göttingen (2001). Dissertation, Universität Hannover.
- [153] Masoud, M. *Diffusivity and ionic conductivity in lithium niobate and related glasses and glass composites*. Dissertation, Universität Hannover (2005).
- [154] Massiot, D., Fayon, F., Capron, M., King, I., Le Calvé, S., Alonso, B., Durand, J.-O., Bujoli, B., Gan, Z., and Hoatson, G. *Magn. Reson. Chem.* **40**, 70–76 (2002).
- [155] Massiot, D. *Dmfit Program*. NMR Spectrum Fitting Software, ver. 20090330, CRMHT - CNRS (2009) • <http://nmr.cemhti.cnrs-orleans.fr/Dmfit/Default.aspx>.
- [156] Eichele, K. *WSolids1*. Solid-State NMR Spectrum Simulation, ver. 1.19.11, Universität Tübingen (2009) • <http://anorganik.uni-tuebingen.de/klaus/soft/index.php?p=wsolids1/wsolids1>.
- [157] Ailion, D. C. and Slichter, C. P. *Phys. Rev. Lett.* **12**, 168–171 (1964).
- [158] Slichter, C. P. and Ailion, D. C. *Phys. Rev.* **135**, A1099–A1110 (1964).
- [159] Wolf, D. *Phys. Rev. B* **10**, 2724–2732 (1974).
- [160] Fukushima, E. and Roeder, S. B. W. *Experimental Pulse NMR: A Nuts and Bolts Approach*. Addison-Wesley, Reading (1981).



# Acknowledgments

Many thanks are due to my advisor, Prof. Dr. Martin Wilkening, not only for his support and supervision in my scientific endeavors but also for the unique opportunity of joining him here in Graz, where I had the great fortune to witness our group grow and prosper. I also greatly appreciate the fact that he always has a friendly ear and encouraging words for those in need of either or both.

I am grateful to Prof. Dr. Paul Heitjans for introducing me to the very interesting field of solid-state NMR during his supervision of my diploma thesis in Hannover and for all the helpful discussions contributing to my understanding of the field. His input to publications are also greatly appreciated. Further, a big thank you for his kind willingness to assume the rôle of the second reviewer of the present work.

Many thanks are also due to our collaborators, without whom the majority of the publications presented here would not have been possible. Here the groups of Prof. Heitjans (Hannover), Prof. Binnewies (Hannover), Prof. Deiseroth (Siegen), Prof. Lerch (Berlin), Prof. Thangadurai (Calgary), and Prof. Mautner (Graz) are well worth mentioning.

Also many, many thanks to my colleagues – present and former. Not only did they provide many fruitful discussions and helpful pointers, they were also “responsible” for a very relaxed working atmosphere and generally good times. I consider myself very lucky to have met every single one of them.

Last, but certainly not least, my deepest gratitude is without any doubt due to my parents, Lilli and Peter Epp, whose unconditional support and encouragement made this work possible in the first place. Thank you very, very much!

